

Dissertation
Faculty of Civil Engineering
Graz University of Technology

**The analysis of rotational and sliding
modes of failure for slopes, foundations,
and underground structures in blocky,
hard rock**

Reviewers

Prof. Wulf Schubert

Prof. Richard E. Goodman

Author

Markus Pötsch

Acknowledgement

On having completed the dissertation I would like to extend my sincerest thanks to all of the many persons who supported me with guidance, ideas, discussions, and of course hands-on experience and help.

In particular, I am most grateful to my research supervisor, Prof. Wulf Schubert, for motivating me to dare and perform this project, his open doors when having concerns, giving free space to develop own approaches and his skilful advice. I would also like to thank for his constant patience and his confidence in concluding this work.

It is a pleasure to thank Prof. Richard E. Goodman for reviewing the thesis and his involvement during completing the document. It was an honour to receive comments, ideas and impulses directly from the founder of block theory, a highly relevant topic in this work.

I owe my deepest gratitude to Dr. Andreas Gaich from 3G Software & Measurement for his will to initiating and supporting this research, technically and financially, and for the whole lot of time spending advice for continuing and finishing the work.

This work has been partially funded by the FFG, the Austrian Research Promotion Agency, which is hereby cordially acknowledged.

I would like to thank my fiends and former colleagues at the Institute for Rock Mechanics and Tunnelling, Dr. Karl Großbauer, Nedim Radončić, and Thomas Pilgerstorfer for their valuable time of discussion and help at and after work. I am also grateful to Gerald Pischinger from the Institute for Applied Geosciences for his highly appreciated collaboration when doing the first applications with the new measurement system.

I am deeply grateful to Thomas Schieg and Christian Seywald for their great laboratory work and related achievements. I would like to thank Dr. Manfred Blümel and Anton Kaufmann for their advice and assistance in the laboratory tests.

I would like to extend my sincerest thanks to my parents for the support and understanding during the last years. Finally, I would like to express my gratitude to my companion Karin and daughter Anna for their support, patience and love during the many hours I could not spend with them. Thank you!

Abstract

The analysis and stability assessment of rock blocks forms part of the tasks covered by rock mechanics. Rock blocks are defined by fractures or other zones of weakness (discontinuities) within the rock mass. It is thus crucial to correctly determine the fracture system of a rock mass for a meaningful block stability assessment. Fractures have traditionally been mapped and characterised by using the methods of engineering geology. In the past decade remote measurement systems based on laser technology or photogrammetry have been developed and applied for the collection of discontinuity data at exposed rock faces. Especially 3D imaging systems are suitable to identifying relevant fractures and measuring the corresponding geometric properties. Geologic assessments of 3D images mark a new data quality in engineering geology. Methods for a fast and consistent processing of these data towards rock mechanics analyses are, anyhow, still missing.

This work presents a procedure for integrating discontinuity measurements from 3D images into a block analysis method. The procedure includes (1) data collection in the field using an image based remote measurement system, (2) 3D image generation and registration, (3) assessment of the 3D image with respect to discontinuities, (4) establishment of a geometric model of the rock surface and discontinuities, (5) identification of finite (isolated) blocks, (6) determination of the blocks's metric properties, (7) analysis of the kinematic movability of finite blocks, and (8) analysis of the block stability. Methods from engineering geology, digital photogrammetry, computer vision, digital image processing, computational geometry, numerical analysis, laboratory testing, general mechanics, and rock mechanics are applied in this procedure.

In detail, the dissertation discusses important requirements on remote measurement systems for geologic data collection at exposed rock faces such as accuracy, resolution, working range, etc. It reviews frequently used systems including laser scanning, image based systems, and radar systems. As a result, image based systems comply with the requirements on geologic data collection. ShapeMetriX3D, a 3D imaging system based on computer vision and photogrammetry has been exemplarily applied within this work. Its principles, field application, and provided results and measurements are described and their practical reliability investigated.

Discontinuity measurements from a 3D image and the excavation topography are used to establish a geometric model of the excavation surface. The geometric model is a trace network on an irregular surface. A trace search and intersection algorithm together with Goodman & Shi's theorem of finiteness allows identifying isolated blocks within the geometric model. The definition of the block geometry requires the vertex co-ordinates, the block planes and the corresponding blockside halfspaces, and the connectivities of the parameters. The

blocks's metric properties such as mass or the inertia tensor are directly calculated using the blocks's vertex coordinates obtained in the previous process.

The sliding behaviour of rock blocks is, most of all, dominated by the properties of the joints between the blocks and the rock mass. Three typical stages of the shear behaviour of rough, unfilled joints are distinguished including mobilisation of shear stress, mobilisation of dilation, and surface degradation. A constitutive relationship describes the normal and shear stresses, and normal and shear displacements for each of the stages. The constitutive law considers material properties (friction angle, compressive strength, etc.), surface properties (roughness), and initial and boundary conditions (constraints). A parametric study outlines the behaviour of the constitutive law and discusses the influence of the input parameters.

Isolated blocks might be prone to motion. It is the aim of the kinematic analysis to distinguish movable and non-movable blocks. As a basis position, displacements, velocities and accelerations of unconstrained and constrained rigid bodies are described. The possible kinematic constraints of a block are introduced as the kinematic constraint equations – algebraic equations describing kinematic constraints mathematically at position, velocity, and acceleration level. For a single rock block 16 basic kinematic modes are distinguished each of which related to a set of kinematic constraint equations.

The kinematic analysis of rock blocks is limited to the investigation of the block movability at the instant of incipient motion. A complete kinematic analysis throughout the block's motion is not possible since kinematic constraints depend on the (at this stage unknown) reaction forces. Goodman & Shi's block theory provides a general analytical solution for translations of blocks with arbitrary geometries. The kinematic analysis of rotational modes has been restricted to tetrahedral blocks only. This work establishes an analytical method for the kinematic analysis of pure rotational motion of blocks including corner and edge rotation, and a numerical method for the kinematic analysis of remote axis rotation. The analytical methods for translation and pure rotations give a complete picture of a block's movability with respect to the investigated modes. The numerical method for remote axis rotation, in contrast, gives only one set of solution parameters, if there is any. The application of the kinematic analysis allows distinguishing movable blocks from unmovable (tapered) ones just based on geometric information of the block.

The stability of a movable block is a major concern in any block analysis. Most of all, limit equilibrium methods have traditionally been applied for the block stability assessment. Although their application is easy, they do not comply with the full set of Newton's and Euler's equations of motion. This may lead to a wrong stability assessment independent of it would be conservative or unconservative. This work derives the full set of equations of motion for a constrained rigid block subjected to conservative and non-conservative forces. It outlines the integration of the equations of motion based on an implicit multi-step

method for describing and analyzing the block behaviour dynamically. Equilibrium is a necessary criterion for block stability. It is a particular case of a block's dynamic behaviour. A procedure based on the continuation method and derived from the equations of motion is established in order to approach an equilibrium state or failure directly. The procedure considers large block deformations, kinematic constraints, and conservative and non-conservative forces. The equilibrium path plots displacements versus loads or load related parameters and monitors the behaviour of a block with increasing loading and/or displacement. The proposed procedure allows identifying critical points along the equilibrium path, the static and dynamic mode of failure, and the verification of the stability of the equilibrium path itself.

This work integrates geologic data from remote measurement systems in general and discontinuity measurements in particular into a mechanical analysis of rock blocks. The method features different levels of automatic measurements including interaction, semi-automatic (guided) analysis, and fully automatic analysis. The kinematic analysis and the stability analysis have been generalised to arbitrary block shapes, arbitrary motion, general loading conditions, and non-conservative forces. The presented procedure allows automatically identifying single isolated blocks from a discontinuity trace map which has been generated from measurements on 3D images. With analytical methods the kinematic movability of block can be determined for both, translational and rotational motion by only knowing the geometry of the block. More complex numerical methods are necessary to perform a block stability analysis considering general motion and loading conditions.

Kurzfassung

Die Bestimmung der Standsicherheit von einzelnen Felsblöcken wird den Methoden der Felsmechanik zugeordnet. Felsblöcke werden durch Klüfte, Störungen oder andere Schwächezonen (sogenannte Trennflächen) im Gebirge gebildet. Es ist für eine aussagekräftige Standsicherheitsuntersuchung daher wichtig, das Trennflächensystem eines Gebirges sorgfältig und richtig zu bestimmen. Trennflächen werden konventionell mit Hilfe der Methoden der Ingenieurgeologie kartiert und charakterisiert. Im vergangenen Jahrzehnt wurden Systeme der Fernerkundung vermehrt für die Datenerfassung von Trennflächen an Felsaufschlüssen entwickelt und eingesetzt. Der Großteil der angewendeten Systeme verwenden Lasertechnologie oder Photogrammetrie. Speziell 3D Bilderfassungssysteme sind dazu geeignet, relevante Trennflächen zu erkennen und deren geometrische Eigenschaften zu messen. 3D Bildmessungen von Trennflächen stellen demzufolge einen neuen Qualitätsstandard in der Ingenieurgeologie dar. Es fehlen jedoch nach wie vor Methoden, mit denen die so gewonnenen Daten schnell und konsistent einer felsmechanischen Analyse zugeführt werden können.

Diese Arbeit stellt eine Prozedur vor, welche Trennflächenmessungen aus 3D Bildern in eine Methode zur Blockanalyse integrieren. Die Prozedur umfasst (1) die Datenerfassung im Gelände mit einem bildbasierten Fernerkundungssystem, (2) die 3D Bilderzeugung und –referenzierung, (3) die Auswertung der 3D Bilder hinsichtlich etwaiger Trennflächen, (4) die Erzeugung eines geometrischen Modells der Felsoberfläche und den Trennflächen, (5) die Identifikation endlich großer (isolierter) Blöcke, (6) die Bestimmung der metrischen Eigenschaften der Felsblöcke, (7) die Analyse der kinematischen Beweglichkeit der endlich großen Blöcke, und (8) die Bestimmung der Standsicherheit der Felsblöcke. In der vorgeschlagenen Prozedur werden Methoden der Ingenieurgeologie, digitalen Photogrammetrie, Computer Vision, digitalen Bildverarbeitung, algorithmischen Geometrie, numerischen Mathematik, felsmechanischen Laborversuchstechnik, allgemeinen Mechanik und Felsmechanik eingesetzt.

Im Detail werden in der Dissertation wichtige Anforderungen an Fernerkundungssysteme zur geologischen Datenerfassung an Felsaufschlüssen erläutert, wie zum Beispiel Anforderungen an Genauigkeit, Auflösung, Reichweite, usw. Es werden die häufig eingesetzten Systeme Laserscanning, Photogrammetrie und Computer Vision, und Radar besprochen. Die Besprechung zeigt, dass bildbasierte Systeme wesentliche Anforderungen zur geologischen Datenerfassung erfüllen. In dieser Arbeit wurde ShapeMetriX3D, ein bildbasiertes Messsystem, beispielhaft eingesetzt. Es werden die Grundlagen des Systems, die Anwendung im Gelände und die gewonnenen Ergebnisse und Messungen beschrieben und deren Zuverlässigkeit untersucht.

Die Topographie der Felsoberfläche und die Trennflächenmessungen aus einem 3D Bild werden zu einem geometrischen Modell der zu untersuchenden Gebirgsoberfläche verarbeitet. Das geometrische Modell ist im Wesentlichen ein Netzwerk der Ausbisslinien auf einer unregelmäßigen Oberfläche. Innerhalb des geometrischen Modells werden isolierte Blöcke durch die Anwendung eines Suchalgorithmus entlang vorhandener Ausbisslinien, eines Verschnittalgorithmus und des Endlichkeitstheorems für Blöcke nach Goodman & Shi identifiziert. Die Blockgeometrie wird durch die Koordinaten der Eckpunkte, die blockbegrenzenden Ebenen, die blockbildenden Halbräume und die Konnektivitäten untereinander beschrieben. Aus den Koordinaten der Eckpunkte werden die metrischen Eigenschaften der identifizierten Blöcke wie zum Beispiel die Masse oder der Trägheitstensor berechnet.

Das Gleitverhalten von Felsblöcken wird neben den metrischen Blockeigenschaften auch von den Eigenschaften des Kontakts des Blockes zum umgebenden Gebirge entlang von Trennflächen bestimmt. Es werden drei typische Stufen des Scherverhaltens einer rauen, ungefüllten Trennfläche unterschieden. Die Stufen umfassen die Mobilisierung der Schubspannung, die Mobilisierung der Dilatation und die Abnahme der Oberflächenrauheit. Ein Stoffgesetz beschreibt die entsprechenden Normal- und Schubspannungen und die Normal- und Scherverschiebungen in den einzelnen Stufen. Das Stoffgesetz berücksichtigt die Materialeigenschaften des Felses (z.B. Reibungswinkel, Druckfestigkeit, usw.), Oberflächeneigenschaften (z.B. Rauheit), und Anfangs- und Randbedingungen (Bindungen). Das Verhalten des Stoffgesetzes und der Einfluss der Eingabeparameter auf das Verhalten werden in einer Parameterstudie gezeigt.

Durch Trennflächenverschnitte gebildete Blöcke können beweglich sein. Die kinematische Analyse zielt auf die Unterscheidung beweglicher und unbeweglicher Blöcke ab. Als Grundlage werden die Position, die Verschiebungen, die Geschwindigkeiten und die Beschleunigungen ungebundener und gebundener starrer Körper beschrieben. Mögliche kinematische Bindungen eines Blocks werden als kinematische Bindungsgleichungen eingeführt – das sind algebraische Gleichungen, welche die kinematischen Bindungen mathematisch auf den Positions-, Geschwindigkeits- und Beschleunigungsebenen beschreiben. Für einen einzelnen Block werden 16 kinematische Modi unterschieden, denen jeweils eine bestimmte Anzahl kinematischer Bindungsgleichungen zugeordnet werden.

Die kinematische Analyse von Felsblöcken beschränkt sich auf die Untersuchung der Blockbeweglichkeit im Moment der anfänglichen Bewegung. Eine umfassende kinematische Analyse über die gesamte Blockbewegung ist nicht möglich, da die kinematischen Bindungen von den hervorgerufenen Reaktionskräften abhängen. Diese sind jedoch in dieser Phase nicht bekannt. Die Blocktheorie nach Goodman & Shi beinhaltet unter anderem eine allgemeine analytische Methode für die kinematische Untersuchung von Translationsbewegungen von Blöcken mit beliebiger Geometrie. Die kinematische Analyse

für Rotationsbewegungen ist nach wie vor auf tetraederförmige Blöcke beschränkt. Diese Arbeit führt eine analytische Methode für die kinematische Untersuchung der reinen Drehbewegungen, d.h. der Eck- und Kantenrotation, und eine numerische Methode für die kinematische Untersuchung der Drehbewegungen mit einer vom Block getrennten Drehachse ein. Die analytischen Methoden für Translationen und reine Rotationen geben ein vollständiges Bild über die Blockbeweglichkeit bezüglich der untersuchten Modi wieder. Die numerische Methode für den Modus mit einer vom Block getrennten Drehachse hingegen ergibt lediglich einen Satz von Lösungsparametern, falls einer existiert. Mit Hilfe der kinematischen Analyse können unbewegliche Blöcke von beweglichen unter ausschließlicher Kenntnis geometrischer Parameter unterschieden werden.

Die Bestimmung der Standsicherheit beweglicher Felsblöcke ist eine Kernaufgabe jeder Blockanalyse, wobei überwiegend Grenzgleichgewichtsbetrachtungen zum Einsatz kommen. Ihre Anwendung ist vergleichsweise einfach, jedoch erfüllen die üblicherweise verwendeten Methoden nicht alle Bewegungsgleichungen nach Newton und Euler. Das kann zu einer falschen Einschätzung der Standsicherheit führen, unabhängig davon, ob sie konservativ oder nicht konservativ sei. In dieser Arbeit werden die Bewegungsgleichungen eines gebundenen Starrkörpers, welcher konservativen und nicht konservativen Einwirkungen ausgesetzt ist, hergeleitet. Die Integration der Bewegungsgleichungen erfolgt mit einem impliziten Mehrschrittverfahren und führt zur Beschreibung des dynamischen Blockverhaltens. Gleichgewicht ist eine notwendige Bedingung der Standsicherheit eines Blocks. Es stellt einen Sonderfall des dynamischen Verhaltens dar. Aus den Bewegungsgleichungen wird eine auf einem Homotopieverfahren basierende Prozedur zur direkten Annäherung an einen Gleichgewichts- oder Versagenszustand abgeleitet. Die Prozedur berücksichtigt große Blockverschiebungen, kinematische Bindungen und konservative und nicht konservative Einwirkungen. Der Gleichgewichtspfad beschreibt das Verhalten des Blocks vom Anfangszustand bis zum Gleichgewicht bzw. Versagen. Typischerweise werden Verschiebungen und Lasten bzw. lastbezogene Parameter gegenüber gestellt. Mit der vorgeschlagenen Prozedur werden kritische Punkte entlang des Gleichgewichtspfades, der statische und dynamische Versagensmodus erkannt und die Stabilität des Gleichgewichtspfades verifiziert.

Die Arbeit verbindet geologische Daten aus speziellen Fernerkundungssystemen im Allgemeinen und Trennflächenmessungen im Speziellen mit der felsmechanischen Analyse von Blöcken. Die vorgestellte Methode bietet unterschiedliche Automatisierungsebenen, nämlich Interaktion, semi-automatische (geführte) Analyse und vollautomatische Analyse. Die Ansätze der kinematischen Analyse und Standsicherheitsuntersuchung wurden verallgemeinert, um beliebige Blockgeometrien, beliebige Bewegungen, allgemeine Belastungssituationen und nicht konservative Einwirkungen. Mit der vorgestellten Prozedur werden isolierte Blöcke automatisch in einem Trennflächennetzwerk identifiziert. Das Trennflächennetzwerk wurde im

Speziellen aus 3D Bildmessungen erstellt. Mit analytischen Methoden kann die kinematische Beweglichkeit eines isolierten Blocks hinsichtlich Translations- und Rotationsbewegungen einzig durch Kenntnis der Blockgeometrie bestimmt werden. Für eine konsistente und umfassende Standsicherheitsuntersuchung werden komplexere numerische Methoden eingesetzt.

Contents

1	Introduction	1
1.1	Problem statement	1
1.2	Objectives	2
1.3	Structure of the dissertation	2
1.4	Symbols and abbreviations	4
1.4.1	Vectors and matrices	4
1.4.2	Scalars	5
1.4.3	Abbreviations	6
1.5	Mathematical peculiarities	7
2	Geological and geotechnical data collection	8
	Application of remote measurement systems at exposed rock faces	8
2.1	Remote measurement systems	8
2.1.1	Characteristics and requirements	8
2.1.2	Brief review of image based systems	15
2.1.3	Brief review of laser based systems	16
2.1.4	Comment on radar based systems	17
2.2	Application of a computer vision system	18
2.2.1	Principles	18
2.2.2	Field procedures	23
2.2.3	Examples	26
2.3	Discontinuity measurements from scaled 3D images	30
2.3.1	Basic measurements	30
2.3.2	Practical reliability of measurements	32
2.3.3	Interactive and automatic measurements	36
2.4	Summary	39

3	The shear behaviour of discontinuities	41
3.1	Shear behaviour and influencing factors	41
3.2	The shear behaviour of matched discontinuities	45
3.2.1	Stage A: Mobilisation of the shear stress	45
3.2.2	Stage B: Mobilisation of dilation	46
3.2.3	Stage C: Surface degradation	47
3.2.4	Stage D: Residual stage	49
3.2.5	Peculiarities	49
3.3	Constitutive model	51
3.3.1	Assumptions	51
3.3.2	Mobilisation of shear stress (Stage A):	52
3.3.3	Mobilisation of dilation (Stage B):	52
3.3.4	Surface degradation (Stage C)	56
3.3.5	Peak dilation angle	58
3.3.6	Incorporation of the boundary conditions	62
3.3.7	Determination of model parameters	67
3.4	Parametric study	70
3.4.1	Pre-peak behaviour and peak shear strength	70
3.4.2	Post-peak behaviour	72
3.4.3	Joint normal stiffness	74
3.4.4	Influence of the joint normal stiffness on the shear response	76
3.5	Summary	80
4	Description and properties of blocks	81
4.1	Geometric description of blocks	81
4.1.1	Characteristics of a polyhedron	81
4.1.2	Parameters for the description of a polyhedron	83
4.2	Finiteness of blocks	85
4.2.1	Plane pyramids	85
4.2.2	The finiteness theorem for simple polyhedra	86
4.2.3	Determination of the excavation pyramid	88
4.3	Identification of finite blocks from trace maps	92
4.3.1	Establishment of a geometrical model	92
4.3.2	Identifying surface patches of blocks	94
4.3.3	Determination of the block geometry from surface patches	96

4.4	Metric properties of tetrahedra	98
4.4.1	Volume	98
4.4.2	Mass	99
4.4.3	Centre of gravity	99
4.4.4	Areas of face triangles	100
4.4.5	Inertia matrix	100
4.5	Metric properties of simple polyhedra	101
4.5.1	Distinction between convex and non-convex polyhedra	102
4.5.2	Decomposition of convex polyhedra	103
4.5.3	Decomposition of non-convex polyhedra	104
4.5.4	Merging of simplex properties	107
4.6	Examples for metric properties for simple blocks	109
4.7	Summary	111
5	Kinematics and kinematic analysis of blocks	112
5.1	Basics of kinematics of rigid bodies	114
5.1.1	The position and orientation of a rigid body	114
5.1.2	Unconstrained motion	117
5.1.3	Constrained motion	118
5.1.4	The general displacement of a rigid body	127
5.1.5	Kinematically feasible displacements	128
5.2	Analysis of translations	129
5.3	Analysis of rotations	133
5.3.1	Constrained rotational displacement	134
5.3.2	Corner and edge rotation	136
5.3.3	Rotation about a remote axis	146
5.4	Illustrative examples	152
5.4.1	Convex block	152
5.4.2	Non-convex block	156
5.4.3	Block in a tunnel crown	160
5.5	Summary	164

6	Dynamic Behaviour and Stability Analysis	167
6.1	Introduction	167
6.2	Literature review	167
6.3	The equations of motion	170
6.3.1	General	170
6.3.2	Time integration of the equations of motion	173
6.3.3	Equilibrium	179
6.4	Stability analysis	190
6.4.1	Block model	190
6.4.2	Forces and moments	191
6.4.3	Stiffness matrix	197
6.4.4	Equilibrium path	201
6.5	Illustrative example	208
6.5.1	Description of the situation	208
6.5.2	Removable blocks, kinematics and stability according to block theory	209
6.5.3	Single block analysis	212
7	Conclusion	221
	References	224

1 Introduction

1.1 Problem statement

Rock mechanics deals with the description and analysis of the mechanical behaviour of rock masses. They exhibit a broad variety of different behaviours. A sub-discipline covers the analysis of failure of discrete blocks. Zones of weakness in the rock mass such as joints, faults, shears, bedding planes, etc., control their failure. They define the size and shape of blocks, and also the properties of contacts. For a meaningful analysis it is a paramount requirement to thoroughly collect information on discontinuities in the rock mass. Traditionally, information could only be obtained at locations with direct access to the discontinuity at an outcrop or at samples extracted from the rock mass, e.g. samples from core drillings (e.g. Riedmüller et al. 2002, Brosch et al. 2001, Harer 2009). In the last decade new technologies emerged in the field of rock mechanics for the contact-free measurement of surfaces (Roberts & Poropat 2000, Fasching et al. 2001, Slob et al. 2002, Gaich et al. 2003, Kemeny et al. 2003, Haneberg 2008). The technologies are mostly related to laser scanning and 3D imaging. They provide new possibilities to characterise the rock mass, and more specifically, to collect information about discontinuities without the need of physical access. 3D imaging technology provides both accurate geometric information and aligned photorealistic image information. This allows the user to determine discontinuity measurements wherever visible and resolved in a 3D image. The knowledge of the size at the outcrop, position and orientation of specific discontinuities opens up new ways to approach analyses in rock mechanics. With focus on block failures, a major part of the necessary data for determining the geometry of rock blocks has become available. The data have not been integrated in a standard rock mechanics design, nor have straightforward tools been available to process and use the data.

Mechanical analyses of rock blocks aim at determining their stability and the associated factor of safety. Practically applied methods are often limited to limit equilibrium analyses accounting typically only for cohesion and friction of discontinuities and inherently assume a translational failure mode (John & Deutsch 1974, Kovári & Fritz 1978, Hoek & Bray 1981, Gianni 1992, Brady & Brown 2004). Block theory (Warburton 1981, Goodman & Shi 1985) provides a consistent framework for analysing different translational failure modes of blocks depending on the resultant external force. Complex loading conditions, however, can only be considered with coarse simplifications. In contrast to these methods, it is supposed that a block failure is more likely to happen through a combined translational-rotational failure mode (Chan & Einstein 1981). A general method for determining the stability of a rock block under a true (not assumed) failure mode is not available in rock mechanics unless extensive numerical methods are applied (Hart et al. 1988, Eberhardt 2003).

1.2 Objectives

The dissertation pursues several objectives. A key objective is to establish a method to integrate discontinuity measurements from remote sensing data into an analysis procedure for determining the stability of rock blocks. Discontinuity measurements comprising their size, position and orientation are obtained from a three-dimensional photorealistic model (3D image) of the exposed rock surface which in turn defines the free surface. Based on this information fully defined blocks shall be identified in the discontinuity network. The identified rock blocks are subject to the mechanical analysis including kinematic analysis and stability analysis.

The kinematic analysis can already be performed with the sole knowledge about geometric data and provides information about potential movability of a rock block. Translational kinematics has already been described comprehensively by several authors (Londe et al. 1969 and 1970, Warburton 1981, Goodman & Shi 1985). Unlike translations, rotational kinematics has been limited to pure rotation modes of tetrahedral blocks (Mauldon & Goodman 1990 and 1996, Tonon 1998). Another key objective is the extension of the theory of block kinematics to general roto-translational motion for arbitrary block geometries.

Any consistent mechanical analysis in engineering in static or low-velocity environment shall be based on Newton's and Euler's equations of motion. For a rock block whose deformability compared to the movability along bounding joints is low, there are six degrees of freedom, three translational and three rotational. Due to its low deformability the rock block can be considered as a rigid body. Another key objective is to establish a method for the mechanical analysis of rigid blocks to assess their stability under general non-conservative loading conditions. Stability shall be assessed without predefining displacements as shown by Karzulovic (1988) and Pötsch (2002). The method shall be able to process any type of mechanical loading and comply with the kinematic constraints imposed by discontinuities.

1.3 Structure of the dissertation

The dissertation is organised into seven chapters. The current chapter introduces the topic, outlines the goals of the work, and provides an overview and basics to the topic.

The second chapter introduces the remote sensing technology and its application to geologic and geotechnical data acquisition. It outlines the requirements on the measurement system for the intended application (geologic mapping and data collection) and reviews different approaches. In this work a computer vision

system based on stereo-photogrammetry has been used. The principles of the system as well as its field application are addressed. Finally, discontinuity measurements are described and their reliability discussed. This chapter answers the question whether reasonable remote sensing systems are available for geologic data collection, how they can be practically used and if the measurements are reliable enough to be used in a relevant rock mechanics analysis.

The third chapter investigates the zones of weakness (discontinuities) forming the block. It deals with their properties and the associated mechanical behaviour with special focus on the shear behaviour. After addressing factors influencing the discontinuity shear behaviour the stages of shearing of an unfilled, matched and rough discontinuity are described. Based on the findings, a constitutive model for constrained discontinuity shear behaviour is formulated. The constitutive model provides a framework which can be used to determine the interaction of a block with the rock mass in terms of displacements and stresses. A parametric study highlights the sensitivity of the constitutive model to variation of the input parameters.

The fourth chapter deals with properties of blocks with an arbitrary polyhedral geometry. The chapter provides a method for distinguishing fully defined blocks (finite blocks) from infinite blocks. The method is based on Goodman & Shi's theorem of finiteness of non-convex blocks (Goodman & Shi 1985). The chapter continues with the descriptions of the calculations for determining the metric properties such as the block's volume or inertia matrix. A method for identifying finite blocks in a three-dimensional discontinuity network is also presented. This chapter provides methods for determining all block data required for the subsequent kinematic and stability analysis.

The fifth chapter is dedicated to the kinematics of a rigid body. It extensively discusses the mathematical relationships of feasible block displacements and outlines the algebraic kinematic constraint equations. Thereupon the methods for the kinematic analysis of translational, rotational and roto-translational motion are reviewed and established, respectively. The chapter has two major impacts. On the one hand, it provides the constraint equations which are later used for formulating the equations of motion of a constrained block. On the other hand, the methods for the kinematic analysis allow distinguishing movable from unmovable blocks. Critical blocks are limited to the set of movable ones. Valuable information can be obtained from a comprehensive kinematic analysis only with geometric input data.

The sixth chapter finally introduces a method for assessing the stability of a rock block. It is based on the complete set of Newton's and Euler's equations of motion and takes advantage of the methods developed in the previous chapters. In detail, the equations of motion are derived for a constrained rigid body and

methods for their integration are provided. The methods are cast into a concept to derive relevant conclusions for the stability of a block.

The seventh chapter concludes the dissertation. It summarises the key achievements and findings, but also lists topics which have not been (sufficiently) addressed.

Every chapter is more or less a complete sub-topic. Every chapter is introduced by a review of the state of the art and relevant articles. Unlike the introduction chapter every other chapter concludes with a summary of the findings and points out the need for the next topic.

1.4 Symbols and abbreviations

1.4.1 Vectors and matrices

$\mathbf{A}^{(ij)}$	Rotation matrix between coordinate system i and j
$\mathbf{C}_j\mathbf{R}$	Vector pointing from point C_j to point R
\mathbf{d}	Normal distance vector
\mathbf{D}	Plane code vector
\mathbf{D}_P	Matrix transforming generalised block displacement to point displacements
\mathbf{d}_{ij}	Vector pointing from body i to body j
$\delta\boldsymbol{\pi}$	Virtual rotation
$\delta\mathbf{r}$	Virtual displacement
$\Delta\mathbf{x}$	Corner displacement
\mathbf{E}	Euler parameter transformation matrix
\mathbf{e}_i	Unit vector of coordinate axis i
\mathbf{e}_{ij}	Edge vector between points i and j
\mathbf{F}^a	External force vector
$\mathbf{f}_i, \mathbf{g}_i$	Vector fixed to body i
\mathbf{G}	Euler parameter transformation matrix
\mathbf{H}_p	Matrix rotating a block fixed vector to its new orientation
\mathbf{I}	Identity matrix
\mathbf{I}_{ij}	Intersection vector between two planes
\mathbf{I}_k^{ij}	Signed intersection matrix
\mathbf{J}	Inertia matrix
\mathbf{k}_i	Edge vector at body i
\mathbf{K}	Stiffness matrix of a block
\mathbf{M}^a	External moment vector
\mathbf{n}_i	Normal vector of a plane i

N	Normal vector matrix
p	Vector of Euler parameters (Quaternion)
q	Generalised displacements
Q	Generalised forces
r	Position vector
R	Position vector of a point along the rotation axis
res	Residual force vector
s	Body fixed vector
S	Scaling matrix
T	Testing matrix
u	Rotation axis
v_C	Displacement vector of the centre of gravity
v_N	Normal displacement vector of a point
v_P	Displacement vector of a point
v_S	Shear displacement vector of a point
z	Vector of the stiffness matrix's null space
γ	Constraint factor
λ	Lagrange multiplier
ω	Angular velocity

1.4.2 Scalars

<i>A</i>	Area
<i>a</i>	Seywald's correlation factor
<i>A₀</i>	Maximum potential contact area
<i>C</i>	Grasselli's roughness parameter
<i>c₁, c₂</i>	Degradation parameters
<i>C_{ijk}</i>	Corner number of plane intersection <i>i</i> , <i>j</i> , and <i>k</i>
<i>e_i</i>	Euler parameter
<i>G_k</i>	Dissipative forces
<i>i</i>	Dilation angle
<i>J_{ii}, J_{ij}</i>	Moment or product of inertia
<i>k_n</i>	Normal stiffness
<i>k_s</i>	Shear stiffness
<i>K_{tot}</i>	Total normal stiffness
<i>L</i>	Length
<i>L_{step}</i>	Increment size
<i>m</i>	Mass
<i>N_f</i>	Number of property <i>f</i>
<i>O</i>	Origin of coordinate system

p	Eigenvalues of the differential equation of the unforced and undamped block
pV	Penalty value
t	Spline control parameter
t	Time
T^*	Fictitious kinetic energy
u	Shear displacement
u_{peak}	Shear displacement at peak shear strength
V	Volume
v	Normal displacement
V^*	Fictitious potential
v_m	Maximum joint closure
W	Shear energy
α	Angle between displacement vector and normal vector
α_{max}	Maximum asperity angle
β^p, β^c	Adams-Bashforth-Moulton integration terms
ε	Rotation angle
φ	Friction angle
φ_b	Basic friction angle
ϑ_{ijk}	Vector turn angle at corner C_{ijk}
λ_{stage}	Stage control parameter
ν	Poisson's ratio
Θ	Kinematic constraint equation
Θ^*_{max}	Maximum apparent asperity angle
ρ	Density
σ_n	Normal stress
τ	Shear stress
ψ	Scaling parameter

1.4.3 Abbreviations

BP	Block pyramid
CNL	Constant normal load
CNS	Constant normal stiffness
EP	Excavation pyramid
JCS	Joint wall compressive strength
JP	Joint pyramid
JPC	Corner joint pyramid
JRC	Joint roughness coefficient
SP	Space pyramid
UCS	Unconfined compressive strength

1.5 Mathematical peculiarities

The applied formalism uses matrix operations. Vectors are considered as column matrices. All rules for matrix operations are applicable including rules for addition, subtraction, products, transposing, and inverting. Since many operations originate from vector operations, equivalent operations of the scalar and vector product have to be used. For the scalar product one can use expression (1).

$$\mathbf{n} \circ \mathbf{m} = \mathbf{n}^T \cdot \mathbf{m} \quad (1)$$

The vector product can be expressed with a matrix multiplication (2) by introducing an operation transforming the vector to a skew symmetric matrix.

$$\mathbf{k} = \mathbf{n} \times \mathbf{m} \rightarrow \mathbf{k} = \mathbf{n}^* \cdot \mathbf{m} \quad (2)$$

The skew symmetric matrix \mathbf{n}^* is defined as shown in expression (3).

$$\mathbf{n} = (n_1 \quad n_2 \quad n_3)^T \Leftrightarrow \mathbf{n}^* = \begin{pmatrix} 0 & -n_3 & n_2 \\ n_3 & 0 & -n_1 \\ -n_2 & n_1 & 0 \end{pmatrix} \quad (3)$$

The asterisk operation of matrices obeys also the following relationships:

$$\begin{aligned} \mathbf{n}^{*T} &= -\mathbf{n}^* \\ \mathbf{n}^* \cdot \mathbf{m} &= -\mathbf{m}^* \cdot \mathbf{n} \\ \mathbf{n}^* \cdot \mathbf{m}^* &= \mathbf{m} \cdot \mathbf{n}^T - \mathbf{n}^T \cdot \mathbf{m} \cdot \mathbf{I} \\ (\mathbf{n}^* \cdot \mathbf{m})^* &= \mathbf{m} \cdot \mathbf{n}^T - \mathbf{n} \cdot \mathbf{m}^T = \mathbf{n}^* \cdot \mathbf{m}^* - \mathbf{m}^* \cdot \mathbf{n}^* \end{aligned} \quad (4)$$

2 Geological and geotechnical data collection

Application of remote measurement systems at exposed rock faces

Remote measurement systems for the collection of rock mass parameters have been gaining increasing use and importance in the daily engineering geologic work. The developments in this respect in the last few decades focused on increasing the working range and speed, and easing the field application at an affordable cost. The advances in computational power and sensing capabilities together with the development of specific software tools to handle the obtained data led to mature systems which can be applied in the daily work. This chapter gives a brief introduction to remote measurement systems for geological and geotechnical data acquisition at exposed rock faces. It shows also a list of characteristics and requirements for performing the stated tasks. Subsequently, the chapter describes the application of an image based measurement system with its principles and required field and computational procedures. The chapter concludes with the discussion of the obtained data, as well as the prime use of these systems to rock face characterisation.

2.1 Remote measurement systems

Remote measurement systems in geological data collection aim at the measurement of the rock mass structure and the geometry of a rock face. Surveyed structures are in this case rock fractures such as joints, faults, foliation and bedding planes, contacts, etc. Typical figures of the rock face geometry are the height and dip of the slope as well as the change of the geometry over time.

2.1.1 Characteristics and requirements

Geological and geotechnical data collection is basically a surveying task. Due to the nature of the investigated data and the number of required measurements the measurement systems have to comply with several requirements whose importance is different to conventional surveying. A conventional survey focuses on the determination of the position of a certain point in space at a sufficiently high accuracy (Joeckel et al. 2008). Geological and geotechnical data collection focuses on the identification and survey of relevant structures in a rock mass and

its special relation to the free faces. One significant difference between the two methods is that in the latter we do not know during the data acquisition where the relevant measurement has to be placed. For spatial measurements we need therefore a high density of points (a point cloud) and a means of relating the relevant structures to the point cloud. State-of-the art systems as introduced in the following sections provide a dense cloud of points. The point cloud is triangulated which forms an irregular surface – in most of the cases this is a triangulated irregular network. Additional attributes can be assigned to the points or surface triangles. The following list gives an overview of the characteristics of measurement systems. It addresses point or surface attributes, the point density, the relative point accuracy, the accuracy of the absolute position in space, the ground resolution, and the working distance.

Point or surface attributes:

- None: If no other than geometric information is available, the surface can be represented only in a shaded manner. Surface irregularities can be geometrically, but hardly visually identified (Figure 1 top left).

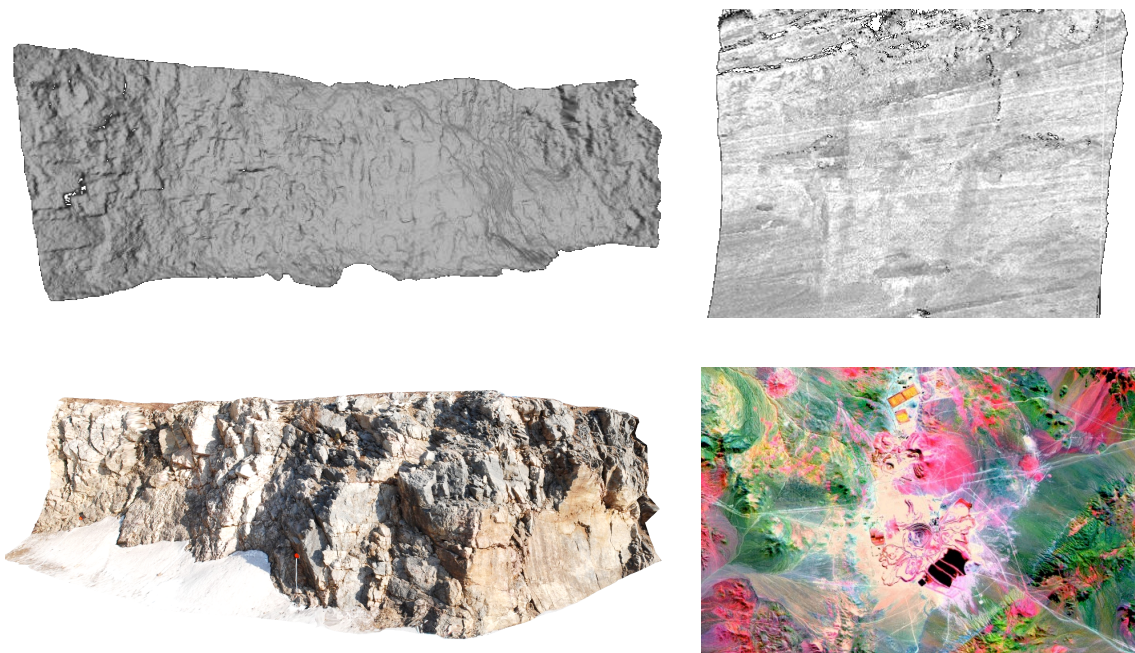


Figure 1: *Top left:* grey shaded irregular surface of a rock face without additional point attributes – *Top right:* laser intensity image from Bellian (2003) – *Bottom left:* 3D image of a rock face in RGB colour – *Bottom right:* ASTER (Advanced spaceborne thermal emission and reflection radiometer) image of Escondida mine, Chile. Colours indicate different rock types and alteration (downloaded from <http://asterweb.jpl.nasa.gov/> on January 24, 2009).

- **Intensity:** The intensity value gives information on the reflective properties of the rock mass additionally to the geometry. Intensity changes can indicate different humidity or rock types, but not in an absolute scale (Figure 1 top right).
- **Colour:** Colour information with 24 or 48 bit depth allows a true representation of the rock mass. The colour information together with an irregular surface is referred to as a 3D image (Figure 1 bottom left).
- **Multi-spectral information:** Today sensors are available which capture the electromagnetic radiation emitted by the rock mass (Prost 1980, Ninomiya et al. 2005). Since rock types comprise a characteristic set of minerals each related to a frequency of radiation, multi-spectral information allows identifying rock types and weathering degrees in an absolute scale (Figure 1 bottom right). To the author's knowledge, these types of sensors are currently applied in remote sensing and exploration but not as a standard tool in daily engineering geological and geotechnical investigation.

Point density: The point density describes the number of 3D points per unit area. The point density of a point cloud varies due to different distances of the rock face to the sensor. An average value over the entire point cloud is characteristic. The point density is important for several respects.

- It determines the level of detail of the investigated rock face's model. The more detail the point cloud has, the more accurately it describes the real shape of the face, and also the more detailed structures and smaller-scale properties can be determined.
- The higher the point density, the more robust are orientation measurements taken from a point cloud (see below).

The point density can depend on the size of the rock face, the working distance, the angular or image resolution of the sensor, etc.

Relative point accuracy: The relative point accuracy describes the spatial variation of the points within a point cloud. It is also called measurement noise or point cloud thickness. The latter name is derived from the phenomenon that a point cloud of real point measurements of a plane is not planar but shows a small thickness. The relative point accuracy together with the point density influences orientation and joint roughness measurements.

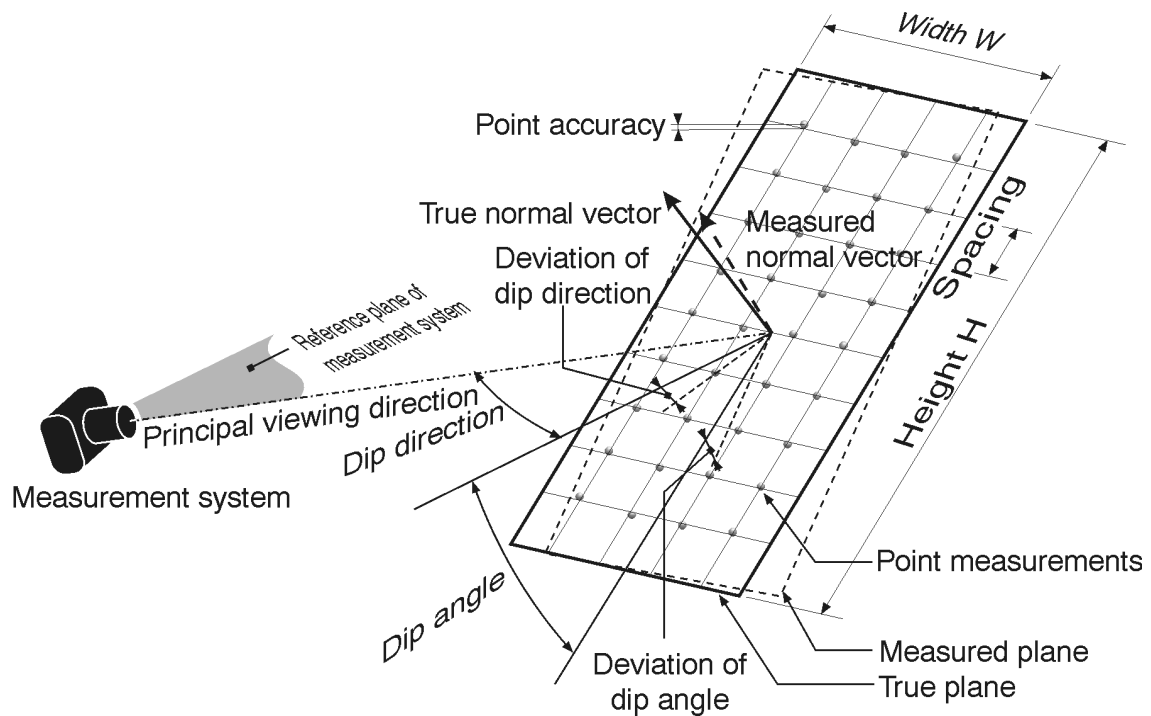


Figure 2: Model for the analysis of theoretical errors of plane orientation measurements

Ferrero et al. (2008) discuss the influence of the relative point accuracy on dip angle and dip direction measurements, but they do not discuss the true angular deviation (angle between the true and measured normal vector of a plane). Their error analysis has been performed through computing variance propagation and investigates the orientation errors due to plane orientations, point density, shape of the plane, and measurement noise.

The following paragraphs outline a similar study performed by Monte Carlo simulation. The study also considers the absolute angular deviation between true and measured normal vector increasing the significance of the findings compared to analysing dip direction and dip angle alone. The model considers the relative point accuracy, the size and shape of the plane, the grid spacing, and the orientation of the plane relative to the measurement system (dip direction and dip angle). The applied range of values is typical for point clouds obtained from remote measurement systems.

Figure 2 shows model for the analysis of errors of plane orientation measurements using point clouds obtained from a remote measurement system. The point cloud originates from a plane. The orientation measurement is related to the best-fit plane to the point measurements. It is assumed that the point accuracy is isotropic and normally distributed. Figure 3 and Figure 4 show selected results for the theoretical orientation measurement errors. The diagrams show the absolute angular deviation (i.e. the angle between the true and measured normal vector), and the deviations of the dip angle and dip direction.

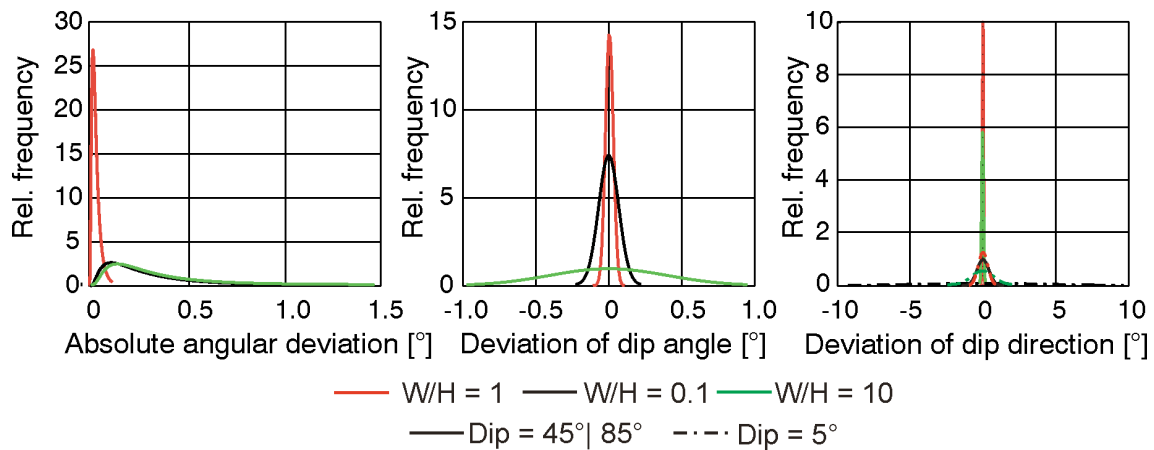


Figure 3: Orientation measurement errors from point clouds. Relative point accuracy is 0.5% of the maximum plane dimension. Grid spacing is 10% of the maximum plane dimension.

Figure 3 investigates the shape of the plane (ratio between width and height) and the dip angle of the plane. It shows that narrow shapes result in a stronger deviation from the true value than square shapes. The absolute angular deviation is insensitive to the plane's aspect ratio. The dip angle is more sensitive to wider rectangles, while the dip direction is more sensitive to higher rectangles. Flat planes (below 10° dip angle) strongly influence the dip direction although they do not affect the absolute angular deviation. No significant influence of the plane's dip direction towards the measurement device has been encountered.

Figure 4 shows the influence of the grid spacing and relative point accuracy on the measured orientation in case the plane is a square. The dip angle is 5°. Red lines refer to a ten times higher relative point accuracy than black lines. Solid lines refer to an 11x11 point grid while dot-dashed lines refer to a 3x3 point grid.

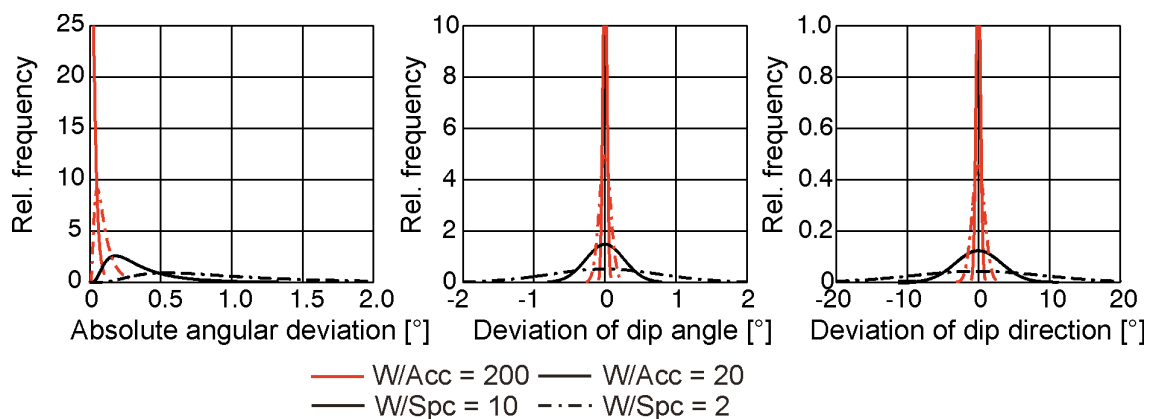


Figure 4: Orientation measurement errors from point clouds. Ratio between width and height is 1. Dip angle is 5°.

The results show that the absolute angular deviation and dip angle deviation remain widely below one degree. The deviation of dip direction is noticeable for the lower relative point accuracies and even more pronounced with lower point density. It shall be noted that the latter observation involves pessimistic assumptions such as flat dip angle, low point density and low relative point accuracy.

The results in measurement deviations agree well with the observations of Ferrero et al. (2008). Anyhow, the most relevant absolute angular deviation remains in most of the cases below 1° . It can be concluded that orientation measurements are sufficiently reliable with point densities and accuracies typically achieved with remote measurement systems.

Accuracy of the absolute position of a point in space: This characteristic describes the deviation of a point measurement from the true value within a superior coordinate system. Superior coordinate systems can be global, national, site or project-specific coordinate systems. The absolute position in space can only be checked at points with known coordinates, so-called ground control points. It shall be noted that even a real measurement of a ground control point wears an error depending on the applied measurement system (e.g. total station).

The accuracy of the absolute position in space is the mean of the control point deviations. It is a measure how well a 3D point cloud fits into a given coordinate frame. Its influence on geological measurements is minor. Figure 5 shows as an example a model for determining joint orientations due to errors in absolute position in space.

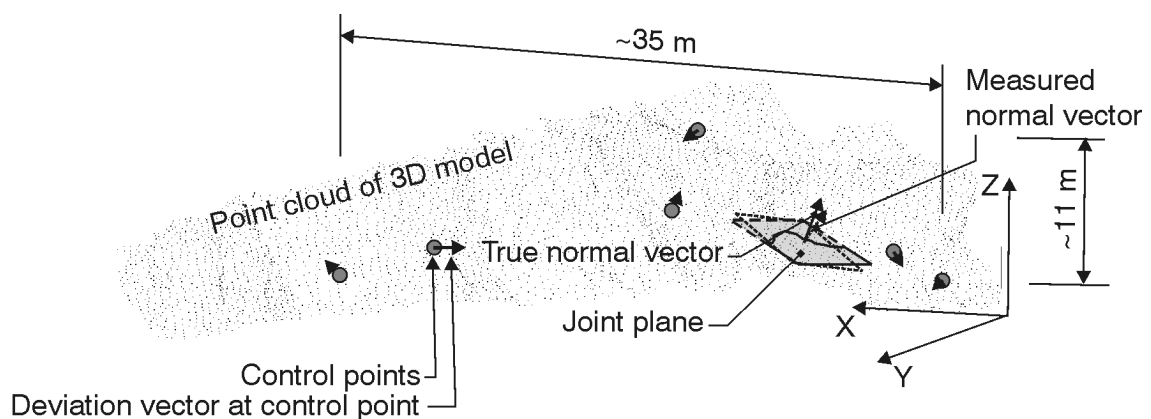


Figure 5: Model for deviations in joint orientation due to errors in absolute position in space.

The point cloud is registered at the control points with residuals (deviation vector at control point). The control point region (containing 6 control points) has a height of 11 m and a width of about 35 m. The deviation vectors have exemplarily a mean length of 0.1 m (which is considered as a bad accuracy). The vector length is normally distributed; the vector orientation is random.

Figure 6 shows the deviations of the orientation measurement for a 5° dipping joint and the model deviation from the true values. No significant deviation from the true value can be observed; only the dip direction shows a deviation of 2° . No influence of the dip direction of the joint on the deviation could be observed. Angular deviations become smaller with increasing control point distance and improved control point accuracy.

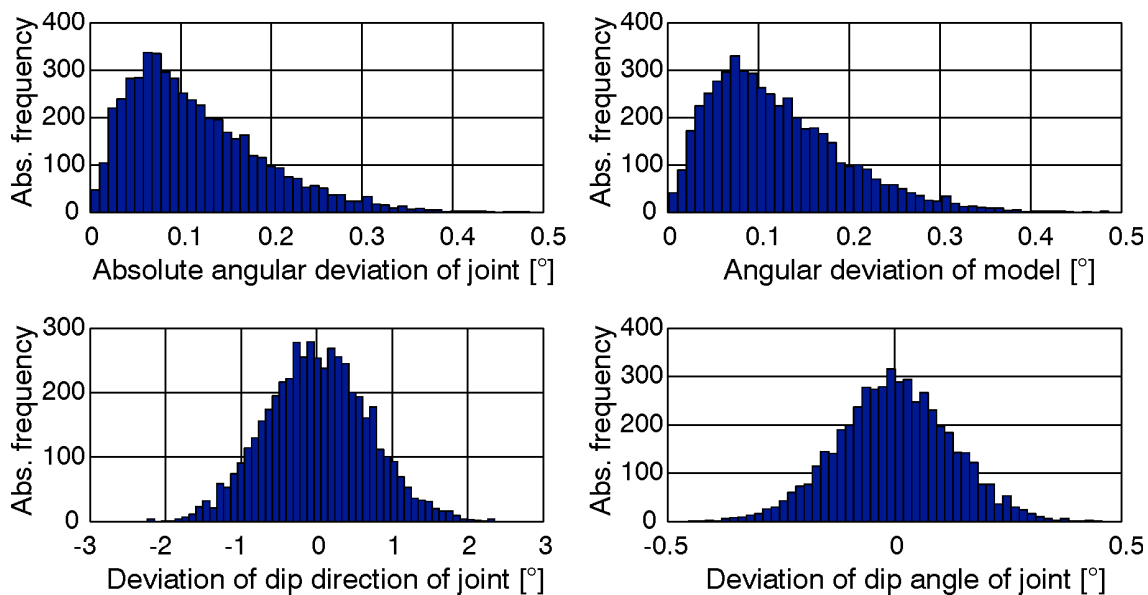


Figure 6: Absolute frequency diagram of orientation measurement error for a flatly dipping joint

Ground resolution: Sensors can resolve the ground to a certain limit. Image based systems describe the resolution with the ground pixel size, i.e. the square area of ground covered by one pixel. Laser based systems give a beam divergence angle, i.e. the divergence of the laser beam with distance. One can determine the diameter of the laser beam's footprint on the ground using the beam divergence.

Working range: The working range of a system indicates the applicable distances from the measuring unit to the rock face which still deliver reasonable results. The larger the working range, the more flexible is its field application. Working ranges of measurement systems currently used for geological data acquisition are from less than a metre up to a couple of hundred / thousand metres depending on the principle. For more details refer to sections 2.1.2 and 2.1.3.

The above parameters describe the expected quality and suitability of a point cloud for geotechnical evaluations. Depending on the measurement system these parameters can be partially adjusted to meet specific requirements. A higher quality can be achieved by enhancing the applied hardware, the registration method, increasing the resolution of the object, or increasing the number of control points. An enhanced hardware refers to, for example, a camera with a higher image size, or a laser scanner with a smaller angular increment. This leads finally to a higher number of points per unit area. Subdividing an object into overlapping patches also increases the object's resolution. The use of control points increases the accuracy of the spatial position while an increased number of control points provides redundant information and enables error balancing. All these measures lead to an increased effort for the data acquisition, especially during the field work.

A frequent application of a measurement system though requires an easy application in the field and delivers the data fast and robustly. The author has also experienced a more frequent application of remote measurement systems, the more portable and less bulky the hardware has been.

2.1.2 Brief review of image based systems

Image based measurement systems acquire the information on the rock mass primarily from one or several images of the rock mass. The images have traditionally been photographs taken with film cameras. Nowadays, digital cameras are available and allow taking photographs in formats suitable for digital image processing.

One image, either analogue or digital, serves for identifying the structure of a rock mass. It allows identifying joint traces and daylighting areas including their boundaries. Since only two coordinates describe the position of a point in a photograph, no 3D measurements can be performed. However, it is possible to determine relative lengths and apparent angles from a photograph. Goodman (1976) describes the use of a gnomonic net for measuring angles of joint traces from a photograph. It requires the knowledge of the interior orientation of the camera (without lens distortion).

3D measurements require at least two images of the same object taken from different positions. This is referred to as stereoscopic view and the corresponding photographs are called a stereoscopic image pair, or, simply, a *stereo pair*. The reconstruction of a 3D point from a stereoscopic image pair has already been addressed by photogrammetry and described in textbooks (e.g. Wolf & Dewitt 2000). Point reconstructions from photographs of film cameras are tedious and never found a routine application in rock mass characterisation. Applications have been reported, anyhow, by Linkwitz (1963), Rengers (1967), Vieten (1970), Ross-Brown et al. (1973), Hagan (1980), Franklin et al. (1988), Rorke & Brummer (1985), and Crosta (1997). Digital photogrammetry covers the principle of classical photogrammetry and peculiarities of digital photography and image processing. A 3D point can be reconstructed if the positions and attitudes of the two cameras and the corresponding points in the two images are known. One application has been reported by Roberts & Poropat (2000) where camera orientations have been determined by external measurements. This requires surveying the cameras in the field and is thus difficult to apply. Another possibility of determining the external camera orientation is the observation of well-defined control points with known coordinates. The corresponding method is the block bundle adjustment (e.g. Wolf & Dewitt 2000). Lee et al. (2000) present a model and field test of digital stereophotogrammetry and report orientation errors between manual and photogrammetry measurements less than 5°.

In the 1990s new approaches and algorithms emerged easing the coding and steps for data acquisition and computation. These newer methods are all summarised under the term Computer Vision (Faugeras 1993). Computer Vision addresses besides the principles of photogrammetry also the determination of the relative camera orientations without any control points, the calibration of cameras with zoom lenses, and the point reconstruction from multiple view images. Gaich et al. (2003) addressed also calibration and 3D image generation using high-resolution panoramic cameras for geotechnical data acquisition in tunnelling.

2.1.3 Brief review of laser based systems

Laser based systems rely on the feedback of a laser pulse emitted by a laser diode and detected by a sensor. Laser distance meters and range finders provide the distance from the instrument's position to the point at which the laser signal has been reflected (Joeckel et al. 2008).

A total station or tachymeter is a theodolite combined with a laser distance meter both calibrated to the viewing direction (Joeckel et al. 2008). Thus, it allows the measurement of a 3D point with an oriented laser beam. The 3D point coordinates can be determined using calculations in polar co-ordinates.

Depending on the required positional accuracy of the point and its distance to the measurement unit, correction factors considering earth curvature, temperature and air pressure, have to be used. Although Feng et al. (1999) and Bulut & Tüdes (1996) have reported such an approach, total stations have not been used as a standard tool in geological data acquisition.

The realisation of narrow-focused laser beams and the rapid measurability of laser pulses led to the development of 3D laser scanners (also known as LIDAR). Originally used for airborne application, laser scanners are now available for terrestrial applications. Rotating mirrors inside the equipment guide the laser pulse and control its emitted direction (Joeckel et al. 2008). Modern laser scanners determine the distance to the point of reflexion with two possible methods. The first method is the “Time of Flight” (ToF) measurement. A highly accurate clock detects the time of departure and arrival of the laser pulse. The elapsed time together with the speed of light in the corresponding medium determines the distance. The second method is the “phase shift” (PS) measurement. It relies on counting the periods of a modulated signal and evaluating the phase shift between emitted and detected signal (Joeckel et al. 2008). Applied ToF lasers nowadays have a range up to approx. 2000 m while PS lasers have a range up to approx. 200 m (U.S. Department of Transportation 2008). Compared to PS lasers ToF lasers are slower. Since the laser signal only gives the coordinate of a point and the intensity of the reflexion, laser scanners have been equipped with cameras in order to gather colour information of the object (Przybilla 2006). Both perspective and panoramic cameras have been used. The mounting of the camera must be defined to the laser. Terrestrial laser scanners register the data either through defined installation over a known point or at ground control points within the scanning area.

Application of terrestrial laser scanners to geological and geotechnical problems have been presented, for instance, by Kemeny et al. (2003), Slob et al. (2005), Strouth & Eberhardt (2006), Ghirrotti & Genevois (2007), and Sturzenegger et al. (2007).

2.1.4 Comment on radar based systems

More recently, bigger open cut mines have been using mobile radar systems for slope monitoring (Harries et al. 2006). The system is used for continuous monitoring of slope movements. The achieved accuracy of absolute position in space is beyond one millimetre and thus suitable for remote displacement monitoring. Although their accuracy is high, the achieved resolution of currently used systems is lower than one metre per pixel. These systems are not capable of gathering data on the rock mass structure. It is also difficult to relate observed movements to their origin. A thorough analysis is required to distinguish between moving vehicles, falling rock blocks and large and fast slope displacements.

2.2 Application of a computer vision system

In this work a computer vision system is used for the remote geological data acquisition. The reasons for selecting a computer vision system are manifold:

- An image based measurement system is especially suitable for the geological / geotechnical data collection due to combined geometric and image information
- The computer vision approach used entails simpler field work and data processing only with minor user-interaction compared to classical photogrammetry systems.
- Cameras can be properly selected for a variety of applications depending on the working distance or rock face height.
- Data acquisition procedures can be easily adjusted to meet specific site criteria.
- Equipment is not bulky – it entails only a camera and portable scaling figures. Thus, the application in rough terrain is no problem

The used computer vision system is commercially available as JointMetriX3D for calibrated high-resolution panoramic line scan cameras, and ShapeMetriX3D for calibrated off-the-shelf digital SLR cameras.

2.2.1 Principles

The system relies on stereoscopic imaging, i.e. two digital images of the same area from different positions are required. The images serve for determining the corresponding points in the image pair, the relative orientation between the two cameras and the reconstruction of the spatial position of the points relative to the cameras. The principle is also known as Shape from Stereo (Figure 7). Several computation steps are necessary to obtain a 3D image allowing for true-scale measurements:

Image matching

Image matching is the process of fully automatically, robustly, and accurately finding corresponding points between two images of the same object (Sonka et al. 1999). For a realistic description of the rock surface a dense grid of points is indispensable. A 3D image used for discontinuity measurements comprises at least a couple of hundred thousand points. Image matching for about 300,000 points takes on a 2GHz dual core processor about 1 minute. Point correspondences in a digital image can be found at an accuracy of 0.1 pixels (Sonka et al. 1999).

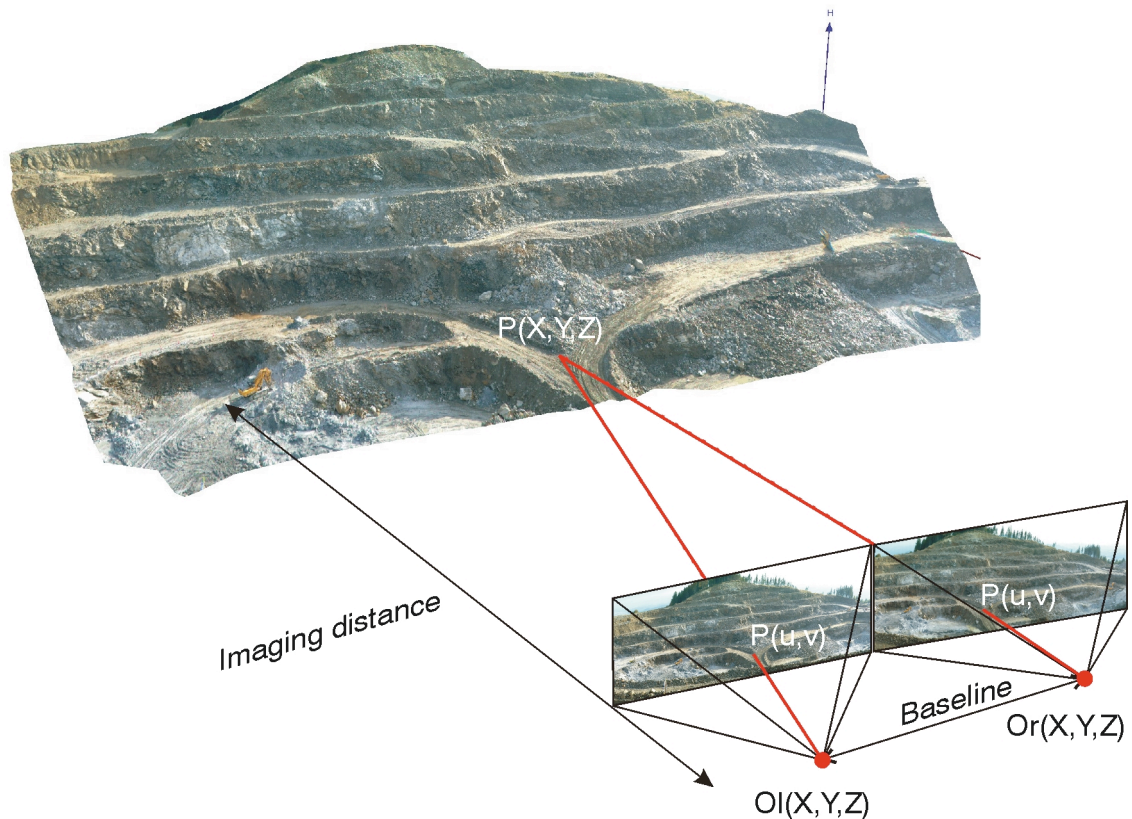


Figure 7: Shape from Stereo. A stereoscopic image pair taken with a calibrated camera system is used to identify a dense grid of match points; determine the exterior orientation; reconstruct the point cloud; and render the rock face surface combined with a digital photograph.

Relative camera orientations

Based on the set of match points the system determines the relative orientation between the two cameras. Relative camera orientations are determined using computer vision principles and optimisation procedures (3G Software & Measurement 2006).

Point reconstruction, triangulation and image alignment

Once the match points and relative camera orientation has been determined, the original points are reconstructed using the Shape from Stereo principle (see Figure 7). The result is a so-called point cloud, a set of a high number of unordered points. In order to obtain an irregular surface the point cloud is triangulated and, finally, the digital image aligned with the surface using the connectivity between match points and 3D points. Since every point has its origin at a photograph, the alignment of a photograph is determined for every point and does not need interpolation. The 3D image at this stage is geometrically correct but has no transformation to the real world, i.e. it has an arbitrary orientation and scale. This is referred to as a *generic 3D image*.

Camera calibration

Camera calibration refers to the determination of the image formation process within a camera. It includes the determination of the accurate focal length (distance from the image sensor to the focal point), the principal point (piercing point of the optical axis), and the lens distortion. This is also referred to as the interior orientation. Since off-the-shelf cameras have originally not been intended for measurements, their mechanical stability and manufacturing accuracy does not yield accurate measurements.

Classical photogrammetry requires the use of three-dimensional calibration objects, i.e. which have depth in all three spatial directions together with lenses with a fixed focal length. The computer vision approach introduces the use of zoom lenses and planar calibration patterns (Figure 8) – all of it easing the field work and use of the camera. Pre-calibrated cameras can be used.

The lens distortion results in a deviation of points of the ideal image and the real image. This deviation is almost zero in the centre of the image at the principal point and increases with the distance. Distortions may be distinguished into radial and decentering contributions (Brown 1971). Deviations may be as high as 40 pixels especially with short focal lengths (smaller than 20 mm).

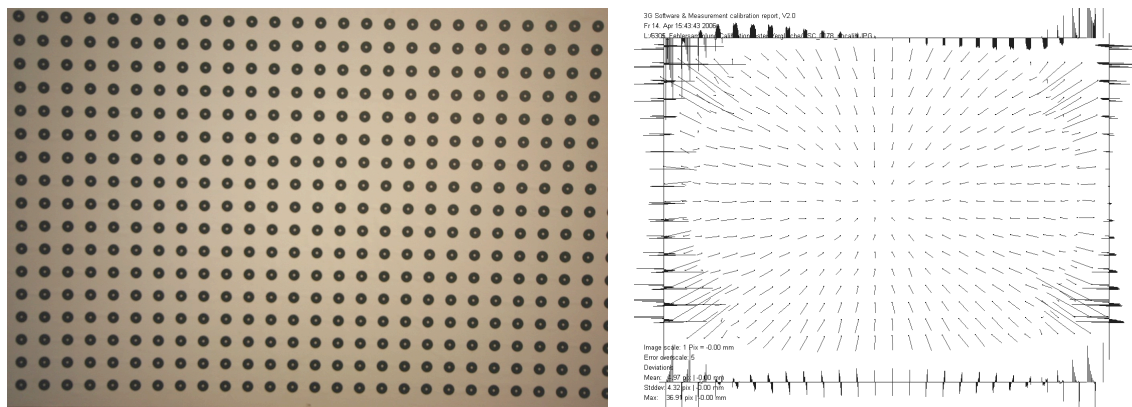


Figure 8: Planar calibration target with a regular point pattern (left). Deviations between ideal and real image of a regular pattern. Deviations are largest at the corners (right).

Registration of a generic 3D image

In order to obtain measurements in a real world coordinate system the generic 3D image needs registration to a known coordinate system. It is done by observation of a known figure which is visible in the stereoscopic image pair. The known figures are traditionally ground control points, i.e. non-collinear points with known coordinates distributed over the rock face or its boundary, respectively. This kind of registration is referred to as georeferencing, especially if the reference system is a global or national coordinate system. A minimum of three ground control points is required to define the transformation. Any additional point gives redundancy and allows for error analysis. The ground control coordinates are usually determined with a total station or accurate GPS (differential, RTK, etc.). Control point accuracy should be better than ± 5 cm, otherwise the control point error governs the accuracy of the 3D image.

ShapeMetriX3D also features the use of range poles to transform a generic to a scaled 3D image. Although the absolute position in space is less accurate compared to the use of ground control points, it turned out that for geological mapping the position accuracy is more than sufficient. A range pole is a vertically installed pole comprising two targets at a known distance (Figure 9 left). At least one range pole is required. The range pole allows the transformation to the vertical and the correct size.

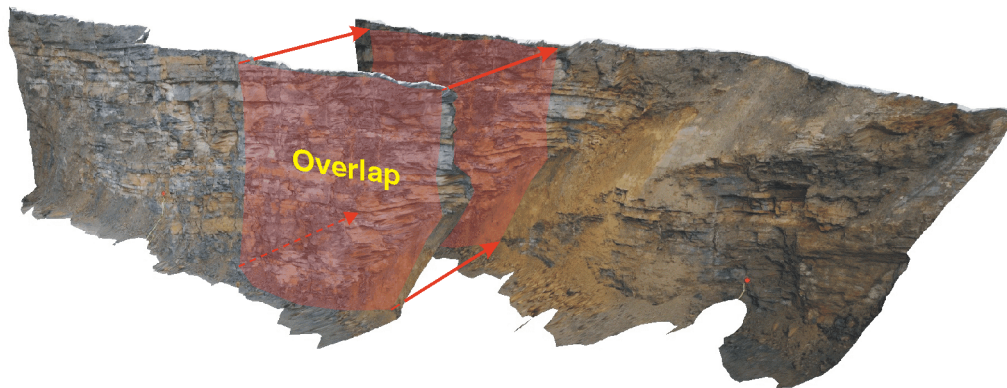


Figure 9: Installing a range pole in front of a rock face (left). Determining the azimuth of a reference line for North correction. Note the two marking elements (right).

The azimuth can be corrected to north using the observation of a reference line between two points. It is sufficient to measure the azimuth with a compass (Figure 9 right). If these measurements should be related to a geographic coordinate system, deviation between geographic and magnetic North may need to be considered. In case of the presence of magnetite or other magnetic rocks, compass readings may be replaced by coordinate or gyro measurements. To the author's knowledge, gyro measurements in this context have not been reported so far.

The reference figures must be well visible in the stereoscopic image pair. Each target requires a minimum of eight by eight pixels for defining its centre consistently. In consequence, the size of the targets and the used camera (image size) limit the height of the rock face. Using a 10 Megapixel camera and targets with 25 cm diameter the practical upper limit of the rock face is 50 m.

Two single 3D images with partial overlap



Merged 3D image

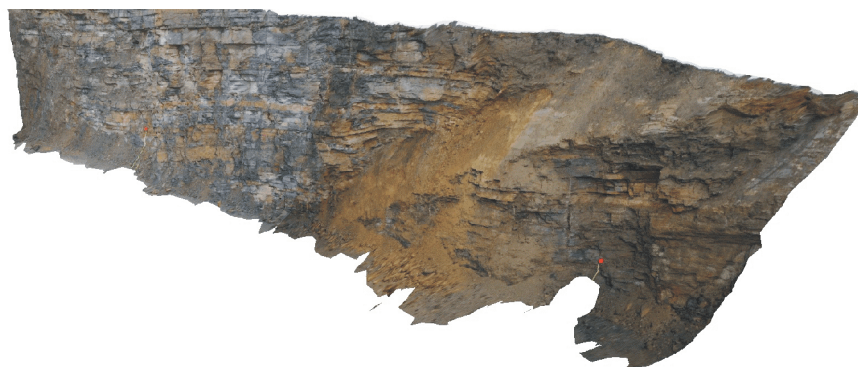


Figure 10: Merging of 3D images. Two single 3D images show a partial overlap (top). The overlap is used to align the two images and unify them (bottom)

Merging of 3D images

If 3D images have a sufficiently big overlap, they can be merged to one combined 3D image (Figure 10). Merging follows a master-slave strategy in which the slave 3D image is registered at the master 3D image. It is necessary to have geometric point information in the overlap. For performing the transformation a good initial guess of the correspondence has to be interactively provided.

2.2.2 Field procedures

The field procedures corresponding to 3D image data using the described computer vision system basically focus on the proper capture of the stereoscopic image pair. For merged models sufficient overlap between single stereo pairs is recommended. It should be around one third to one quarter of the image height or width, respectively. In general, the field procedures include the installation of the reference figures (control targets or range pole), and capturing the images. The process is essentially the same for underground and open-air applications.

Taking the photographs

It is not necessary to survey the camera positions and attitudes. Therefore, the images can be taken free-hand. It is necessary that the lens settings remain the same for one stereo pair. The images of a stereo pair can have an overlap of almost 100 percent. Flash must not be used.

In underground environments with low light conditions, the camera should be used on a tripod in order to provide stability during exposure. Survey of the camera is not necessary. The automatic cameras should be used in the aperture control mode with the aperture kept on a high value, for instance F8 or F16. This ensures a wide range of depth sharpness. Increased exposure time with high aperture is not a problem when using a tripod. Shaking the camera during shutter release can be avoided by using a remote trigger. Flash must not be used because image quality becomes bad due to dusty air. Flash fixed to the camera additionally causes different shadows on the face (light emission from different positions). The image processing in consequence would partially deliver geometrically incorrect point correspondences.

The stereoscopic image pair

The next step is the capture of the stereoscopic image pair. Two images of the same rock face from different positions are necessary. The line between the two imaging positions is called the base line and the distance between is the base length. The base line should be at best parallel to the strike of the rock face. The base length should be between one fifth to one eighth of the distance to the rock face; for example, if the imaging distance is 50 m, the base length is in the range of 6 m to 10 m. Selection of the base length is a trade-off between accuracy and matching. Matching performance increases the smaller is the base length, while accuracy improves with increasing base length. If the base length becomes too big, the perspective distortion of the two images is too big: The images do not show the same object – matching would fail. If the base length becomes too small, the holonomic rays intersect at an acute angle and point position becomes insecure and the determination of camera orientation fails.

The images should be taken from about the same altitude and with the same lens setting, i.e. same focal length and focus.

Ground control points – open air

Ground control points (GCP) are used if the area captured by a photographic survey becomes larger than the limits outlined for the range pole (typically 40 - 50 m) or if the measurements are necessary directly in a certain coordinate frame. This is especially the case for panoramic surveys or for merged 3D images.

Instead of a reference figure, points with known coordinates in the coordinate frame can also be used. A minimum of three points is necessary to define the transformation. A higher number of points is redundant but allows for error analysis. The ground control points or reference points are marked with targets sufficiently large to be visible in the images. Their arrangement must not be collinear – collinear points only define an axis. The ground control points have to be defined in a right-handed coordinate system. Using ground control points the 3D image is directly transformed into the target coordinate system; that is, into a geographic coordinate system as opposed to compass directions. The deviation between geomagnetic and geographic north depends on the position on earth and may reach significant values. The Geological Survey of Canada provides an online calculator for the determination of the magnetic declination at <http://geomag.nrcan.gc.ca/apps/mdcal-eng.php> depending on current time and geographic position (longitude and latitude).

Applying more than three ground control points, the errors between the 3D image measurements and the GCP can be analysed. The deviations are typically in the range of < 5 cm with single convergent image pairs and 2 – 15 cm in case of merged 3D images. The accuracy of the ground control points should thus be in the range of only a few centimetres (ca. 1 - 3 cm), otherwise the accuracy of the ground control points governs the accuracy of the 3D image.

Ground control points – underground

Ground control points are also used in underground excavations, especially if they are present at the tunnel face. From the imaging point of view, ground control points would be most favourable when directly on the face. However, installation of GCP on the face in a standard procedure is time consuming and thus not reasonable. In some cases targets from displacement monitoring appear in a stereo pair. The coordinates of these targets can be used without any additional effort.

A specific method for referencing in relation to panoramic cameras is used in underground excavations. The panoramic camera's attitude extends to capture not only the face but also the already excavated tunnel. In civil tunnelling there are displacement monitoring targets available for referencing. This approach is possible due to the defined scanning of the tunnel, i.e. the angle between the targets and face is inherently given by the panoramic photographs. This is much more difficult with conventional cameras, since an entire model of the tunnel including face, sidewalls, and lining back to the portal would be required. For this reconstruction a merged 3D image is required and additionally the entire tunnel would have to be illuminated. An example is provided in the next section.

2.2.3 Examples

This section gives some examples of 3D images obtained with the described computer vision system. It includes both surface and underground examples.

2.2.3.1 3D images from single stereo pairs

3D images from single stereo pairs are obtained with minor field effort and few computation steps. They are primarily used for fast assessments (on site and short term) and mobile applications, especially at remote locations. Figure 11 (left) shows a 3D image from a bench face generated from a single stereo pair. The right hand side shows the stereo pair corresponding to the 3D image. It is slightly converging. One should note that only a part of the photos has been used for 3D image generation. A range pole has been placed on the left hand side of the rock face.

Figure 12 shows a series of 3D images from drift tunnel faces. The face of each round has been gathered and a 3D image generated. 3D images have been registered to the same coordinate system using four to seven ground control points at the face. The right hand side of Figure 12 shows the general setup of the cameras relative to the face.

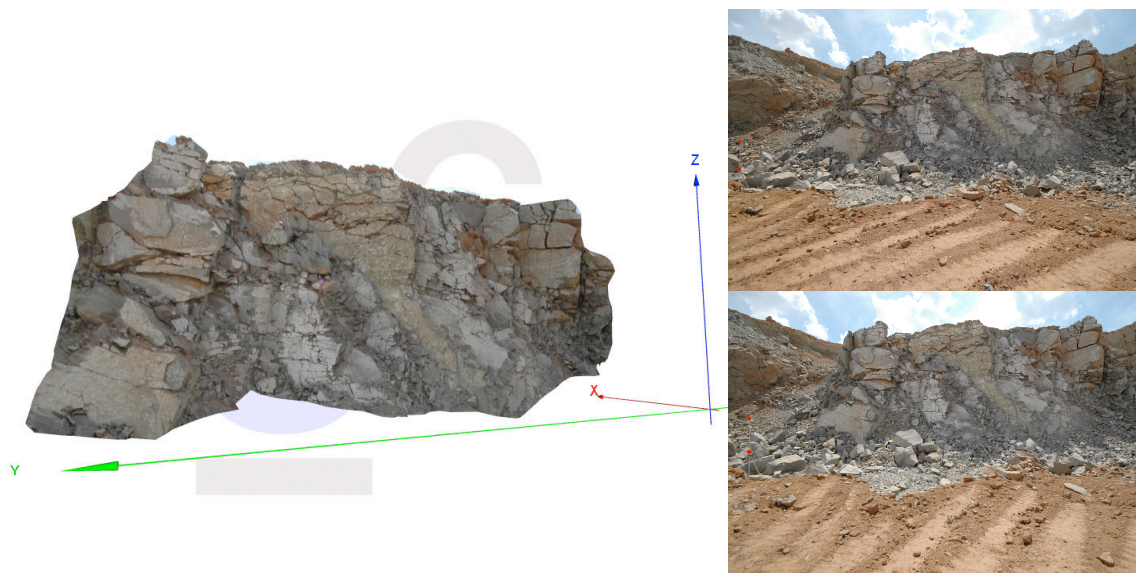


Figure 11: 3D image from a bench from a single stereo pair (left). Stereoscopic image pair used for 3D image generation (right).

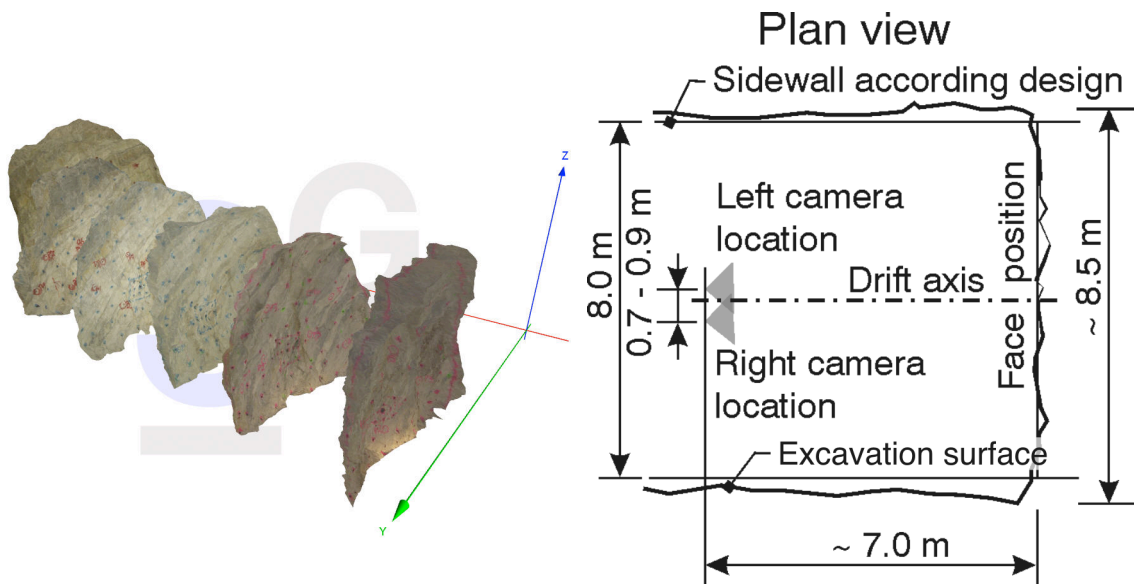


Figure 12: Series of 3D images of a drift tunnel. Each 3D image has been generated from a single stereo pair and georeferenced to the same coordinate system using ground control points (left). General camera setup relative to the face (right).

Images from panoramic cameras have some advantages over images from still cameras. Panoramic images nowadays still have a significant higher image size (up to 400 Megapixel). This entails the conservation of fine details in one image. Panoramic images show the tunnel area in both directions, to the face and the portal. The area towards the portal captures also existing displacement monitoring targets which are used for georeferencing of the 3D image. Figure 13 top shows two parts of a panoramic image, one is used for 3D image generation while the other is used for registration. Figure 13 bottom shows the setup of panoramic cameras for tunnel face mapping and the 3D image obtained from a panoramic image pair.

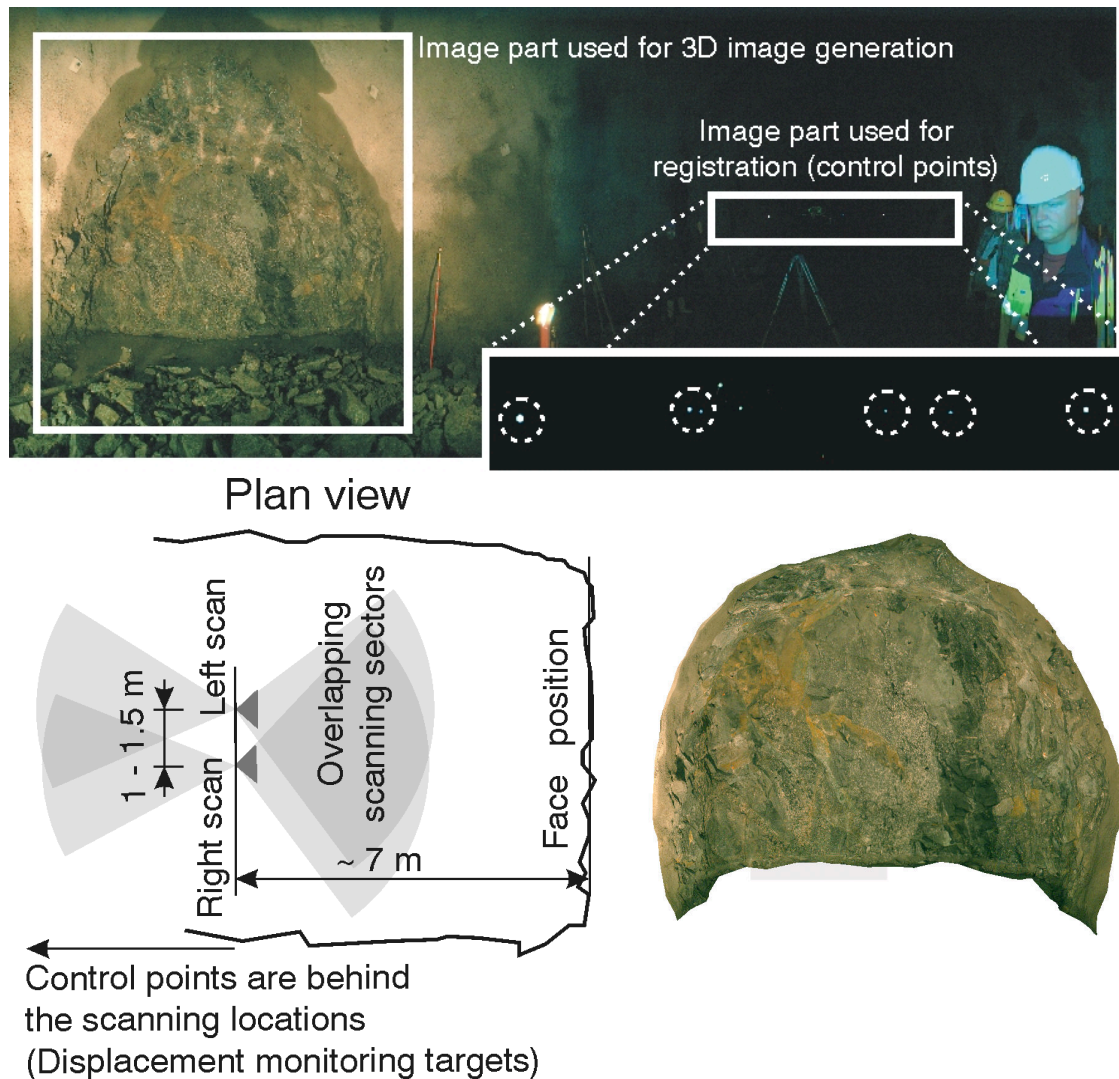


Figure 13: 3D image generation and registration from panoramic images in tunnelling. Panoramic image provides information for 3D image generation and registration (top). Scanning areas and positioning of panoramic cameras for tunnel face mapping (bottom left). 3D image of a tunnel face obtained from a panoramic image (bottom right).

2.2.3.2 Merged 3D images

Merged 3D images are those combined from two or more overlapping individual 3D images. The generation of a merged 3D image involves more steps. Apart from the generation of the individual 3D images, it requires the definition of the overlap and merging calculation.

Figure 14 (left) shows a merged 3D image of a quarry covering an area of about 150 m height and 200 m width. Stereo pairs have been acquired from a dam at

the toe of the slope and from opposing benches within the quarry. Figure 14 (right) shows the patches of the single 3D images and the corresponding camera positions (grey cones). The 3D image comprises 11 convergent image pairs.

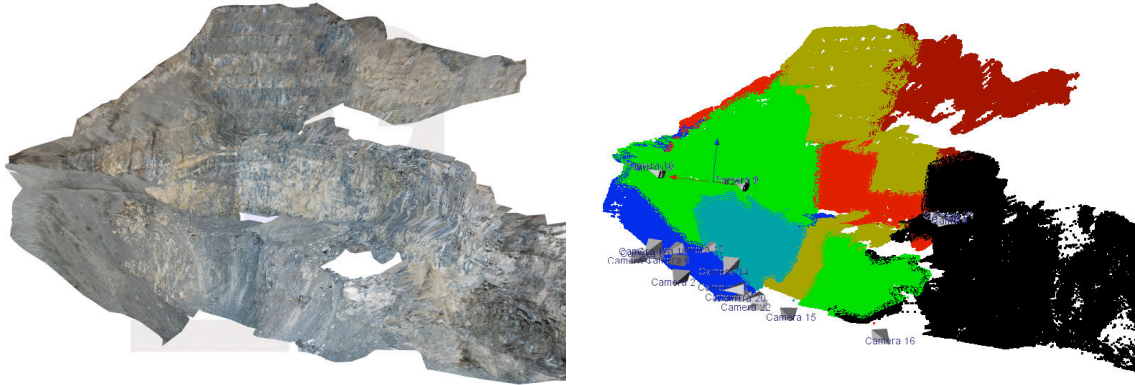


Figure 14: Merged 3D image from a quarry. It comprises 11 stereo pairs. The 3D image covers a height of about 150 m and width of about 200 m (left). Individual 3D point clouds in the merged position and camera positions (right).

Figure 15 is an example from an underground drift tunnel showing the face together with the sidewalls and the crown. It has been merged from four single 3D images whose patches are shown on the right hand side. The patches are shown with the corresponding camera positions. The 3D image has been scaled and oriented using a range pole and compass.

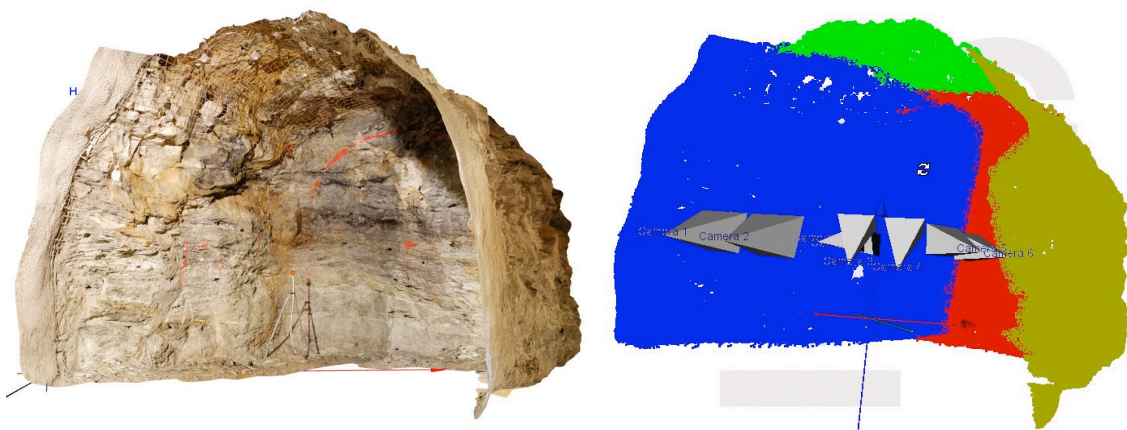


Figure 15: Merged 3D image from a drift tunnel showing the face, crown and sidewalls. Note the range pole at the left hand side of the face (left). Individual 3D point clouds in the merged position and camera positions (right).

2.3 Discontinuity measurements from scaled 3D images

From a rock mechanics aspect the prime use of a 3D image is, aside from the description of the slope and/or free faces, the measurement of discontinuity parameters. The considered parameters include at large scale the position, orientation and extent of discontinuities and at small scale the surface irregularity and roughness of the joints (Priest 1993). This section describes in detail the measurements which can be taken with the JMX Analyst software and using the data from the above described computer vision system. JMX Analyst is an assessment software for 3D images and forms part of the ShapeMetriX3D and JointMetriX3D software (3G Software & Measurement 2010).

2.3.1 Basic measurements

Individual orientations

Any location on the 3D image can be touched with a special kind of cursor. It follows the actual 3D shape of the reconstructed surface and changes its pointing direction according to the actual orientation of the surface. In this way orientation measurements are possible corresponding to the application of a compass-clinometer device on any particular location (Figure 16 left).

Linear features

The measurement of linear rock mass features such as joints, lithological borders, or strata is performed by marking the visible joint trace on the 3D image. The result of these markings is a three-dimensional poly-line. It consists of 3D surface point measurements. If the 3D poly-line shows a significant change in depth, a plane is automatically fitted to the set of surface points. The orientation of the fitted plane corresponds to the spatial orientation of the discontinuity that was marked, thus the three-dimensional orientation is determined only by marking the joint trace (Figure 16 middle).

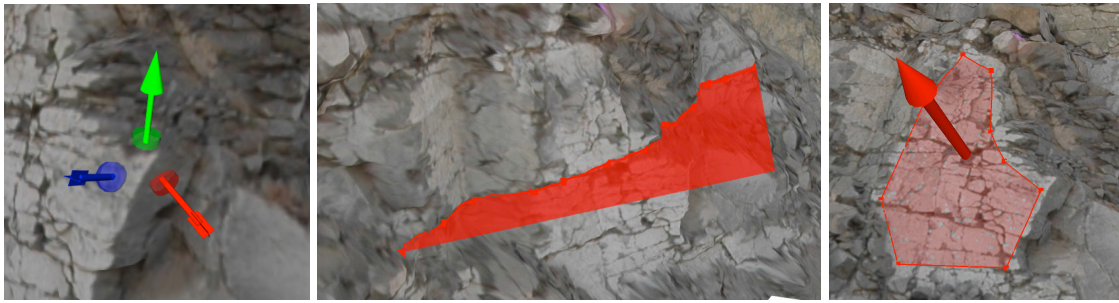


Figure 16: *Left*: Individual orientation measurements. *Middle*: Joint trace at an outcrop. The joint orientation is determined by fitting a plane through the spatial joint polygon. It is represented by a square. *Right*: Joint plane as an area. The joint orientation is determined as the mean orientation of the surface elements enclosed by the polygon. It is represented by the upward normal vector.

Areas

Areas are regions of similar geological attributes (e.g. lithology or same degree of fracturing) or joint surfaces. When an area is marked, a closed 3D poly-line is defined. Without difficulty it is possible to determine that part of the 3D surface that is inside the marked area. From the marked part the mean orientation is computed and instantly provided as dip angle and dip direction. Figure 16 right shows an example of a marked area and the resulting surface normal that indicates the spatial orientation.

Structure maps

Basic measurements, such as joints and areas, orientations, as well as coordinates, or distances are organised in structure maps. Structure maps comprise one or several structure sets that can represent geological units, e.g. discontinuity sets. Figure 17 shows an example of a 3D image with several structure sets marked. Structure sets allow for automatic calculation of set-related rock mass parameters such as orientation statistics, spacing and trace length distributions of discontinuities, etc. The combined information on orientation and spacing eases the determination of true and apparent spacing values.

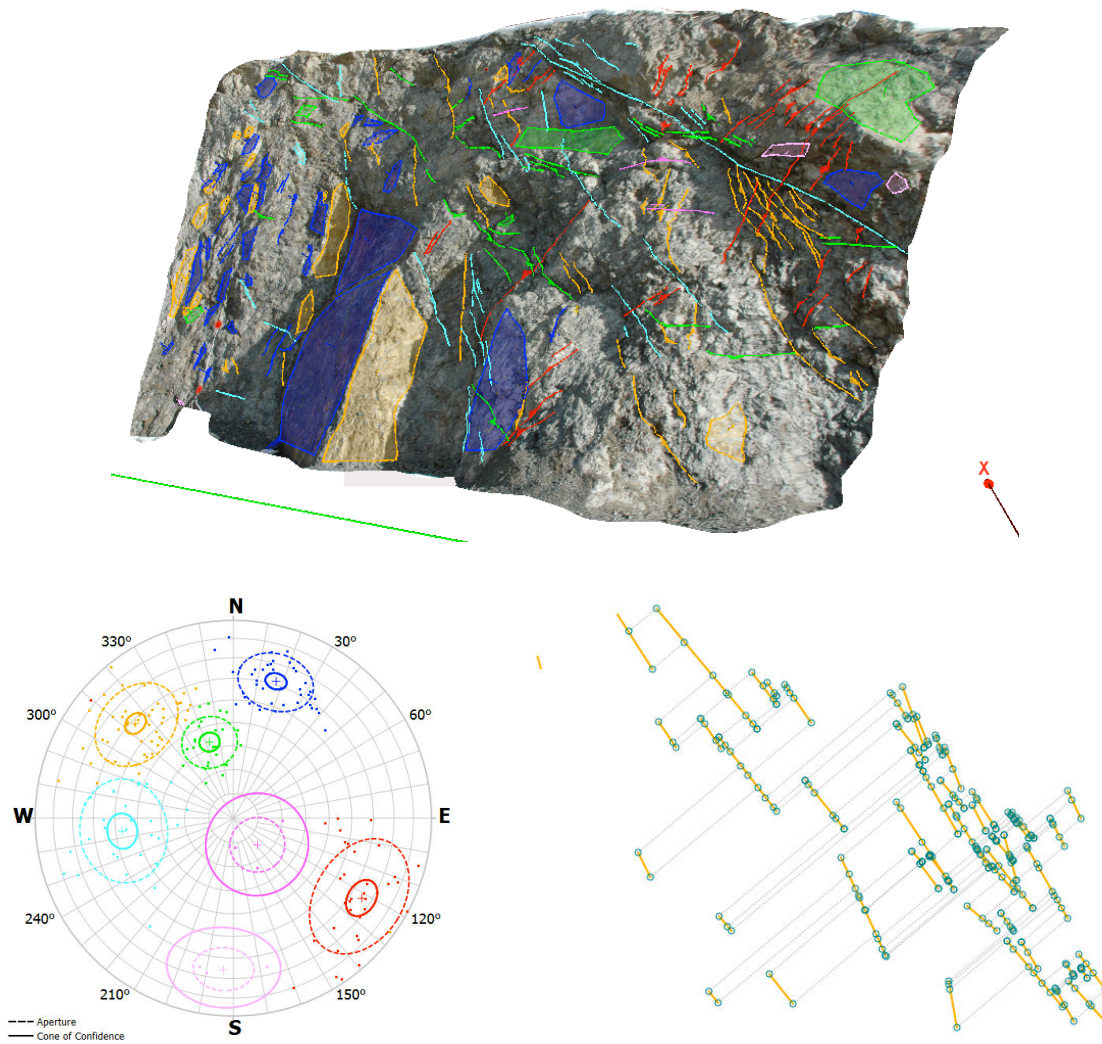


Figure 17: 3D image with structure map, orientation measurements in stereographic projection, and joint spacing for one structure set.

2.3.2 Practical reliability of measurements

Besides the theoretically achievable measurement accuracy as shown in section 2.1.1 the measurements for practical applications are faced with an additional number of influencing factors. The most important of these influencing factors are:

- Non-planarity of fracture surfaces:
The manual measurement is strongly influenced by the local orientation of a fracture surface (comprising waviness and roughness) while the remote measurement averages the orientation over the exposed fracture area.

- Relative orientation of rock face to the viewing direction of the measurement device:
Fractures striking sub-parallel to the instrument's viewing direction appear less prominent in a point cloud and are predominantly visible as traces.
- Partially or completely invisible fractures:
Data acquisition from one or few similar positions may not show the entire fracture system since fractures may be blind due to rock face orientation and small size, or obstacles. Fractures may also be seen just as traces rather than areas.
- Resolution of the image:
The image resolution determines the smallest feature (fracture or composition of fractures) identifiable from a 3D image.
- Resolution of the point cloud:
Point cloud resolution determines the smallest feature which can be measured from a 3D image.

These factors do not necessarily decrease the model accuracy but they complicate comparisons with single manual measurements. They may also induce directional bias. We note that different features may be represented at different levels of detail (Sturzenegger & Stead 2009). The following sections show comparisons of manually and remotely mapped fractures using a geological compass and remote measurement system, respectively. The author emphasises that this is a comparison between two methods; since each measurement has its own technical implications with respect to accuracy, the ground truth is unknown, or known with uncertainty!

2.3.2.1 Mean orientations

Table 1 shows four comparisons of mean orientations between hand-mapped and remotely-mapped fractures (Pischinger 2006, Ferrero et al. 2007, Coggan et al. 2007). The table includes the mean orientations of the fracture sets in terms of dip direction and dip angle, the difference between the mean orientations for each set in terms of dip direction, dip angle, and absolute angular deviation, and the remote sensing method. Case study *Feiglbauer* includes 118 hand mapped fractures and 544 fractures mapped with 3D images. Case study *Arnad* comprises about 190 hand mapped fractures (including 1 principal and 3 secondary sets not mentioned in Table 1) and 288 fractures mapped with photogrammetry. Case study *Tremough entrance* comprises 149 hand mapped, and 276 and 280 fractures mapped with laser scanning and photogrammetry, respectively.

Table 1: Comparison between hand-mapped and remotely-mapped fracture orientations. The shown values are mean orientations of sets.

Joint set	Hand mapped		Remote measurement		Difference		
	Dip direction	Dip angle	Dip direction	Dip angle	Dip direction	Dip angle	Absolute angular deviation
	<i>Case study: Feiglbauer</i>		<i>Author: Pischinger (2006)</i>		<i>Method: Photogrammetry</i>		
SF	156	49	156	47	0	2	2.00
KH1	20	81	16	76	4	5	6.35
KH2	234	79	241	83	7	4	7.99
KH3	272	41	273	42	1	1	1.20
	<i>Case study: Arnad</i>		<i>Author: Ferrero et al. (2008)</i>		<i>Method: Photogrammetry</i>		
Sev1	140	75	143	78	3	3	4.18
Sev2	195	75	200	73	5	2	5.21
J1	238	78	238	81	0	3	3.00
J7	295	36	283	39	12	3	7.88
	<i>Case study: Tremough entrance</i>		<i>Author: Coggan et al. (2007)</i>		<i>Method: Photogrammetry</i>		
1	320	88	319	86	1	2	2.24
2	191	88	184	85	7	3	7.60
3	230	67	221	70	9	3	8.89
4	25	49	20	53	5	4	5.57
	<i>Case study: Tremough entrance</i>		<i>Author: Coggan et al. (2007)</i>		<i>Method: Laser scanning</i>		
1	320	88	315	88	5	0	5.00
2	191	88	184	85	7	3	7.60
3	230	67	231	63	1	4	4.10
4	25	49	16	51	9	2	7.17

Table 1 shows that the absolute angular deviation between hand mapped and remotely measured for all the reported joint sets is smaller than 9 degrees. The majority of the deviation is smaller than 6 degrees. As would be expected from section 2.1.1, the dip direction shows a stronger variance than the dip angle, thus is more sensitive to influencing factors and measurement bias. The stereographic projection in Figure 18 is related to the data from Pischinger (2006). On the left hand side, the hand mapped data and on the right hand side the data from 3D images are shown. The three joint sets SF, KH1 and KH2 are well defined in both data sets while one joint set KH3 is only prominent in the data from 3D images. The reason has been that accessibility was not granted for mapping manually KH3. Pischinger (2006) also reports a decrease of the cone of confidence in this example to about 50 % from manual to remote measurement, i.e. the mean orientation becomes more confident.

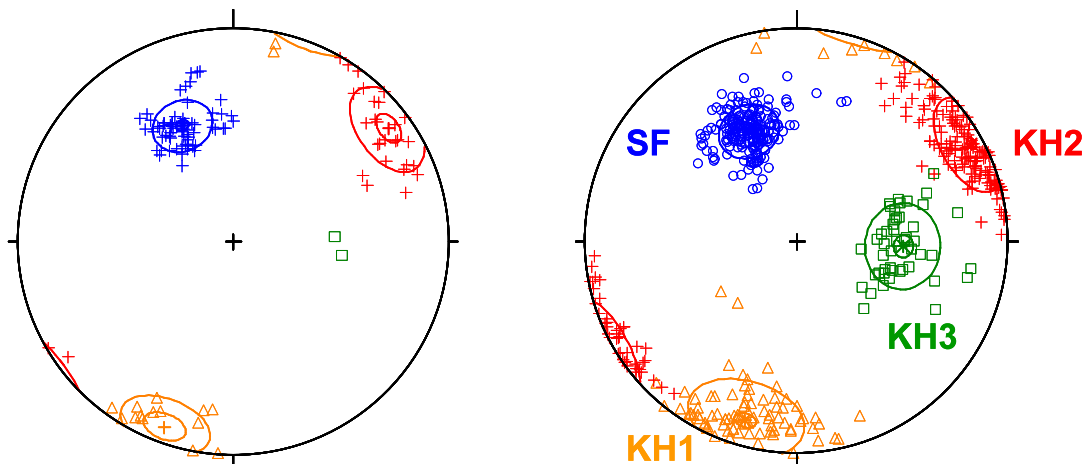


Figure 18: Stereographic projection of fracture orientations (poles) measured by hand (*left*) and photogrammetry (*right*) from Pischinger (2006).

2.3.2.2 Single orientation measurements

Non-planarity of fractures strongly influences the comparison between manual and remote measurements, but also as shown in the examples below, the resolution of the model with respect to identification and possibility for taking the correct measurement. Figure 19 shows histograms of the absolute frequency of angular deviations between direct compass and 3D image measurements. The upper example comprises 28 samples where the majority of the measurements show a deviation smaller than 3 degrees irrespective of comparisons of dip direction or dip angle. The average point spacing of the 3D images has been about 4 cm. Orientation measurements have been taken approximately at the same position. The lower example comprises 9 samples. The majority of the deviations is also lower than 3 degrees although this behaviour is less

pronounced than in the previous example. Indications for the higher spread and higher deviations may be the lower number of samples and the higher average point spacing of the 3D image (approx. 20 cm).

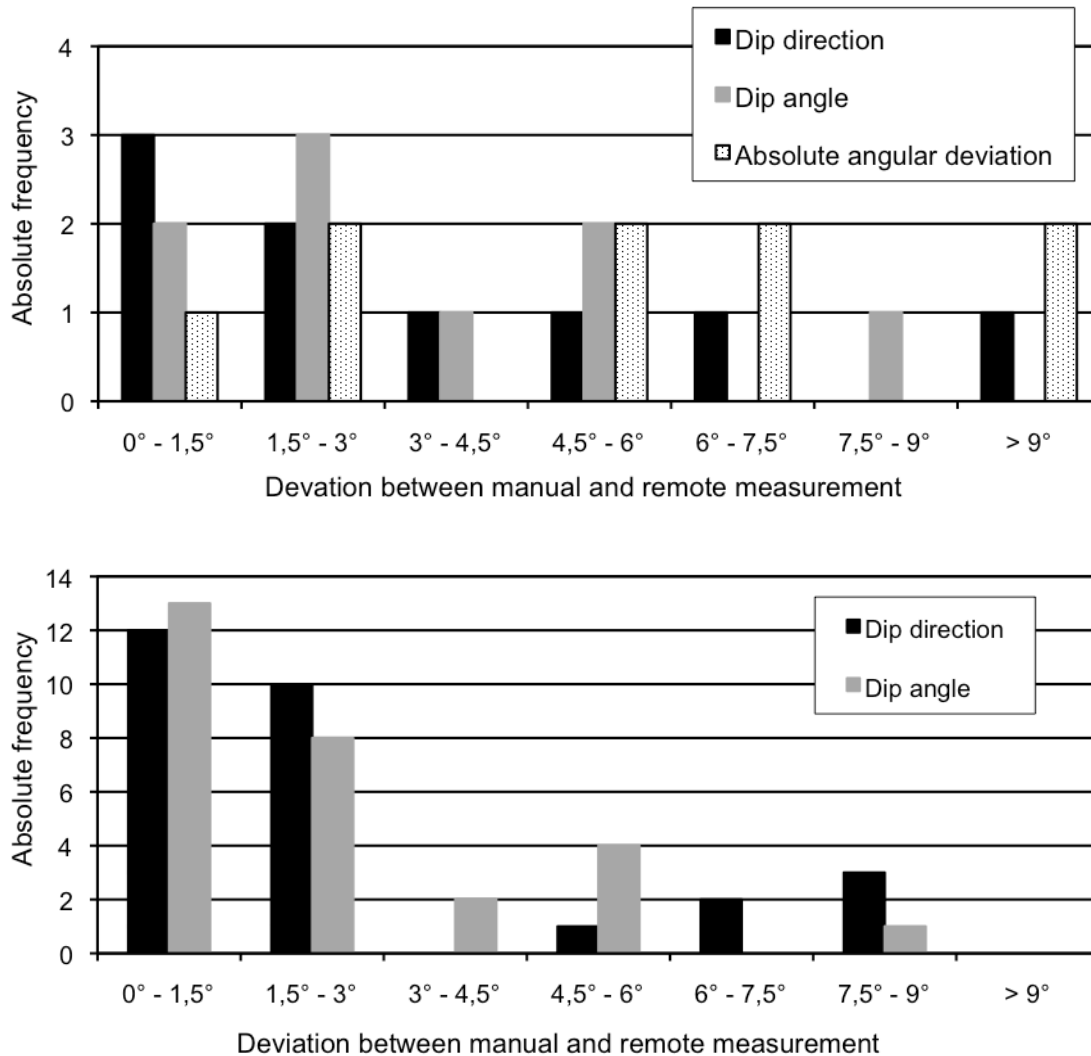


Figure 19: Histograms comparing single fracture orientations manually and remotely measured. The average point spacing of the 3D image in the upper and lower diagram is 4 cm and 20 cm, respectively.

2.3.3 Interactive and automatic measurements

Digital data promote the application of automatic measurement algorithms. They increase the objectivity and productivity of the geological data acquisition.

Objectivity increases since robust algorithms¹ come up with the same result even when slightly changing the input parameters of an objective function. Productivity increases since the computer takes over the segmentation between similar and distinctive data sets using algorithms. Automatic measurements for geological data acquisition from 3D images can be distinguished into three levels (Ferrero et al. 2008) – interactive, automatic and semi-automatic measurements:

2.3.3.1 Interactive measurements

Measurements are taken interactively on the 3D image (or other representations: point cloud, 2D image). The position and/or extent (length, area) of the measurement (see section 2.3.1) are marked with the computer mouse (or any other suitable input tool) after inspection of the 3D image and identification of a rock structure. The judgement of the relevance and proper placing and delineation of a structure is entirely left to the user. The user has to be a person with proper knowledge and experience on geologic mapping. Interactive measurements are a digital simulation of geological field mapping. Interactive measurements have been described by Gaich et al. (2004).

2.3.3.2 Automatic measurements

Position, extent and delineation of measurements are fully algorithmically determined based on a set of input data. Reported algorithms in geological literature work on the point cloud or the digital images. Hybrid point cloud – image algorithms have not been reported to the author's knowledge. Point cloud algorithms aim at the segmentation of planar regions within the point cloud (Figure 20 left). These regions are then related to daylighting areas of discontinuities. Image processing algorithms aim at the delineation of discontinuity traces and areas. They use significant contrast in the image to determine these boundaries (Figure 20 right). Automatic segmentation and delineation algorithms for rock masses have been described by Reid & Harrison (2000), Lemy & Hadjigeorgiou (2003), Tseng & Wang (2005), or Kemeny et al. (2006). Kemeny & Post (2003) present a method for estimating fracture orientation from digital images based on automatic fracture delineation and genetic algorithms. Voyat et al. (2006) use the Ransac approach (Fischler & Bolles 1981) for segmenting a point cloud into planar patches without outliers.

¹ A robust algorithm integrates the solution of a geometric problem, the treatment of degenerate cases and numerical calculation. It provides a consistent solution in case of non-perfect "natural" input data.

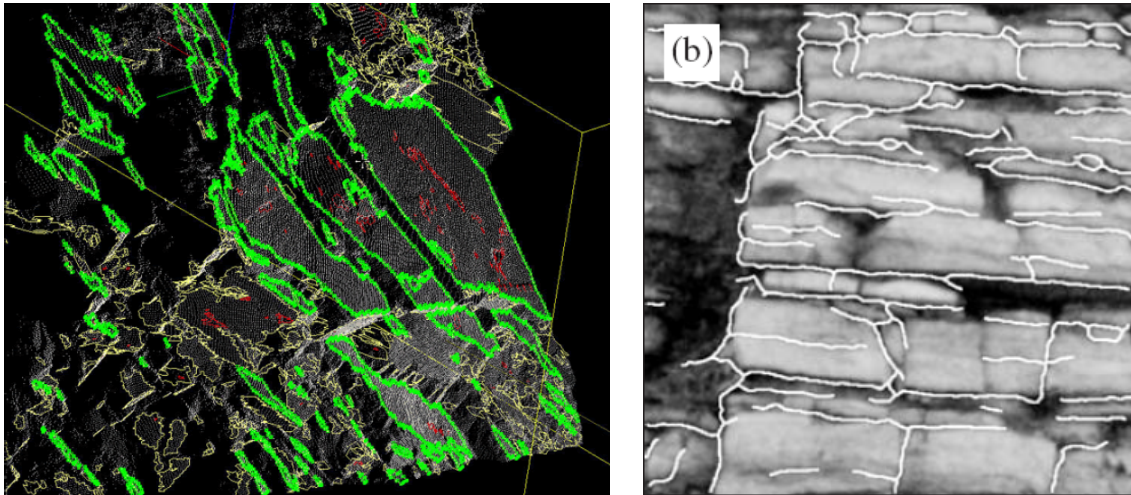


Figure 20: *Left*: Automatic delineation of daylighting fracture patches as green polygons (from Kemeny et al. 2006) *Right*: Automatic delineation of fracture traces (from Lemy & Hadjigeorgiou 2003)

2.3.3.3 Semi-automatic measurements

The semi-automatic approach is a combination of interactive and automatic measurements. The user defines initial values for the used objective function of the measurement. Initial values are positions and orientations in the point cloud or image. The initial values are typically provided by so-called seed points – interactively defined points around which the user assumes a feature complying with the corresponding objective function. Subsequent algorithms aim at finding traces or areas in the vicinity of the initial values.



Figure 21: Semi automatic delineation of fracture traces

An algorithm working on the point cloud aims at the detection of the extension of a joint surface and its orientation based on one single marked location on the joint surface. Usually a planar joint surface is assumed. An algorithm working on the digital images aims at the detection of lineaments. Only a few seed points are marked on the 3D image and the points in between are detected automatically based on image processing algorithms (Figure 21). This approach is also known under the term “live wire” (Falcao et al. 2000).

2.3.3.4 Discussion

The interactive approach leaves the responsibility for the evaluation with the geologist or geological engineer. Since all structures have to be marked manually, it is the least productive approach of the three mentioned ones. The fully automatic analysis of rock mass features has limits in the detection of rock mass properties encountered during practical work, especially when facing changing rock mass conditions and image resolutions. Problems observed thus far include the following:

- Artificial lineaments – excavator scratches or half-barrels from drilling, or even boundaries between light and shadow – may be mistakenly included in the discontinuity data set. Unfortunately, such features are often even more prominent than rock mass features.
- Identification of lineaments strongly depends on the resolution of the images, i.e. the level of detail (Sturzenegger & Stead 2009).
- The automatic identification of joint sets based on topographic surface analysis is only reasonable when a blocky rock mass is present. Analysing the point cloud does not consider difference between rock joints and artificial surfaces.

A semi-automatic approach that supports the interactive assessment from the author’s perspective is the most promising for practical applications. It speeds up interactive marking of geological features but still leaves the decision on the geological relevance of a feature with the experienced geologist or engineer in front of the computer.

2.4 Summary

New technologies for the data acquisition of rock masses emerged during elaborating this work and have proved to be valuable tools for the daily engineering geological and geotechnical practice. This section has given a basic introduction to remote measurement systems including image based and laser-

based technologies and outlined the characteristics involved with these technologies for an appropriate selection to a practical problem. The author discussed the application of a computer vision system for geological and geotechnical data acquisition using digital SLR and panoramic cameras. During this work the system has been developed by the software and measurement device manufacturer 3G Software & Measurement and modified for routine application in the field of mining and rock engineering. As a basic principle, the system generates 3D images from a set of stereoscopic image pairs.

The last section of this chapter focuses on the measurements related to rocks taken from a 3D image and presents data on the reliability of these measurements. It has been shown that mean orientations could be determined with a difference of less than 9° between hand mapped and remotely measured structures (with a majority of measurements less than 5°) together with a typical decrease of the aperture of the cone of confidence of about 50%. The majority of single orientation measurements differs only by 3° . In these comparisons, it is not clear which set of measurements – from 3D images or by hand – is the more correct one; thus neither can be accepted as the control set.

The final section discusses automatic measurements to enhance objectivity and productivity in data acquisition. Available approaches include interactive, automatic, and semi-automatic assessments. Semi-automatic assessments are preferred since they increase productivity, robustness, and objectivity while leaving the final decision about the relevance of the measurement at the assessing geologist or engineer.

3 The shear behaviour of discontinuities

The mechanical behaviour of blocks depends on the blocks's properties and the properties of the blocks's faces, edges and corners abutting the rock mass.. Discontinuities are fractures in the rock mass that fully separate the block; they are usually approximated by planes. The shear behaviour is especially important if sliding on discontinuities is involved with block motion. This chapter discusses the parameters involved with respect to the sliding mechanisms and outlines the different stages of the shear behaviour of a matched discontinuity. Based on the conclusions from literature (which are outlined in the following section) and a more detailed investigation described by Schieg (2006) and Seywald (2006) a constitutive model for the joint shear behaviour under general boundary conditions is proposed including a summary of the required parameters and their determination. The chapter concludes with a parametric study of the constitutive model.

3.1 Shear behaviour and influencing factors

The shear behaviour of a discontinuity is the response of the shear and normal stresses acting on a discontinuity and the related shear and normal displacements of the contact area due to a loading and/or constraint. The formal description of these relationships is the constitutive model, allowing studying, analysing, simulating and predicting the shear behaviour mathematically. The shear behaviour depends on several factors, summarised below:

- Friction of the rock material:
The friction concept basically is an engineering substitute for the quantification of electromagnetic processes and interactions taking place at irregularities at a microscopic scale (Persson 2000). Friction in a rock mechanics sense is the sliding resistance of technically planar rock joints which is also referred to as the Coulomb friction model. In this model the frictional resistance is directly proportional to the normal load and independent of the sliding velocity. The friction is expressed in terms of the friction angle φ ; $\tan \varphi$ determines the ratio between frictional strength and normal load. This friction angle φ is also called the basic friction angle φ_b .
- Surface irregularity of the discontinuity plane (roughness):
The discontinuity roughness is the irregularity of a natural joint surface, i.e. its deviation from a plane. It can be classified into the waviness and unevenness (ISRM 1977). Waviness corresponds to large scale

undulations while unevenness is the small scale irregularity. The term “small scale” refers to a lower bound of irregularity size which can be measured by available methods such as a comb (Barton & Choubey 1977), linear profiling, compass-disc-clinometers, and mechanical and contact-free methods (mechanical profilometers, 3D laser scanners, photogrammetry, etc.).

The roughness influences various aspects of the shear behaviour. Due to the slope of the rising asperities, the relative angle between the resulting force and the shear plane increases; this increases the shear resistance (Patton 1966). At even higher normal loads the asperities fail and cause a “cohesional” contribution to the shear resistance (Patton 1966, Ladanyi & Archambault 1970, Handanyan et al. 1990, Maksimovic 1996, Seidel & Haberfield 2002). In confined conditions the displacements perpendicular to the shear plane (due to the slope of the asperities) increase the normal load and the corresponding shear resistance (Archambault et al. 1990, Ohnishi & Dharmaratne 1990).

- Discontinuity aperture:

In nature it is common to find discontinuities, appearing open, i.e. opposing joint walls, are separated. The aperture is defined as the distance between the joint walls along the mean normal vector of the plane (Priest 1993). Completely open discontinuities without any contact area and stress transfer potential are beyond the scope of this chapter.

Discontinuities can display a certain aperture yet retain partial contacts. This is called a mismatched joint. The upper bound of the aperture for a mismatched joint is, by virtue of geometrical conditions, twice the amplitude of the roughness.

Aperture basically influences the deformability of a joint perpendicular to its plane. The normal stiffness decreases with increasing aperture following a hyperbolic law (Priest 1993, Bandis et al. 1983 cited in Bandis 1990, Goodman 1976). It is supposed that the shear stiffness also decreases with increasing aperture, although no investigation results could be found.

The aperture influences also the dilational behaviour. Matched joints usually show a purely dilational characteristic (Seywald 2006) while mismatched joints can show a contractual behaviour, especially during the initial stage of shearing (Barton & Choubey 1977).

- Infillings:

Infillings are frequently encountered in open discontinuities. They can consist of recrystallised minerals (e.g. quartz), granular soil, or clayey material. While a compact recrystallised or cemented material tends to act as a sealing and reinforces the rock mass, the others tend to weaken the joint and influence the shear behaviour (Indraratna & Haque 2000).

Critical parameters are the infilling material and the relative thickness of the infilling. The relative thickness is defined as the ratio between the

mean thickness of the infilling and the amplitude of the joint roughness. Indraratna & Haque (2000) concluded the following important facts:

- The shear strength drops significantly towards the strength of the infilling even with a small infilling thickness.
- The shear behaviour is exclusively controlled by the infilling material beyond a critical value of the relative thickness. Depending on the joint roughness, infilling material and boundary conditions (confinement) the critical value of the relative thickness may be between 1.2 and 1.8. A relative thickness below this value causes an interaction between infilling and surface asperities.
- The shear displacement at peak shear strength significantly decreases if the relative thickness exceeds the critical value. This observation requires further explanation. The authors consider the absolute peak shear strength – a value which includes shear strength increase due to normal stress increase caused by suppressed dilation (CNL tests). If the joint is clear or the infilling is thin, normal stress increases with shear displacement. If the joint (soft) infilling is thick, the joint does not tend to dilate and no significant increase of the normal stress is observed. The peak shear strength occurs when the infilling fails at relatively low shear displacements. In this dissertation the author uses the relative shear strength (the ratio between current shear and normal stress) instead of the absolute shear strength. This parameter provides more meaningful insights into the shear behaviour and eases the interpretation.
- The peak shear stress drops exponentially with increasing relative thickness until the critical relative thickness.
- Filled joints are prone to contractive behaviour.
- Consolidation of the infilling plays an important role with varying shear displacement rates which is critical, for instance, with seismic loading.

Indraratna et al. (2005, 2008) have performed further experimental and theoretical investigations. Figure 22 shows the role between φ_b and φ_{fill} after Indraratna et al. (2005). If the discontinuity is perfectly closed, the frictional resistance is directly related to the basic friction angle and the surface

irregularity. If the relative thickness in the discontinuity exceeds the critical value of 1.4, the shear resistance is exclusively controlled by the frictional properties of the infilling. In the transition zone an approximate negative exponential decrease of the shear resistance of the discontinuity is observed.

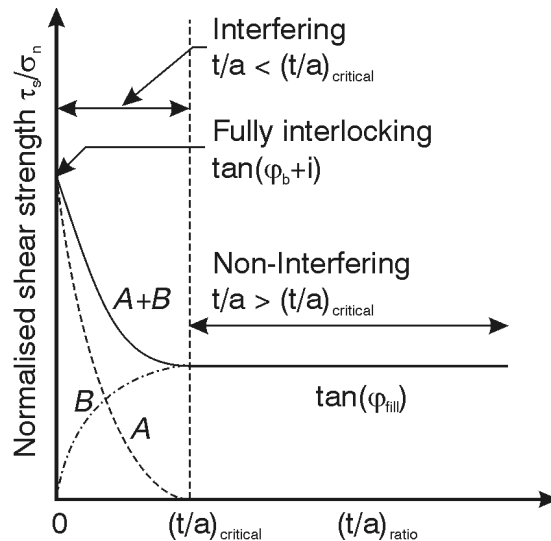


Figure 22: Shear strength model for infilled joints showing the role of φ_b and φ_{fill} (figure modified after Indraratna et al. 2005)

- **Strength of the rock material:**
The strength of the rock material controls the transition between asperity sliding mode and asperity shearing mode. It affects the peak shear strength and dilational behaviour. The existing models describe the asperity strength either by the unconfined compressive strength (Barton & Choubey 1977), tensile strength (Handanyan et al. 1990), cohesion and friction angle (Patton 1966), or all of them combined (Ladanyi & Archambault 1970).
- **Deformability of the rock material:**
The deformability of the asperities influences the elastic shear stiffness and subordinately the dilation under varying normal stress (Seidel & Haberfield 1995).
- **Initial normal stress:**
The normal stress acting perpendicularly on the joint predominantly influences the shear resistance. Additionally, the initial normal stress defines the initial normal stiffness (Bandis et al. 1983). Thus, it affects the development of dilation. It also controls the transition between the asperity sliding and shearing modes.

- **Boundary conditions:**
The boundary conditions are referred to as the perpendicular confinement of the joint. Boundary conditions are related to the joint normal stiffness adjacent to the joint and act like a spring. If the normal stiffness does not vary with the displacement, this condition is defined as a constant normal stiffness (CNS). Since normal displacements occur during shearing of a rough joint, the normal stiffness affects the normal stress, and hence, influences dilation and peak shear stress. In the absence of normal stiffness the condition is referred to as a constant normal load (CNL).
- **Petrographical properties:**
The properties of the minerals, especially hardness and brittleness, influence the behaviour of the material that is formed after asperity shearing (asperity wear). Depending on normal stress and mineral composition, sheared asperities can form granular or cohesive layers. Under certain circumstances the formation of slickensides is possible as well. Slickensides significantly reduce the residual friction angle (Seywald 2006).
- **Rock fabric:**
Foliation of the rock may influence the asperity failure mechanisms depending on the orientation relative to the shear plane as shown by the experimental investigations of Button (2004).

3.2 The shear behaviour of matched discontinuities

This chapter describes the mechanical phenomena occurring during shearing which provide the basis for the establishment of the constitutive model in section 3.3. In order to account for the interaction with blocks, the general description of the joint shear behaviour requires the determination of the shear stress, normal stress, and dilation throughout the shear displacement, and the stress path. The shear behaviour of a rough joint has several typical stages. In the following paragraphs these stages are described for a quasi-homogeneous and isotropic material, well-matching joint walls, and for constant normal load conditions. At the end of the chapter the peculiarities of other influencing factors are addressed.

3.2.1 Stage A: Mobilisation of the shear stress

Before shearing takes place, the joint is perpendicularly loaded resulting in stresses acting on each asperity face in contact. After shear initiation a stress redistribution takes place loading the asperity slopes facing the shear direction

and unloading the slopes opposing the shear direction. The asperities are deformed by elastic strains. Slip in the contact areas does not take place. Thus, the joint does not dilate. The shear load increases almost linearly with the shear displacement.

3.2.2 Stage B: Mobilisation of dilation

With increasing shear displacement the joint starts slipping at portions of the joint area at which the local resultant force exceeds the slip limit (Coulomb's law). Typically, these portions are flat relative to the shear direction or point towards it. The slip leads to an additional stress redistribution to steep asperities (opposing the shear direction) which are not at slip yet. With increasing shear load the areas at which slip occurs, become gradually steeper. The upper limit of asperity angles at which slip can occur depends on the ratio between shear and normal load, and the surface friction angle. This value is defined as α_{\max} in expression (5). H in this case is the shear load while V is the normal load. Since H and V can also be considered to be external loads (instead of local forces), α_{\max} is the maximum global angle that can result from joint dilation. Asperities which are steeper than the maximum asperity angle are consequently sheared off.

$$\alpha_{\max} = \arctan \frac{H - V \cdot \tan \varphi}{H + V \cdot \tan \varphi} \quad (5)$$

In this stage relative shear displacements between the joint walls take place. For kinematical reasons displacements perpendicular to the shear plane take place as well. Since with increasing shear displacements the slip portions become steeper, the dilation rate successively increases. During this stage the mobilisation of dilation takes place due to sliding on asperities and also shearing off steep ones. The shear stress curve is typically non-linear.

Figure 23 highlights the shear behaviour during the stages A and B by data obtained from a CNL shear test. The bold solid line represents the mobilised shear resistance in terms of the apparent friction angle. It is the inclination of the resultant of the external forces. The dashed lines are the mobilised dilation angle of the joint and the basic friction angle, respectively.

In stage A the shear stress mobilises almost linearly with displacement which can be observed in the bold solid line. The joint does not dilate. Once the inclination of the external resultant exceeds the basic friction angle, the joint starts dilating following a non-linear mobilisation law (Stage B). The mobilisation of dilation reaches the peak together with the maximum shear resistance which represents the end of stage B.

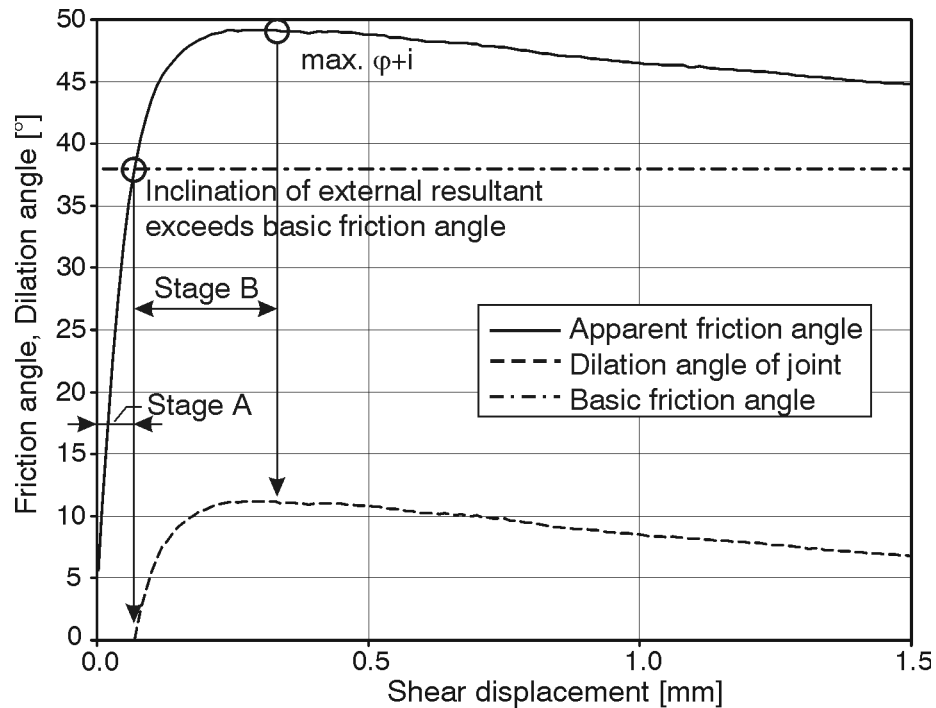


Figure 23: Shear behaviour of a matched rough joint during stages A and B, assuming that the tangential component of joint slip is restricted to a single linear path.

3.2.3 Stage C: Surface degradation

After reaching the maximum shear resistance the joint is fully at slip and dilating at its maximum rate. In the same instance the contact area becomes gradually smaller due to asperity sliding. The smaller contact area increases local stresses on the asperities together with a decrease of the asperity section. As a consequence, the asperities degrade causing a decrease of the joint's potential for dilation. Degradation is a result of shearing of asperities, grinding of sheared asperities, filling the void with sheared material, material compaction, etc. (Huang et al. 1993).

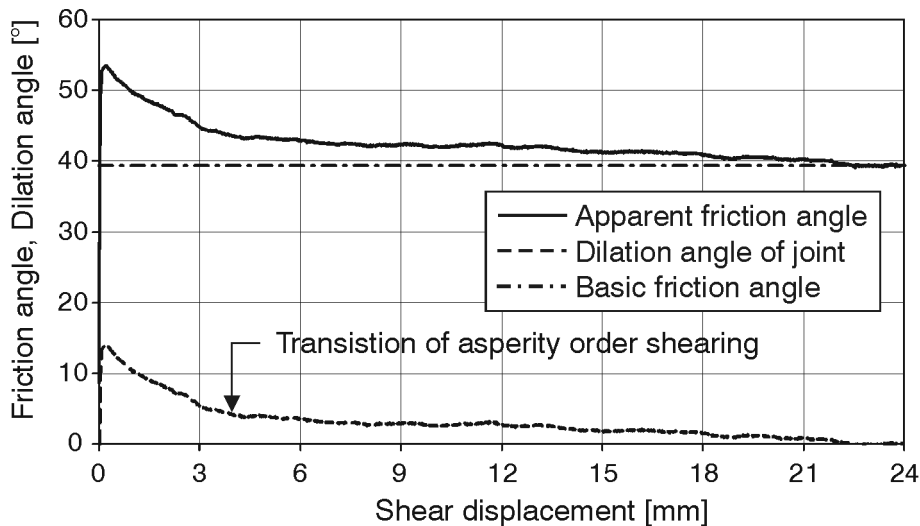


Figure 24: Shear behaviour of a rough rock joint in stage C – asperity degradation

Figure 24 shows the shear behaviour after the maximum shear resistance. The shear stress decreases proportionally to the dilation rate. The assumption of a constant basic friction angle throughout the shear displacement is reasonable as well. For the tested material, the basic and residual friction angles are almost identical under the applied normal stress level; this has also been addressed by Ladanyi & Archambault (1970).

The degradation gradient decreases with the shear displacement. The dilation curve also shows a smooth kink at an approximate shear displacement of four millimetres (in the test shown in Figure 24). These phenomena can be explained by the wear theory of Plesha (1987). In this theory the dilation angle of a rough joint with degrading asperities decreases following a negative exponential law. The asperity surface degradation is inversely proportional to the performed shear energy. The shear energy is the plastic tangential work per unit volume and the integral sum of the shear stress over the shear displacement. The kink in the dilation curve is a consequence of the surface morphology. Plesha classifies the asperities into first-order and second-order asperities following the ideas of Deere et al. (Deere et al. 1966 cited in Plesha 1987). Figure 25 shows the concept of first and second order asperities. It becomes obvious that the first order asperities are the mean of the second order asperities considering a finite sampling length. It is also obvious that the orientation of the second order asperities varies more significantly than those of the first order ones, and that second order asperities are steeper than first order ones relative to the shear plane. For this reason second order asperities are earlier sheared off and the surface degradation exhibits a higher gradient compared to shearing off the first order asperities. The kink represents the transition from shearing second-order asperities to first-order asperities.

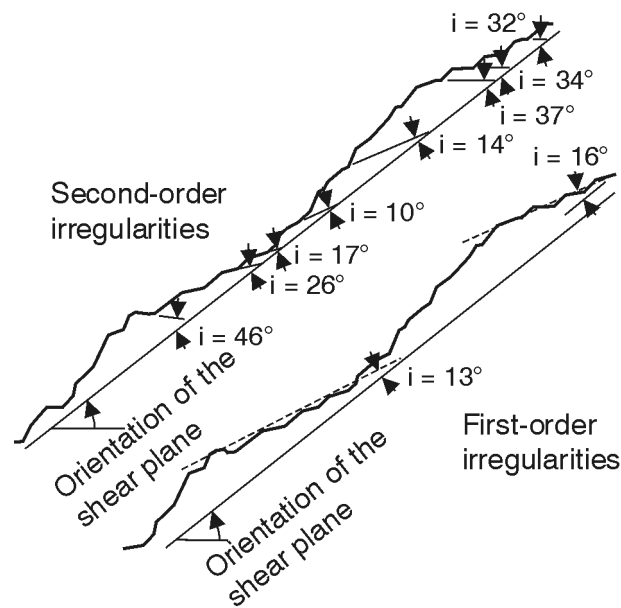


Figure 25: The concept of first and second order irregularities (asperities), modified and redrawn after Deere et al. (1966)

3.2.4 Stage D: Residual stage

Ideally, after sufficient shear displacement all asperities failed and the void had filled with debris. The surface has a residual shape. In this stage the shear stress approaches the residual value while dilation does not take place any longer.

3.2.5 Peculiarities

The above outlined behaviour is typical for a joint with matched walls, homogeneous and isotropic material, and constant normal load. For a foliated material the orientation of foliation planes relative to the shear direction plays an important role in the failure of the asperities. It can induce contractive behaviour if the foliation dips towards the shear direction. Different orientations of the foliation can even cause a complete change of the asperity failure mechanisms, for instance from interlayer slip to rotational mechanisms such as *micro-toppling* (Button 2004). If a porous material is sheared, contraction rather than dilation occurs under sufficiently high normal stresses. The behaviour will also be different if the shearing of asperities dominates the asperity sliding mechanism. In this case the principles of shearing of intact rock seem to be more suitable. It is the case if the stresses concentrated in the solid portion of the asperities are in the order of their strength (irrespective of the occurring asperity failure mode), or if the majority of asperity slopes are steeper than the sliding limit defined in expression (5). For a mismatched joint it is likely that contraction takes place in

the initial shear stages until the joint walls have come into contact. This has been observed by a number of authors, for instance (Barton & Choubey 1977, Szymakowski & Haberfield 2001, Olsson & Barton 2001). As a side comment, contractive behaviour has also been observed after overriding distinctive asperities. This behaviour has been shown, for instance, by Boulon et al. (2002) on joints in granodiorite and Indraratna et al. (2005) on artificial saw-teeth shaped samples.

Another remarkable property is the decrease of the residual friction angle with increasing normal stress as observed by Seywald (2006). Figure 26 shows the results for three test series, one obtained from CNL multi-stage shear tests at a sheared surface, the other ones were obtained from CNS tests where in the latter no dilation was admitted. The normal stress is considered at peak shear strength at the beginning of stage C. The decrease of the residual friction angle can be explained by compaction of sheared material and grinding of the surface in case of the CNL test, and the formation of slickensides in case of the CNS tests. Seywald (2006) reports a strong formation of slickensides in case of the “zero dilation” test, decreasing the residual friction angle from 39° to 29° for high normal stresses. The maximum normal stress at the peak shear strength has been observed with 23% of the unconfined compressive strength of the sample material. The normal stress has increased to maximum 28% of the unconfined compressive strength during shearing.

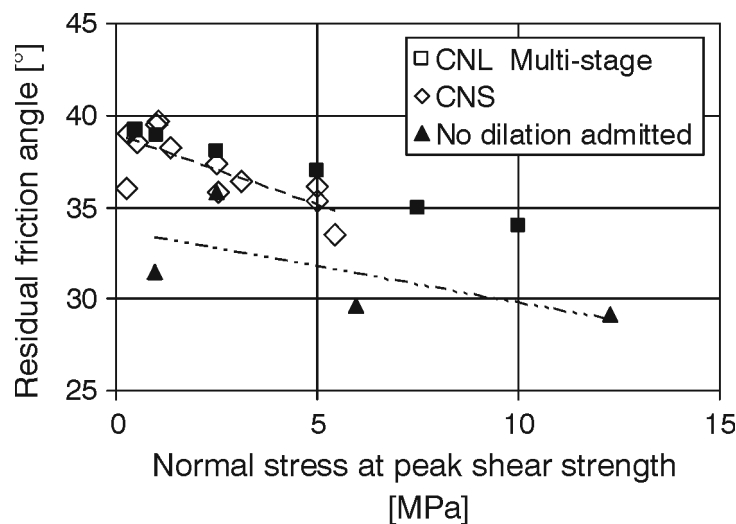


Figure 26: Decrease of residual friction angle with increasing normal stress

3.3 Constitutive model

The facts of section 3.2 lead to the formulation of a constitutive model for the shear behaviour of matched rough joints. It includes only parameters which can be obtained by engineering testing methods, either laboratory or field methods. The constitutive model comprises the stages A, B, and C: the linear mobilisation of shear stress, the mobilisation of dilation and the surface degradation. Stage D is considered to be the limit value after a theoretically infinitely long shear displacement. The constitutive model considers shear and normal displacements. Hence, it is capable to describe the behaviour under normal stiffness boundary conditions.

3.3.1 Assumptions

Most of the constitutive models include assumptions that only approximately match nature. However, for the engineering level of accuracy these inadequacies are either of limited significance or conservative. The proposed constitutive model relies on the following assumptions:

- Joints cannot sustain tensile stress.
It does not apply to healed or cemented, or only partially persistent joints.
- The shear resistance of local joint wall contacts is only frictional, i.e. cohesion of the contact is not considered.
- The asperity material is isotropic and homogeneous.
Rock types often possess an expressed fabric (e.g. phyllites, schists, etc.) which governs their mechanical behaviour.
- The average normal stress in the joint is significantly lower than the unconfined compressive strength of the asperity material. Hence, the shear behaviour is dominated by dilation and asperity degradation.
The shear behaviour of joints in weak rock masses at great depth is governed by influencing factors not covered by the proposed constitutive law.
- Asperity degradation corresponds to the performed shear energy.
This has not been proved for a practically relevant variety of rock types and thus requires more research and understanding.
- The residual friction angle of the joint material is equal to the basic friction angle.
Differences between the two parameters might be caused by certain montmorillonitic fillings or the formation of slickensides during shearing.
- The dilation angle i corresponds to the dilation rate of the joint and must not be confused with the asperity angle.

- Lateral dilation and end effects are not considered. Lateral dilation tends to be suppressed, for instance, in case of slender rock wedges.

3.3.2 Mobilisation of shear stress (Stage A):

Relative displacements between joint walls (joint slip) cannot take place due to the stress condition according to expression (5). Shear displacements are a result of elastic strains in the rock surrounding the joint. The absence of joint slip also omits dilation. The shear stress increases linearly with the shear displacement following expression (6). The normal stress remains constant. k_s is the joint shear stiffness at the initial stage of shearing.

$$\begin{aligned}\Delta\tau &= k_s \cdot \Delta u \\ \Delta\sigma_n &= 0\end{aligned}\tag{6}$$

Stage A controls the shear behaviour only until joint slip occurs at joint areas parallel to the shear direction, i.e. when inclination of the resultant force relative to the shear plane exceeds the basic friction angle φ_b . Assuming Coulomb friction the shear displacement u_{ini} at which slip initiates can be determined by expression (7):

$$u_{ini} = \frac{\sigma_n \cdot \tan\varphi_b}{k_s}\tag{7}$$

The shear stiffness in this model is a tangential stiffness and only determined by the rock properties. According to Kulhawy (1975) the shear stiffness is determined by the shear modulus, and therefore should be related as shown in expression (8). k_n is the rock mass stiffness with fully closed joints as outlined below in section 3.3.6. Priest (1993) lists other expressions for the tangential shear stiffness which are, however, related to other constitutive concepts.

$$k_s = \frac{k_n}{2 \cdot (1 + \nu)}\tag{8}$$

3.3.3 Mobilisation of dilation (Stage B):

The joint starts dilating when partial slip on asperities and shearing of steep asperities takes place. With dilation the normal stress also increases. The normal stress increment in the joint corresponds to the mobilised dilation angle i and the total normal stiffness K_{tot} of the joint (Expression (9)). The first part of Patton's

law (Patton 1966) in which the effective friction angle is the sum of the basic friction angle φ_b and the dilation angle i , controls the shear stress (Expression (10)).

$$\Delta\sigma_n = K_{tot} \cdot \tan i \cdot \Delta u \quad (9)$$

$$\tau = \sigma_n \cdot \tan(\varphi_b + i) \quad (10)$$

The unknown parameters in this formulation are i and K_{tot} . In this expression, K_{tot} is the total joint normal stiffness and refers to the boundary conditions. Its estimation is outlined in section 3.3.6. For CNL conditions which can be assumed at this point without losing generality, it is zero. The dilation angle i in stage B is a function of the shear displacement. Its development is a quite complex process involving sliding and shearing of irregular asperities. Investigations on sheared rock joints showed a typical non-linear development of the current dilation angle (see section 3.2.2). This behaviour can be approximated by a second-order parabola which has to obey two constraints:

- The shear stress curve at the transition between stage A and B has to be smooth (i.e. continuous and C^1 differentiable).
- The point at the maximum dilation angle is a relative maximum.

A useful function for modelling gradient boundary conditions is the Bezier spline. An introduction to Bezier splines can be found, for instance, in Boehm & Müller (1999). A Bezier spline is surrounded by a so-called control polygon which defines the location and the shape of the spline with respect to gradient and curvature. For the modelling of the mobilisation of dilation an open, two-sided polygon is used (Figure 27).

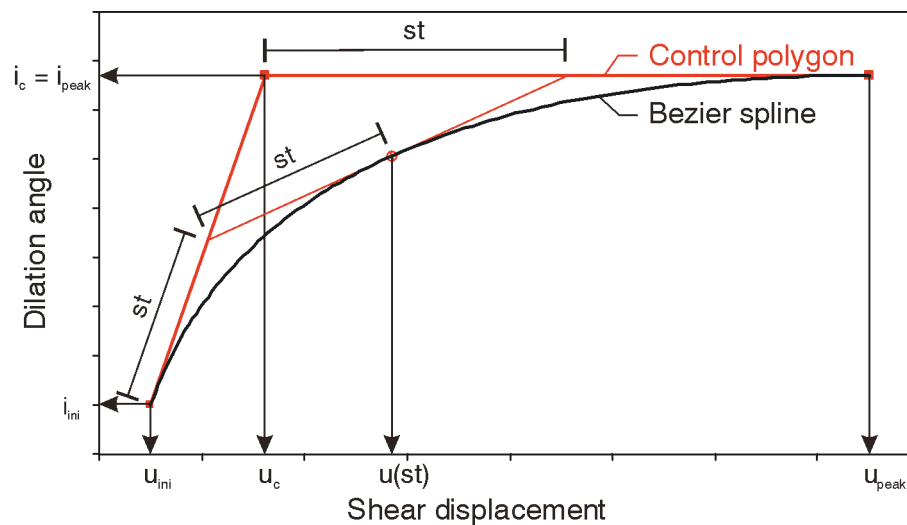


Figure 27: Bezier spline, control polygon, and algorithm of *de Casteljaou*

The chords at the polygon's endpoints define the local gradients. The original formulation of the Bezier spline is parametric. Nevertheless, a corresponding quadratic Bezier spline can be explicitly formulated based on the coordinates of the corners of the control polygon. The relationship between control polygon, Bezier spline, and control parameter st is shown in Figure 27 (Algorithm of de Casteljau (Boehm & Müller (1999))).

For the constitutive model, however, a formulation with respect to the shear displacement u is required. This can be accomplished by a back-calculation of the control parameter st from the current shear displacement and the control polygon (Expression (11)). st is input in the original spline formulation in order to obtain the corresponding dilation angle (Expression (12)).

$$st_{(u)} = \frac{(u_{ini} - u_c) + \sqrt{(u_c - u_{ini})^2 - (u_{peak} + u_{ini} - 2 \cdot u_c) \cdot (u_{ini} - u)}}{u_{peak} + u_{ini} - 2 \cdot u_c} \quad (11)$$

$$i_{(u)} = (1 - st_{(u)})^2 \cdot i_{ini} + 2 \cdot st_{(u)} \cdot (1 - st_{(u)}) \cdot i_c + st_{(u)}^2 \cdot i_{peak} \quad (12)$$

The task is now determining the parameters of the control polygon. The control polygon comprises the corners (u_{ini}/i_{ini}) , (u_c/i_c) and (u_{peak}/i_{peak}) . u_{ini} can be obtained from expression (7). i_{ini} is zero. These two parameters define the first point.

u_{peak} is an input parameter for the constitutive model and has to be separately defined. It is also the upper limit of shear displacements in stage B. Expression (13) is a well-accepted formula to estimate the peak shear displacement. Nevertheless, the author recommends to correlate this relationship with laboratory or, better, with field tests. The corresponding peak dilation angle i_{peak} is derived from existing peak shear strength criteria. It is described in section 3.3.5 for Barton's *JRC* model (Barton & Choubey 1977) and Grasselli's model (Grasselli 2001).

$$u_{peak} = \frac{L_n}{500} \cdot \left(\frac{JRC_n}{L_0} \right)^{-0.33} \quad (13)$$

i_c equals to i_{peak} which ensures a horizontal tangent in the spline's endpoint. u_c can be obtained by intersection of the chord at the spline's initiation and the horizontal chord. As stated above, the shear stress curve at the transition of stage A and B has to be smooth. This is only the case if the shear stress gradient from stage A and B at the transition are identical. The shear stress gradient $d\tau/du$ in stage A is k_s . In stage B the same gradient is obtained by derivating expression (10). For normal stiffness boundary conditions both, i and σ_n depend on the shear displacement u . Hence, the determination of the derivative of expression (10)

would result in an extensive calculation. The solution can be more easily obtained with a closer examination of expression (5).

Section 3.2.2 has shown that the effective dilation curve can be obtained by the Coulomb criterion for maximum asperity angle α_{max} depending on the current external loads and this complies with Patton's law of friction and dilation (Figure 23). On the other hand, the external stresses at the transition point (between stage A and B) are known. Hence, in order to obtain a smooth shear stress transition the gradient of the dilation curve obtained from expression (5) is sufficient if the stresses from stage A are input. The expressions for the forces have to be replaced by the equivalents for the stresses. In this case this is reasonable because the shear and normal stresses are only normalised values of the shear and normal forces by the average shear area. Consequently, the expression for α_{max} is:

$$\alpha = \arctan\left(\frac{\tau - \sigma_n \cdot \tan\varphi_b}{\tau + \sigma_n \cdot \tan\varphi_b}\right) \quad (14)$$

At the transition point τ equals $k_s \cdot u$. Hence, the first derivative is:

$$\frac{d\alpha}{du} = \frac{k_s \cdot \left(\sigma_n - u \cdot \frac{d\sigma_n}{du}\right)}{\sigma_n^2 + k_s^2 \cdot u^2} \quad (15)$$

At the transition point the gradient of the normal stress $d\sigma_n/du$ is zero since no normal stress variation takes place in stage A. This criterion provides also a smooth transition of the normal stress curve. Finally, the shear displacement at the transition point can be obtained from expression (7). Expression (16) is the gradient of the dilation curve at the transition point.

$$\left.\frac{d\alpha}{du}\right|_{\alpha=0} = \frac{k_s}{\sigma_n \cdot (1 + \tan^2 \varphi_b)} \quad (16)$$

Using expression (16) as the gradient of the control polygon in the transition point, the intermediate control point u_c can be determined which completely defines the dilation curve. For comparison, the solution of expression (7) assuming $u = u_{ini}$ and $i_{ini} = 0$ after u_c yields the same result. Expression (7) uses the derivatives of expressions (6), (10), and (31). At the transition point all stiffness-controlled terms vanish, since the dilation gradient is zero.

$$\frac{d\tau_{StageA}}{du} = \frac{d\tau_{StageB}}{du} \Leftrightarrow k_s = \frac{d\sigma_n}{du} \cdot \tan(\varphi + i) + \frac{\sigma_n}{\cos^2(\varphi + i)} \cdot \frac{di}{du} \quad (17)$$

3.3.4 Surface degradation (Stage C)

After exceeding u_{peak} shearing with the applied normal load causes surface degradation. Effectively, the rough joint surface becomes gradually smoother leading to a decrease of the dilation angle. It has been shown by several authors (Plesha 1987, Lee et al. 2001, Hutson & Dowding 1990, Nguyen & Selvadurai 1998, Huang et al. 1993, Qui et al. 1993), that the decrease of the dilation angle follows a negative exponential law with the accumulation of shear energy. Since natural joint surfaces have a rather complex geometry, a two-level negative exponential function proved to be most suitable to describe the degradation of asperities (Seywald 2006). The two-level function (Expression (18)) accounts for first and second order asperities of the joint roughness.

$$i_{(u)} = i_1 \cdot e^{-c_1 \cdot W(u)} + i_2 \cdot e^{-c_2 \cdot W(u)} \quad (18)$$

i_1 and i_2 are conceptionally the first and second order asperity angles in Deere (1966). Seywald (2006) determined the first and second order asperity angles for one joint surface corresponding to the peak dilation angle by back-analysis from direct shear tests. Figure 28 shows a decrease of the asperity angle ratio with increasing acting normal stress. Physically, this reveals the predominant influence of first order asperities on the dilation rate at higher normal stresses which was also observed by Ueng et al. (2003). First order asperities may also sustain higher loads due to their physically wider base. Second order asperities are already sheared off at lower normal stresses.

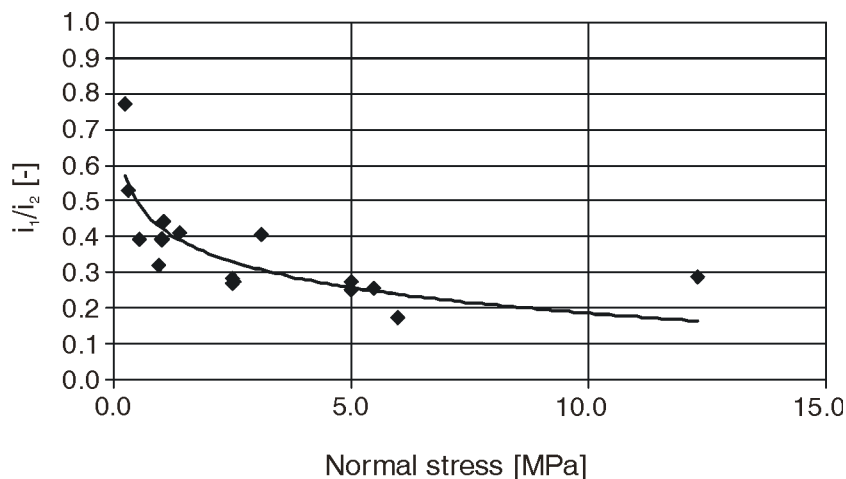


Figure 28: Influence of the normal stress at maximum apparent friction angle on the ratio between first and second order asperity angles

The asperity angle ratio at zero normal stress depends on the roughness of the joints. Ideas for its determination can be taken from Yang et al. (2001) or Renger's method of asperity angle scatters (Fecker & Rengers 1971). Plesha (1987) reports first order asperity angles between 5 and 20° and second order asperity angles between 15 to 45°.

c_1 and c_2 are degradation parameters and affect the curvature of the exponential function. They mainly depend on the material properties of the rock material and the surface roughness (Hutson & Dowding 1990). The unit of the degradation parameters is $[m^2/kJ]$. W is the accumulated shear energy and it is defined by expression (19). Its unit is $[kJ/m^2]$. The total energy accumulated during direct shear includes also contributions from normal stresses. Although normal and shear stress are in the same order of magnitude, the main factor dominating the total energy is the shear displacement. The contribution from the normal energy is low due to the relatively small normal displacements. Nevertheless, the effects of the normal stress variations are inherently coupled with the shear stress and find their way into the shear energy.

$$W(u) = \int_0^u \tau_{(u)} \cdot du \quad (19)$$

In this stage the normal and the shear stresses can be calculated with expression (9) and (10), respectively. Figure 29 shows the degradation function for the dilation angle and the accumulated shear energy.

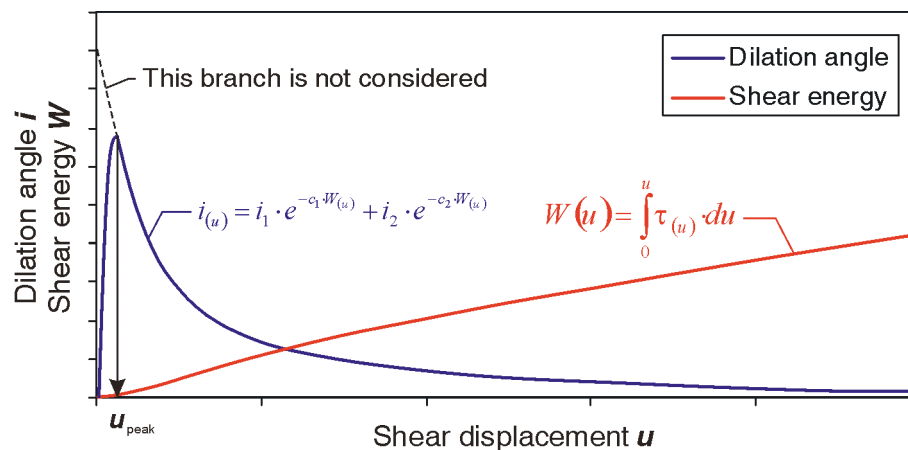


Figure 29: Behaviour of the joint dilation during surface degradation. The degradation function (blue) is considered from u_{peak} to infinity. The red line represents the accumulated shear energy W .

In the early stage of degradation the first and second order asperities contribute to the degradation function which causes a rapid drop of the dilation angle. In the final stage of shearing only first order asperities have an influence. The gradient of the dilation function becomes smaller. Additionally, the shear energy shows a regressive behaviour which damps the degradation as well.

3.3.5 Peak dilation angle

A crucial part for the determination of the shear behaviour in the concept of the constitutive model is the correct prediction of the peak dilation angle. The peak dilation angle depends on the joint roughness, normal stress, basic friction angle, the asperity strength, and the joint size (scale effect). Rougher joints have a higher peak dilation angle up to a degree which depends on the surface friction angle and the current stress condition (Barton & Choubey 1977, Boulon et al. 2002, Homand 2001). The surface friction angle decreases the peak dilation angle especially under low normal stresses (compare expression (5)). Increasing normal stresses also decrease the peak dilation angle due to the increased number of asperity failures (Seywald 2006, Schieg 2006). Larger joints show also a lower peak dilation angle. The relative roughness decreases with increasing joint size (Fardin et al. 2001, Fardin et al. 2004, Barton 1973). In this work two methods are presented to determine, algorithmically, the peak dilation angle for the proposed joint constitutive model. The first method relies on the *JRC* concept while the second method considers a three-dimensional characterisation of the joint surface.

3.3.5.1 Barton's *JRC* model

Barton & Choubey (1977) proposed a shear strength model shown in expression (20) which depends on the current normal stress σ_n , the joint roughness *JRC*, the strength of the joint wall *JCS* and the basic friction angle φ_b . Its formulation is similar to Patton's criterion of friction and dilation (Patton 1966).

$$\tau_{peak} = \sigma_n \cdot \tan \left(\varphi_b + JRC \cdot \log_{10} \left(\frac{JCS}{\sigma_n} \right) \right) \quad (20)$$

The dilational part is represented by expression (21). This expression suggests that the peak dilation angle decreases with increasing normal stress and decreasing joint wall compressive strength. Experiments on the shear behaviour on artificial rock joints showed an expressed logarithmic behaviour.

$$i_{peak} = JRC \cdot \log_{10} \left(\frac{JCS}{\sigma_n} \right) \quad (21)$$

Figure 30 shows test results for the peak dilation angle and the influence of the ratio between normal stress and unconfined compressive strength determined from direct shear tests. On the left hand side, results from joint replicas of tensile fractures are shown (Barton 1973). The solid line is the logarithmic best-fit approximation of the data set while the dashed line is the best-fit following expression (21). As that author mentions that these fractures have been very rough representing the upper practical limit of joint roughness, a JRC of 20 could be derived.

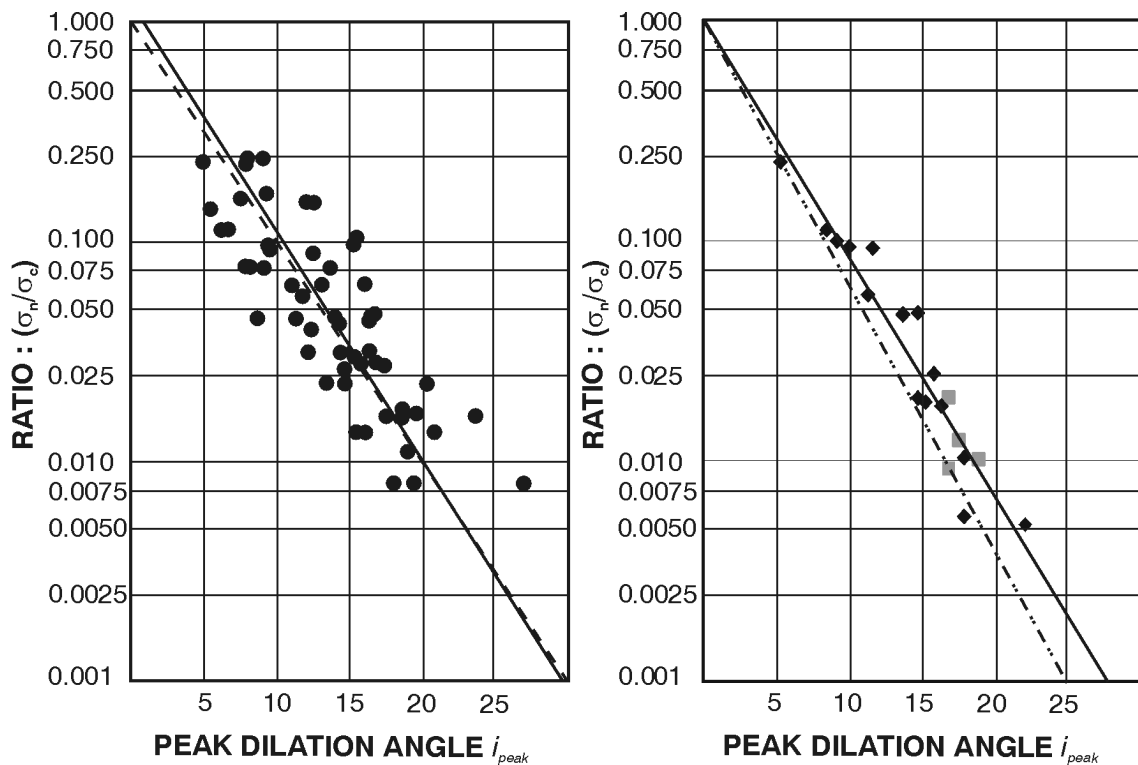


Figure 30: Influence of the ratio between normal stress and unconfined compressive strength on the peak dilation angle. Left: Results from (assumed) CNL shear tests, modified after Barton (1973). Right: Results from CNS and CNL shear tests after Schieg (2006) (grey) and Seywald (2006) (black).

On the right hand side, tests results from Schieg (2006) and Seywald (2006) on replicas of a natural joint surface consisting of mortar are shown. These tests show a significant logarithmic behaviour as well. The solid line is the least-square estimation of the data set resulting in a JRC of 8.8 while the dot and dash

line is a prediction of the dilation angle using expression (21) with a JRC of 7.9 (Pötsch et al. 2007). This value has been determined as a mean out of a sample of 20 expert estimations of the surface's JRC . The right hand side comprises data from CNL and CNS tests while no information about the shear test procedure has been available for the left hand side. However, CNL or multi-stage tests have been assumed.

In CNS tests the normal stress varies with the shear displacement. Thus, the correlation between the peak dilation angle and the normal stress has to be defined. It has been shown by several authors (Barton 1971, Coulson 1970, Drozd 1967 cited in Seywald (2006)) that the peak dilation angle corresponds to the peak shear strength. In CNS tests the behaviour of the shear and normal stress is different. Due to the joint dilation the normal stress increases, hence the shear stresses also increase according to Coulomb's rule even if the surface is almost flattened. The maximum dilation angle occurs when the ratio between τ and σ_n becomes a maximum which can be seen in the diagram of the apparent friction angle $\varphi+i$. The peak dilation angle has been plotted in Figure 30 (right) against the normal stress at the maximum apparent friction angle. A logarithmic correlation similar to CNL tests can be observed.

Barton & Choubey (1977) concluded from their tests that the peak dilation angle determined with the applied methods falls in the range shown by expression (22). For the design purposes they recommend to use half of the value obtained by expression (21). Bandis et al. (1985) outlined to use expression (21) for low normal stresses or high rock wall strength, otherwise expression (22) shall be used; this was later addressed as the damage factor concept (see Bandis 1990). The works from Schieg (2006) and Seywald (2006) showed a significant coincidence of expression (21) with the test results which can be observed in Figure 30 right. Anyhow, Figure 30 left on the other hand agrees well with the expression (22) applying the factor $\frac{1}{2}$ if a JRC of 20 is assumed (as by Barton 1971).

$$i_{peak} = \left(\frac{1}{2} \div 2\right) \cdot JRC \cdot \log_{10} \left(\frac{JCS}{\sigma_n} \right) \quad (22)$$

As mentioned above in section 3.2, the current stress condition and the surface friction limits the maximum asperity angle at which sliding can take place (Expression (5)). For zero normal stress it suggests a maximum sliding angle of $i_{peak} = 90 - \varphi_{res}$. Asperities steeper than this limit are sheared off. In contrast, expression (21) approaches infinity with decreasing normal stress. Barton (1973) empirically limits the maximum shear stress for design purposes with $\tau = \sigma_n \tan 70^\circ$ exceeding a ratio of 100 between JCS and σ_n . A corresponding maximum peak dilation angle with $i_{peak} = 70 - \varphi_{res}$ can be derived.

The peak dilation angle of a rough joint depends also on the size of the joints. The scale-dependant influencing parameters are JRC and JCS . Barton &

Choubey (1977) already established empirical upscaling formulas shown in expression (23) and (24) which have been well-established until now. The index 0 denominates the value at which scale the parameter has been determined. Usually it is a lab scale of 0.1 m. The index n denominates the in-situ scale. More recent investigations to the scale-dependence of joint roughness have been done by Fardin et al. (2001) and Fardin et al. (2004) using 3D point clouds and fractal methods. Ueng et al. (2003) report higher shear strengths of smaller joints at the same roughness, but no scale effect if the roughness is proportionally scaled with sample enlargement.

$$JRC_n = JRC_0 \cdot \left(\frac{L_n}{L_0} \right)^{-0.02 \cdot JRC_0} \quad (23)$$

$$JCS_n = JCS_0 \cdot \left(\frac{L_n}{L_0} \right)^{-0.03 \cdot JRC_0} \quad (24)$$

The major disadvantage in Barton's model is related to the determination of the JRC . Although Barton recommended its determination from back-calculation of direct shear tests or at least from tilt or push tests, it is engineering practice to derive the JRC from selected roughness profiles of the joint. The obtained values are therefore individual estimations which may have a strong deviation from the true value up to $\pm 5^\circ$ to $\pm 8^\circ$ as shown by Schieg (2006) and Beer et al. (2002), respectively. Apart of the strong impact on the dilation and shear strength, the estimation of the JRC by visual comparison provides a value independent from the shear direction. This would only be reasonable for statistically isotropic joints surfaces. In the recent times the call for a more objective determination or consideration of the joint roughness has become stronger. A number of authors proposed methods for the geometrical characterisation of irregular surfaces. These methods basically rely on fractal theory (Seidel & Haberfield 1995, Yang et al. 2001), geostatistics and/or kriging (Gentier et al. 2000, Lopez et al. 2003), or combinations (Kulatilake et al. 1995, Kulatilake 2006). The following section shows an approach for the determination of the peak dilation angle based on Grasselli's method for the characterisation of the surface roughness.

3.3.5.2 Grasselli's model

Grasselli introduced a constitutive model for the shear behaviour of rough rock joints based on a quantified surface description (Grasselli 2001, Grasselli et al. 2002, Grasselli & Egger 2003). The description of the surface morphology is derived from a triangulated irregular network representing the rough joint surface. The irregular surface is evaluated with respect to maximum potential contact area A_0 , maximum apparent asperity angle Θ_{max}^* and the roughness

parameter C which are purely geometrical and depend on the considered shear direction. Thus, anisotropic roughness can be taken into account.

Based on the surface parameters A_θ , Θ_{max}^* , and C Grasselli formulated a peak shear strength criterion. Seywald (2006) used this model for the back-calculation of the peak dilation angle. Unfortunately, Grasselli's formulation of the peak shear strength does not have the form of the apparent friction angle after Patton ($\varphi + i$). The expression for the peak dilation angle becomes rather complex (expression (25)).

$$i_{peak} = \arctan \left\{ \tan \varphi \cdot \left[1 + e^{-\left(\frac{\Theta_{max}^* \cdot \sigma_{n,peak}}{A_\theta \cdot C \cdot \sigma_c \cdot a} \right)} \right] \right\} - \varphi \quad (25)$$

The factor a has been introduced by Seywald in order to account for the deviations of the predicted values from the measured ones. It shifts the values from Grasselli's original formulation. a can be assessed with expression (26).

$$a = 0.62 \cdot \sigma_{n,(\varphi+i)max} + 3.1 \quad (26)$$

Figure 31 shows a synopsis of the measured values the two presented prediction formulae for i_{peak} . The solid line is based on Barton's model using a JRC of 8.8. The dot-dashed line is based on the modified model from Grasselli. The surface parameters are as follows: $A_\theta = 0.50$, $\Theta_{max}^* = 58$, $C = 1.79$. It can be observed that within approximately 90% of the measured stress range the Grasselli's curve fits quite well to the measured values. The mean error is 0.87° with a standard deviation of 0.74° . However, outside of the tested stress ranges the model shows increasing deviations from the logarithmic behaviour. In the literature there are no data available showing the behaviour of the dilation angle in the stress range of σ_n / σ_c higher than 0.25 and lower than 0.005. Only Maksimovic's theoretical (Maksimovic 1996) approach suggests an S-type behaviour of the dilation angle over the logarithmic normal stress scale. Although one would assume a logarithmic behaviour, further investigations have to be performed for verification. From the current knowledge both models, Barton's and Grasselli's, should only be applied in the proposed stress range.

3.3.6 Incorporation of the boundary conditions

The above stated conclusions have been derived regardless of the behaviour of the normal stress. Boundary conditions influence the normal stress and in consequence the shear behaviour. Typically, boundary conditions are referred to as the normal stiffness which confines the normal displacement of the joint.

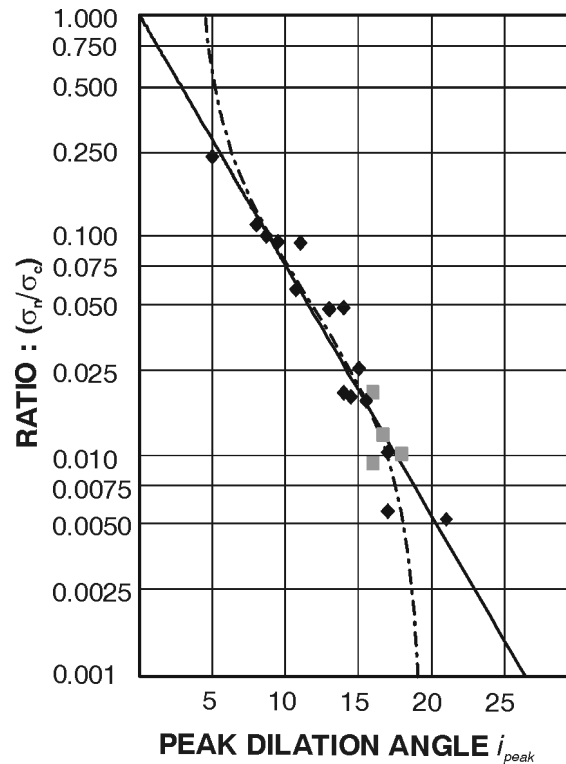


Figure 31: Comparison of measured values and the prediction models for the peak dilation angle. The solid line follows expression (21) while the dot-dashed line follows expression (25).

As shown above, the determination of the normal stress increment considers the parameter K_{tot} . It represents the total normal stiffness imposed at the joint. Although it is defined as a boundary condition, its magnitude depends on the properties of the joint and the surroundings. It is necessary to distinguish between the external and internal normal stiffness. The external normal stiffness considers boundary conditions such as support or elastic properties of the rock mass. For reasons of simplicity the external normal stiffness is usually assumed to be constant (CNS) leading to a linear stress-displacement relationship. It is, however, possible to apply any stiffness characteristics without the loss of applicability. The internal normal stiffness describes the behaviour within the joint. It considers the effects of joint closure and aperture, as well as the elastic deformation of the asperities. The normal stiffness concept has already been applied by several authors for the simulation and prediction of the joint shear behaviour under CNS conditions (Goodman 1976, Bandis et al. 1985, Saeb & Amadei 1992, Dong & Pan 1996, Indraratna & Haque 2000, Seidel & Haberfield 2002). Pötsch (2002) showed the application of the CNS concept for detaching joint walls under an initial stress state. Most of them used a simplified dilation model which would lead to non-relevant predictions of the shear behaviour for a natural rock joint as shown by Seywald (2006).

Several authors showed that the relationship between normal stress and normal displacement of a discontinuity is non-linear. It follows a combined linear and hyperbolic law described by Bandis et al. (1983), Bandis (1990), and earlier Goodman (1976). Expression (27) shows the hyperbolic joint normal stiffness after Bandis.

$$k_{hyp} = k_{ni} \cdot \left(\frac{k_{ni} \cdot v_m + \sigma_n}{k_{ni} \cdot v_m} \right)^2 \quad (27)$$

Expression (27) indicates that the internal normal stiffness k_{hyp} depends on the current normal stress σ_n and the maximum joint closure v_m . Figure 32 shows a typical stress-displacement behaviour of a rough rock joint perpendicular to its plane. The black dots are data obtained from laboratory tests. The red curve is the functional approximation of the measurement data by a combined linear and hyperbolic relationship. The green curve represents the linear normal stiffness behaviour while the blue curve refers to the hyperbolic behaviour of expression (27). It can be observed that a completely closed joint does not deform even if the normal stress increases.

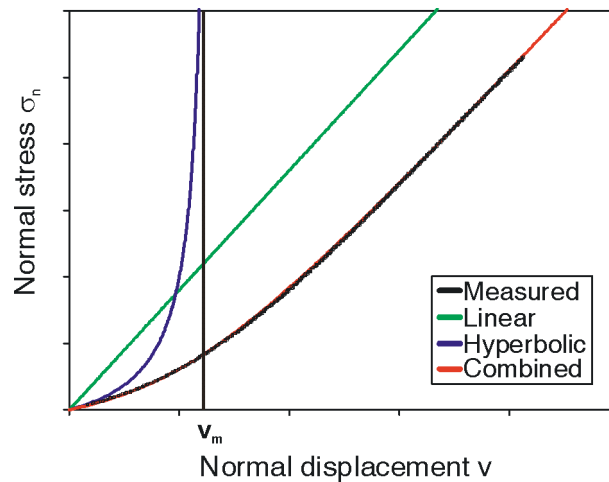


Figure 32: Typical stress-displacement behaviour of a rock joint perpendicular to its median plane

It can be seen that several stiffness characteristics influence the boundary condition of the joint. These different characteristics have to be combined to the total normal stiffness. Mechanically, a multi spring model is used to derive the total joint normal stiffness K_{tot} of a joint (Figure 33). In a general denomination $k_{n,i}$ represents the internal normal stiffness while $k_{n,j}$ is the external normal stiffness. Consider the lower block in Figure 33 as vertically fixed and the upper

block as movable. The normal displacement dv is due to the shear displacement du and the asperity angle i . The normal displacement affects the normal stress σ_n with $k_{n,i}$ and $k_{n,j}$. In the following paragraphs the determination of the total normal stiffness is outlined for two springs. This procedure can be simply extended to an arbitrary number of springs regardless of internal or external normal stiffness. Since the presented formulation is incremental, it eases general non-linear spring characteristics.

On the one hand, an incremental variation of the normal stress causes a normal displacement within the joint affected by the internal normal stiffness $k_{n,i}$.

$$dv - dv^* = \frac{d\sigma_n}{k_{n,i}} \quad (28)$$

On the other hand, the same incremental variation of the normal stress causes a normal displacement dv^* which can be detected outside the joint. It is affected by the external normal stiffness $k_{n,j}$.

$$dv^* = \frac{d\sigma_n}{k_{n,j}} \quad (29)$$

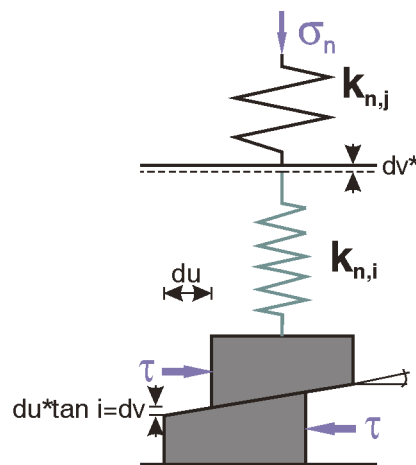


Figure 33: Multi spring model of a joint

The normal displacement increment of a joint with a variation of the normal stress can be calculated by expression (30). It is obtained after inserting expression (29) into (28) and subsequent rearrangement.

$$dv = \frac{d\sigma_n}{k_{n,i}} + \frac{d\sigma_n}{k_{n,j}} \quad (30)$$

Conversely, the variation of the normal stress due to a joint normal displacement can be calculated by expression (31). The fraction term is a combined stiffness of two springs and refers to as the total normal stiffness K_{tot} .

$$d\sigma_n = \frac{k_{n,i} \cdot k_{n,j}}{k_{n,i} + k_{n,j}} \cdot dv \quad (31)$$

If a normal stiffness component obeys a nonlinear relationship, the values for k_n have to be determined for the current normal displacement or normal stress. Different or combined characteristics of the internal or external normal stiffness can be considered by adding the appropriate stiffness function to either expression (28) or (29). In the end it does not matter for the determination of the total normal stiffness whether the added normal stiffness is internal or external, as can be seen from expression (30). Following the procedure of expressions (28) to (31) the formula for the calculation of the total normal stiffness with an arbitrary number of normal stiffness components is given by expression (32) in which m is the number of stiffness components.

$$K_{tot} = \frac{\prod_{i=1}^m k_{n,i}}{\sum_{j=1}^m \prod_{k=1}^m k_{n,k}} \quad (32)$$

$$j = k \rightarrow k_{n,k} = 1$$

Three typical situations have to be considered for the use of expression (32).

- (a) All components are positive finite and non-zero. K_{tot} is also finite.
- (b) One or more components are zero. K_{tot} is zero since the numerator becomes zero and the denominator remains finite. This is consistent with the mechanical point of view: If there is in any position no resistance, then the external springs are not affected by normal displacement.
- (c) One or more components are infinite. Infinite components must not be considered in expression (32). If one or more components are infinite, the fraction results in an indefinite term ∞/∞ . It can be solved by l'Hôpital's rule using the first derivations of numerator and denominator. In this case, infinite components disappear.

3.3.7 Determination of model parameters

The proposed constitutive model comprises several input parameters for the description of the outlined behaviour. In this chapter these parameters are summarised and their determination is discussed. Their determination could not always be extensively investigated within this work.

3.3.7.1 Material parameters

- Friction angle φ , φ_b , φ_{res} :
 - Tilt and push test on a technically flat surface
 - Multi-stage shear test on a technically flat surface (basic friction angle)
 - Multi-stage shear test on a shear surface (residual friction angle)

- Unconfined compressive strength UCS , JCS
 - Unconfined compression test
 - Schmidt hammer rebound test
 - Weathering of joint wall has to be considered

- Joint shear stiffness k_s
 - Expression (8)
 - Cyclic shear tests with low shear displacements

- Peak shear displacement u_{peak}
 - Expression (13)
 - Laboratory shear test under conditions similar to in-situ conditions
 - Large scale shear test under conditions similar to in-situ conditions

- Degradation parameters c_1 , c_2
 - Back-calculation from a shear test under conditions similar to in-situ conditions (the author recommends the perform more investigations in this respect)

3.3.7.2 Surface parameters

- Joint roughness coefficient JRC
 - Comb measurements and standardised profiles
 - Tilt tests
 - Back-calculation from shear tests; particularly from a shear test at normal stress equal to one tenth of the asperity compressive strength
 - 3D surface analysis
- Potential contact area A_0 , maximum relative asperity angle Θ_{max}^* and roughness parameter C
 - 3D surface analysis
- Ratio between first and second order asperity angles i_1/i_2
 - Fractal analysis, asperity angle scatter analysis (the author recommends the perform more investigations in this respect)

3.3.7.3 Initial and boundary conditions

- Initial normal stress σ_{ni}
 - Dead load calculation
 - Approximations with analytical plane strain methods
 - Estimations with numerical methods (finite element, boundary element)
 - Stress measurement and stress transformation
- External normal stiffness k_{ext}
 - Stiffness of support including bolts, anchors, shotcrete, etc. in the designed / constructed assembly
 - Stiffness of adjacent rock masses or other containing elements
- Initial joint normal stiffness k_{ni}
 - Normal loading loops on joints in normal stress ranges similar to in-situ conditions

- Maximum joint closure v_m
 - Normal loading loops on joints in normal stress ranges similar to in-situ conditions
 - Measurement of in-situ joint aperture

- Linear joint normal stiffness k_{lin}
 - Boundary element method
 - Elastic settlement of an equivalent circular area of influence (Tonon 2007b)
 - Areas close to corners may have a normal stiffness significantly different from areas in the centre of a joint.

3.3.7.4 Others

- In-situ joint size L_n
 - Mean diameter / mean chord length of sliding face
 - Cross joint spacing
 - Discrete fracture network modelling

3.4 Parametric study

This study on the joint constitutive model shall outline the influence of the model parameters on the response and their interactions. The study commences with the parameters governing the pre-peak behaviour and peak shear strength in section 3.4.1 including the shear stiffness k_s , peak shear displacement u_{peak} and joint roughness coefficient JRC , and the influence of the initial normal stress σ_{ni} on the pre-peak behaviour. The influence of the joint wall compressive strength is not shown. Its influence depends on the ratio between the joint wall compressive strength and the normal stress. It has already been discussed by Barton (1971) and Barton & Choubey (1977). Section 3.4.2 discusses the influence of the post-peak parameters on the joint response. Section 3.4.1 and 3.4.2 consider CNL conditions. The diagrams show the current ratio between shear and normal stress in terms of the apparent friction angle $\varphi+i$. Since the normal stress is constant, the diagrams can be directly related to the shear stress and also the dilation angle.

Section 3.4.3 shows the influence of the external and initial normal stiffnesses k_{ext} and k_{ni} , and the maximum joint closure v_m on the total normal stiffness K_{tot} . Section 3.4.4 shows, finally, the influence of initial and boundary conditions, and post-peak parameters on the joint behaviour under constrained shearing. The diagrams include the $\varphi+i$ lines, the stress paths, and the normal and shear stress over shear displacement. For all examples in these sections unless otherwise indicated the joint wall compressive strength is 100 MPa and the basic / residual friction angle φ 30°.

3.4.1 Pre-peak behaviour and peak shear strength

Figure 34 shows the shear behaviour for six sets of parameters affecting the shear stiffness and peak shear displacement. The constant normal stress is 1.0 MPa and JRC is 10. The peak shear displacement varies from 0.5 mm to 2.0 mm and the shear stiffness from 1.0 MPa/mm to 5.0 MPa/mm. For the black, red and blue set the shear stiffness has been kept constant. A change in the peak shear displacement only affects the Bezier spline of stage B but also keeps the initial gradient of the spline equal to the shear stiffness. The blue, green and orange sets have the same peak shear displacement, only the shear stiffness shows a variation. This variation affects both, the behaviour in stage A and B. Lower shear stiffness causes a lower gradient of the curve.

Figure 35 shows the influence of the joint roughness coefficient and the normal stress on the shear behaviour in stages A and B. The shear stiffness k_s is 10.0 MPa/mm and the peak shear displacement u_{peak} is 0.5 mm. The black, red and blue sets have a JRC of 5, 10 and 15, respectively.

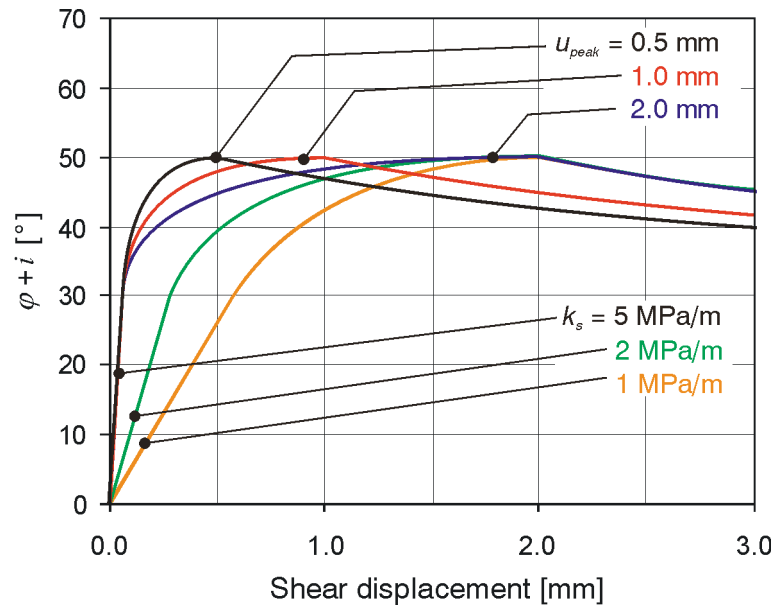


Figure 34. Variation of the shear stiffness k_s and the peak shear displacement u_{peak} . CNL conditions. $\sigma_{ni} = 1.0$ MPa. $JRC = 10$.

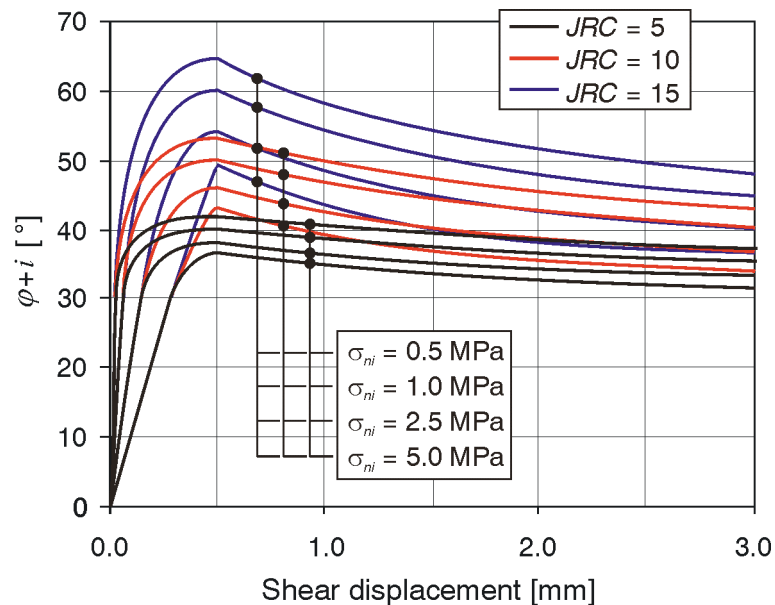


Figure 35: Variation of the joint roughness coefficient JRC and the normal stress σ_{ni} . CNL conditions. $k_s = 10$ MPa/mm. $u_{peak} = 0.5$ mm

As expected, a higher JRC causes a higher shear resistance at the same normal load. The increase of the normal load, on the other hand, causes a decrease of the relative shear resistance (ratio between shear and normal stress in degrees) for the same joint roughness coefficient. This must not be mixed up with the

absolute shear resistance (shear stress, e.g. in MPa) which, of course, grows with a normal load increase. The relative shear resistance changes from 41.5° to 36.5° for *JRC* 5, from 53° to 43° for *JRC* 10, and from 64.4° to 49.5° for *JRC* 15 with an increase of the normal stress from 0.5 MPa to 5.0 MPa. It also appears in Figure 35 that the gradient in stage A decreases with increasing normal stress despite the same shear stiffness. The shear stress at a certain shear displacement in stage A is the same for all sets. The ratio between shear and normal stress decreases with increasing normal stress resulting in a lower gradient of the curve in stage A.

3.4.2 Post-peak behaviour

This section discusses the influence of the degradation parameters, the ratio of asperity angles and the influence of normal stress on the shear behaviour in stage C.

Figure 36 shows the shear behaviour resulting from 12 parameter sets for CNL conditions and identical behaviour in stage A and B. The different colours indicate different values of c_2 , while different line styles indicate different values of c_1 . Generally, the higher the values of the degradation parameters, the faster the apparent friction angle decreases. Usually, c_2 is higher than c_1 and i_2 higher than i_1 . c_2 has its influence sphere directly after the peak while c_1 becomes more relevant in an advanced stage of shearing. The green and the blue line show this property clearly.

Figure 37 shows the influence of the ratio between i_1 and i_2 on the shear behaviour. Low values relate to a dominating influence of i_2 (secondary asperities) while a value of 1 means an equal influence. The lower the ratio, the higher is the curvature in the apparent friction angle line and the more expressed is the decrease of the same after peak. A low value together with a high degradation parameter signifies a sudden breakdown of a rough surface.

Figure 38 includes results for parameter sets with varying normal stress. The line styles are related to different normal stresses while the black set corresponds to a low degradation parameter c_2 and the red line to a high degradation parameter. The *JRC* has been adjusted to the applied normal stress in order to obtain the same peak shear strength for all sets. This eases the comparison. An increase of the normal stress also increases the shear stress, thus more shear energy accumulates. The decrease in the apparent friction angle is significantly higher compared to lower normal stresses. This is consistent with experiments where higher normal loads lead to a sheared surface, which is smoother, more compact and shows more crushed areas (Seywald 2006).

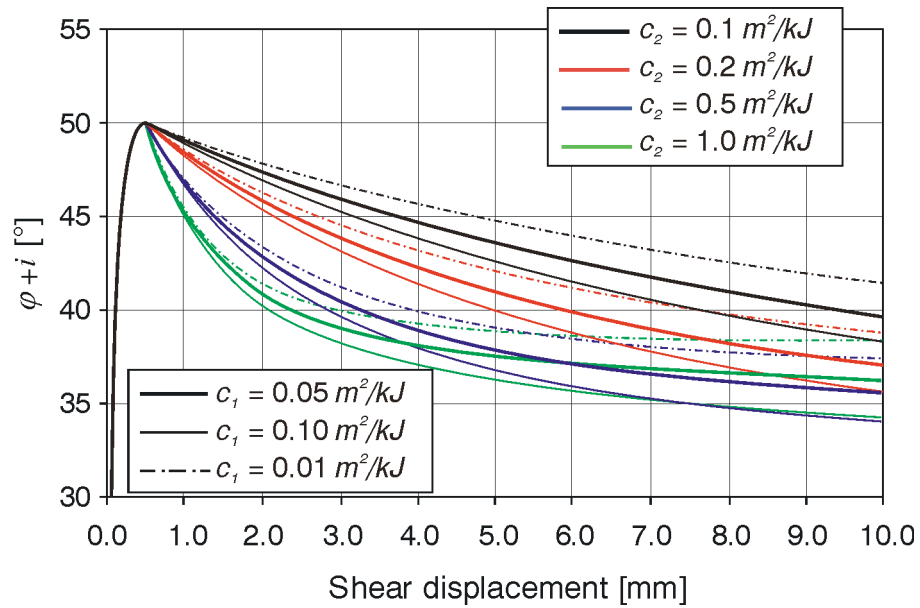


Figure 36: Variation of the degradation parameters c_1 and c_2 . CNL conditions. $\sigma_{ni} = 1.0$ MPa. $u_{peak} = 0.5$ mm. $k_s = 10$ MPa/mm. $i_1/i_2 = 0.5$. $JRC = 10$.

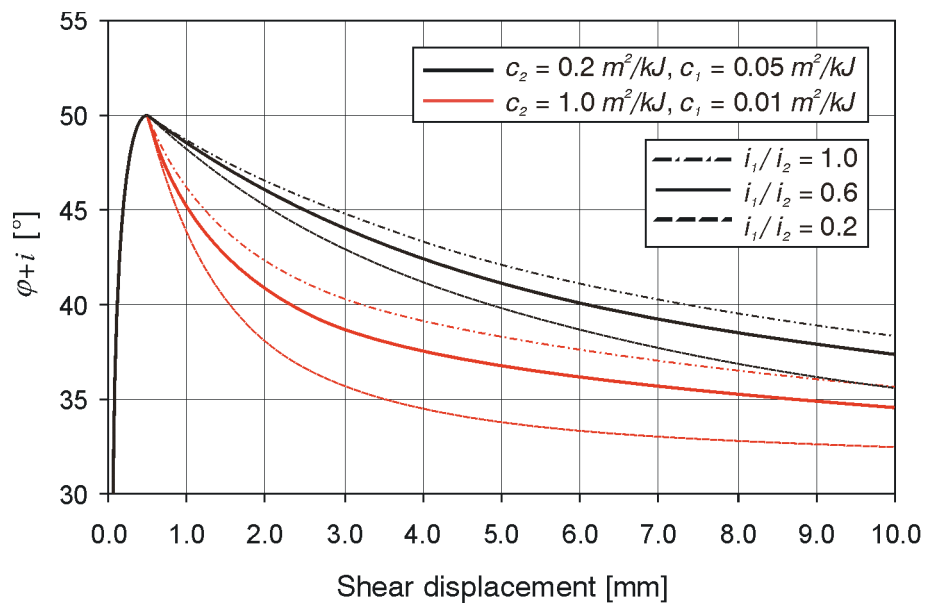


Figure 37: Variation of the degradation parameters c_1 and c_2 and the ratio between the asperity angles i_1 and i_2 . CNL conditions. $\sigma_{ni} = 1.0$ MPa. $u_{peak} = 0.5$ mm. $k_s = 10$ MPa/mm. $JRC = 10$.

Figure 38 shows also the accumulated shear energy for the simulations with 5.0 MPa normal stress. The decrease in the shear resistance due to the higher degradation parameter causes less energy accumulation. Thus, the gradient decreases after a certain shear displacement compared to a lower degradation parameter.

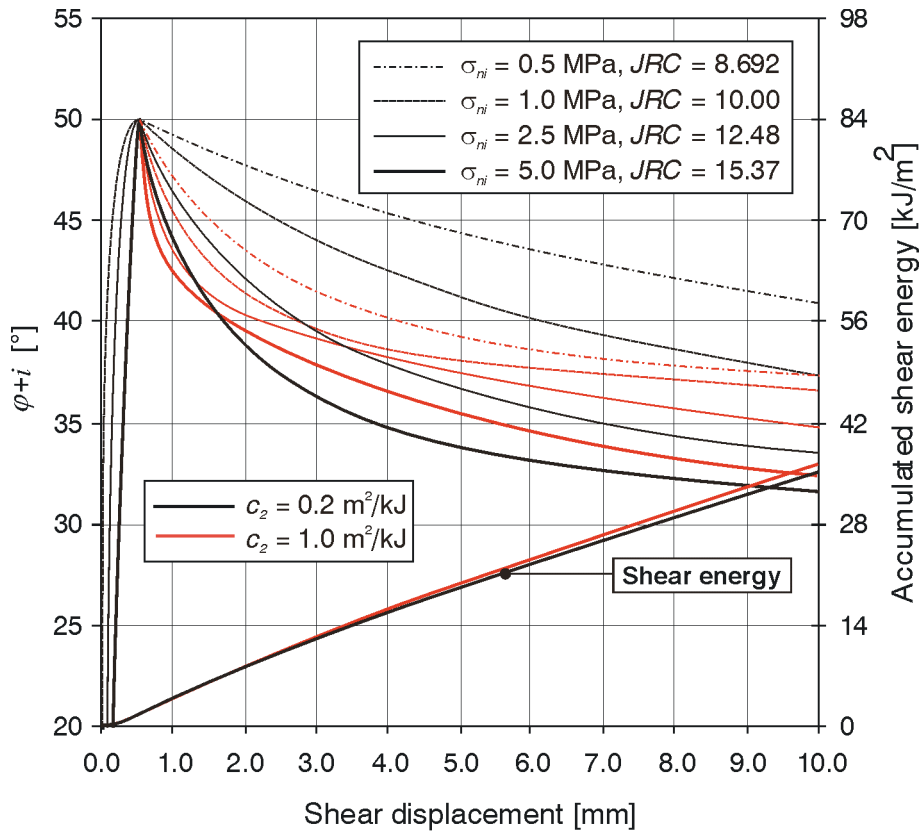


Figure 38: Variation of the normal stress σ_{ni} and the degradation parameter c_2 with constant peak dilation angle i_{peak} . $u_{peak} = 0.5$ mm. $k_s = 10$ MPa/mm. $c_1 = 0.05$ m²/kJ.

3.4.3 Joint normal stiffness

The joint normal stiffness is one of the most essential parameters influencing the shear behaviour under constrained conditions. The author distinguished between linear and hyperbolic contributions. The hyperbolic contributions depend on the maximum joint closure, the initial normal stiffness and the current normal stress, each of which are related to the joint. The linear contributions are basically model simplifications covering the deformation properties of the rock and support. Figure 39 shows the behaviour of the total normal stiffness K_{tot} over the current normal stress. The values have been determined using expression (27)

and (32). Different colours indicate the parameter sets outlined in the legend. The curves of one parameter set relate to different maximum joint closures, those values are shown in the rectangles adjacent to the curves. All the sets include a linear normal stiffness k_{lin} of 20 MPa/mm. The total normal stiffness curve starts at a lower boundary and approaches an upper boundary with increasing normal stress. The upper boundary of the values (at high normal stress) depends on the linear contributions k_{lin} and k_{ext} . The maximum joint closure influences the curvature. The lower the maximum joint closure, the lower is the normal stress at which it reaches the upper boundary. The initial normal stiffness (hyperbolic contribution) affects the interval between upper and lower boundary. The lower the initial normal stiffness, the higher is the interval of the total normal stiffness across the normal stress variation.

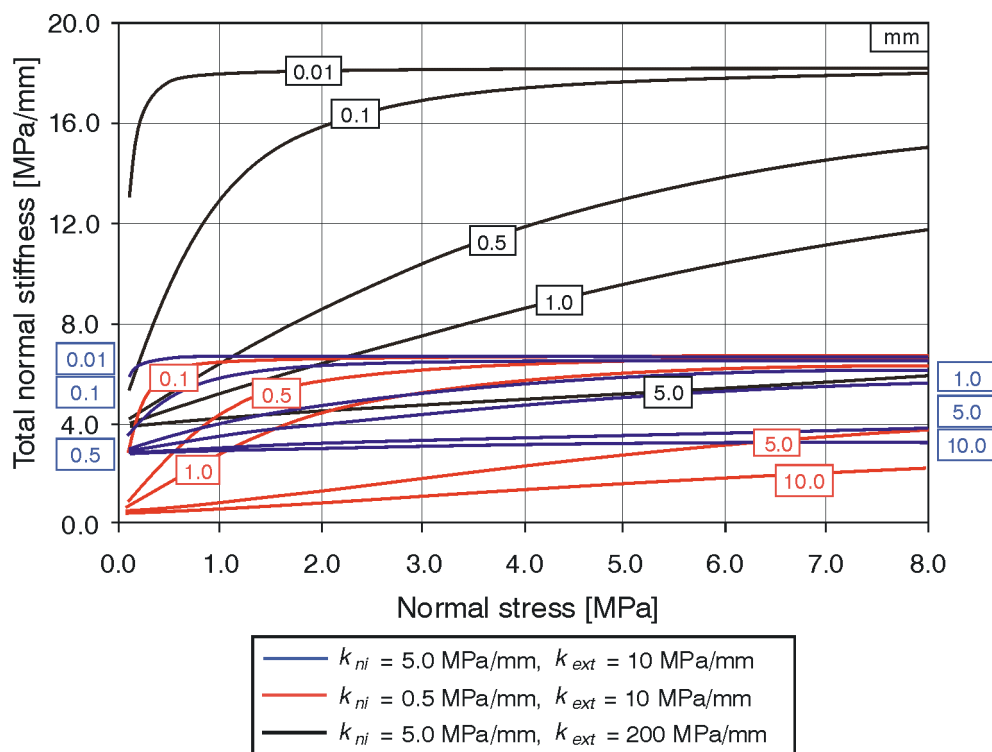


Figure 39: Total normal stiffness and variation of initial normal stiffness k_{ni} , external normal stiffness k_{ext} , and maximum joint closure v_m

3.4.4 Influence of the joint normal stiffness on the shear response

This section shows two examples for the influence of the total normal stiffness on the shear behaviour of a dilating joint. The first example includes variations of the initial normal stress σ_{ni} and the external normal stiffness k_{ext} . The second example includes a variation of the post peak parameters c_1 , c_2 , and i_1/i_2 , and the maximum joint closure v_m . For all the sets the peak shear displacement has been 1 mm, the shear stiffness 10 MPa/mm, the *JRC* 10, the initial normal stiffness 5 MPa/mm, and the linear normal stiffness 20 MPa/mm. The corresponding figures include the apparent friction angle and the shear and normal stresses over shear displacement, and the stress path.

Figure 40 shows the behaviour for an initial normal stress of 0.5 MPa and 2.5 MPa, respectively. The lower initial normal stress results in less accumulation of shear energy, thus less surface degradation. In consequence, the normal stress increases with a higher rate from a lower normal stress level compared to the higher normal stress level. It also remains at a higher normal stress rate for a longer shear displacement. At an external normal stiffness of 10 MPa/mm the normal stress almost increases from 0.5 MPa normal stress level to the same level as from 2.5 MPa normal stress level. The shear stress increases steadily throughout shear displacement at the two higher normal stiffness levels for the 0.5 MPa initial normal stress curves. It only increases steadily throughout shear displacement for the highest normal stiffness for the 2.5 MPa initial normal stress curve. This is explained by the stronger roughness degradation at higher normal loads.

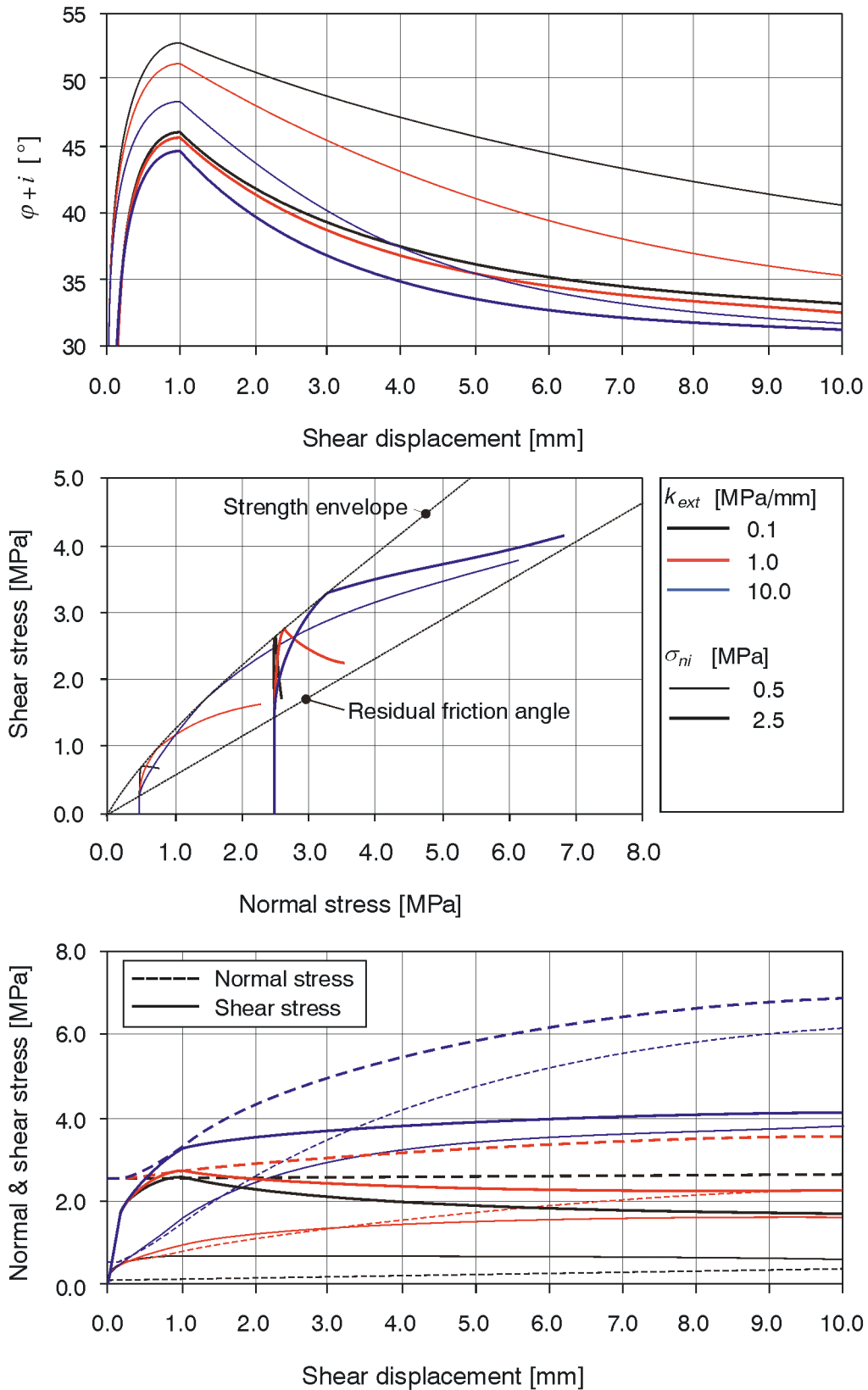


Figure 40: Shear behaviour under different normal stiffnesses k_{ext} and initial normal stresses σ_{ni}

Figure 41 shows the influence of the post peak parameters and the maximum joint closure on the shear behaviour. The initial normal stress was kept at 0.5 MPa for all variations. The maximum joint closure has been 0.1 mm and 1.0 mm resulting in different normal stiffness behaviours. In consequence, under constrained conditions the normal stress is also different causing different peak dilation angles. Thus, the maximum joint closure affects the shear behaviour already in the pre peak stage B.

The influence of the post peak parameters on the apparent friction angle has already been discussed in section 3.4.2 under CNL conditions. The dilatational part now causes also a normal stress variation which subsequently influences the joint normal stiffness and also the accumulated shear energy. Stronger degradation means less dilation, less normal stress increase, and a lower gradient of the shear energy accumulation. On the other hand, less shear energy damps the degradation. Less normal stress also results in less normal stiffness. The shear behaviour in the post peak stage is thus a complex interaction between degradation, normal stress and normal stiffness. From Figure 41 one can derive the following influences:

- Increasing the maximum joint closure results in less shear and normal stress mobilisation
- Higher degradation parameters result in less shear and normal stress mobilisation
- A lower ratio i_1/i_2 causes less mobilisation of shear and normal stresses

The author recommends increasing the knowledge about this model in a more extensive parametric study.

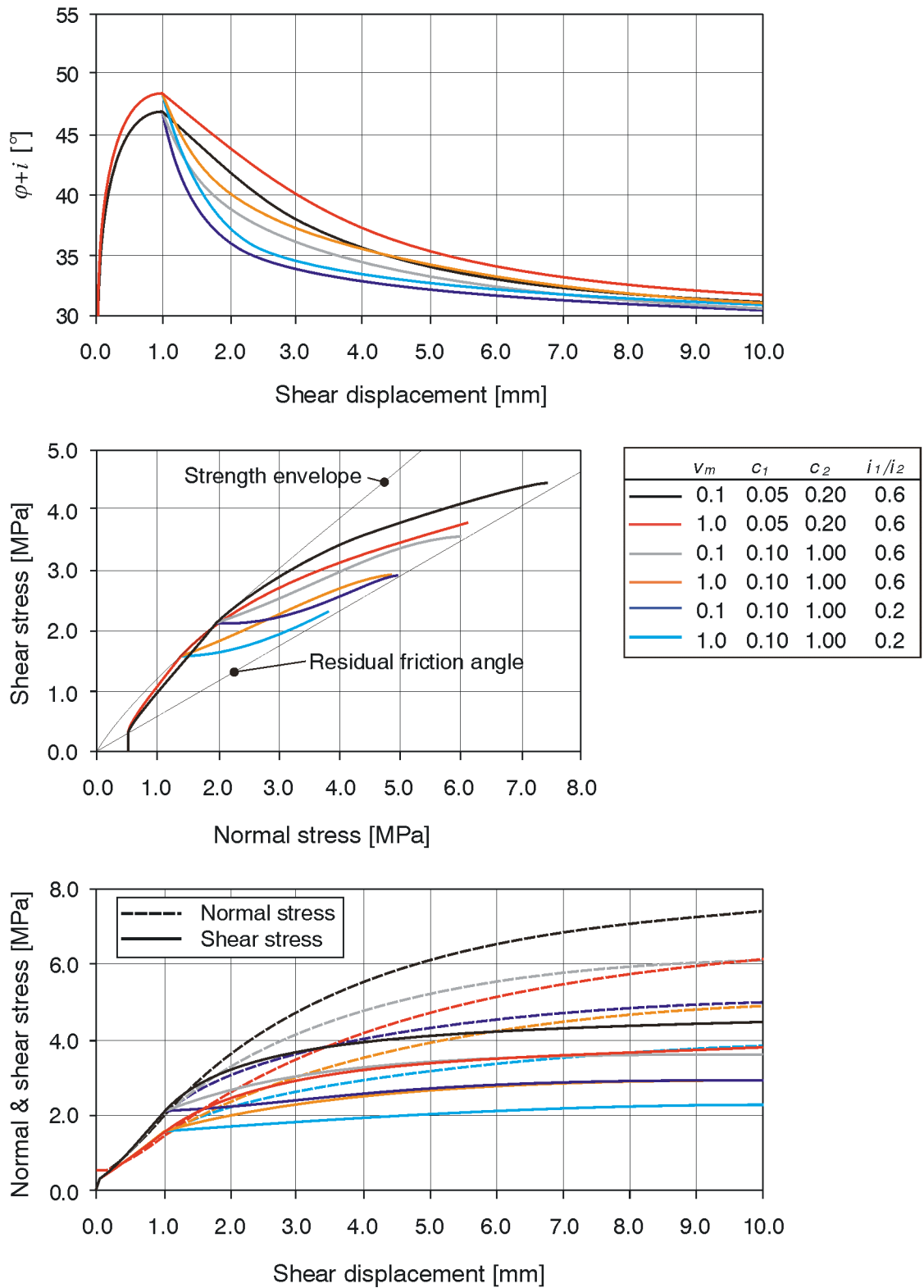


Figure 41: Shear behaviour under constrained conditions with different post-peak parameters

3.5 Summary

This section described and discussed the shear behaviour of rough rock joints under shear and normal loading and under constrained normal stiffness conditions. The focus was pointed but not limited to matched discontinuities. The most relevant factors influencing the discontinuity shear behaviour have been identified as the friction of the rock material, surface irregularity, aperture, infillings, strength of the rock material, deformability of the rock material, initial normal stress, boundary conditions (confinement), petrographical properties, and rock fabric.

The typical stages of the shear behaviour of a matched rough discontinuity have been described, based on experience from literature and a shear test series performed by Schieg (2006) and Seywald (2006). The stages include the mobilisation of shear stress, the mobilisation of dilation, surface degradation, and the residual stage. The author especially pointed out the importance of dilation of a joint in the shear behaviour. Mathematically, an established constitutive model describes these stages of shearing. The constitutive model allowed investigating the influencing factors and provided further insight in the complex interactions between material properties, surface roughness, accumulated shear energy and wear, boundary conditions and the resulting stresses and strength. Results were presented in a parametric study with stress-displacement curves and stress paths.

4 Description and properties of blocks

The mechanical analysis of a block may aim at different directions such as stability analysis, design of support, dynamic response, rock fall simulation, etc. each of which is based on the laws of motion. The formulation of the differential equations of motion depends on the geometry of the mechanical system, inertia properties of the involved bodies and, of course, the forces acting on the body (Goldstein et al. 2006). In a rock engineering sense, the bodies are rock blocks enclosing a finite volume of rock. In the idealised mechanical model, blocks are bounded by a closed surface comprising planar facets, each of which is bounded by a polygon. The considered block geometries are arbitrary simple polyhedra. This chapter introduces a suitable representation of polyhedral block geometries, discusses the finiteness theorem of blocks, and finally provides algorithms and analytical formulae for the calculation of the metric properties of a block required for a comprehensive mechanical analysis.

4.1 Geometric description of blocks

4.1.1 Characteristics of a polyhedron

A polyhedron is a subset of the Euclidean space comprising piecewise planar elements. If the polyhedron can be completely enclosed by a sphere, the polyhedron is bounded (Klee 1959). Descriptions include quantities which can be measured (metric properties) and which can only be counted (topological properties). Metric properties are, for instance, the volume, mass, face areas, angles, etc, while topological properties include the number of vertices, edges and faces (Jing 2000). A simple polyhedron is topologically equivalent to a sphere and consists only of simple polygons. A simple polygon consists only of a single polygonal chain that does not intersect itself (de Berg et al. 2000).

A polyhedron consists of vertices, edges, and faces. A vertex is the intersection of three faces or three edges. An edge is the line of intersection between two faces bounded by two vertices. A face is a planar subset of 3D space bounded by a closed polygonal loop of edges. All of these elements except vertices can be directed which leads to the definitions given by Lu (2002):

Directed edge:

A directed edge is an edge of finite length between its starting and end vertices according to its orientation. The twin edge is a directed edge with the same

vertices but switched starting and end vertex. Thus, it has the opposite orientation. Two faces can be associated to a directed edge.

Directed loop:

A directed loop is a closed planar polygon formed by ordered and directed edges such that the end vertex of a directed edge coincides with the starting vertex of the following edge, and additionally having a counterclockwise spin if the normal vector of the associated face points towards the observer. Lu (2002) defines this as an exterior loop in contrast to interior loops – a distinction we omit since we neglect holes.

Directed face:

A directed face is a plane with finite size bounded by its directed loop and its normal pointing outside of the polyhedron.

Directed polyhedron:

A directed polyhedron is a finite space enclosed by directed faces.

An important topological characteristic of a polyhedron is the Euler-Poincaré characteristic stated in expression (33).

$$N_v + N_f - N_e = 2 \cdot (N_b - N_h) \quad (33)$$

In this expression N_v , N_f , N_e , N_b , and N_h are the number of vertices, faces, edges, bodies, and holes, respectively. In the following we consider only polyhedra which have no holes. The Euler-Poincaré characteristic for one polyhedron without holes is 2. These types of polyhedra are relevant for rock engineering. The algorithms, anyhow, described in the subsequent sections can be extended for polyhedra with holes with low effort.

Mechanical analyses require the inertia properties (mass, moments of inertia, products of inertia) of the considered blocks. They are derived from the geometric properties. Analytical formulas are usually not available for arbitrary polyhedra. Section 0 and 4.5 describe algorithms and formulas aiming at the determination of the required metric properties and include polyhedron decomposition into simplices and merging of simplex properties. All formulas are based on the block's vertex coordinates.

4.1.2 Parameters for the description of a polyhedron

This section proposes the minimum set of parameters to define an arbitrary polyhedral block (a simple polyhedron). For an integral description we need to link vertices, edges and faces as they have been defined in section 4.1.1. Degenerate cases such as intersection of four planes in one point are not described but have to be treated separately.

First of all, a description of the planes forming the faces is required. It includes the position and orientation of the plane, and the corresponding halfspace forming part of the block. The position vector of an arbitrary point $\mathbf{r}_{P,i}$ on plane i represents the position, two angles known as the dip direction and dip angle represent orientation, and an index for the upper or lower halfspace represent the halfspace. Dip direction and dip angle allow determining the normal vector \mathbf{n}_i of the plane. The halfspace index is required to determine which side of the plane forms the block. For an arbitrary polyhedron this needs to be valid only in the close vicinity of the plane. These data are already sufficient for the computation of a convex block which is the intersection of all halfspaces of the corresponding plane. Goodman & Shi (1985) describe, for instance, the convex block algorithm.

For a non-convex polyhedron it is not possible to determine all the required links from the plane data alone. A connectivity list provides the topological relationships. The connectivity list links the plane data to the vertices, i.e. each vertex C_{ijk} is linked to three planes i, j , and k forming the vertex. The connectivity list together with the plane data allows determining:

- the position of a block vertex $\mathbf{r}_{P,ijk}$ as the intersection of three planes i, j , and k using expression (34). Figure 42a shows the relationships.

$$\mathbf{r}_{P,ijk} = \mathbf{N}^{-1} \cdot \mathbf{d} \text{ where} \quad (34)$$

$$\mathbf{N} = \begin{pmatrix} \mathbf{n}_i^T \\ \mathbf{n}_j^T \\ \mathbf{n}_k^T \end{pmatrix} \text{ and } \mathbf{d} = \begin{pmatrix} \mathbf{n}_i^T \cdot \mathbf{r}_{P,i} \\ \mathbf{n}_j^T \cdot \mathbf{r}_{P,j} \\ \mathbf{n}_k^T \cdot \mathbf{r}_{P,k} \end{pmatrix}$$

- the block edges: every pair of vertices having the same two plane indices form a block edge. Switching the two indices forms the twin edge pointing in the opposite direction (Figure 42b).
- the faces – every face comprises only vertices having the index of the corresponding plane. The face vertices are oriented and ordered such that each starting point of a face edge is the end point of the previous face edge (Figure 42c).

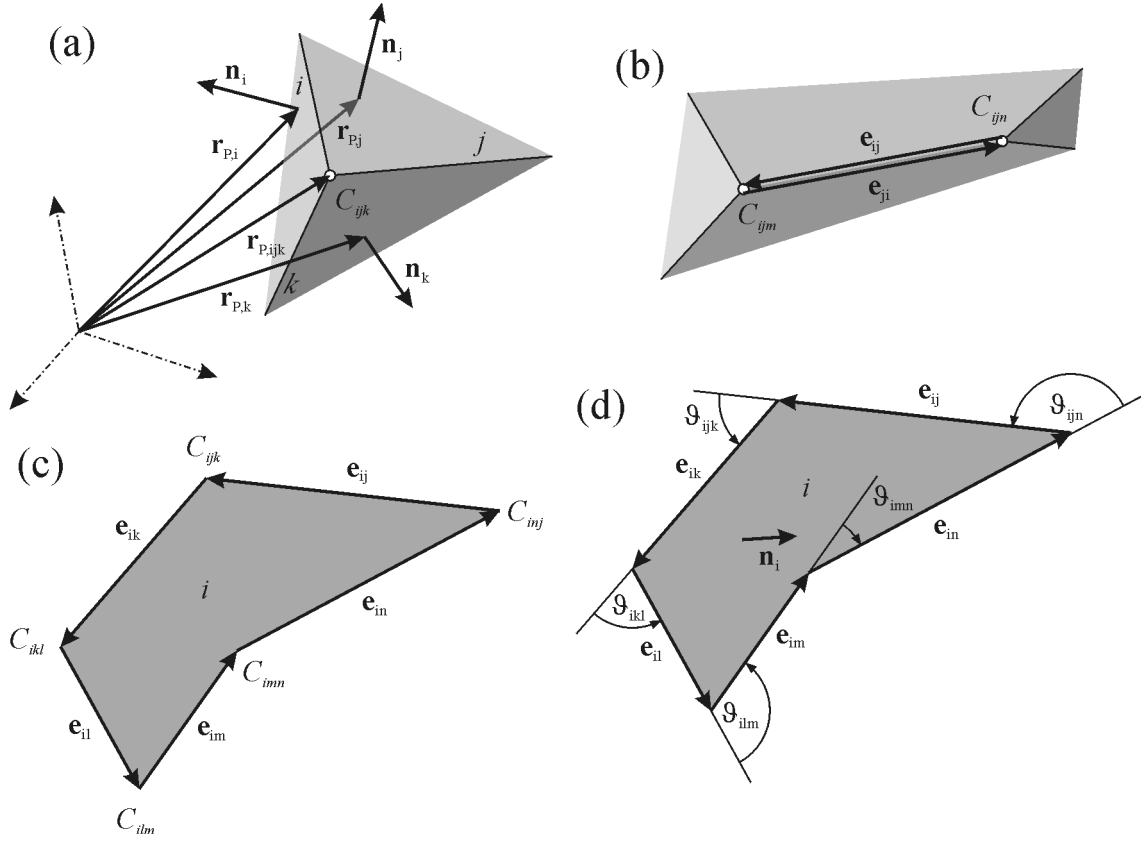


Figure 42: Description of polyhedra and topological links

For the initial description using the connectivity list the halfspace information is not required. It becomes effective for decomposition strategies and analysis of kinematics. The halfspace information allows distinguishing between the face's normal vector pointing outside and inside the block in the vicinity of the plane. For directing a face, the outside normal vector comes into play. A directed face belonging to a directed polyhedron owns a counterclockwise loop of edges when looking from outside into the block. A loop has a counterclockwise spin if the sum of the turn angles ϑ_{ijk} between two directed edges of a loop is 2π (Chan 1987). Otherwise, the loop has a clockwise spin. Figure 42d shows the relationships and expression (35) the determination of the turn angles ϑ_{ijk} .

$$\sum_{\forall C_{ijk}} \vartheta_{ijk} = 2\pi \quad \text{where}$$

$$\vartheta_{ijk} = \arccos\left(\frac{\mathbf{e}_{ij}^T \cdot \mathbf{e}_{ik}}{|\mathbf{e}_{ij}| \cdot |\mathbf{e}_{ik}|}\right) \quad \text{if } \mathbf{n}_i^T \cdot \mathbf{e}_{ik}^* \cdot \mathbf{e}_{ij} \geq 0$$

$$\vartheta_{ijk} = -\arccos\left(\frac{\mathbf{e}_{ij}^T \cdot \mathbf{e}_{ik}}{|\mathbf{e}_{ij}| \cdot |\mathbf{e}_{ik}|}\right) \quad \text{if } \mathbf{n}_i^T \cdot \mathbf{e}_{ik}^* \cdot \mathbf{e}_{ij} < 0$$
(35)

4.2 Finiteness of blocks

The finiteness theorem is a cornerstone of block theory (Goodman & Shi 1985). In its first hierarchy block theory distinguishes finite and infinite blocks. Only finite blocks can be subject to movement and instability, thus merit further analysis. The second hierarchy is related to the kinematics (see chapter 5) where moveable blocks are separated from non-movable blocks. Blocks are simple polyhedra bounded by piecewise planar areas and described according to section 4.1. Proving finiteness is also essential when having only limited data on the block geometry such as in exposed rock faces.

The finiteness theorem in block theory states that a convex block is finite if its block pyramid is empty (Goodman & Shi 1985). Conversely, a convex block is infinite if its block pyramid is not empty. At a first glance this statement may appear simple. This section outlines the general finiteness theorem and some peculiarities relevant to arbitrary polyhedra in excavation faces.

4.2.1 Plane pyramids

A plane subdivides the space into two halfspaces. A block bounded by planes is the intersection of halfspaces of these planes and, occasionally, the union of these intersections. The intersection of halfspaces contains all points common in the entire set of halfspaces. The union of halfspaces contains all points which are contained in at least one of the halfspaces of the set.

Let us consider the set of planes bounding the block. The planes are distinguished into joints and free faces. Shifting the set of planes with their halfspaces into the origin without any rotation forms a pyramid with the origin as the apex. Goodman & Shi's block theory denominates these intersections of different sets of planes for a convex block:

- The block pyramid BP is the intersection of origin-shifted blockside-halfspaces of all planes bounding the convex block.
- The joint pyramid JP is the intersection of origin-shifted blockside-halfspaces of all joint planes of the convex block.
- The excavation pyramid EP is the intersection of origin-shifted blockside-halfspaces of all free faces of the convex block.
- The space pyramid SP is the union of origin-shifted spaceside-halfspaces of all free faces of the convex block

4.2.2 The finiteness theorem for simple polyhedra

4.2.2.1 Convex blocks

A convex block B is finite if its block pyramid is empty. Conversely, a convex block is infinite if its block pyramid is not empty (Goodman & Shi 1985). Since the block pyramid is the intersection of the joint pyramid and the excavation pyramid, we can also state: A convex block is finite if the intersection between joint pyramid and excavation pyramid is empty (Expression (36a)). This is equivalent to the statement that the space pyramid entirely contains the joint pyramid (Expression (36b)). Conversely, if the intersection between joint pyramid and excavation pyramid is not empty, the block is infinite. If only the joint or only the excavation pyramid is empty, the block is finite as well.

$$\begin{aligned} \text{(a) } BP &= EP \cap JP = 0 \\ \text{(b) } JP &\subset SP \end{aligned} \tag{36}$$

Figure 43 shows joint and excavation pyramids in the stereographic projection. The green pyramid is the excavation pyramid and the blue one is the joint pyramid. The left side shows the situation for an infinite block. Joint and excavation pyramid intersect – the intersection relates to the block pyramid. The right side shows the situation for a finite block where the intersection of joint and excavation pyramid is empty.

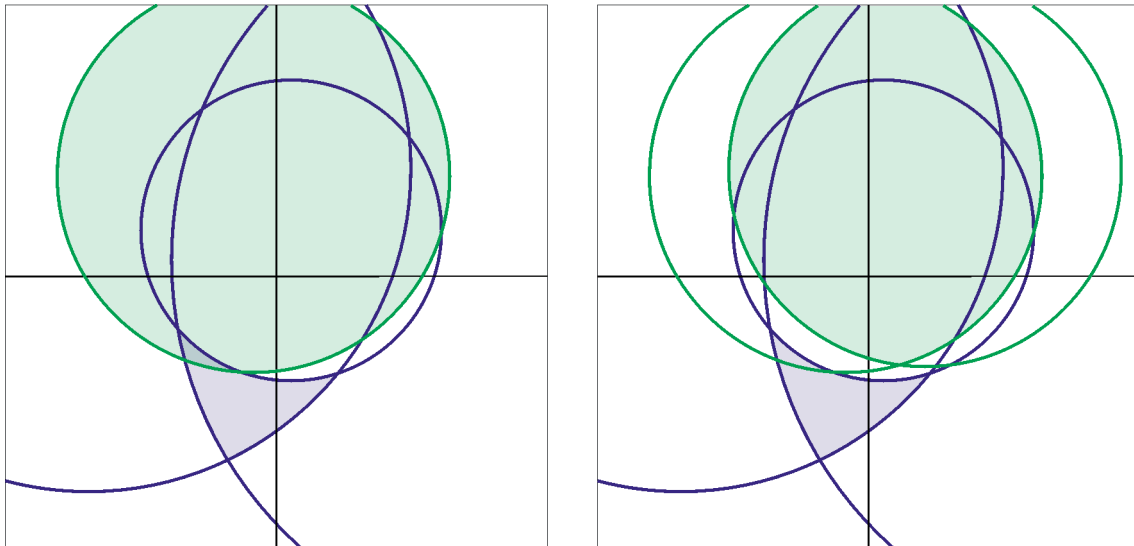


Figure 43. Block pyramids shown as the intersection of joint pyramid (shaded in blue) and excavation pyramid (shaded in green) of a convex block. The nonempty intersection (left) relates to an infinite block and the empty intersection (right) relates to a finite block.

4.2.2.2 Non-convex blocks

Let a non-convex block B be a union of convex subblocks $B(A_i)$ each of which is formed by the intersection of a set of halfspaces of B such that each point A_i forms part of $B(A_i)$. The properties are summarised in expressions (37) through (41). A detailed discussion is found in Goodman & Shi (1985), pages 121ff. Zhang & Kulatilake (2003) describe the analysis of a non-convex block with one *reflex edge*² at the free face.

$$B = \bigcup_{i=1}^h B(A_i), \text{ where } i=1 \dots h \text{ and } A_i \in B \text{ are } h \text{ points of } B. \quad (37)$$

$$B(A_i) = \bigcap_{l \in D} UB(\mathbf{n}_l), \text{ where } UB \text{ is a halfspace containing the} \quad (38)$$

blockside normal vector \mathbf{n}_l . D is the set of halfspaces which contain A_i .

According to Goodman & Shi (1985) the necessary condition for the finiteness of a non-convex block is similar to the condition for convex blocks shown in expression (39).

$$BP = EP \cap JP = 0 \quad (39)$$

The joint pyramid of a non-convex block is the intersection of the joint pyramids of all convex subblocks. Since the joint pyramids of the convex subblocks are also the intersections of related halfspaces of joints, the joint pyramid of a non-convex block is the intersection of all blockside halfspaces of joints. Thus,

$$JP = \bigcap_{i=1}^h JP(A_i) \quad (40)$$

The excavation pyramid of a non-convex block is the union of the excavation pyramids of the individual subblocks. The excavation pyramid of an individual subblock is the intersection of the blockside free face halfspaces. Thus,

$$EP = \bigcup_{i=1}^h EP(A_i) \quad (41)$$

Figure 44 shows joint and excavation pyramids related to a non-convex block. The joint pyramid in blue is the intersection of joint halfspaces equivalent to convex blocks. The green shaded area is the excavation pyramid of the non-convex block. It is the union of the excavation pyramids of two convex subblocks. These excavation pyramids are indicated by a green and red dashed line. Since the intersection between excavation pyramid and joint pyramid is empty, the situation indicates a finite block.

² The definition of a *reflex edge* is provided in section 4.2.3.

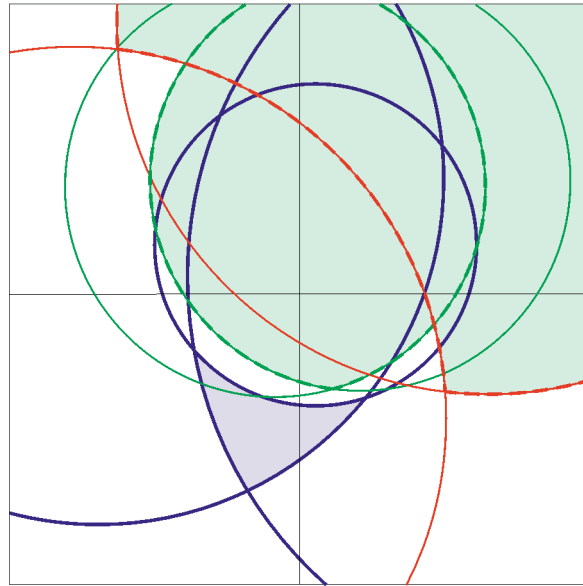


Figure 44. Block pyramid of a non-convex block. The excavation pyramid (shaded in green) is the union of the excavation pyramid of convex block subsets.

4.2.3 Determination of the excavation pyramid

For proving the finiteness of a given block it is necessary to determine the joint and excavation pyramid. In any case, the joint pyramid (JP) is just the intersection of all joint halfspaces corresponding to the block side of each block-forming joint. Since the JP is also related to potential block displacements, it is outlined in detail in chapter 5. The current chapter shows the determination of the excavation pyramid.

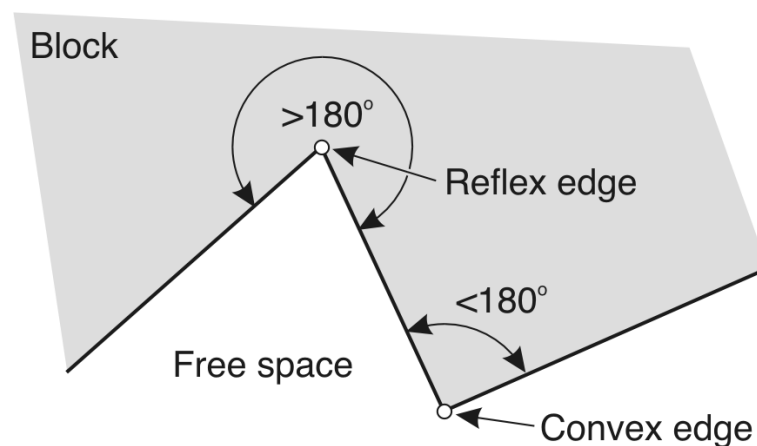


Figure 45. Convex and reflex edge

The geometry of the free faces in general consists of several simple polygons each forming part of a convex subblock. The finiteness theorem is only affected by the convexity of the excavation pyramid. The aim of this section is to group the free faces into subblocks with convex block surfaces and determine their excavation pyramid by intersection of the corresponding blockside halfspaces. In the next step the subblock's excavation pyramids are unified in order to obtain the block's excavation pyramid. Finally, this excavation pyramid is compared to the joint pyramid.

The convex subsets of the excavation pyramid are separated by *reflex edges*. Geometrically, a reflex edge is the intersection of two planes (either free faces or joints) between which the angle measured inside the block is also reflex, i.e. greater than 180° . In contrast, a convex edge is the intersection of two planes between which the angle measured inside the block is acute or obtuse, i.e. smaller than 180° (Figure 45). Figure 46 bottom shows a block with both, convex and reflex edges. Convex edges are drawn as solid black lines while reflex edges are dashed-dotted white lines.

For an efficient determination of the convex subsets of the excavation pyramid one has to find the minimum set of relevant test points A_i . As we consider only the excavation pyramid, relevant test points lie only on the free face. As stated above, the free face is continuous and finite, and the polyhedron is simple. In consequence, it is not necessary to test points inside the free face but only on its boundary. Relevant test points are thus linked at least to one joint plane. Relevant convex subsets are planes between *reflex edges* along the boundary of the free surface.

The algorithm is as follows:

- Find all edges and faces lying on the free face
- Classify edges into convex and reflex (non-convex) edges
- Determine the closed directed three-dimensional polygon representing the boundary between joints and free surface
- Separate the closed three-dimensional polygon into open subpolygons with endpoints at the reflex edges
- Find the planes and halfspaces belonging to the subpolygons
- Group the halfspaces into convex intersections according to their affiliation to the subpolygons
- Compute the excavation pyramid for each convex subset
- Compute the intersection of the joint pyramid with each of the excavation pyramids
- If all intersections are empty, the block is finite, otherwise it is infinite.

Figure 46 shows a block with four joints and a non-convex free surface with five planar pieces. The geometric data of this block are shown in Table 2 and Table 3. The block has in total 14 corners which have been defined by a connectivity list. Joint planes are shaded in blue. The planes of the free surface have different colours (red, green and magenta) each corresponding to a convex subset of the free surface. The algorithm of this section allowed grouping the planes into the shown subsets. The reflex edges indicated by white dashed-dotted lines bound the subsets within the free surface.

Table 2. Corner coordinates for the block shown in Figure 46.

Corners	Coordinates		
	X [m]	Y [m]	Z [m]
C_1	-1.00	-3.00	-1.50
C_2	-1.90	-3.50	-2.42
C_3	-1.00	-3.23	-1.30
C_4	1.22	-4.71	-3.35
C_5	-2.84	-4.46	-3.00
C_6	1.53	-4.78	-4.21
C_7	0.06	-5.03	-4.09
C_8	1.24	-4.76	-3.42
C_9	0.15	-3.72	-0.42
C_{10}	-0.56	-4.23	-1.08
C_{11}	1.03	-4.98	-2.83
C_{12}	-1.50	-2.36	-1.59
C_{13}	0.09	-2.10	-0.24
C_{14}	0.70	-2.20	-1.93

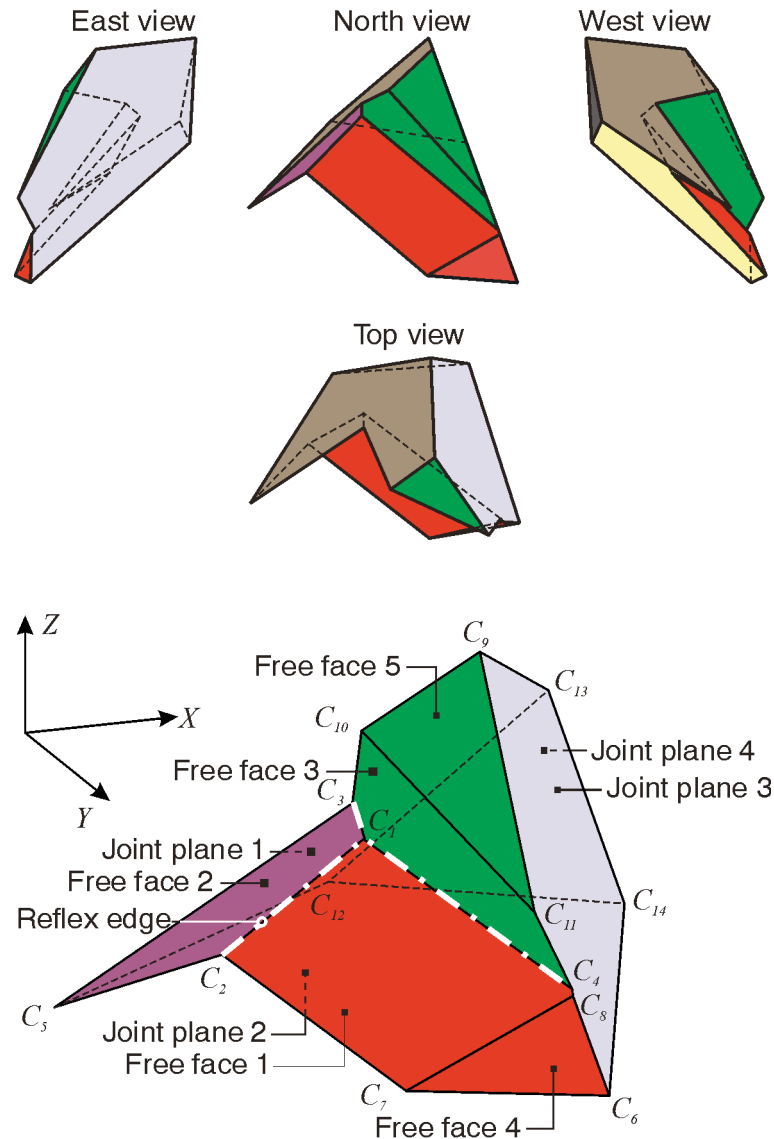


Figure 46. Block with a non-convex free surface. Joints are blue. Convex subsets of the free surfaces have different colours (red, green, and magenta). The reflex edges are white dashed-dotted lines.

Table 3. Data on joints and free faces for the block shown in Figure 46.










Planes	Orientation		Point on plane			Halfspace	Colour
	Dip direction [°]	Dip angle [°]	X [m]	Y [m]	Z [m]		
Joint plane 1	260	40	0.00	0.00	0.00	lower	
Joint plane 2	165	40	0.00	0.00	0.00	upper	
Joint plane 3	90	70	0.00	0.00	0.00	lower	
Joint plane 4	175	85	1.00	-2.00	0.00	upper	
Free face 1	190	55	-1.00	-3.00	-1.50	lower	
Free face 2	300	60	-1.00	-3.00	-1.50	upper	
Free face 3	60	60	-1.00	-3.00	-1.50	upper	
Free face 4	170	85	1.00	-4.90	-4.50	lower	
Free face 5	170	60	0.00	-3.50	0.00	lower	

Figure 47 shows the stereographic projection of the joints and free faces of the block shown in Figure 46. Joint planes are shown with blue great circles. The joint pyramid is the intersection of the joint halfspaces given in Table 3. It is shaded in blue. The free faces are great circles with different colours (red, green, and magenta) related to the convex subsets of the free surface according to the algorithm of this section. The dashed arcs of the great circles indicate the boundaries of the excavation pyramids of the convex subsets which are the intersections of the corresponding free face halfspaces. The halfspace of each free face is given in Table 3. As it is an upper focal point projection, the lower halfspace projects inside the great circles and the upper one outside the great circle. The excavation pyramid of the block is the union of the subsets's excavation pyramids. It is shaded in green and surrounded by the envelope of the subsets's excavation pyramids. The intersection between joint and excavation pyramid is empty. Thus, the block is finite which has been obvious from the perspective view in Figure 46.

4.3 Identification of finite blocks from trace maps

In order to use the discontinuity data from 3D image measurements as described in chapter 2 for block analyses it is necessary to characterise the discontinuity network with respect to blocks. Only finite blocks as defined in the previous section are relevant. The computation involves three steps including establishing a geometrical model of the rock mass, delineating polygonal patches on the model surfaces, and determining the block geometries. The properly assessed 3D image with discontinuity measurements suffices as input for the subsequent computation.

4.3.1 Establishment of a geometrical model

The geometrical model contains geometric information about the geometry of the rock structure (natural slope, benched mine slope, tunnel, cavern, etc.) and the discontinuity system. The rock structure forms the free surfaces. It consists of intersected planar patches which approximate the irregular rock surface. The free surface is defined by the orientations of the plane, and the corners and the edges of their intersections.

Stereographic projection - equal angle - upper focal point

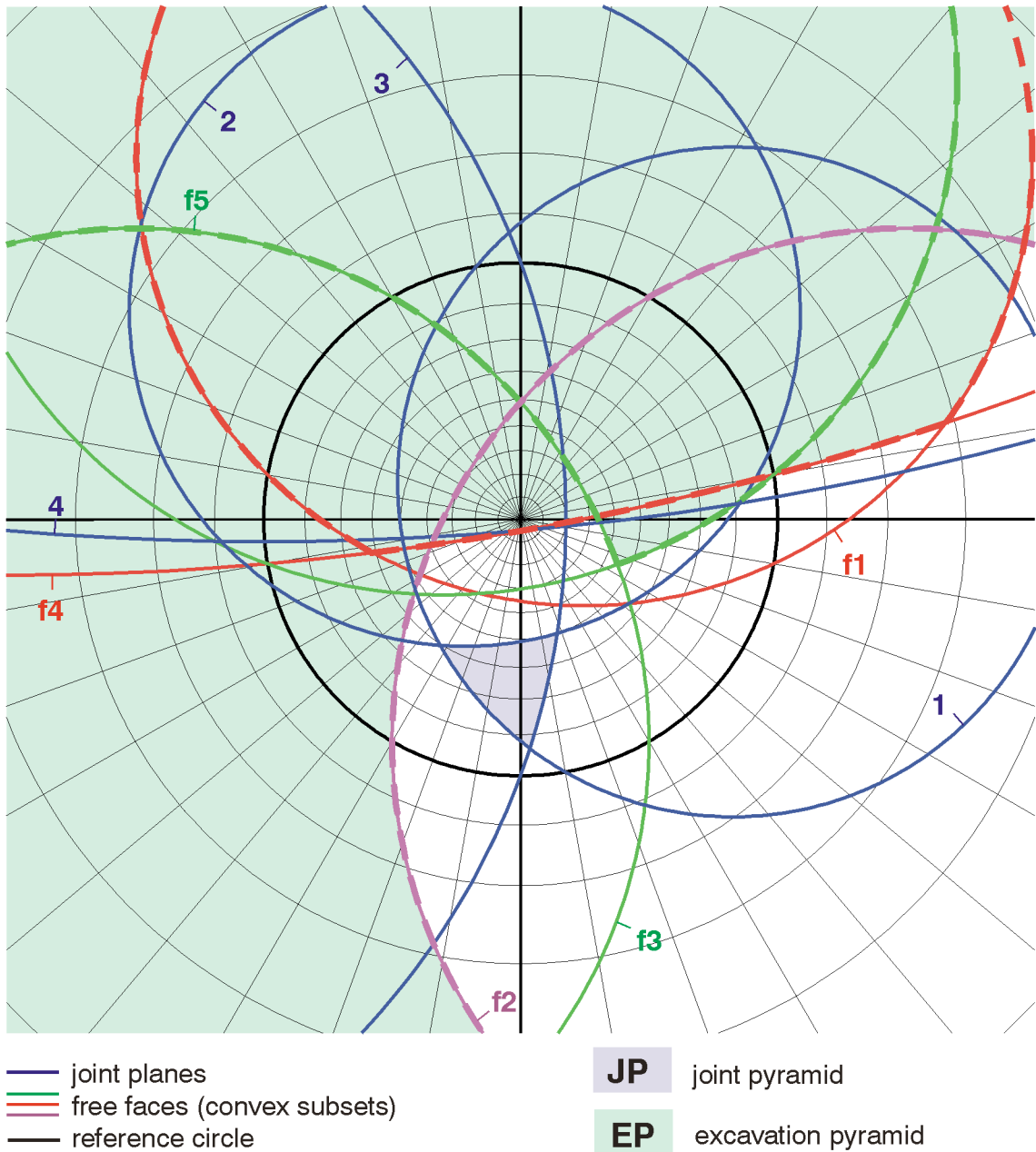


Figure 47. Joint and excavation pyramid for the block shown in Figure 46. Colours of the free faces correspond to convex subsets. The excavation pyramids of the subsets are indicated by dashed arcs of the great circles.

The measured discontinuities are intersected with the free surfaces and form a network of joint traces. The position and extension of the joints is directly visible. Each trace has the orientation of the joint attached to it. It is assumed that the discontinuities persist infinitely into the rock mass although finite extent does not limit this approach (for instance the circular disc model (Baecher et al. 1977) could be applied). Anyhow, the size of discontinuities is usually not known a priori. For the subsequent computation it is not necessary to have the joints grouped into sets. Each joint is treated individually. Figure 48 shows a simple geometrical model consisting of five rectangular patches forming the free surface and several intersecting joint traces along the free surface.

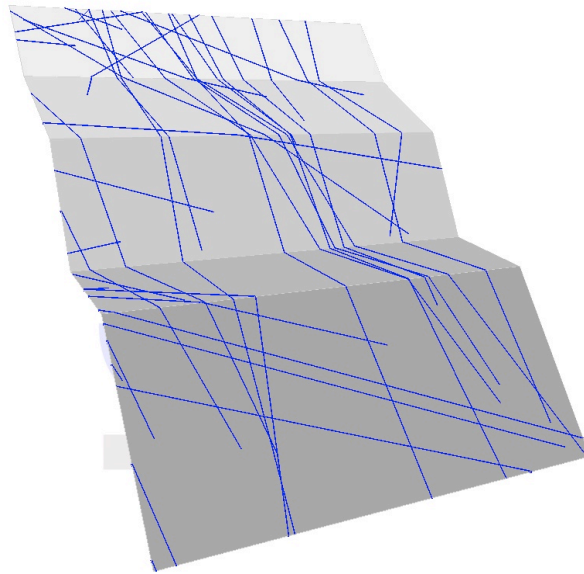


Figure 48: Geometrical model of a slope comprising the traces of the joint system (blue) and the geometry of the slope (grey)

4.3.2 Identifying surface patches of blocks

Once the geometrical model has been established, the trace network is searched for closed polygons (loops) of traces in order to identify the superficial block faces (Lu 2002). The result is a dense assembly of finite surface patches each of which corresponding to a – finite or infinite – block. The patch identification requires the following computational steps after Lu (2002).

First of all, the traces are subdivided into stretches between their intersections. Intersection points are stored. Twin directed traces are assigned to each stretch, i.e. one vector points from one intersection point of the stretch to the other and another vector (the twin vector) points in the reverse direction (Figure 42b). The

first trace is randomly selected. The subsequent traces of the patch are determined in a recursive computation until the original starting point has been encountered again (Figure 42c).

The recursive computation comprises steps to determine the trace following the current one. At the same time the former endpoint becomes the new starting point. Any selected trace is flagged and cannot be selected again for another patch. The subsequent trace complies with the following two constraints:

- The subsequent directed trace must point away from the endpoint of the current directed trace.
- The subsequent directed trace is the one which forms the maximum right-handed angle with the current directed trace whereby 360° are treated as 0° . The right-handed angle is determined according to expression (42).

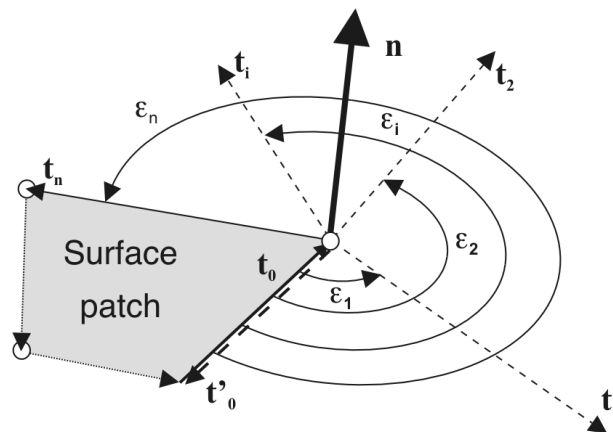


Figure 49: Trace search criterion (modified after Lu (2002))

Figure 49 represents the sketch of the trace search criterion applied at a random corner of a patch. \mathbf{t}_i indicates the directed traces, ε_i indicates the right-handed angle, and \mathbf{n} indicates the normal vector of the plane. \mathbf{t}_0 is the current trace whose subsequent trace has to be determined. \mathbf{t}_0' is the reverse directed trace of \mathbf{t}_0 . Reverse directed traces of the other traces are not shown in Figure 49. Candidates for the subsequent trace are those traces \mathbf{t}_i which have an index “i” greater than zero and \mathbf{t}_0' as well. Applying the above stated constraints trace \mathbf{t}_n is determined as the subsequent trace. The endpoint of \mathbf{t}_0 becomes the new starting point and the algorithm is repeated until the traces arrive at the starting point of \mathbf{t}_0 .

$$\begin{aligned}
\varepsilon_i &= \pi - \arccos\left(\frac{\mathbf{t}_0^T \cdot \mathbf{t}_i}{|\mathbf{t}_0| \cdot |\mathbf{t}_i|}\right) & \text{if } (\mathbf{t}_i^* \cdot \mathbf{t}_0)^T \cdot \mathbf{n} \geq 0 \\
\varepsilon_i &= \pi + \arccos\left(\frac{\mathbf{t}_0^T \cdot \mathbf{t}_i}{|\mathbf{t}_0| \cdot |\mathbf{t}_i|}\right) & \text{if } (\mathbf{t}_i^* \cdot \mathbf{t}_0)^T \cdot \mathbf{n} < 0
\end{aligned} \tag{42}$$

The trace search criterion is applied to the entire trace map. This results in a subdivision of the slope surface into polygons. Each polygon forms part of the free surface of a block. Figure 50 shows the resulting polygons of the geometrical model in Figure 48.

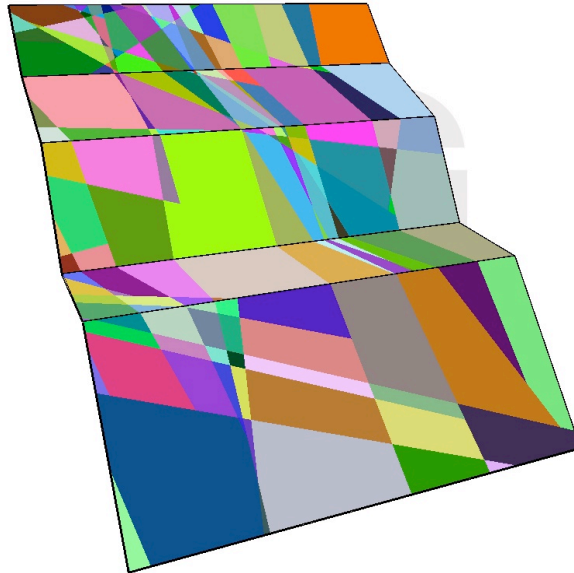


Figure 50: Polygon patches determined with a trace-search algorithm based on the traces shown in Figure 48.

4.3.3 Determination of the block geometry from surface patches

Each of the identified polygons contains the information about the orientation and halfspaces of both, the discontinuities and free surfaces. By determining the joint and block pyramids, each polygon can be analysed to determine the finiteness of the corresponding block (Goodman & Shi 1985 outlined in section 4.2). This is applied for blocks with one free surface as well as for those at edges (two free surfaces), corners (three free surfaces), and more complex slope

geometries. Figure 51 shows finite blocks with one free surface for the trace map in Figure 48.

Basic keyblock analyses do not cover the entire block failure mechanisms which can occur in rock slopes. A number of blocks which are not necessarily individually removable can form a removable keyblock. These types of blocks are referred to as united keyblocks. Chan (1987) proposes a mathematical formulation for identifying united keyblocks. The drawback of this formulation is that it is applicable only for joint sets containing perfectly parallel discontinuities. A generalisation for joints sets with non-parallel discontinuities has been undertaken but not yet finished.

Finally, the block geometry including corners, edges and faces has to be determined. At this stage it is assumed that from the superficial trace discontinuities persist infinitely into the rock mass. If the surface patch is convex, then a corresponding finite block is also convex. In this case Goodman & Shi's (1985) method for determining the block geometry can be applied. In case of non-convex patches the finite block comprises reflex edges. Algorithmic determination of block geometry requires sequential edge intersection of adjacent planes, and corner intersection of adjacent edges until all planes and edges are connected. The algorithm is similar to the algorithm for geometric roof design.

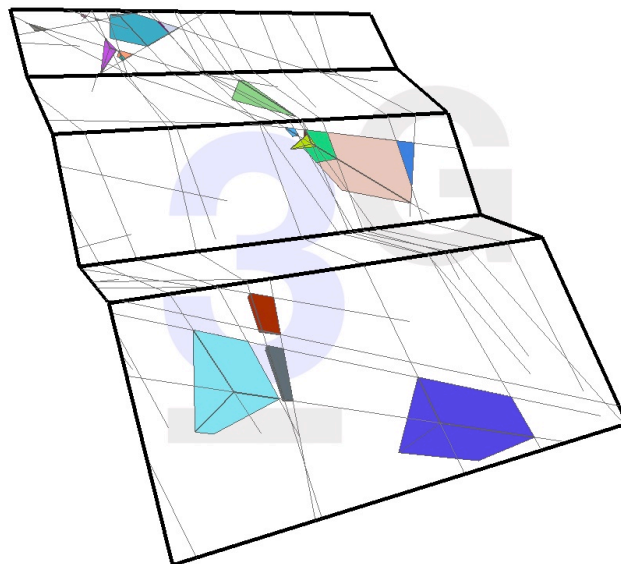


Figure 51: Finite removable blocks with one free surface

4.4 Metric properties of tetrahedra

A tetrahedron is a simplex³ in three-dimensional Euclidean space. It consists of four vertices, each determined by the position vector $\mathbf{r}_{P,i}$ with $i=1,\dots,4$. Each possible vertex triple lies in one plane. This section introduces analytical formulae for determining the metric properties required for rigid body dynamics, each based on the known vertex coordinates. The derivation of these analytical formulae is described in a variety of articles and textbooks; those based on vertex coordinates for instance in Goodman & Shi (1985) and Tonon (2004).

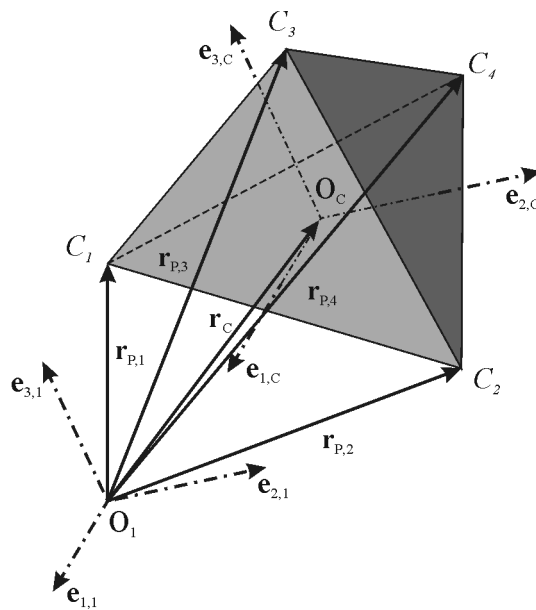


Figure 52: Tetrahedron – definitions and relationships

4.4.1 Volume

The scalar triple product gives the volume of a parallelepiped defined by three vectors, each pointing from one vertex to one of the three remaining vertices. A parallelepiped is made up of six tetrahedra defined by these vertices. Hence, the volume of a tetrahedron is one sixth of the scalar triple product. Expression (43) gives the analytical formula.

³ A simplex in n -dimensional space is the convex hull of $n+1$ vertices.

$$V_i = \frac{1}{6} \cdot \begin{vmatrix} 1 & x_1 & y_1 & z_1 \\ 1 & x_2 & y_2 & z_2 \\ 1 & x_3 & y_3 & z_3 \\ 1 & x_4 & y_4 & z_4 \end{vmatrix} = \frac{1}{6} \cdot \begin{vmatrix} x_2 - x_1 & x_3 - x_1 & x_4 - x_1 \\ y_2 - y_1 & y_3 - y_1 & y_4 - y_1 \\ z_2 - z_1 & z_3 - z_1 & z_4 - z_1 \end{vmatrix} \quad (43)$$

4.4.2 Mass

The mass of a body is a scalar value. With uniform density ρ , it is proportional to the volume as shown in expression (44).

$$m_i = \rho \cdot V = \frac{\rho}{6} \cdot \begin{vmatrix} x_2 - x_1 & x_3 - x_1 & x_4 - x_1 \\ y_2 - y_1 & y_3 - y_1 & y_4 - y_1 \\ z_2 - z_1 & z_3 - z_1 & z_4 - z_1 \end{vmatrix} \quad (44)$$

4.4.3 Centre of gravity

The position vector of the centre of gravity of a tetrahedron with uniform density is the sum of the vertex vectors divided by the number of vertices following the rule for simplices in n -dimensional space. Expression (45) can be obtained assuming that median lines for triangles divide by 1:2 and for tetrahedra by 1:3.

$$\mathbf{r}_{C,i} = \frac{1}{4} \cdot \sum_{j=1}^4 \mathbf{r}_{P,j} \quad (45)$$

This work does not distinguish between the centre of gravity, centre of mass, and centroid, since the gravitation gradient is neglected and uniform density within a tetrahedron is assumed.

4.4.4 Areas of face triangles

The norm of the cross product of two vectors is equal to the area of the corresponding parallelogram. The area of a triangle is the half of this norm, each of the vectors pointing from one vertex towards one of the remaining vertices. Expression (46) shows this relationship in matrix formulation.

$$A_i = \frac{1}{2} \cdot \left\| \left(\mathbf{r}_{P,j} - \mathbf{r}_{P,i} \right)^* \cdot \left(\mathbf{r}_{P,k} - \mathbf{r}_{P,i} \right) \right\|_{\substack{i,j,k=1 \\ i \neq j \neq k}}^4 \quad (46)$$

with $[\mathbf{r}_{P,i}, \mathbf{r}_{P,j}, \mathbf{r}_{P,k}] \in A_i$

4.4.5 Inertia matrix

The inertia matrix of a rigid body is a 3×3 symmetric matrix comprising the second order mass moments as shown in expression (47). The diagonal elements are the mass moments of inertia which can only take positive values. The negative off-diagonal elements are the mass products of inertia which can take either positive or negative values.

$$\mathbf{J}_i = \begin{pmatrix} J_{xx} & -J_{xy} & -J_{xz} \\ -J_{xy} & J_{yy} & -J_{yz} \\ -J_{xz} & -J_{yz} & J_{zz} \end{pmatrix} \quad (47)$$

The elements of the inertia matrix with respect to the vertex coordinate system (position and orientation) are calculated according to the expressions (48a) - (48f). The derivation is shown in Tonon (2004). Section 0 discusses the translation and rotation of the inertia matrix to different reference frames.

$$\begin{aligned}
\text{(a)} \quad J_{xx} &= \frac{m_i}{10} \cdot \left(\sum_{i=1}^4 (y_i^2 + z_i^2) + \sum_{\substack{k,l=1 \\ l>k}}^4 (y_k \cdot y_l + z_k \cdot z_l) \right) \\
\text{(b)} \quad J_{yy} &= \frac{m_i}{10} \cdot \left(\sum_{i=1}^4 (x_i^2 + z_i^2) + \sum_{\substack{k,l=1 \\ l>k}}^4 (x_k \cdot x_l + z_k \cdot z_l) \right) \\
\text{(c)} \quad J_{zz} &= \frac{m_i}{10} \cdot \left(\sum_{i=1}^4 (x_i^2 + y_i^2) + \sum_{\substack{k,l=1 \\ l>k}}^4 (x_k \cdot x_l + y_k \cdot y_l) \right) \\
\text{(d)} \quad J_{xy} &= \frac{m_i}{20} \cdot \left(2 \cdot \sum_{i=1}^4 x_i \cdot y_i + \sum_{\substack{k,l=1 \\ l \neq k}}^4 x_k \cdot y_l \right) \\
\text{(e)} \quad J_{xz} &= \frac{m_i}{20} \cdot \left(2 \cdot \sum_{i=1}^4 x_i \cdot z_i + \sum_{\substack{k,l=1 \\ l \neq k}}^4 x_k \cdot z_l \right) \\
\text{(f)} \quad J_{yz} &= \frac{m_i}{20} \cdot \left(2 \cdot \sum_{i=1}^4 y_i \cdot z_i + \sum_{\substack{k,l=1 \\ l \neq k}}^4 y_k \cdot z_l \right)
\end{aligned} \tag{48}$$

4.5 Metric properties of simple polyhedra

In general blocks have an arbitrary polyhedral shape. Planes define the surface of a block, intersecting at edges and corners (vertices). Blocks can have notches and entrants, thus can have a non-convex shape significantly different from a tetrahedron. The formulae of the previous section can be used for the determination of block properties if one accomplishes a suitable segmentation of the polyhedral block into tetrahedra. Segmentation strategies are different for convex and non-convex polyhedra. After segmentation and determination of the properties of the individual tetrahedra merging of the obtained parameters leads to the properties of the original block. This section provides methods for distinguishing convex and non-convex polyhedra, decomposition strategies for both types of polyhedra, and formulae for merging the individual properties.

4.5.1 Distinction between convex and non-convex polyhedra

A convex polyhedron is the nonempty intersection of a finite number of halfspaces bounded by planes. A non-convex polyhedron can be seen as the union of a finite number of convex polyhedra (Edelsbrunner 1995). Two necessary criteria for the convexity of a polyhedron are as follows:

- All vertices of the polyhedron lie on the convex hull of the polyhedron.
- All faces of the polyhedron are convex polygons.

In other words, if there is any point inside the convex hull, although all faces are convex, the block is non-convex. If there is any face having a non-convex boundary, although all points lie on the convex hull, the block is non-convex. Figure 53 shows a convex polyhedron (a), a non-convex polyhedron with only convex faces (b), and a non-convex polyhedron with all vertices lying on the convex hull. The following algorithm covers also the combination of case (b) and (c) which has been omitted in the figure.

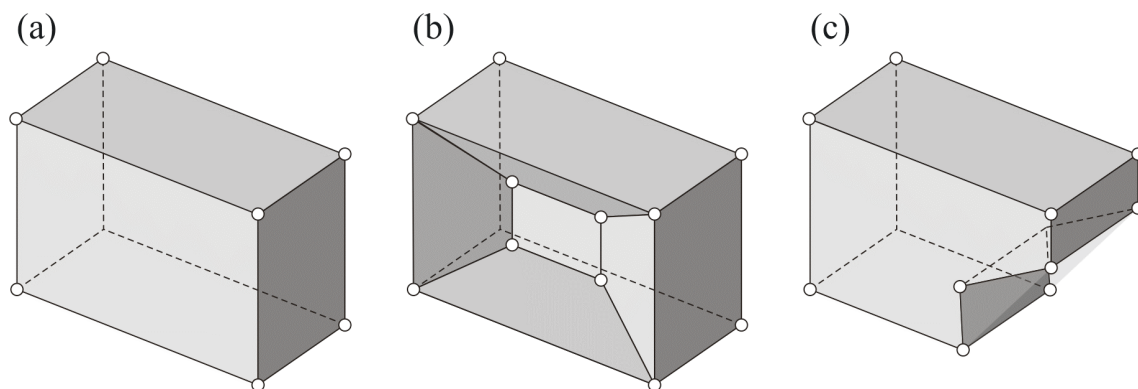


Figure 53: Characteristics of polyhedra. (a) Convex polyhedron – all points lie on the convex hull and all faces are convex polygons. (b) Non-convex polyhedron – a set of points lies inside the convex hull, although all faces are convex. (c) Non-convex polyhedron – all points lie on the convex hull but some faces are non-convex.

The algorithm for determining block convexity is below:

- Compute the three-dimensional convex hull for the set of block corners. Algorithms for computing the three-dimensional convex hull are standard and available from textbooks on computational geometry, for instance, de Berg et al. (2000). The author used the Matlab function *convhulln*.

- Test whether the corners of the block lie on the convex hull
Increase a test counter by one if no coincidence could be found, and store the index of this point.
- For each face, transform the face corners into a two-dimensional coordinate system
- Compute the two-dimensional convex hull for each set of face points
Algorithms for computing the two-dimensional convex hull are standard and available from textbooks on computational geometry, for instance, de Berg et al. (2000). The author used the Matlab function *convhull*.
- Test each face whether the points of the face coincide with one of the points of the face's convex hull
Increase a test counter by one in case no coincidence could be found, and store the index of this point.
- If the test counter is zero, the block is convex – non-convex decomposition is not required. Otherwise, the block is non-convex and non-convex decomposition has to take place.

4.5.2 Decomposition of convex polyhedra

The decomposition of a convex polyhedron is straightforward and has been already described in various textbooks, for instance, Goodman & Shi (1985), de Berg et al. (2000).

- Select one (and only one) arbitrary corner C_{ijk} of the convex polyhedron. The three planes i, j , and k , form this corner.
- Subdivide all faces of the polyhedron into triangles
 - Select the loops of each face
 - Select one (and only one) arbitrary corner C_{lmn} from the loop
 - Connect every two subsequent corners C_{lno} and C_{lop} of the loop to corner C_{lmn}
 - Store an indicator of the number of the original face for each triangle
- Connect the corners of every triangle $C_{lmn}-C_{lno}-C_{lop}$ except those lying in planes i, j , and k to the apex point C_{ijk} to form the decomposed tetrahedra of the polyhedron.

The decomposition consists of a link list of tetrahedra each described by four indices pointing to the corresponding vertex coordinates. Figure 54 describes the algorithm graphically.

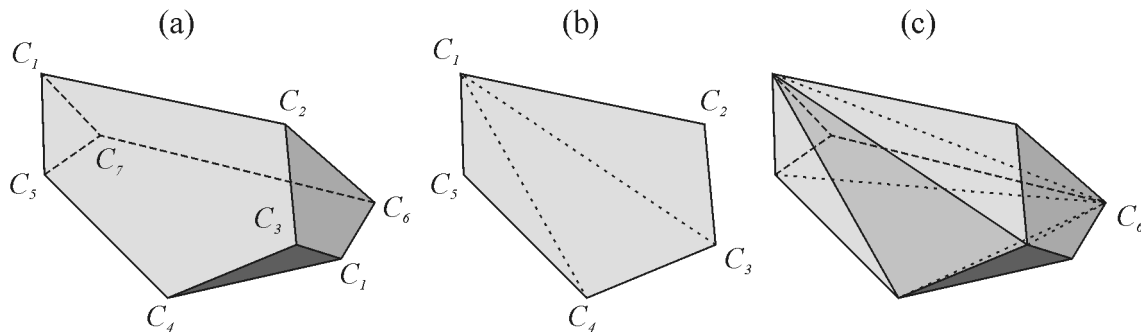


Figure 54: Convex decomposition of polyhedra. (a) Convex block comprising seven vertices. (b) Triangulation of faces. (c) Connection of triangles with stored vertex C_6 to form tetrahedral

4.5.3 Decomposition of non-convex polyhedra

The convex block segmentation fails in the case of non-convex polyhedra. It can be even impossible to subdivide a non-convex polyhedron into tetrahedra without adding new vertices (Ruppert & Seidel 1992). A possible approach to overcome this problem is the decomposition of the block into convex subblocks and, subsequently, decomposition of the subblocks into tetrahedra. The algorithmic treatment of the decomposition into convex polyhedra requires following major steps:

- Definition of cutting planes which have infinite extent
- Formation of new vertices
 - Intersections of polygon edges with all single cutting planes
 - Intersections of polygon faces with pairs of cutting planes
 - Intersections of cutting plane triples inside the polyhedron
- Establish new directed edges and links to the faces and cutting planes
- Application of Lu's algorithm for identification of directed loops (Lu 2002)
 - Maximum right-handed angle criterion for directed edges
- Application of Lu's algorithm for identification of directed convex polyhedra (Lu 2002)
 - Extended maximum right-handed angle criterion for directed faces

Figure 55a exemplarily shows a block with 8 faces, 12 vertices and 18 edges. It has one reflex edge which defines the cutting planes. Figure 55b shows the new vertices and directed edges as the basis for Lu's loop and polyhedron search. The convex subblocks and tetrahedra are shown in Figure 55c and Figure 55d.

Although conceptionally easy, the algorithm requires several algebraic operations, special treatment for degenerate cases, rearrangements, and search operations making it slow.

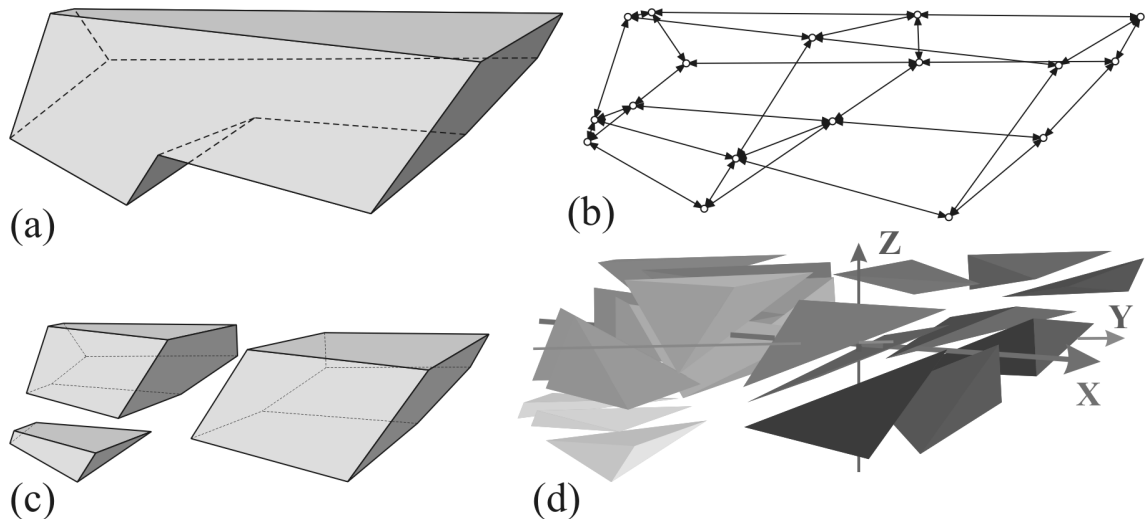


Figure 55: Decomposition of a non-convex polyhedron into tetrahedra. (a) Original block (b) New vertices and directed edges (c) Non-overlapping convex subblocks (d) Non-overlapping tetrahedral

There are two groups of methods for calculating volume properties of non-convex polyhedra avoiding the decomposition into non-overlapping standard geometric forms: Divergence theorem methods and direct integration methods. Divergence theorem methods take advantage of Gauss's divergence theorem which states that a volume integral is equivalent to the surface integral over the oriented boundary of the volume. Representatives of this approach are Gonzalez-Ochoa et al. (1998) and Mirtich (1996).

Direct integration methods break the volume into overlapping smaller volumes which can be efficiently integrated. The central projection algorithm used here is based on the methods of Lien & Kajiya (1984), outlined by Ohanian (2005). It is suitable for piecewise polygonal surfaces and bodies with constant density. Tonon (2007a) describes an efficient derivative of the central projection algorithm used for the maximum block around a tunnel with the block's apex as the projection centre.

The direct integration requires triangulation of the polygonal block faces. Triangulation of a polygon without adding new vertices is always possible (de Berg et al. 2000). In consequence, there is no need for determining new vertices at all, which is the basis for the algorithm's efficiency. The triangles are

connected to an arbitrary point (for instance the origin) to form tetrahedra. For these tetrahedra the volume and mass properties are calculated. Those tetrahedra, whose outside normal vector of the body triangle points towards the apex, have a negative volume and mass contribution. Those with an outside normal vector pointing away from the projection centre contribute positively. Figure 56 shows the central projection algorithm exemplarily for two tetrahedra, one contributing positively and the other negatively, depending on the outside normal vector of the surface triangles.

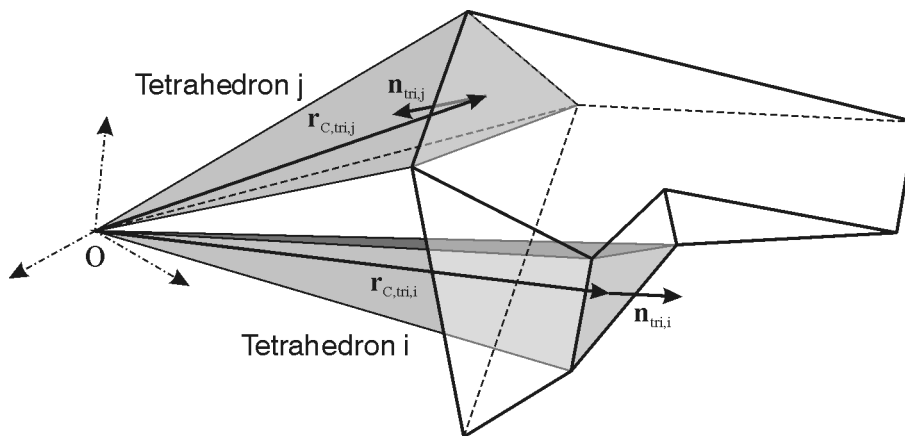


Figure 56: Central projection algorithm (direct integration). Surfaces triangles are connected to apex O . Tetrahedron i has a positive and tetrahedron j a negative contribution.

Choosing a block vertex as the apex of the tetrahedra avoids triangulation of the three faces forming the vertex. Due to the surface triangulation the face areas can also be easily calculated. For area calculation the entire surface has to be triangulated. The algorithm in detail is as follows:

- Decomposition of the face polygons into monotone polygons (Garey et al. 1978)
- Triangulation of the monotone polygons (Lee & Preparata 1977)
- Calculation of the outside normal vector of the triangles
- Calculation of volume, mass and centre of gravity
 - Selection of a block vertex as tetrahedron apex. Favourably, the vertex, where the sum of the triangles of the adjacent faces is maximum, should be selected.

- Formation of tetrahedra using the apex and triangles
- Calculation of the volume, mass and centre of gravity of the tetrahedra (see section 0)
- Merging of tetrahedra properties (see section 4.5.4)
- Calculation of the inertia matrix
 - Selection of the block's centre of gravity as the tetrahedra apex
 - Formation of tetrahedra using the apex and triangles
 - Calculation of the moments and products of inertia for the tetrahedra (see section 0)
 - Merging of tetrahedra properties (see section 4.5.4)
- Calculation of the face areas
 - Calculation of the areas of the surface triangles (see section 0)
 - Face-wise summation of the triangle sizes (see section 4.5.4)

4.5.4 Merging of simplex properties

After tetrahedral decomposition (sections 4.5.2 and 4.5.3) and calculating the properties of each individual tetrahedron (section 4.4) the individual properties are merged in order to get the properties of the original block. Each of the properties may require different merging strategies.

4.5.4.1 Volume and mass

The volume and the mass of the block is the sum of the volumes or masses of all individual tetrahedra. Note that tetrahedra of a decomposition may have a negative volume and mass using direct integration methods.

$$(a) \quad V_{tot} = \sum_{i=1}^n V_i \quad (b) \quad m_{tot} = \sum_{i=1}^n m_i \quad (49)$$

with n as the number of individual tetrahedra

4.5.4.2 Centre of gravity

The vector to the block's centre of gravity is the sum of the static moments of the individual tetrahedra about the origin divided by the mass of the block. Note that tetrahedra of a decomposition may have a negative volume and mass using direct integration methods.

$$\mathbf{r}_C = \frac{1}{m_{tot}} \cdot \sum_{i=1}^n m_i \cdot \mathbf{r}_{C,i} \quad (50)$$

with n as the number of individual tetrahedra

4.5.4.3 Inertia matrix

The inertia matrix of a block one determines with the individual tetrahedra and application of Steiner's theorem. Steiner's theorem assumes parallel coordinate systems. Expression (51) shows the relationships. \mathbf{J}_i are the inertia matrices of the individual tetrahedra as described by expressions (48a) – (f). $\mathbf{r}_{c,i}$ are the reference points for each tetrahedron, usually the centres of gravity for the tetrahedra. If these reference points coincide with the centre of gravity of the block, the second summand vanishes. Note that tetrahedra of a decomposition may have a negative volume and mass using direct integration methods.

$$\mathbf{J}_C = \sum_{i=1}^n \left\{ \mathbf{J}_i - m_i \cdot (\mathbf{r}_{C,i} - \mathbf{r}_C)^* \cdot (\mathbf{r}_{C,i} - \mathbf{r}_C)^* \right\} \quad (51)$$

with n as the number of individual tetrahedra

Rotation of the inertia matrix about the centre of gravity

$$\mathbf{J}_C^{(2)} = \mathbf{A}^{(12)T} \cdot \mathbf{J}_C^{(1)} \cdot \mathbf{A}^{(12)} \quad (52)$$

where $\mathbf{A}^{(12)}$ is the rotation matrix transforming from coordinate system (2) to (1). The rotation matrix is discussed in chapter 5.

Moment of inertia related to an axis \mathbf{u} passing through the origin of the reference system

$$J_u = \mathbf{u}^T \cdot \mathbf{J} \cdot \mathbf{u} \quad (53)$$

Principal moments of inertia and principal axes of inertia

The principle moments of inertia are the Eigenvalues of the inertia matrix. The principal axes of inertia are the corresponding Eigenvectors. The radius of the inertia ellipsoid along the principal axes is the reciprocal of the square root of the principal moment of inertia.

4.5.4.4 Face areas

The face areas of the block are the sums of the triangle areas making up each of the faces.

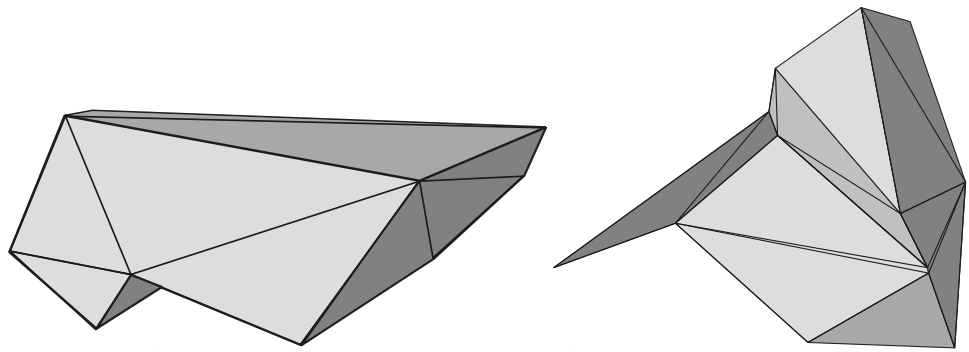
$$A_{face,i} = \frac{1}{2} \cdot \sum_{j=1}^n \left\| \left(\mathbf{r}_{P,2}^{(j)} - \mathbf{r}_{P,1}^{(j)} \right) * \left(\mathbf{r}_{P,3}^{(j)} - \mathbf{r}_{P,1}^{(j)} \right) \right\| \quad (54)$$

with n as the number of triangles at the considered face

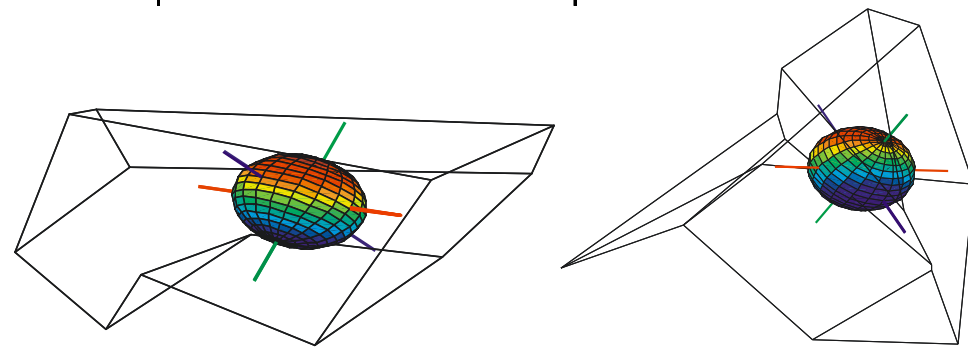
4.6 Examples for metric properties for simple blocks

The following Table 4 shows the metric properties of two blocks determined by using the expressions of sections 0 and 4.5. The geometry of the block in the left column is described in chapter 5, section 5.4.2. The geometry of the block in the right column is described in Table 3 and Table 2 in section 4.2.3. The properties include volume, mass, centroid, moments and products of inertia, and face areas. These values have been determined based only on the block's vertices. The sketches at the table's top show the blocks in a perspective view including the face triangulation. The sketches at the table's bottom show the inertia ellipsoid and principle axes relative to the block at the centroid. The inertia radius is not to scale.

Table 4. Two examples for the determination of block properties



Volume	[m³]	V	6839	V	6.38
Mass	[t]	m	18464	m	17.24
Centroid	[m]	x_c	8.704	x_c	-0.020
		y_c	2.763	y_c	-3.428
		z_c	-4.357	z_c	-1.985
Moments of Inertia	[kgm²]	J_{xx}	6.534E+08	J_{xx}	2.044E+04
		J_{yy}	5.093E+09	J_{yy}	2.005E+04
		J_{zz}	5.313E+09	J_{zz}	1.586E+04
Products of Inertia	[kgm²]	J_{xy}	3.424E+08	J_{xy}	-2.848E+03
		J_{xz}	5.120E+07	J_{xz}	-2.907E+03
		J_{yz}	2.149E+08	J_{yz}	6.786E+03
Face areas	[m²]	JP1	293.85	JP1	4.26
		JP2	48.38	JP2	8.93
		JP3	716.70	JP3	6.43
		JP4	254.03	JP4	1.78
		JP5	432.86	FF1	4.45
		JP6	17.61	FF2	0.83
		FF1	979.13	FF3	2.67
		FF2	662.26	FF4	0.57
				FF5	1.36



4.7 Summary

This chapter introduced the description of rock blocks as arbitrary simple polyhedra. Required data are the position and orientation of the planes, the halfspaces forming part of the blocks, and a list connecting planes and vertices (connectivity). The method of directed polyhedra and its related sub-elements is useful in finding the internal and external relationships of the block. The general formulation of the finiteness theorem of block theory was algorithmically applied for proving the finiteness of blocks with an arbitrary polyhedral shape. An algorithm for the identification of finite blocks in trace maps was presented. Finally, formulas for calculation of the geometric and inertia properties of tetrahedra and arbitrary polyhedra were presented. The methods of this chapter allow both, direct access to the block elements (faces, edges, vertices), and to the related properties. This is frequently required for the subsequent analysis of kinematics and block dynamics.

5 Kinematics and kinematic analysis of blocks

Kinematics basically deals with the position and orientation of systems in space and their variation with time. It does not consider the loadings on a system which cause changes in the position and orientation. Kinematics is also called the geometry of spatial relationships and movements (Magnus & Müller 1990). Bodies can only move if they have a kinematical freedom. In other words, a block can fail if and only if it is kinematically free. For studying the kinematics of rock blocks the principles of rigid body dynamics are applied.

Several authors already addressed the importance of the kinematic analysis within the stability assessment of blocks. Early works are related to John (1968) and Markland (1972) who discussed the kinematics of slopes with daylighting joint intersections and planes (daylighting envelope). Londe et al. (1969, 1970) discussed possible failure modes of a tetrahedral block including rotation and proposed graphical analysis methods. Rotation of blocks was also addressed in Wittke's (1965) pioneering work (cited in Wittke 1984). Rotation of blocks is also related to the forward rotation ("Toppling") and backward rotation ("Slumping"). Goodman & Bray (1977) described the former and Kieffer (1998) the latter. The textbook of Goodman & Shi (1985) about block theory represents a milestone in rock mechanics by providing a general solution of the analysis of translations of block with arbitrary polyhedral shapes including the theorems on finiteness and removability, and clearly distinguishing between kinematics, failure modes and stability analysis. At almost the same time Warburton (1981) proposed a method for vector stability analysis of polyhedral blocks. Compared to Goodman & Shi's method Warburton does not explicitly analyse block kinematics but implicitly takes it into account. First attempts to extend block theory were done by Mauldon & Goodman (1990, 1991, 1996) by introducing rotational kinematics for three-joint pyramids and tetrahedral blocks. Mauldon (1992) addressed also the kinematics of four-joint pyramids. Tonon (1998) outlined the relationships of motion of a rigid body in the context with rock blocks. Daehnke et al. (2000) used a two-dimensional approach for analysing rotational kinematics of keyblocks in the roof of underground mines.

All the approaches presented are subject to assumptions limiting the applicability to engineering problems – assumptions of which practicing engineers are often not entirely aware. The kinematic test of daylighting joints or intersections inherently assumes a finite block which only can be proved by the finiteness theorem. Daylighting of an intersection or plane is not a sufficient condition for removability (Only the theorem of removability is a sufficient condition!). Goodman & Shi's and Warburton's methods are limited to translational block motion only. The developments of block rotations are so far addressing tetrahedral blocks only. They also address only pure rotational modes and neglect the general motion of a rigid body. On the other hand, they allow for a quick

analysis whether a joint pyramid related to a block is non-rotatable or may be rotatable for pure rotational modes. The method outlined in Daehnke et al. (2000) does not account for the three-dimensional properties of rotation and thus is limited to the rotation of prismatic blocks about an edge. It shows, however, the dependence of rotational displacements on the true shape of the block.

Goodman (1995) gives an overview on block theory including rotational modes. Figure 57 shows several types of block motion which can be related to failure modes. Type (a), (b) and (c) are the translational modes lifting, single face sliding and double face sliding, respectively. They are covered by block theory. Types (d) and (e) are pure rotational modes about a block edge or corner, respectively. These modes are covered by Mauldon & Goodman's theory on rotations but limited to tetrahedral blocks. Type (f) is a pure rotation with simultaneous sliding on one plane referred to as torsional sliding. Type (g) is a block rotation about a remote axis with simultaneous sliding on two faces usually referred to as slumping.

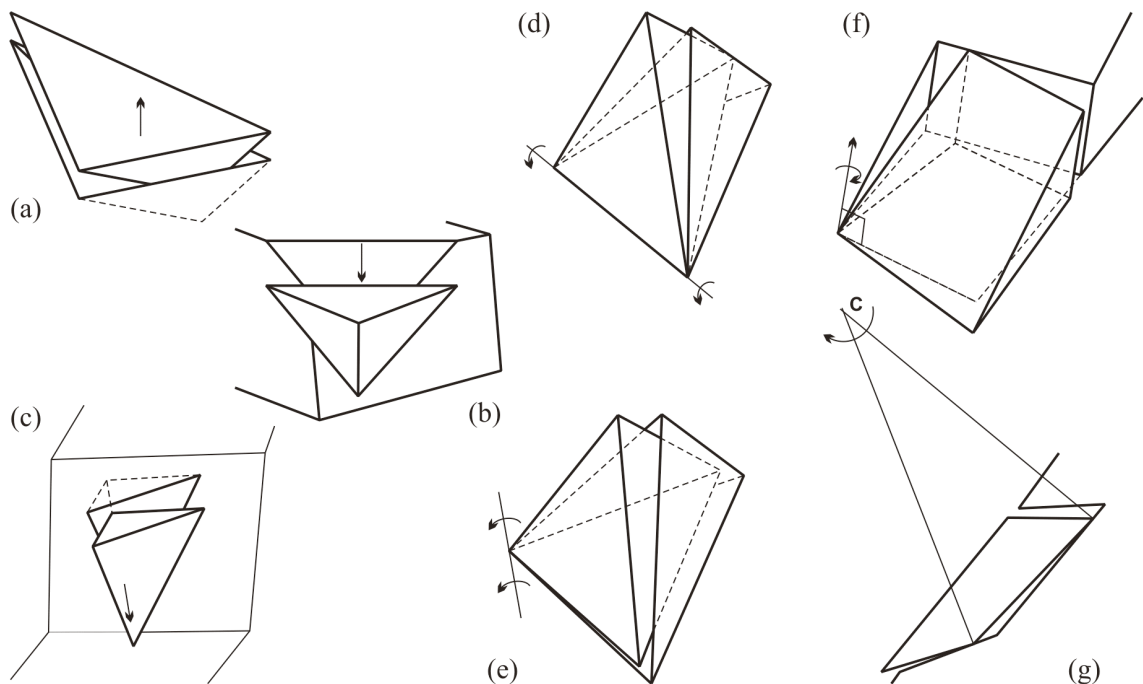


Figure 57: Types of block motion related to failure modes: (a) Lifting; (b) Single face sliding; (c) Double face sliding; (d) Rotation about an edge; (e) Rotation about a corner; (f) Rotational sliding on a plane – Torsional slide; (f) Slumping. Redrawn after Goodman & Shi (1985) and Goodman (1995).

This chapter presents a general solution for the kinematic analysis of single rock blocks with arbitrary polyhedral shapes considering any type of block motion. It is not limited to special failure modes. As far as the analytical solutions allowed, it follows the terms and methods used in block theory (Goodman & Shi 1985), and in the works of Mauldon & Goodman (1990, 1991, 1996) and Mauldon (1992). The assumptions involved for this analysis are that

- the block is a rigid body,
- the block is finite, and
- it has a polyhedral shape (no curved surfaces).

The first section of this chapter discusses the basics of rigid body kinematics in order to develop the analysis method, to provide physical reasoning and valid simplifications. It describes the position and displacements of a rigid body from a pure geometric standpoint and shows that the formulation of rigid body motion involves systems of nonlinear equations. It introduces the concept of the corner joint pyramid for defining feasible block displacements. The first section finally leads to the kinematic description of constraint block motion distinguishing 16 kinematic modes.

The second section discusses translational analysis of blocks based on the ideas of Goodman & Shi's block theory repeating the theorem of removability and showing the basic graphical and vector methods. The aim of the second section is not to introduce a new method but to outline the analysis steps of an established method and apply these steps in the subsequent section. The third section is dedicated to the analysis of block rotations including corner and edge rotation, and remote axis rotation as well. While for the former two modes an analytical solution is available, for the latter only numerical methods can be applied. Finally, the chapter concludes with illustrative examples showing the application of the presented methods for a convex and a non-convex block. A last example outlines the methods for a block in a tunnel crown and discusses several aspects of the methods.

5.1 Basics of kinematics of rigid bodies

5.1.1 The position and orientation of a rigid body

Let us consider a Cartesian coordinate system O_1 fixed in space and another Cartesian coordinate system O_2 fixed to the block. The coordinate systems are formed by the unit vectors $\mathbf{e}_{1,1}$, $\mathbf{e}_{2,1}$, $\mathbf{e}_{3,1}$ and $\mathbf{e}_{1,2}$, $\mathbf{e}_{2,2}$, $\mathbf{e}_{3,2}$, respectively. In the initial position O_2 coincides with O_1 . The block moves from its initial position to an arbitrary position as shown in Figure 58.

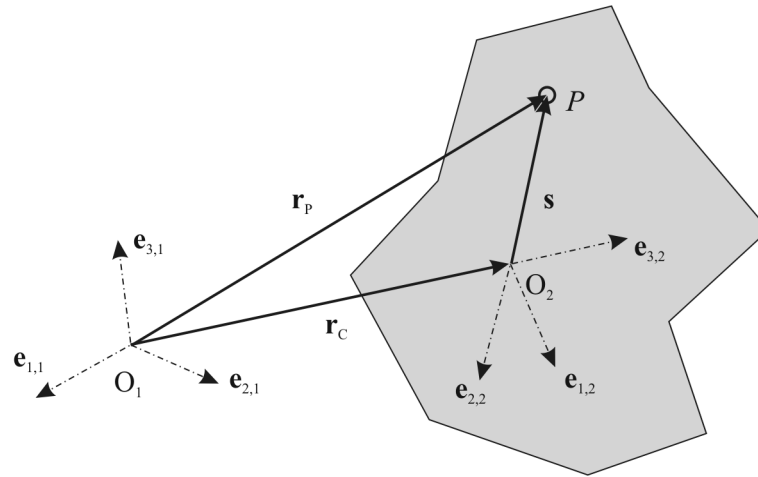


Figure 58: Position of a point P of a rigid body in a coordinate system O_1 fixed in space

The current position of point P can be calculated by expression (55).

$$\mathbf{r}_P^{(1)} = \mathbf{r}_C^{(1)} + \mathbf{A}^{(12)} \cdot \mathbf{s}^{(2)} \quad (55)$$

The right hand side of expression (55) comprises a translational and a rotational component. The translational component \mathbf{r}_c describes the displacement of the origin of O_2 expressed in the coordinate system O_1 . This vector has three components whose coordinates are independent representing three degrees of freedom. The vector \mathbf{s} points to the position of a point P relative to the origin of O_2 while $\mathbf{A}^{(12)}$ describes the relative orientation between O_1 and O_2 . \mathbf{s} and $\mathbf{A}^{(12)}$ together form the rotational component. \mathbf{r}_c and $\mathbf{A}^{(12)}$ vary with time while \mathbf{s} is constant assuming a rigid body.

$\mathbf{A}^{(12)}$ is a 3×3 rotation matrix which maps every vector expressed in O_2 into O_1 by a linear transformation provided that both coordinate systems have the same origin. It is an orthogonal matrix with all elements smaller than one; thus its transpose is equal to its inverse. Since rotation has also three degrees of freedom, three elements of $\mathbf{A}^{(12)}$ can be independently chosen.

According to Euler's rotation theorem two three-dimensional coordinate systems with the same origin are related to a finite rotation about an axis through the origin. The rotation matrix for a finite rotation about an axis \mathbf{u} by an angle ε is calculated using expression (56). One may be interested in the derivation which can be found in Goldstein et al. (2006).

$$\begin{aligned}\mathbf{A}^{(12)} &= \mathbf{I} + (1 - \cos \varepsilon) \cdot \mathbf{u}^* \cdot \mathbf{u}^* + \sin \varepsilon \cdot \mathbf{u}^* \\ \mathbf{A}^{(12)} &= \mathbf{I} + 2 \cdot \sin^2 \frac{\varepsilon}{2} \cdot \mathbf{u}^* \cdot \mathbf{u}^* + \sin \varepsilon \cdot \mathbf{u}^*\end{aligned}\quad (56)$$

The rotation axis \mathbf{u} is a unit vector characterised by the eigenvector of the rotation matrix $\mathbf{A}^{(12)}$ with the corresponding unit eigenvalue. If we know the orientation of the rotation axis and the rotation angle, we can determine the rotation matrix using the Euler parameters (not to be confused with the Euler angles) using expression (57). The derivations of Euler parameters for rotations can also be found in Goldstein et al. (2006).

$$\begin{aligned}e_0 &= \cos\left(\frac{\varepsilon}{2}\right) \\ (e_1 \ e_2 \ e_3)^T &= \mathbf{u} \cdot \sin\left(\frac{\varepsilon}{2}\right) \\ \mathbf{p} &= (e_0 \ e_1 \ e_2 \ e_3)^T\end{aligned}\quad (57)$$

In consequence, expression (58) shows the formulation of the rotation matrix constructed by the Euler parameters.

$$\mathbf{A}^{(12)} = \begin{pmatrix} 2 \cdot (e_0^2 + e_1^2) - 1 & 2 \cdot (e_1 e_2 - e_0 e_3) & 2 \cdot (e_1 e_3 + e_0 e_2) \\ 2 \cdot (e_1 e_2 + e_0 e_3) & 2 \cdot (e_0^2 + e_2^2) - 1 & 2 \cdot (e_2 e_3 - e_0 e_1) \\ 2 \cdot (e_1 e_3 - e_0 e_2) & 2 \cdot (e_2 e_3 + e_0 e_1) & 2 \cdot (e_0^2 + e_3^2) - 1 \end{pmatrix}\quad (58)$$

Euler parameters arranged in a column matrix is a unit quaternion (Kuipers 1998) satisfying the normalisation condition of expression (59).

$$e_0^2 + e_1^2 + e_2^2 + e_3^2 = 1\quad (59)$$

The formulation of the rotation using Euler parameters has several computational advantages. It reduces numerical inaccuracies, is free of singularities, avoids multiplying several rotation matrices and provides only two real solutions related to right-hand and left-hand rotation, respectively. One should also note that finite rotations cannot be described by a vector.

In the subsequent formulations the transformation from Euler-Newton space to Euler parameter space and vice versa is required. This is performed with the Euler parameter transformation matrices \mathbf{E} and \mathbf{G} .

$$\mathbf{E} = \begin{bmatrix} -e_1 & e_0 & -e_3 & e_2 \\ -e_2 & e_3 & e_0 & -e_1 \\ -e_3 & -e_2 & e_1 & e_0 \end{bmatrix} \quad (60)$$

$$\mathbf{G} = \begin{bmatrix} -e_1 & e_0 & e_3 & -e_2 \\ -e_2 & -e_3 & e_0 & e_1 \\ -e_3 & e_2 & -e_1 & e_0 \end{bmatrix} \quad (61)$$

The following relationships apply:

$$\begin{aligned} \mathbf{A} &= \mathbf{E} \cdot \mathbf{G}^T \\ \mathbf{E} \cdot \mathbf{E}^T &= \mathbf{G} \cdot \mathbf{G}^T = \mathbf{I}_{3 \times 3} \\ \boldsymbol{\omega}^{(2)} &= 2 \cdot \mathbf{G} \cdot \dot{\mathbf{p}} \\ \boldsymbol{\omega}^{(1)} &= 2 \cdot \mathbf{E} \cdot \dot{\mathbf{p}} \end{aligned} \quad (62)$$

5.1.2 Unconstrained motion

Block failure involves the kinematics of block motion. This includes also the description of velocities and accelerations. The determination of reaction forces under general loading conditions outlined in a subsequent chapter also requires a more detailed discussion of the kinematics of unconstrained and constrained rigid body motion. Expression (55) describes the position of a point of a rigid body varying with time. Time dependent terms are \mathbf{r}_c and $\mathbf{A}^{(12)}$. $\mathbf{s}^{(2)}$ remains constant during motion. Expression (63) describes the velocity of a point of a rigid body obtained by derivation of expression (55) with respect to time. After derivation and rearranging one obtains (Roberson & Schwertassek 1988):

$$\dot{\mathbf{r}}_P^{(1)} = \dot{\mathbf{r}}_C^{(1)} + \mathbf{A}^{(12)} \cdot \boldsymbol{\omega}^{*(2)} \cdot \mathbf{s}^{(2)} \quad (63)$$

$\boldsymbol{\omega}$ can be interpreted as a vector and is called the angular velocity. Subsequent derivation of expression (55) with respect to time leads to the acceleration of a point of a rigid body shown in expression (64).

$$\ddot{\mathbf{r}}_P^{(1)} = \ddot{\mathbf{r}}_C^{(1)} + \mathbf{A}^{(12)} \cdot \dot{\boldsymbol{\omega}}^{*(2)} \cdot \mathbf{s}^{(2)} + \mathbf{A}^{(12)} \cdot \boldsymbol{\omega}^{*(2)} \cdot \boldsymbol{\omega}^{*(2)} \cdot \mathbf{s}^{(2)} \quad (64)$$

$\dot{\boldsymbol{\omega}}$ is the angular acceleration which can again be interpreted as a vector. Expression (64) shows that the acceleration of a rigid body point does not only depend on the translational and angular acceleration but also on the angular velocity. Thus, the velocity status of a rigid body influences the rigid body acceleration and in consequence the interaction with forces.

5.1.3 Constrained motion

Constraints govern the motion of a rigid body. Physical constraints are formulated as a combination of basic constraints. Basic constraints are geometric conditions between points or vectors, i.e. the constraints lock the motion between two points or vectors.

5.1.3.1 Basic constraints

Basic constraints are mathematical conditions between points or vectors fixed or connected to a rigid body. They are the basis for formulating physical constraints. The shown expressions are presented in Dietmair (2007).

5.1.3.1.1 Position constraints

Consider two rigid bodies i and j with their body-fixed coordinate systems O_i and O_j with arbitrary orientations as shown in Figure 59. The position vectors \mathbf{r}_i and \mathbf{r}_j define their positions in the space-fixed coordinates system O_1 . Arbitrary points P_i and P_j on the rigid bodies are determined by the body-fixed vectors \mathbf{s}_i and \mathbf{s}_j . Vector \mathbf{d}_{ij} connects two points each of which located on a different body. The vectors \mathbf{a}_i and \mathbf{a}_j are fixed to each body at an arbitrary position and orientation.

\mathbf{d}_1 constraint (dot-1): Two vectors \mathbf{a}_i and \mathbf{a}_j remain perpendicular throughout motion: $\mathbf{a}_i \perp \mathbf{a}_j$

Thus, the vectors comply with a \mathbf{d}_1 constraint if the scalar product remains zero. Expression (65) shows the \mathbf{d}_1 constraint in matrix formulation. It locks one degree of freedom.

$$\Theta^{\mathbf{d}_1}(\mathbf{a}_i, \mathbf{a}_j) = \mathbf{a}_i^{(i)T} \cdot \mathbf{A}^{(ij)} \cdot \mathbf{a}_j^{(j)} = 0 \quad (65)$$

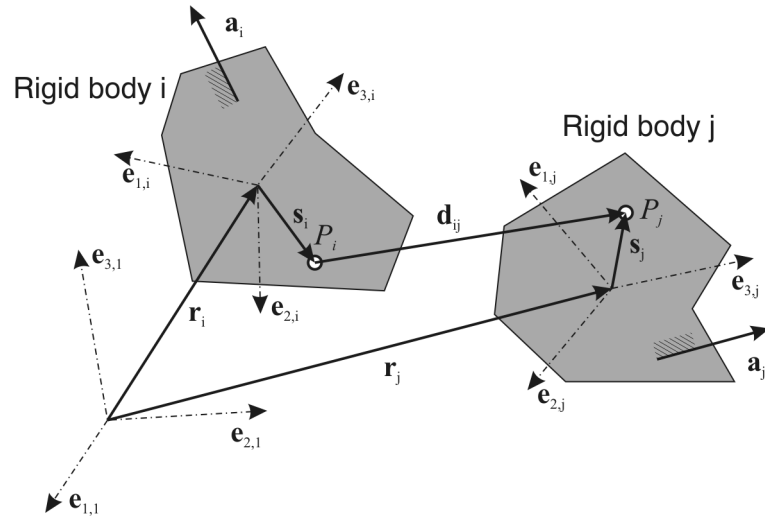


Figure 59: Kinematic conditions between points or vectors of two rigid bodies

d_2 constraint (dot-2): Two vectors, \mathbf{a}_i on body i and \mathbf{d}_{ij} connecting bodies i and j , remain perpendicular throughout the motion: $\mathbf{a}_i \perp \mathbf{d}_{ij}$

The scalar product of the two vectors has to be zero. Since \mathbf{d}_{ij} connects two bodies, expression (66) is a slightly more complex formulation. It also locks one degree of freedom.

$$\begin{aligned} \Theta^{d_2}(\mathbf{a}_i, \mathbf{d}_{ij}) &= \\ &= \mathbf{a}_i^{(i)T} \cdot \mathbf{A}^{(1i)T} \cdot (\mathbf{r}_j^{(1)} + \mathbf{A}^{(1j)} \cdot \mathbf{s}_j^{(j)} - \mathbf{r}_i^{(1)}) - \mathbf{a}_i^{(i)T} \cdot \mathbf{s}_i^{(i)} = 0 \end{aligned} \quad (66)$$

s constraint (spherical): Two points P_i and P_j on two distinct bodies coincide. The sum of the position vectors of both points has to be a zero vector. It locks three degrees of freedom.

$$\Theta^s(P_i, P_j) = \mathbf{r}_j^{(1)} + \mathbf{A}^{(1j)} \cdot \mathbf{s}_j^{(j)} - \mathbf{r}_i^{(1)} - \mathbf{A}^{(1i)} \cdot \mathbf{s}_i^{(i)} = \mathbf{0} \quad (67)$$

5.1.3.1.2 Variation and derivation of the basic constraints

The variations of the basic constraints with respect to the generalised coordinates $[\mathbf{r}_i, \mathbf{p}_i, \mathbf{r}_j, \mathbf{p}_j]^T$ of bodies i and j follow expression (68).

$$\begin{aligned} \delta\Theta^0 = & \Theta_{\mathbf{r}_i^{(i)}} \cdot \delta\mathbf{r}_i^{(1)} + 2 \cdot \Theta_{\pi_i^{(i)}} \cdot \mathbf{G}_i \cdot \delta\mathbf{p}_i + \\ & + \Theta_{\mathbf{r}_j^{(j)}} \cdot \delta\mathbf{r}_j^{(1)} + 2 \cdot \Theta_{\pi_j^{(j)}} \cdot \mathbf{G}_j \cdot \delta\mathbf{p}_j \end{aligned} \quad (68)$$

Table 5 gives the expression for calculating the coefficient matrices $\Theta_{(\)}$ for each factor of expression (55) discriminated for d_1 , d_2 , and s constraint.

Table 5: Coefficient matrices for calculation of the variation of basic constraints

Constraint	$\Theta_{\mathbf{r}_i^{(i)}}$	$\Theta_{\mathbf{r}_j^{(j)}}$	$\Theta_{\pi_i^{(i)}}$	$\Theta_{\pi_j^{(j)}}$
$\Theta^{d1}(\mathbf{a}_i, \mathbf{a}_j)$	$\mathbf{0}$	$\mathbf{0}$	$-\mathbf{a}_j^{(j)T} \cdot \mathbf{A}^{(1)T} \cdot \mathbf{A}^{(1i)} \cdot \mathbf{a}_i^{*(i)}$	$-\mathbf{a}_i^{(i)T} \cdot \mathbf{A}^{(1i)T} \cdot \mathbf{A}^{(1j)} \cdot \mathbf{a}_j^{*(j)}$
$\Theta^{d2}(\mathbf{a}_i, \mathbf{d}_{ij})$	$-\mathbf{a}_i^{(i)T} \cdot \mathbf{A}^{(1i)T}$	$\mathbf{a}_i^{(i)T} \cdot \mathbf{A}^{(1i)T}$	$\mathbf{a}_i^{(i)T} \cdot \mathbf{s}_i^{*(i)} - \mathbf{d}_{ij}^{(1)T} \cdot \mathbf{A}^{(1i)} \cdot \mathbf{a}_i^{*(i)}$	$-\mathbf{a}_i^{(i)T} \cdot \mathbf{A}^{(1i)T} \cdot \mathbf{A}^{(1j)} \cdot \mathbf{s}_j^{*(j)}$
$\Theta^s(\mathbf{P}_i, \mathbf{P}_j)$	$-\mathbf{I}$	\mathbf{I}	$\mathbf{A}^{(1i)} \cdot \mathbf{s}_i^{*(i)}$	$-\mathbf{A}^{(1j)} \cdot \mathbf{s}_j^{*(j)}$

The first derivation of the kinematic constraints with respect to time in absence of kinematic drivers and non-holonomic constraints has to be a zero vector for each constraint. Expression (69) shows the relationships for nk bodies. Note that this is a system of linear equations.

$$\sum_{i=1}^{nk} \left\{ \Theta_{\mathbf{r}_i} \cdot \dot{\mathbf{r}}_i + \Theta_{\pi_i} \cdot \omega_i \right\} = \mathbf{0} \quad (69)$$

After applying the product rule on expression (69), rearrangement and taking advantage of using only the partial derivations (instead of the total) one obtains expression (70) showing the relationships of the accelerations of basic constraints. Note that this is also a system of linear equations.

$$\sum_{i=1}^{nk} \left\{ \Theta_{\mathbf{r}_i} \cdot \ddot{\mathbf{r}}_i + \Theta_{\pi_i}^{(i)} \cdot \omega_i^{(i)} \right\} = \gamma \quad (70)$$

γ is the velocity dependent coefficient vector influencing the acceleration of a rigid body. Its components are calculated by using the expressions in Table 6 for each basic constraint.

Table 6: Expressions for calculating the acceleration components γ for basic constraints

γ^{d1}	$\mathbf{a}_j^{(j)T} \cdot \left(\mathbf{A}^{(1j)T} \cdot \mathbf{A}^{(1i)} \cdot \omega_i^{*(i)} - \omega_j^{*(j)} \cdot \mathbf{A}^{(1j)T} \cdot \mathbf{A}^{(1i)} \right) \cdot \mathbf{a}_i^{*(i)} \cdot \omega_i^{(i)} +$ $\mathbf{a}_i^{(i)T} \cdot \left(\mathbf{A}^{(1i)T} \cdot \mathbf{A}^{(1j)} \cdot \omega_j^{*(j)} - \omega_i^{*(i)} \cdot \mathbf{A}^{(1i)T} \cdot \mathbf{A}^{(1j)} \right) \cdot \mathbf{a}_j^{*(j)} \cdot \omega_j^{(j)}$
γ^{d2}	$2 \cdot \omega_i^{(i)T} \cdot \mathbf{a}_i^{*(i)} \cdot \mathbf{A}^{(1i)T} \cdot \left(\dot{\mathbf{r}}_i^{(1)} - \dot{\mathbf{r}}_j^{(1)} \right) +$ $2 \cdot \mathbf{s}_j^{(j)T} \cdot \omega_j^{*(j)} \cdot \mathbf{A}^{(1j)T} \cdot \mathbf{A}^{(1i)} \cdot \omega_i^{*(i)} \cdot \mathbf{a}_i^{(i)} - \mathbf{s}_i^{(i)T} \cdot \omega_i^{*(i)} \cdot \omega_i^{(i)} \cdot \mathbf{a}_i^{(i)} -$ $\mathbf{s}_j^{(j)T} \cdot \omega_j^{*(j)} \cdot \omega_j^{(j)} \cdot \mathbf{A}^{(1j)T} \cdot \mathbf{A}^{(1i)} \cdot \mathbf{a}_i^{(i)} - \mathbf{d}_{ij}^{(1)T} \cdot \mathbf{A}^{(1i)} \cdot \omega_i^{*(i)} \cdot \omega_i^{(i)} \cdot \mathbf{a}_i^{(i)}$
γ^s	$\mathbf{A}^{(1i)} \cdot \omega_i^{*(i)} \cdot \omega_i^{(i)} \cdot \mathbf{s}_i^{(i)} - \mathbf{A}^{(1j)} \cdot \omega_j^{*(j)} \cdot \omega_j^{(j)} \cdot \mathbf{s}_j^{(j)}$

5.1.3.2 Physical constraints for blocks

Three basic constraints are used for block kinematics each of which is known as the Θ^{d1} , Θ^{d2} and the Θ^s constraint in rigid body dynamics. Θ^{d1} preserves a right angle between two unconnected vectors. It is used to keep a defined orientation between two blocks. Θ^{d2} preserves a right angle between a vector on one block and a connecting vector between two blocks. It is used to keep a block in contact with a defined plane. Θ^s locks the divergence between two points on two blocks – they remain coinciding. It is used to define a rotation point.

Depending on the degrees of freedom of constraint blocks one or several of the basic constraints are combined to meet the characteristic displacement behaviour. In total 16 kinematic modes describe the different physical constraints of blocks. Table 7 shows an overview of these modes including a brief description, the degrees of freedom, and the applied basic constraints to describe the modes. With increasing mode number, the number of degrees of freedom decreases. Figure 60 shows the typical displacements of each kinematic mode. It also shows the vectors involved with the formulation of the basic and physical constraints.

Table 7: Overview of constrained motion of single polyhedral blocks described by basic constraints

Number	Mode	Degrees of freedom	Constraints
1	Unconstrained motion	6	no constraints
2	Rotation about a corner which slides on a plane	5	$\Theta^{d2}(\mathbf{n}_i, \mathbf{d}_{ij})$
3	Rotation of an edge about an edge and sliding in contact point	5	$\Theta^{d2}(\mathbf{n}_{ij}, \mathbf{d}_{ij})$ $\mathbf{n}_{ij} = \mathbf{k}_j^{*(j)} \cdot \mathbf{A}^{(ij)T} \cdot \mathbf{k}_i^{(i)}$
4	Rotation about a corner sliding along a line	4	$\Theta^{d2}(\mathbf{n}_{i1}, \mathbf{d}_{ij})$ $\Theta^{d2}(\mathbf{n}_{i2}, \mathbf{d}_{ij})$
5	Rotational slide of an edge with rotation about the edge	4	$\Theta^{d1}(\mathbf{n}_i, \mathbf{f}_j)$ $\Theta^{d2}(\mathbf{n}_i, \mathbf{d}_{ij})$
6	Rotational slide of a plane about an edge	4	$\Theta^{d1}(\mathbf{f}_i, \mathbf{f}_j)$ $\Theta^{d2}(\mathbf{f}_j, \mathbf{d}_{ij})$
7	Rotation of an edge about a corner and sliding in contact point	4	$\Theta^{d2}(\mathbf{n}_{ij1}, \mathbf{d}_{ij})$ $\Theta^{d2}(\mathbf{n}_{ij2}, \mathbf{d}_{ij})$ $\mathbf{n}_{ij1} = \mathbf{k}_j^{*(j)} \cdot \mathbf{A}^{(ij)T} \cdot \mathbf{k}_{i1}^{(i)}$ $\mathbf{n}_{ij2} = \mathbf{k}_j^{*(j)} \cdot \mathbf{A}^{(ij)T} \cdot \mathbf{k}_{i2}^{(i)}$
8	Pure rotation about a static corner	3	$\Theta^s(\mathbf{r}_i, \mathbf{r}_j, \mathbf{s}_j)$
9	Rotational slide of a plane	3	$\Theta^{d1}(\mathbf{f}_i, \mathbf{f}_j)$ $\Theta^{d1}(\mathbf{g}_i, \mathbf{f}_j)$ $\Theta^{d2}(\mathbf{n}_i, \mathbf{d}_{ij})$
10	Rotational slide of an edge with translation of rotation point and rotation about the edge	3	$\Theta^{d1}(\mathbf{n}_{i1}, \mathbf{f}_j)$ $\Theta^{d2}(\mathbf{n}_{i1}, \mathbf{d}_{ij1})$ $\Theta^{d2}(\mathbf{n}_{i2}, \mathbf{d}_{ij2})$

Number	Mode	Degrees of freedom	Constraints
11	Sliding rotation of a plane while rotation point slides along line	2	$\Theta^{d1}(\mathbf{n}_{i1}, \mathbf{f}_j)$ $\Theta^{d1}(\mathbf{n}_{i1}, \mathbf{g}_j)$ $\Theta^{d2}(\mathbf{n}_{i1}, \mathbf{d}_{ij1})$ $\Theta^{d2}(\mathbf{n}_{i2}, \mathbf{d}_{ij2})$
12	Rotational slide of an edge with static rotation point	2	$\Theta^s(\mathbf{r}_i, \mathbf{r}_j, \mathbf{s}_j)$ $\Theta^{d1}(\mathbf{n}_{i1}, \mathbf{f}_j)$
13	Sliding of an edge along a line with rotation about the edge	2	$\Theta^{d1}(\mathbf{n}_{i1}, \mathbf{f}_j)$ $\Theta^{d1}(\mathbf{n}_{i2}, \mathbf{f}_j)$ $\Theta^{d2}(\mathbf{n}_{i1}, \mathbf{d}_{ij1})$ $\Theta^{d2}(\mathbf{n}_{i2}, \mathbf{d}_{ij2})$
14	Double plane sliding	1	$\Theta^{d1}(\mathbf{n}_{i1}, \mathbf{f}_j)$ $\Theta^{d1}(\mathbf{n}_{i1}, \mathbf{g}_j)$ $\Theta^{d1}(\mathbf{n}_{i2}, \mathbf{f}_j)$ $\Theta^{d2}(\mathbf{n}_{i1}, \mathbf{d}_{ij1})$ $\Theta^{d2}(\mathbf{n}_{i2}, \mathbf{d}_{ij2})$
15	Edge rotation	1	$\Theta^s(\mathbf{r}_i, \mathbf{r}_j, \mathbf{s}_j)$ $\Theta^{d1}(\mathbf{n}_{i1}, \mathbf{f}_j)$ $\Theta^{d1}(\mathbf{n}_{i2}, \mathbf{f}_j)$
16	Sliding rotation on a plane about a static corner	1	$\Theta^s(\mathbf{r}_i, \mathbf{r}_j, \mathbf{s}_j)$ $\Theta^{d1}(\mathbf{f}_i, \mathbf{f}_j)$ $\Theta^{d1}(\mathbf{g}_i, \mathbf{f}_j)$

After a thorough inspection of the manifold modes one will identify already known modes while others may be not well known. The author agrees that some of these modes have no relevance in a static analysis, especially in an undisturbed rock mass (before any block displacement has taken place). Considering a disturbed state of the rock mass, all of these modes could be potential starting points for a static analysis. The mechanical system of the analysed mode may yield an unstable equilibrium. This may be obvious *a priori* or identified by using the methods introduced in chapter 6. In Figure 60 modes 1 - 5, 7, 10, 12, and 13 can be related to an unstable equilibrium situation. From a kinematic and dynamic perspective, however, the presented modes are equivalent.

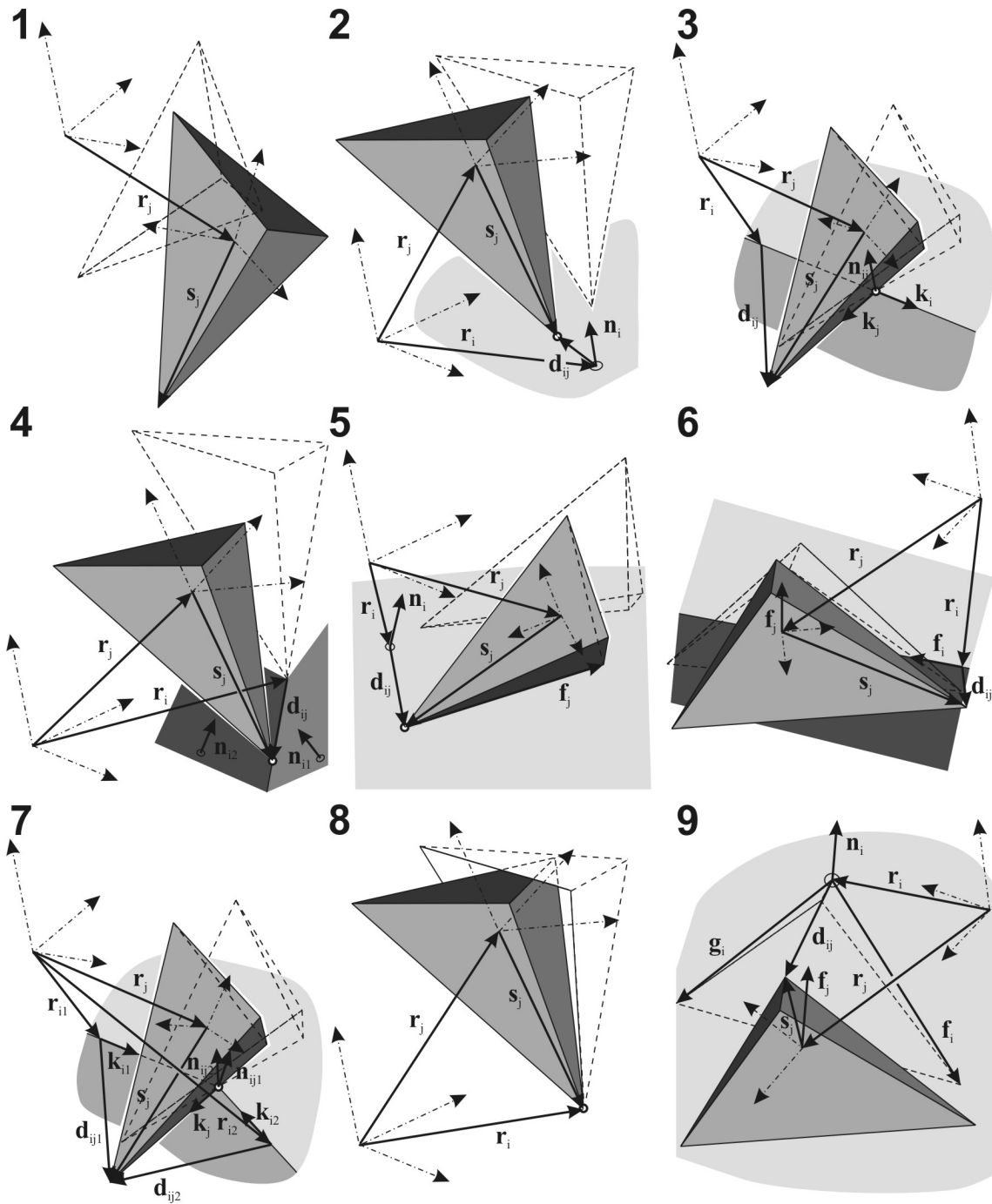


Figure 60: Constrained motion of single polyhedral blocks based on basic constraints between points or vectors

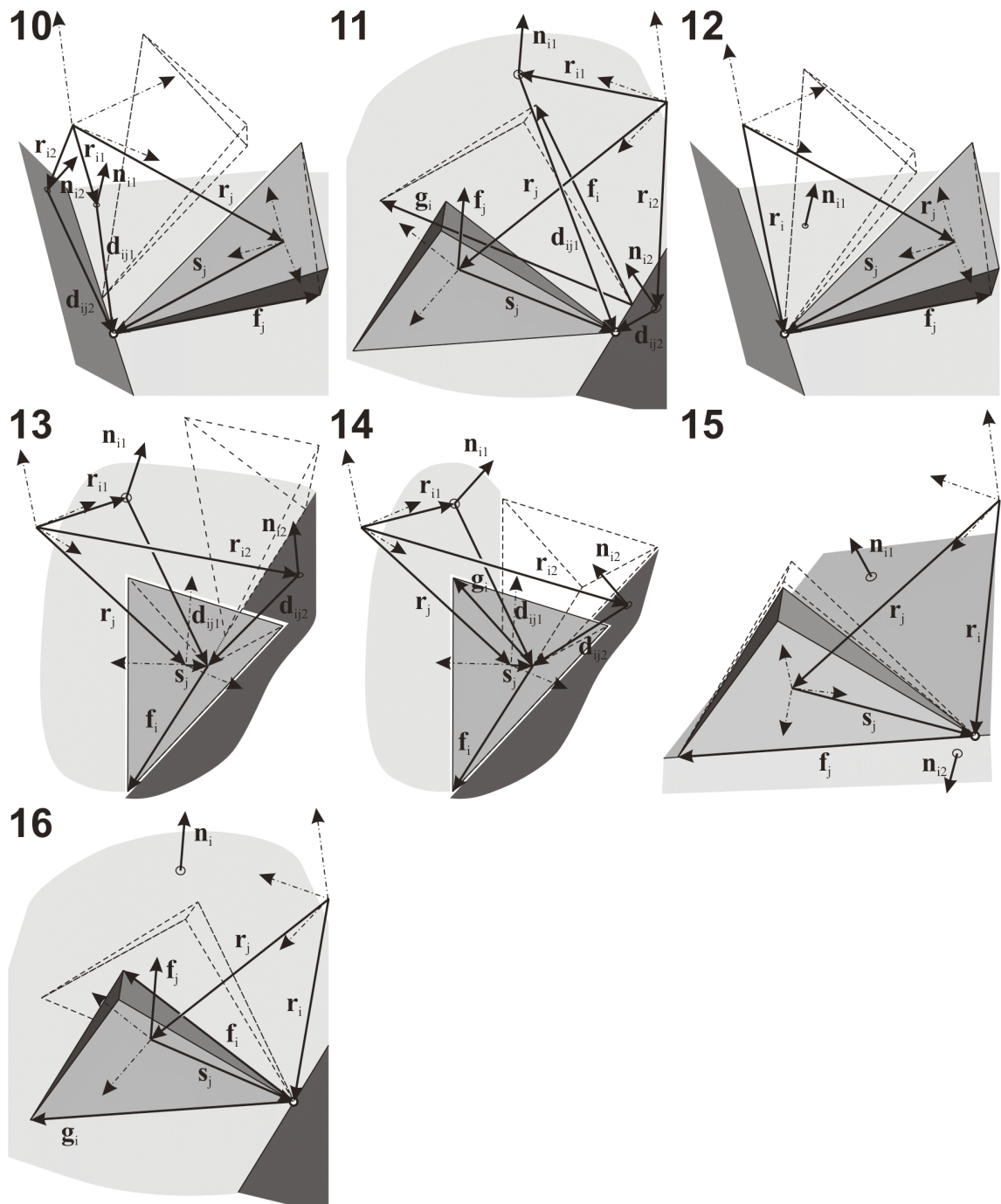


Figure 60: Constrained motion of single polyhedral blocks based on basic constraints between points or vectors (continued)

The kinematic modes can be compared to those shown in Figure 57. Mode 1 is equal to the lifting mode. Mode 8 is equal to the corner rotation. Mode 9 can be related to the torsional slide. Mode 14 corresponds to double face sliding. Mode 15 corresponds to the edge rotation. The combination of the according constraints of the modes 2, 4, 5, 10 and 11 at two different corners or edges of a block allows defining slumping modes. One will also note that the single face sliding in translation cannot be related to a kinematic mode. Single face sliding of blocks is frequently observed in a rock mass. Nevertheless, it requires apart of the kinematic constraints (mode 9 – two translational and one rotational degree of freedom) an additional dynamic criterion on the acting forces. They must not generate a moment acting parallel to the sliding plane's normal vector. Otherwise, a torsional sliding motion of the block will take place.

The presented physical constraints are also rigid and lock motion independent of the magnitude and orientation of the reaction force. Blocks are not able to transfer tensile forces into the rock mass and they start sliding once the frictional resistance of a constraint has been exceeded. In these cases the constraints have to adjust according to the currently acting forces. This can only be performed, if we have control over the reaction forces. This is in agreement with the block theory approach in which the active (Goodman & Shi 1985) and reactive (Tonon 1998) forces come into play in the mode analysis.

Reaction forces depend on the kinematic constraints and on Newton's and Euler's equations of motion. The determination of reaction forces is introduced in the subsequent chapter together with the description of the equations of motion. For adding new constraints at new contacts contact detection algorithms are necessary. This is, however, out of scope of this work.

Summarising from a *purely geometric standpoint* the kinematic modes cannot be determined. As shown by other authors, it is indeed possible to analyse the kinematic movability of blocks from a *geometric standpoint* according to the feasibility of displacements in the incipient motion of a block. The next sections define kinematically feasible displacements, review the method for analysing the translational movability, and introduce a method for analysing the rotational movability of blocks.

5.1.4 The general displacement of a rigid body

The general displacement of a point on a rigid body \mathbf{v}_P is the vector between two positions of the point at two different times (Tonon 2007b).

$$\begin{aligned}\mathbf{v}_P^{(1)} &= \mathbf{r}_{C,t2}^{(1)} + \mathbf{A}_{t2}^{(12)} \cdot \mathbf{s}^{(2)} - \mathbf{r}_{C,t1}^{(1)} - \mathbf{A}_{t1}^{(12)} \cdot \mathbf{s}^{(2)} \\ \mathbf{v}_P^{(1)} &= \mathbf{v}_C^{(1)} + \left(\mathbf{A}_{t2}^{(12)} - \mathbf{A}_{t1}^{(12)} \right) \cdot \mathbf{s}^{(2)} \\ \mathbf{v}_P^{(1)} &= \mathbf{v}_C^{(1)} + \left(\mathbf{A}_{rot} - \mathbf{I} \right) \cdot \mathbf{A}_{t1}^{(12)} \cdot \mathbf{s}^{(2)}\end{aligned}\quad (71)$$

\mathbf{A}_{rot} is the rotation matrix considering the rotational displacement of the block, while \mathbf{A}_{t1} is the rotation matrix transforming the vectors in the body fixed coordinate system (2) to the space fixed coordinate systems (1) at the beginning of displacement. \mathbf{v}_C is the displacement vector of the block's centre of gravity.

The variation of the point displacement can be obtained by forming the derivative of expression (71) as shown in expression (72).

$$\begin{aligned}\dot{\mathbf{v}}_P^{(1)} &= \dot{\mathbf{v}}_C^{(1)} + \dot{\mathbf{A}}_{rot} \cdot \mathbf{A}_{t1}^{(12)} \cdot \mathbf{s}^{(2)} = \dot{\mathbf{v}}_C^{(1)} + \boldsymbol{\omega}^{*(1)} \cdot \mathbf{A}_{rot} \cdot \mathbf{A}_{t1}^{(12)} \cdot \mathbf{s}^{(2)} \\ \dot{\mathbf{v}}_P^{(1)} &= \dot{\mathbf{v}}_C^{(1)} + \left(2 \cdot \mathbf{E} \cdot \dot{\mathbf{p}} \right)^* \cdot \mathbf{A}_{rot} \cdot \mathbf{A}_{t1}^{(12)} \cdot \mathbf{s}^{(2)} \\ \dot{\mathbf{v}}_P^{(1)} &= \dot{\mathbf{v}}_C^{(1)} - 2 \cdot \left(\mathbf{A}_{rot} \cdot \mathbf{A}_{t1}^{(12)} \cdot \mathbf{s}^{(2)} \right)^* \cdot \mathbf{E} \cdot \dot{\mathbf{p}} \\ \dot{\mathbf{v}}_P^{(1)} &= \mathbf{D}_P \cdot \dot{\mathbf{q}} \quad \text{with} \quad \dot{\mathbf{q}} = \begin{bmatrix} \dot{\mathbf{v}}_C^{(1)T} & \dot{\mathbf{p}}^T \end{bmatrix}^T \\ &\quad \mathbf{D}_P = \begin{bmatrix} \mathbf{I} & -2 \cdot \left(\mathbf{A}_{rot} \cdot \mathbf{A}_{t1}^{(12)} \cdot \mathbf{s}^{(2)} \right)^* \cdot \mathbf{E} \end{bmatrix}\end{aligned}\quad (72)$$

Expression (73) provides the rotation of an arbitrary vector attached to the block's coordinate system.

$$\mathbf{s}_u^{(1)} = \mathbf{A}_{rot} \cdot \mathbf{A}_{t1}^{(12)} \cdot \mathbf{s}^{(2)} \quad (73)$$

The corresponding variation of the vector rotation can be obtained with a similar derivation as shown in expression (72).

$$\begin{aligned}\dot{\mathbf{s}}_u^{(1)} &= \dot{\mathbf{A}}_{rot} \cdot \mathbf{A}_{t1}^{(12)} \cdot \mathbf{s}^{(2)} = -2 \cdot \left(\mathbf{A}_{rot} \cdot \mathbf{A}_{t1}^{(12)} \cdot \mathbf{s}^{(2)} \right)^* \cdot \mathbf{E} \cdot \dot{\mathbf{p}} \\ \dot{\mathbf{s}}_u^{(1)} &= \mathbf{H}_P \cdot \dot{\mathbf{q}} \quad \text{with} \quad \mathbf{H}_P = \begin{bmatrix} \mathbf{0} & -2 \cdot \left(\mathbf{A}_{rot} \cdot \mathbf{A}_{t1}^{(12)} \cdot \mathbf{s}^{(2)} \right)^* \cdot \mathbf{E} \end{bmatrix}\end{aligned}\quad (74)$$

5.1.5 Kinematically feasible displacements

The rock mass surrounding the block constrains its motion and is called the constraint space. Displacements are only kinematically feasible if no interpenetration of the block with the constraint space takes place. If the constraint space allows for kinematically feasible displacements of the block, then the block is movable. Constraints are also rigid. This is only feasible if no rupture of the rock takes place and no soft layers form the constraint space (Soft layers would allow for indentation). The block is in contact with the constraint space. Physically, the contact areas are joints, faults, shears, slickensides, etc., in other words, any zone of weakness in the rock mass. For the later analysis the contact areas are referred to as joints and geometrically approximated by planes. Free (sur)faces are contacts of the block with the free space; they do not constrain motion.

Let us have a glance on an infinitesimal displacement increment in the incipient motion of a block. In this case it is not necessary to deal with large displacements and contact detection. A joint divides the space into two halfspaces, the rockside halfspace and the blockside halfspace. An arbitrary block displacement is kinematically feasible if it plots inside the blockside halfspace of a joint. For a polyhedron it is sufficient to test the kinematic feasibility at its corners only. If the displacements are kinematically feasible at the block corners, then they are feasible at any other point of the block surface as well. This can be proved by extending the derivations shown in Tonon (1998) to arbitrary simple polyhedra.

A block corner is an intersection of three nonparallel planes. Corners inside the rock mass always comprise three joints while corners at the free face can comprise two, one or even no joint. As only joints constrain motion, the analysis has merit only for corners comprising joints. The intersection of the blockside halfspaces of joints at corner C_j is the corner's joint pyramid JPC_j . A displacement at this corner is kinematically feasible if the displacement vector $\Delta\mathbf{x}$ plots inside the corner's joint pyramid. Hence, no interpenetration of the block and rock mass takes place. This criterion holds for both, convex and concave corners. This becomes obvious from the 2D analogy shown in Figure 61 and agrees with Shi's theorem for non-convex blocks (Goodman & Shi 1985).

$\mathbf{n}_{i,c}$ are the blockside normal vectors of the joint planes forming the corner C_j . The displacement vector is kinematically feasible if no component moves towards the rock mass. Let m_j be the number of joints at C_j , then the sufficient condition for kinematic feasibility of infinitesimal displacements at block corners in the incipient motion is

$$\Delta\mathbf{x}^T \cdot \mathbf{n}_{i,c} \geq 0 \text{ with } i = 1, \dots, m_j \quad (75)$$

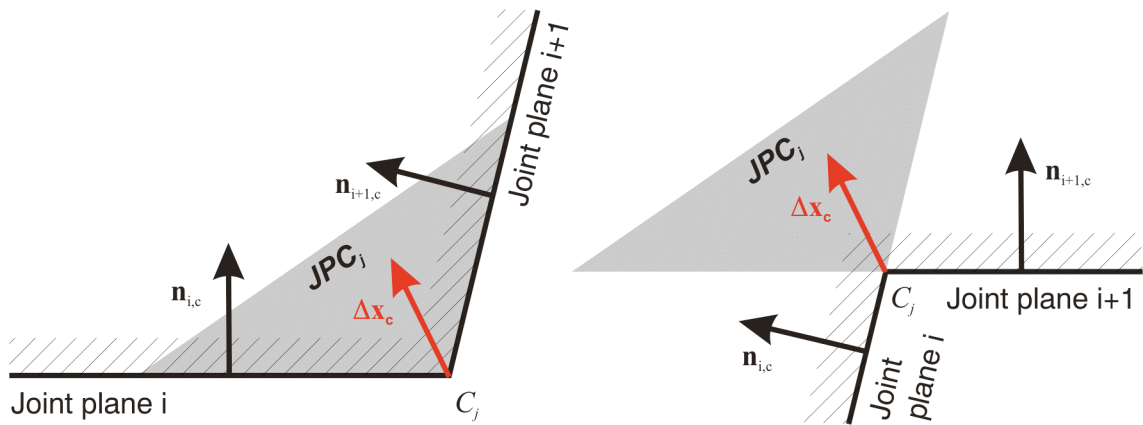


Figure 61: 2D analogy for kinematically feasible displacements $\Delta \mathbf{x}$ at convex (*left*) and concave (*right*) corners C_j plot inside the corner's joint pyramid JPC_j

5.2 Analysis of translations

The analysis of translations of blocks has been a topic since the science of rock mechanics emerged in the early nineteen fifties. The most extensive and relevant work has been done by Goodman & Shi (1985) with the development of block theory. This section outlines the basic concepts of block theory in order to prepare for the subsequent sections dealing with the rotational analysis.

Expression (55) implies that the translational part of a rigid body displacement is a vector pointing from the origin of its initial position to the origin of its displaced position. Hence, it is independent of the absolute position of the block. Note that in Figure 58 the initial position coincides with the coordinate system O_1 . For the analysis of removability we are not interested in the magnitude of the displacements. The only required reference parameter is the orientation of the displacement vector.

Kinematically feasible displacements plot inside the corner's joint pyramid JPC_j which is the intersection of all blockside halfspaces of corner joints. In the case of pure translations this is independent of whether displacements are finite or infinitesimal. Since the orientation of the displacement vector is identical at all corners, we can virtually shift all corners into a common point together with JPC_j . It becomes obvious that all kinematically feasible displacement vector orientations must plot inside the intersection of all corner joint pyramids (Expression (76)). It is the intersection of all blockside halfspaces of joints of the block which originally has been defined as the joint pyramid JP by Goodman & Shi (1985).

$$JP = \bigcap_{j=1}^{m_c} JPC_j \text{ with } m_c \text{ as the number of corners} \quad (76)$$

Removability is the term related to kinematic movability of finite polyhedral blocks. A finite block is removable if and only if its joint pyramid is not empty. The joint pyramid is the space of kinematically feasible displacement vector orientations. If it is empty, no feasible displacement is possible. Removability also requires the compliance with the finiteness criterion. The joint pyramid has to plot entirely into the free space, i.e. it has to be entirely contained in the space pyramid or, in other words, plot entirely outside the excavation pyramid.

Removability is tested either by graphical or vector methods. The block theory textbook outlines the methods in detail. The stereographic projection is a suitable graphical method to analyse and visualise the kinematic conditions of the block. The use of the entire sphere in the stereographic projection eases block theory analyses. The lower focal point projection shows the upper hemisphere inside the reference circle and the lower hemisphere outside the reference circle. For the upper focal point projection it is converse, respectively. Joints and free faces are great circles. The blockside poles indicate the halfspaces of which the block is formed. Block theory distinguishes between the upper and lower halfspace indicated by the 0 and 1, respectively, for each plane. For each plane pyramid, no matter if it was a joint or block pyramid, there is a plane code vector \mathbf{D}_p indicating the upper or lower halfspace of each plane number with its digits. The joint pyramid is bounded by great circles of joints accounting for the appropriate halfspaces. Figure 62 shows an example for a tetrahedron comprising three joints and one free face, with its data given in Table 8.

Table 8: Data for the tetrahedron: Orientations, positions and halfspaces

Planes	Orientation		Point on plane			Halfspace
	Dip direction [°]	Dip angle [°]	X [m]	Y [m]	Z [m]	
Joint plane 1	110	10	8.332	-11.869	0.934	upper
Joint plane 2	70	85	0.755	5.000	16.371	upper
Joint plane 3	180	90	0.755	5.000	16.371	upper
Free face 1	150	40	0.755	5.000	16.371	lower

Stereographic projection - equal angle - upper focal point

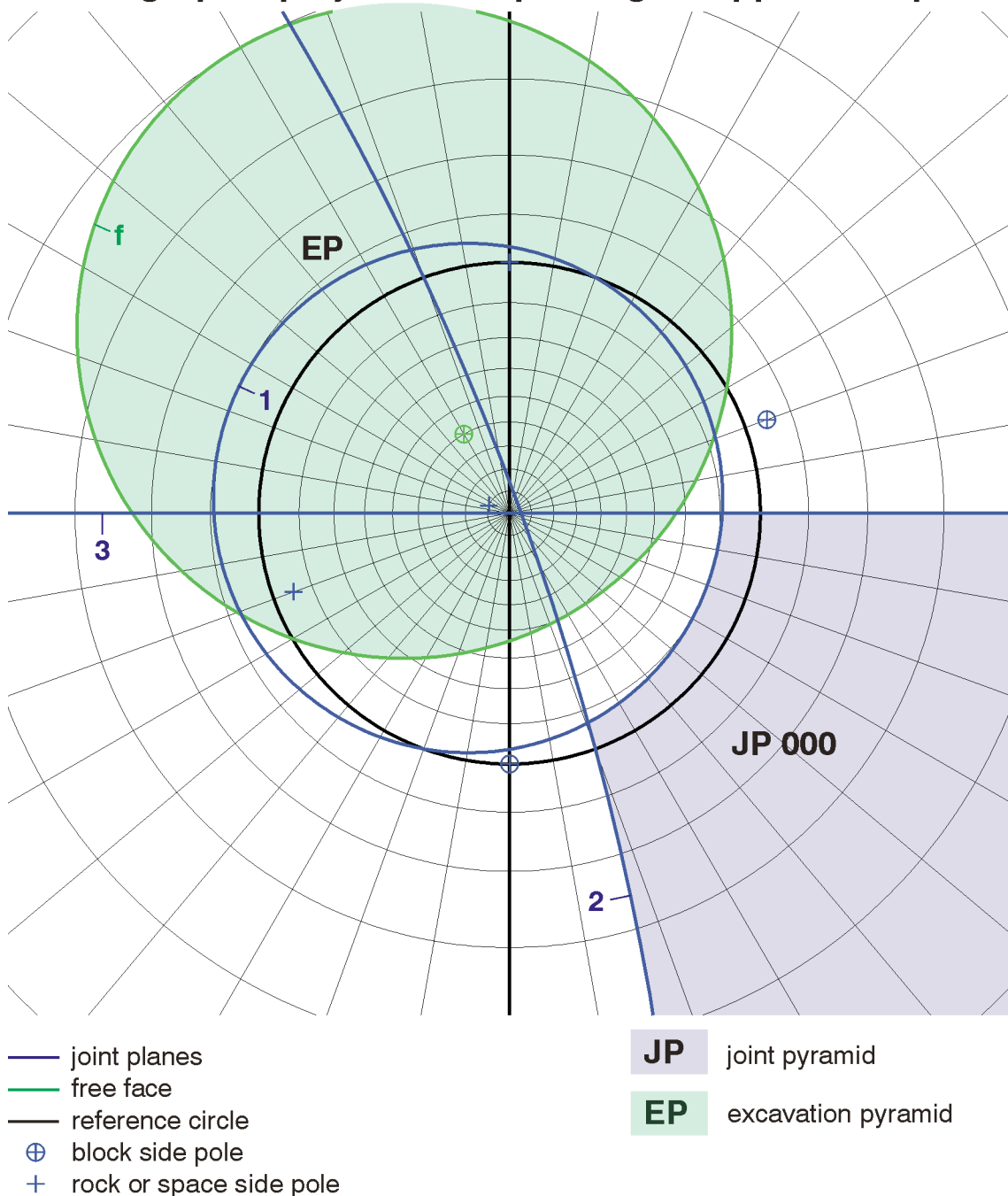


Figure 62: Stereographic projection of joints and free faces of a tetrahedron with three joints and one free face. The joint pyramid is shaded in blue.

The joint pyramid also allows the characterisation of displacements. Displacement vectors plotting inside the joint pyramid cause a lifting motion, i.e. a simultaneous detachment of the block from all joints. Displacements plotting on a great circle characterise a sliding motion on the corresponding joint while those which coincide with an intersection line characterise a sliding motion along an edge of a block.

The computation of the emptiness of a general plane pyramid using vector methods involves the steps outlined by expressions (77) to (80). The steps are modified after Goodman & Shi (1985) for the used matrix formulation. It can be applied for joint pyramids, block pyramids and, as we will see later, for the determination of the rotation space. Let m be the number of planes and p the number of intersections.

- Compute all intersections between the planes

$$\mathbf{I}_{ij} = \mathbf{n}_i^* \cdot \mathbf{n}_j \quad \text{with } i = 1, \dots, m-1 \text{ and } j = i+1, \dots, m \quad (77)$$

- Compute a signed matrix \mathbf{I} with size pxm

$$\mathbf{I}_k^{ij} = \text{sign} \left[\left(\mathbf{n}_i^* \cdot \mathbf{n}_j \right)^T \cdot \mathbf{n}_k \right] \quad (78)$$

with $i = 1, \dots, m-1, j = i+1, \dots, m$ and $k = 1, \dots, m$

- Convert plane code \mathbf{D}_p into a signed joint code \mathbf{D}_s

$$D_s(k) = \begin{cases} +1 & \text{if } D_p(k) = 0 \\ -1 & \text{if } D_p(k) = 1 \end{cases} \quad (79)$$

- Compute a testing matrix \mathbf{T} with size $p \times m$

$$T_k^{ij}(l,k) = I_k^{ij}(l,k) \cdot D_s(k) \quad \text{with } k = 1, \dots, m \text{ and } l = 1, \dots, p \quad (80)$$

If all rows of \mathbf{T} have positive and negative entries, then the plane pyramid corresponding to plane code \mathbf{D}_j is empty. If any row of \mathbf{T} has, apart from zeros, only negative or only positive entries, the plane pyramid corresponding to plane code \mathbf{D}_j is non-empty. The edges of the plane pyramid are the intersections corresponding to the rows of \mathbf{T} which lack positive or lack negative entries. If such a row lacks positive terms, then the edge of the plane pyramid is $-\mathbf{I}_{ij}$. If the row lacks negative terms, then the edge of the plane pyramid is $+\mathbf{I}_{ij}$. For this chapter's example one obtains:

$$\mathbf{D}_s = \begin{pmatrix} 1 & 1 & 1 \end{pmatrix} \quad \mathbf{I}_{ij} = \begin{pmatrix} -0.3407 & 0.9077 & 0.1112 \\ 0.9848 & 0 & -0.1632 \\ 0.0872 & 0 & -0.9361 \end{pmatrix}$$

$$\mathbf{I}_k^{ij} = \begin{pmatrix} 0 & 0 & -1 \\ 0 & 1 & 0 \\ -1 & 0 & 0 \end{pmatrix} \quad \mathbf{T}_k^{ij} = \begin{pmatrix} 0 & 0 & -1 \\ 0 & 1 & 0 \\ -1 & 0 & 0 \end{pmatrix}$$

Since all rows of \mathbf{T} have only positive or negative terms (except zero), the joint pyramid is nonempty with its edges corresponding to each row of \mathbf{I}_{ij} . The real edges are the vector formed by the second row of \mathbf{I}_{ij} and the opposite direction of the vectors in the first and third row of \mathbf{I}_{ij} . This agrees with the joint pyramid in Figure 62.

5.3 Analysis of rotations

Displacements are kinematically feasible if the displacement vectors at all corners plot inside the corresponding corner's joint pyramid. In contrast to translational motion the displacement vector for rotations is different at each corner. Rotational displacements are related to a rotation axis as stated in section 5.1.1. Rotation axes can be fixed or variable during the block motion, i.e. they can change their position and/or orientation (Magnus & Müller 1990). At this stage, however, we do not have any information about the block motion but only information about block geometry. For determining the kinematic movability of a block we are only interested in the *incipient* motion of the block. This involves the following simplifications:

- The rotation axis is fixed in the instant of analysis.
- The block is initially considered to be at rest.
- Displacements are infinitesimal.

These assumptions also hold for virtual displacements. Thus, kinematically feasible displacements are determined at any instant and position. The knowledge of feasible displacements is of limited engineering value once the block has started moving.

Mauldon (1992) described four possible locations of the rotation axis.

- The rotation axis penetrates the block as a minimum at one joint. In this case block rotation is not possible unless the block is formed by only one joint (Wittke 1984). The rotation axis is perpendicular to the joint. This is referred to as *torsional rotation*.
- The rotation axis coincides with a block edge at the transition between joints and free faces. The rotation is referred to as *edge rotation*.
- The rotation axis passes through a block corner at the transition between joints and free faces. This rotation is referred to as *corner rotation*.
- The rotation axis is at a remote location to the block. This rotation is referred to as *remote axis rotation*.

The first case is not uncommon in rock masses but its discussion is routine and therefore omitted here. The second and third case have a rotation axis with its position fixed to the block. For edge rotation we also know its orientation while for corner rotation the orientation of the rotation axis is unknown. The analysis of edge and corner rotation is possible in one step. In the last case we neither know the position nor the orientation of the feasible rotation axes. Remote axis rotation is the most general case of rigid block motion. Only translation and rotation together describe this kind of motion in a coordinate system fixed to the block.

Displacement vectors in rotation are no longer parallel; therefore, in contrast to translations, rotating vectors of motion are not a suitable parameter for characterising a rotation. The rotation axis and its spin unequivocally define the motion. For describing a rotation, it is simpler and more favourable to discuss the orientation of the rotation axis than trying to manage the different orientations and magnitudes of displacement vectors. In the following discussion, right hand rotation is assumed.

5.3.1 Constrained rotational displacement

Every general displacement of a rigid body can be described by a rotation as shown above. Since a finite rotation is not a vector, the stereographic projection and vector methods cannot be applied for now. If we look at the incipient motion however, an infinitesimal small time frame, displacements near the axis (inside the block) are also infinitesimal. Expression (81) shows the variation of the rigid body displacement. $\delta \mathbf{r}_P$ is the virtual rotational displacement of a block point. $\delta \boldsymbol{\pi}$ is the virtual rotation. It is obvious that in this case the virtual rotation *is* a vector which is interpreted as the instantaneous rotation axis (Dietmair 2007). Note that all factors are in the same coordinate system.

$$\delta \mathbf{r}_P^{(1)} = \delta \boldsymbol{\pi}^{*(1)} \cdot \mathbf{s}^{(1)} \quad (81)$$

Since displacements remain infinitesimal and only incipient motion is considered, all relationships can be expressed in one coordinate system. Subsequently, the coordinate indications in the expressions are skipped. Expression (82) defines finally, without loss of generality, the infinitesimal displacement at a corner in the block nomenclature.

$$\Delta \mathbf{x} = \mathbf{u}^* \cdot (-\mathbf{C}_j \mathbf{R}) \quad (82)$$

\mathbf{u} is the vector of the (instantaneous) rotation axis, $\mathbf{C}_j \mathbf{R}$ is a vector pointing from the block corner to an arbitrary point on the rotation axis, $\Delta \mathbf{x}$ is the initial displacement vector of a corner. Figure 63 shows the geometric relationships together with the blockside normal vectors $\mathbf{n}_{i,c}$ of the joints.

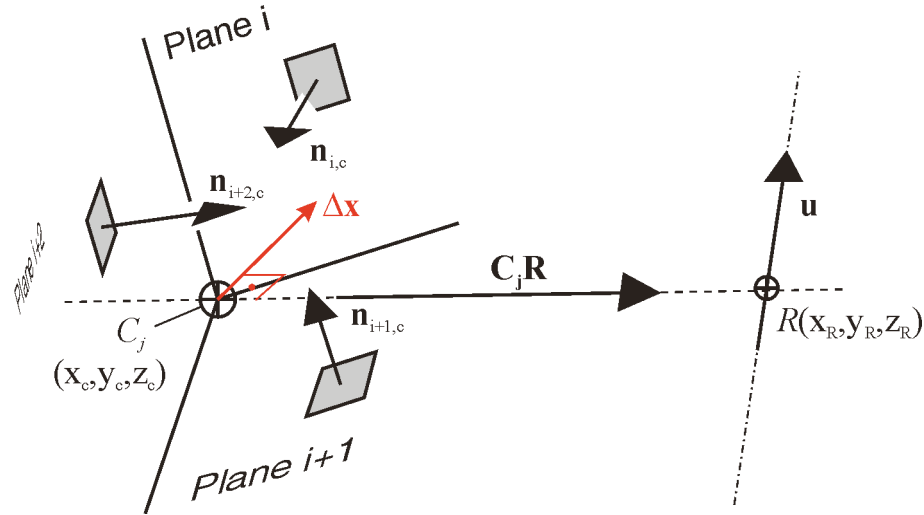


Figure 63: Kinematically feasible displacement $\Delta \mathbf{x}$ at a corner C_j related to the rotation axis \mathbf{u}

Again, one also observes that feasible displacements point in the same direction as the blockside normal vectors, i.e. inside JPC_j . The displacements have to comply with the conditions in expression (83).

$$\Delta \mathbf{x}^T \cdot \mathbf{n}_{i,c} = \left(\mathbf{u}^* \cdot (-\mathbf{C}_j \mathbf{R}) \right)^T \cdot \mathbf{n}_{i,c} \geq 0 \quad (83)$$

with $i = 1, \dots, m_j$ and $j =$ the set of constraint corners

This expression can be mathematically rearranged and leads to the following necessary and sufficient condition on rotatability of blocks for fixed rotation axes:

$$\left(\mathbf{n}_{i,c}^* \cdot \mathbf{C}_j \mathbf{R} \right)^T \cdot \mathbf{u} \geq 0 \quad (84)$$

with $i = 1, \dots, m_j$ and $j =$ the set of constraint corners

\mathbf{C}_j is a vector pointing to a block corner whose intersection planes contain at least one joint. \mathbf{R} is a vector pointing to an arbitrary point on the rotation axis; we assume that it points to the static rotation point on the block. $\mathbf{C}_j \mathbf{R}$ is the vector pointing from a block corner to the static point at the block containing the rotation axis. $\mathbf{n}_{i,c}$ is a blockside normal vector of a joint plane of corner C_j . \mathbf{u} is the vector of the rotation axis. With respect to a particular rotation axis, expression (84) has to comply simultaneously for all constrained corners and their corresponding blockside normal vectors.

5.3.2 Corner and edge rotation

The objective of this analysis is finding the solution space of expression (84) which is the envelope of all possible positions and orientations of rotation axes. The solution space is referred to as the rotation space. For corner and edge rotations we consider only a finite number of discrete points in space. The rotation space is therefore the union of enveloping pyramids at feasible rotation corners. A block is called corner rotatable if the rotation space is non-empty. If there is a possible rotation axis whose vector complies with the rotation spaces of two adjacent corners and the intersection of both corners corresponds to a block edge, then rotation about this edge is possible. In this case the block is called edge rotatable. In consequence, edge rotation is a corner rotation about two corners simultaneously (Mauldon & Goodman 1990).

A closer examination of expression (84) reveals that the matrix product $\mathbf{n}_{i,c}^* \cdot \mathbf{C}_j \mathbf{R}$ is a vector with at least one component pointing in the same direction as the rotation axis. Conversely, the directions of possible vectors complying with expression (84) can be represented by a plane and a corresponding halfspace. This plane is subsequently referred to as the limit plane. As a consequence the rotation space of a corner is the intersection of all halfspaces of limit planes containing feasible rotation axes. For the determination of block rotatability the emptiness of the rotation space in terms of intersections of limit planes has to be computed.

5.3.2.1 Determination of the rotation space using graphical methods

This section discusses the determination of limit planes and rotation space using stereographic projections of planes and edges. In the stereographic projection limit planes are great circles through the blockside pole of a corner's joint plane $\mathbf{n}_{i,c}$ and pole of vector $\mathbf{C}_j \mathbf{R}$ pointing from the block corner to the *static rotation corner*. The static rotation corner is the block vertex where the rotation axis intersects the block. No relative motion takes place at this point. The blockside poles are determined by orientation and halfspace data of joint planes. Blockside poles pointing in the upper halfspace (joint code 0) plot in the upper hemisphere and those pointing in the lower halfspace (joint code 1) plot in the lower hemisphere. For an arbitrary polyhedron the vector $\mathbf{C}_j \mathbf{R}$ depends on the block geometry as shown in expression (85). It cannot be determined in the stereographic projection unless the corner C_j is adjacent to the static rotation point. For a tetrahedron all corners are adjacent to the investigated static rotation corner; thus, the orientations of joints and free faces completely define the tetrahedron's rotatability.

$$C_j \mathbf{R} = \frac{\mathbf{R} - \mathbf{C}_j}{\|\mathbf{R} - \mathbf{C}_j\|} \quad (85)$$

Favourable working with the stereographic projection requires the trend and plunge of $C_j \mathbf{R}$ which can be calculated with expression (86).

$$trend_{C_j \mathbf{R}} = \arctan\left(\frac{C_j R_1}{C_j R_2}\right) + \varepsilon \quad plunge_{C_j \mathbf{R}} = -\arcsin(C_j R_3) \quad (86)$$

$$\varepsilon = 0^\circ \quad \text{for } C_j R_1, C_j R_2 \geq 0$$

$$\varepsilon = 180^\circ \quad \text{for } C_j R_1 \geq 0, C_j R_2 < 0 \quad \text{or } C_j R_1 < 0, C_j R_2 < 0$$

$$\varepsilon = 360^\circ \quad \text{for } C_j R_1 < 0, C_j R_2 \geq 0$$

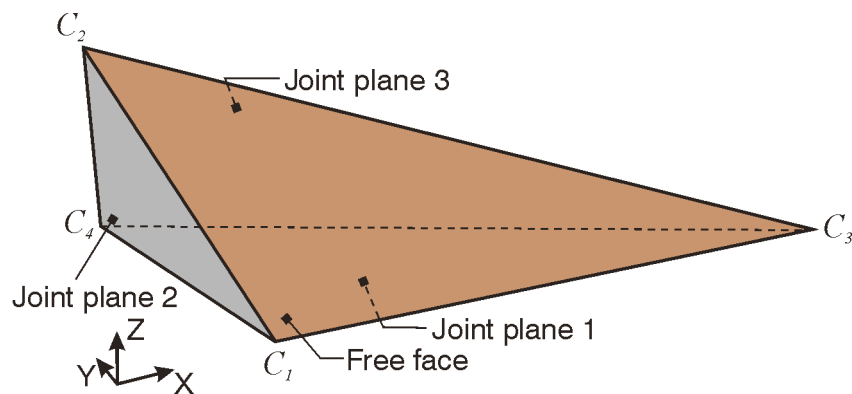


Figure 64: Perspective view of the tetrahedron consisting of three joint planes, one free face and four corners

Table 9: Data on corner coordinates for the tetrahedron

Corners	Coordinates		
	X [m]	Y [m]	Z [m]
C_1	8.332	-11.869	0.934
C_2	0.755	5.000	16.371
C_3	52.612	5.000	-5.386
C_4	2.000	5.000	3.000

The exemplary construction of a rotation space using limit planes for the static rotation point C_1 of tetrahedron in Figure 64 is shown in Figure 65. Table 8 (on page 130) gives the orientations and halfspaces of the block and Table 9 the corner coordinates. Each vertex has joint constraints; vertices on the free face have two joints and the vertex inside the rock mass three. Table 10 gives the data and overview on C_jR including trend and plunge. For this example all C_jR are intersections of block planes which can be observed also in Figure 65, and thus can be graphically determined. For a more complex block these values have to be computed using expression (85). Table 11 shows an overview of required limit planes and the corresponding C_jR and joint constraints $\mathbf{n}_{i,c}$.

Table 10: C_jR vectors for corner C_1

Static rotation point	Constraint corner	C_jR	C_jR vector			Orientation	
			X [m]	Y [m]	Z [m]	Trend [°]	Plunge [°]
C_1	C_2	C_{21}	0.3145	-0.7003	-0.6408	155.8	39.9
	C_3	C_{31}	-0.9263	-0.3529	0.1322	249.1	-7.6
	C_4	C_{41}	0.3491	-0.9301	-0.1139	159.4	6.5

Table 11: Limit planes derived from C_jR and joint constraints for corner C_1

Limit plane	C_jR	$\mathbf{n}_{i,c}$
L_1	C_{21}	$\mathbf{n}_{2,c}$
L_2		$\mathbf{n}_{3,c}$
L_3	C_{31}	$\mathbf{n}_{2,c}$
L_4		$\mathbf{n}_{3,c}$
L_5	C_{41}	$\mathbf{n}_{1,c}$
L_6		$\mathbf{n}_{2,c}$
L_7		$\mathbf{n}_{3,c}$

Great circles through the poles of C_jR and the blockside poles of $\mathbf{n}_{i,c}$ according to Table 11 define the limit planes L_1 to L_7 . The appropriate halfspaces are determined by turning the blockside pole $\mathbf{n}_{i,c}$ by the smaller angle along the limit planes' great circle towards the vector C_jR . According to the right-hand rule, the resulting normal vector $\mathbf{n}_{i,c}^* \cdot C_jR$ indicates the halfspace. An annulus shaded in red and adjacent to the great circles shows the kinematically feasible halfspaces of the limit planes. Data on the limit planes are also given in Table 12.

Stereographic projection - equal angle - upper focal point

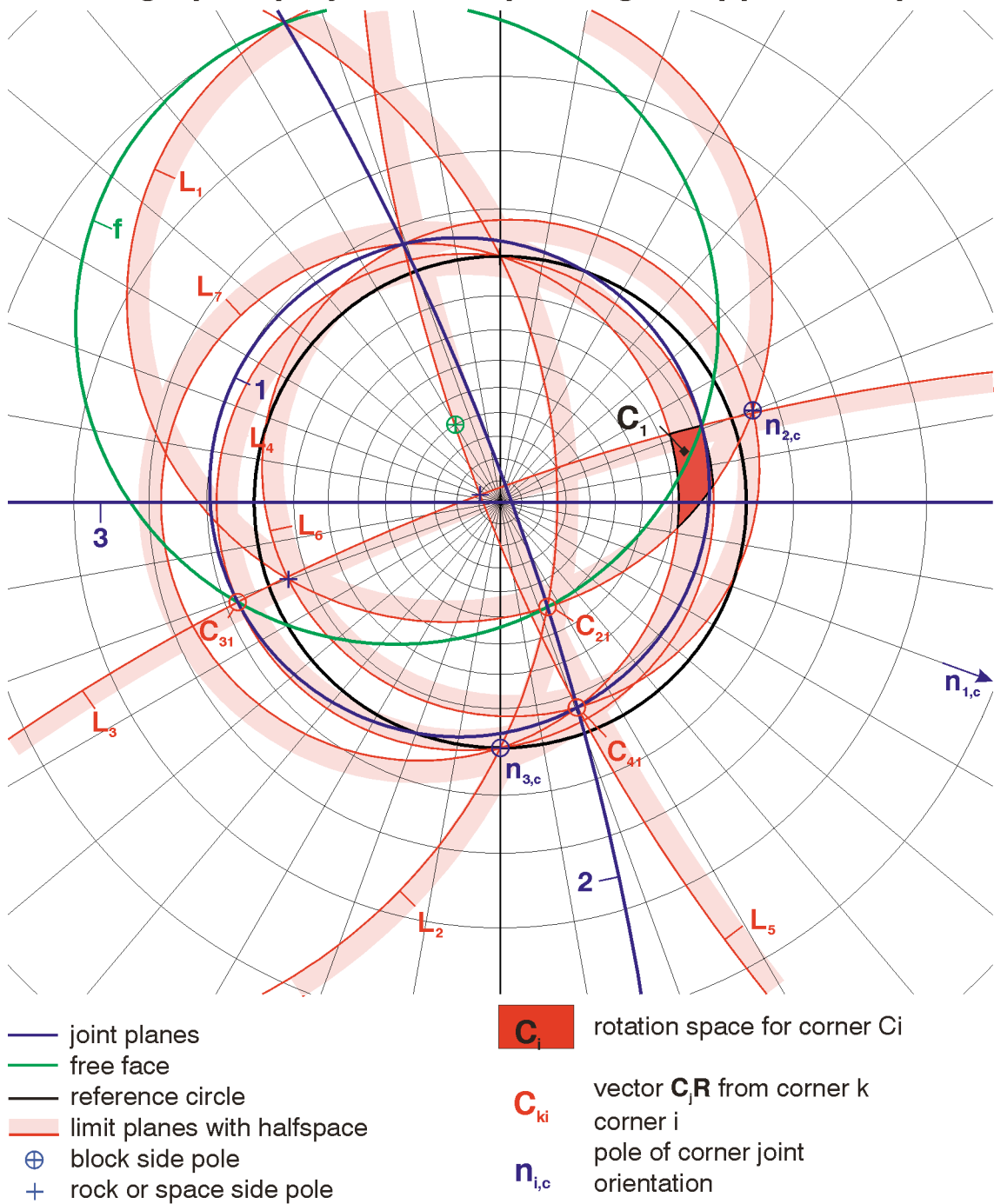


Figure 65: Construction of a rotation space using limit planes

The rotation space is the intersection of the limit plane halfspaces corresponding to each static rotation point. It is the region in which the rotation axis leads to kinematically feasible block displacements. The rotation space for vertex C_1 under the constraint of these limit planes is shown in Figure 65 as a pyramid bold shaded in red. The construction has to be repeated for any other potential rotation point. In this example further suspicious points are C_2 and C_3 .

Figure 66 depicts the rotations space for all corners of the investigated tetrahedron. Together with the joint pyramid it summarises the kinematic condition of the block imposed by the joint planes:

- The block is removable since the joint pyramid plots entirely outside the excavation pyramid
- The block is corner rotatable about the vertices C_1 , C_2 and C_3 since all corresponding rotation space pyramids are non-empty.
- The block is edge rotatable about the edge E_{13} since the rotation spaces for C_1 and C_3 contain this edge.

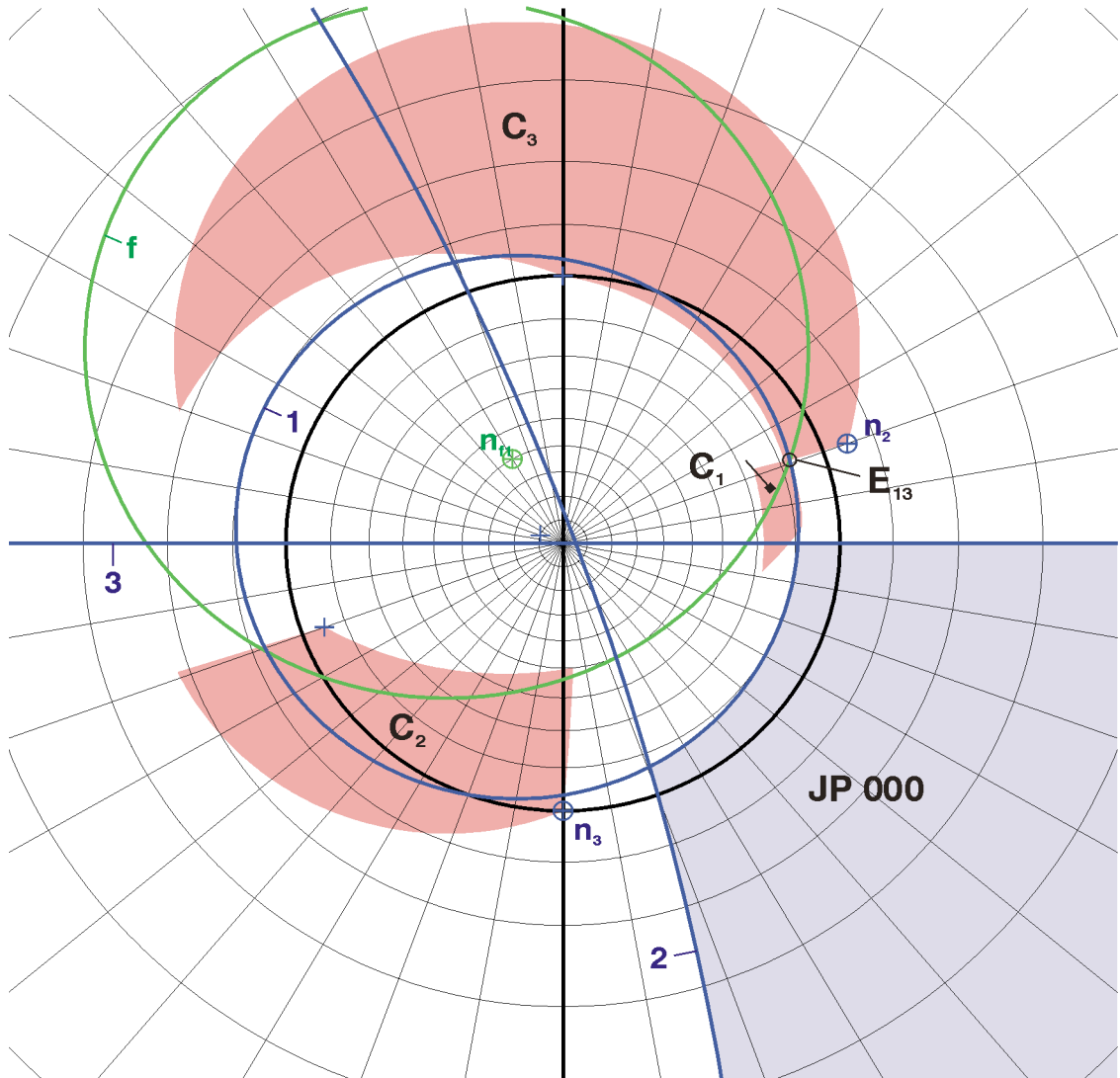
In general, if a rotation axis plots inside the rotation space, the block detaches from all joints simultaneously except at the static rotation point. If it plots on a limit plane, the corresponding corner slides on one plane in the incipient motion increment. If it coincides with an edge of the rotation space pyramid, the corresponding corner slides along the intersection of two adjacent planes in the incipient motion increment.

The number of relevant limit planes varies according to the complexity of the block geometry. Corners formed by three joint planes lie inside the rock mass. Thus, three limit planes correspond to each rotation point. Corners with one or two joint planes lie on the free face. One or two additional limit planes, respectively, correspond to each rotation point. Note that there are no limit planes for the current (static) rotation point. A tetrahedron with three joint planes and one free face requires, for instance, intersecting 21 limit planes.

Table 12: Data of limit planes for corner C_1

Limit plane	Orientation		Normal vector $n_{i,l}$			Halfspace
	Dip direction [°]	Dip angle [°]	X [m]	Y [m]	Z [m]	
L_1	165.9	40.3	-0.1573	0.6273	-0.7627	lower
L_2	90.0	63.9	0.8977	0	0.4406	upper
L_3	340.0	83.5	0.3397	-0.9338	-0.1126	lower
L_4	90.0	8.1	-0.1413	0	-0.99	lower
L_5	248.6	82.5	0.9228	0.3624	-0.131	lower
L_6	197.1	8.2	0.0422	0.1371	-0.9897	lower
L_7	90.0	18.1	0.3102	0	0.9507	upper

Stereographic projection - equal angle - upper focal point



- joint planes
- free face
- reference circle
- ⊕ block side pole
- + rock or space side pole
- C_i** rotation space for corner C_i
- JP** joint pyramid
- E_{ij}** edge from C_i to C_j

Figure 66: Joint pyramid and rotation space for all corners C₁, C₂ and C₃ of the tetrahedron

Figure 67 helps in interpreting the rotation space. On the top left the figure shows a perspective view of the block together with the rotation space pyramids for each corner on the free face. The block is corner rotatable about every corner. The other patches show the intersection of the rotation space pyramid with the unit sphere (red) and the corresponding stereographic projection using the upper focal point (orange). Each rotation space pyramid in the stereographic projection is related to a block corner which has to be clearly indicated.

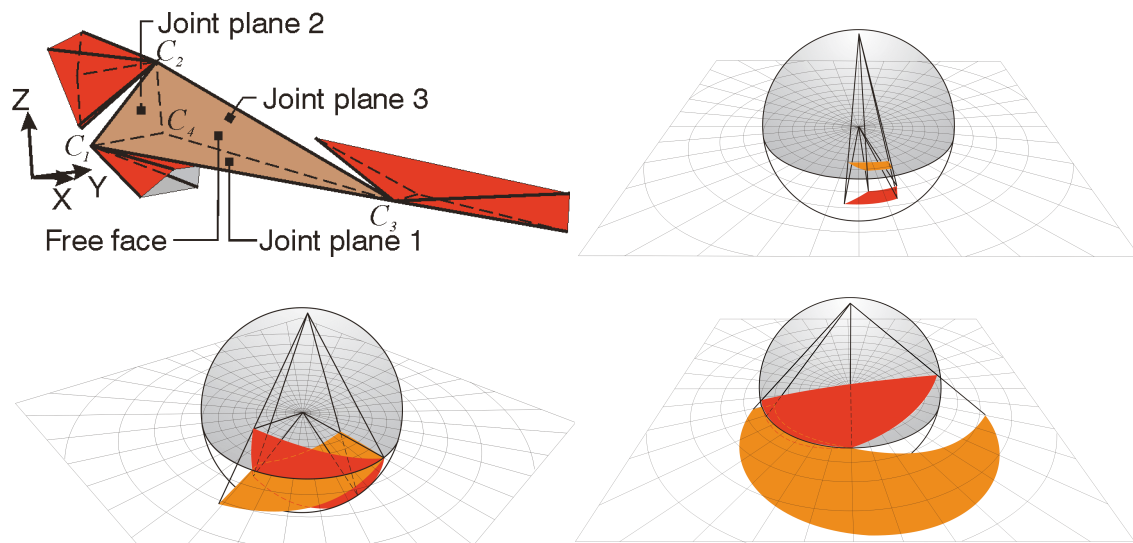


Figure 67: Perspective view of the block and rotation spaces for each corner (*top left*); Stereographic projection of the rotation space for corner C_1 (*top right*), C_2 (*bottom left*), and C_3 (*bottom right*). Upper focal point.

5.3.2.2 Determination of the rotation space using vector methods

The determination of the rotation space using vector methods involves several operations, each of which already is described in previous sections. The operations aim at computing the emptiness of the rotation space pyramids and finding its real edges. The required steps include:

- Computation of the orientations of the vectors $\mathbf{C}_j\mathbf{R}$ for each static rotation corner using expression (85).
- Computation of the orientations of the limit planes $\mathbf{n}_{i,l}$, separately for each static rotation corner, each derived from the blockside normal vector of a constrained corner's joint planes and the corresponding $\mathbf{C}_j\mathbf{R}$ vector.

$$\mathbf{n}_{i,l} = \frac{\mathbf{n}_{i,c}^* \cdot \mathbf{C}_j\mathbf{R}}{\|\mathbf{n}_{i,c}^* \cdot \mathbf{C}_j\mathbf{R}\|} \quad (87)$$

with $i = 1, \dots, m_j$ and $j =$ the set of constrained corners

- Computation of the emptiness of the rotation space pyramid following the steps described in chapter 5.2 and expressions (77) to (80) taking into account to replacing expression (79) by expression (88). Note that $\mathbf{n}_{i,c}$ is the blockside normal vector instead of the upward, and the recurring matrix multiplication ensures proper orientation of $\mathbf{n}_{i,l}$.

$$D_s(k) = 1 \quad \forall k \quad (88)$$

- Determination of the edges of the rotation space

Table 13 to Table 15 show the intermediate and final steps of the computation of the rotation space for the tetrahedron described in the previous chapter.

Table 13: Orientations of C_jR vectors and limit planes for each static rotation point

Static rotation point	Constraint corner	C_jR	C_jR vector			Limit plane	Normal vector $n_{i,l}$		
			X [m]	Y [m]	Z [m]		X [m]	Y [m]	Z [m]
C_1	C_2	C_{21}	0.3145	-0.7003	-0.6408	L_1	-0.1573	0.6273	-0.7627
	C_3	C_{31}	-0.9263	-0.3529	0.1322	L_2	-0.1413	0	-0.99
	C_4	C_{41}	0.3491	-0.9301	-0.1139	L_3	0.0422	0.1371	-0.9897
						L_4	0.3102	0	0.9507
						L_5	0.3397	-0.9338	-0.1126
						L_6	0.8977	0	0.4406
						L_7	0.9228	0.3624	-0.131
C_2	C_1	C_{12}	-0.3145	0.7003	0.6408	L_1	-0.9957	0	-0.0927
	C_3	C_{32}	-0.9221	0	0.3869	L_2	-0.8634	-0.4916	0.1134
	C_4	C_{42}	-0.0927	0	0.9957	L_3	-0.3869	0	-0.9221
						L_4	-0.2269	-0.9737	-0.0211
						L_5	-0.0236	-0.9981	-0.0563
						L_6	0.1573	-0.6273	0.7627
						L_7	0.3393	-0.9402	0.0316
C_3	C_1	C_{13}	0.9263	0.3529	-0.1322	L_1	-0.3468	0.9355	0.0674
	C_2	C_{23}	0.9221	0	-0.3869	L_2	-0.3397	0.9338	0.1126
	C_4	C_{43}	0.9866	0	-0.1635	L_3	-0.236	0.7924	-0.5626
						L_4	-0.1338	0.5743	-0.8077
						L_5	0.0097	0.9982	0.0586
						L_6	0.1635	0	0.9866
						L_7	0.3869	0	0.9221

Table 14: Testing matrices \mathbf{T}_k^{ij} for the emptiness of the rotation space for each static rotation point

\mathbf{T}_k^{ij} for C_1							\mathbf{T}_k^{ij} for C_2							\mathbf{T}_k^{ij} for C_3						
0	0	0	1	1	1	-1	0	0	1	1	-1	-1	0	0	0	1	-1	0	-1	-1
0	0	0	1	1	1	-1	0	-1	0	-1	1	-1	-1	0	-1	0	1	1	-1	-1
0	1	1	0	1	1	1	0	-1	1	0	-1	-1	-1	0	-1	1	0	1	-1	-1
0	1	1	-1	0	1	1	0	-1	1	-1	0	-1	-1	0	0	1	-1	0	-1	-1
0	1	1	-1	-1	0	1	0	-1	-1	-1	1	0	-1	0	1	1	-1	-1	0	1
0	-1	-1	-1	-1	-1	0	0	0	-1	-1	1	1	0	0	1	1	-1	-1	-1	0
0	0	0	1	1	1	-1	1	0	0	-1	1	-1	-1	1	0	0	1	1	1	1
1	0	1	0	1	1	1	1	0	1	0	0	0	-1	-1	1	0	1	0	1	-1
1	0	1	-1	0	0	1	1	0	1	0	0	0	-1	-1	0	0	1	-1	0	-1
1	0	1	-1	0	0	1	1	0	-1	-1	1	0	-1	-1	-1	0	-1	-1	0	1
-1	0	-1	-1	-1	-1	0	0	0	-1	-1	1	1	0	-1	0	-1	-1	-1	-1	0
1	-1	0	0	1	1	1	-1	-1	0	0	-1	-1	-1	-1	-1	0	0	1	-1	-1
1	-1	0	-1	0	-1	1	-1	-1	0	-1	0	-1	-1	-1	-1	0	-1	0	-1	-1
1	-1	0	-1	1	0	1	1	1	0	-1	1	0	-1	-1	1	0	-1	-1	0	1
-1	1	0	-1	-1	-1	0	1	1	0	-1	1	1	0	-1	1	0	-1	-1	-1	0
1	-1	-1	0	0	-1	1	1	0	1	0	0	-1	-1	-1	-1	-1	0	0	0	-1
1	-1	-1	0	1	0	1	1	1	1	0	1	0	1	-1	-1	-1	0	0	0	-1
1	-1	-1	0	-1	-1	0	1	1	1	0	1	-1	0	-1	-1	-1	0	-1	1	0
1	0	1	-1	0	0	1	1	1	1	1	0	0	1	-1	-1	-1	0	0	0	-1
1	-1	-1	1	0	-1	0	1	1	1	1	0	-1	0	-1	-1	-1	1	0	1	0
1	-1	-1	1	1	0	0	1	1	1	1	-1	1	0	0	1	1	1	1	0	0

Table 15: Edges of the rotation space pyramid at each static rotation point

Edges of rotation space			Edges of rotation space			Edges of rotation space		
X	Y	Z	X	Y	Z	X	Y	Z
[m]	[m]	[m]	[m]	[m]	[m]	[m]	[m]	[m]
0.8877	0.3578	-0.2897	-0.9361	-0.3407	-0.0872	-0.8759	0.3127	0.3675
0.9263	0.3529	-0.1322	-0.8783	-0.3046	0.3685	0	1	0
0.9416	-0.1375	-0.3073	0	-1	0	0.9227	0.354	-0.1529
0.9871	0.0763	-0.1409	0.0597	-0.7649	-0.6414	0.9263	0.3529	-0.1322
						0.9361	0.3407	0.0872

Table 14 indicates rows with only non-positive or non-negative entries corresponding to real edges of the rotation space pyramid with a grey shading. Table 15 shows the orientations of the real edges. Each row is an edge orientation vector. The rotation spaces for corners C_1 and C_2 have four edges while for corner C_3 it has five edges. The thorough reader realises that Table 14 indicates seven real edges instead of only five in Table 15. Several edges are redundant if they intersect along a joint normal vector which also corresponds to an edge of the rotation space. In this case it is the blockside normal vector of joint plane 2. This can be also confirmed in Figure 66. The five edges of C_3 are hardly observed in Figure 66. The indication of block edge 13 contains two real edges of the rotation space which are very close to each other (within 1°). They could not be individually resolved in the figure.

5.3.3 Rotation about a remote axis

Corner and edge rotation relies on the assumption that at least one point of the rotation axis is fixed to the block. In the case of corner rotation the fixed point is a vertex at the intersection polygon between free faces and joints, while for edge rotation it is an edge of the same polygon. The physical meaning of this assumption is that the block remains in contact at the considered corner or edge. The described method also holds for any rotation axis with a fixed point no matter if the rotation axis is in contact with the block or not. Since the fixed point can be anywhere in space, the determination of the rotation space is cumbersome. The rotation space has a complex envelope formed by the union of shifted pyramids and is barely interpretable. Thus, it has low engineering value. From an engineering perspective the objectives of the analysis of remote axis rotation are to answer whether there is any remote rotation axis leading to kinematically feasible displacements, and to test suspicious axes if they relate to kinematically feasible motion.

The additional positional freedom of the rotation axes makes the problem significantly more complex requiring the solution of systems of non-linear

equations under constrained conditions. This section outlines two approaches to the problem. The first one is a direct geometric approach highlighting the interdependencies of the problem. The formulation is complex and ill-posed; numerical methods barely find a solution. The second one rejects the complex relationships and uses penalty values instead in order to numerically solve the problem.

5.3.3.1 Geometric approach

A plane perpendicular to a displacement vector also contains the rotation axis. This plane has been originally introduced by Mauldon & Goodman (1990) as the pivot plane. Intersections between two different pivot planes define an intersection representing the axis causing the displacement vectors. (For rotations, pivot planes are non-parallel unless they are coincident, or displacements are pure translations). Any two pairs of pivot planes of arbitrary displacement vectors determine a potential rotation axis. The first objective is finding a set of rotation axes which coincide in position and orientation by varying the orientations of the pivot planes. Per definition, the displacement vector $\Delta \mathbf{x}_j$ is the normal vector \mathbf{n}_{π_j} of the pivot plane. The pivot planes have a fixed position at the considered block corners. Figure 68 shows the situation for three block corners.

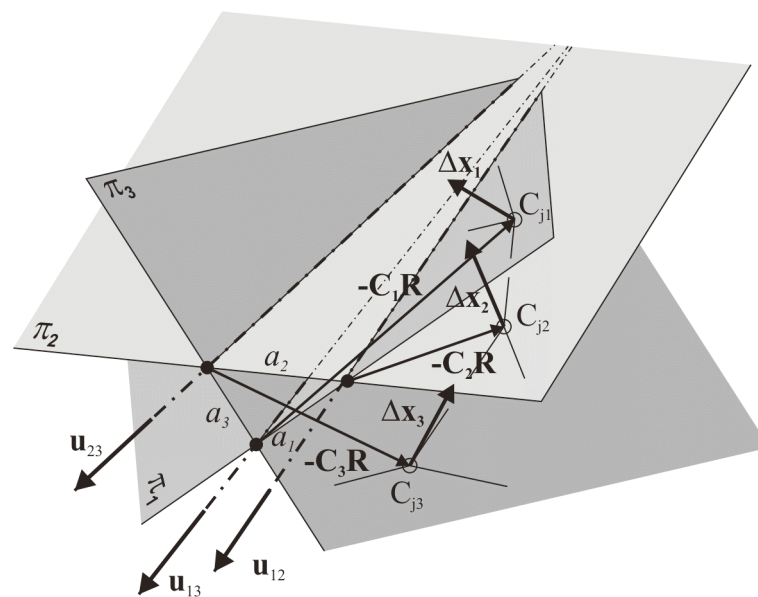


Figure 68: Kinematic relationships for remote axis rotation: Block corners C_j , pivot planes π_i , displacement vectors $\Delta \mathbf{x}$, intersection lines \mathbf{u}

Displacement vectors of the block must have a right-hand or left-hand rotation relative to the rotation axis, i.e. they must have the same spin. This is the second condition which has to be fulfilled. The joints at the block corners constrain the orientation of the displacement vector (Corner joint pyramid) and thus the orientation of the pivot planes as well. The normal vector of the pivot plane considering the appropriate spin must plot inside the corner joint pyramid. Finally, the normal vectors of the pivot planes must remain unit vectors during the variation.

The properties of the geometric problem lead to a constrained non-linear multi-objective optimisation problem. The goal attainment method as implemented in *MatLab*'s optimisation command *fgoalattain* (Gembicki 1974, Brayton et al. 1979, Han 1977, Powell 1978, all cited at <http://www.mathworks.com/help/toolbox/optim/ug/fgoalattain.html>) solves the problem by defining the following objective and constraint functions:

- Define the intersections \mathbf{u} of one pivot plane with any other.
- Determine the direction cosine between the direction vectors \mathbf{u} of the intersections
- Determine the distance a between two points of the intersections in a common plane.
- Calculate the displacement vector relative to the intersection \mathbf{u}_k . k is the number of intersections.

$$\Delta \mathbf{x}_j = \mathbf{u}_k^* \cdot (-\mathbf{C}_j \mathbf{R})$$

- Objectives: The product must attain the value 1 while the distance the value 0.

$$\begin{aligned} \mathbf{u}_l^T \cdot \mathbf{u}_m &= 1 \quad \text{with } l = 1, \dots, k-1 \text{ and } m = l+1, \dots, k \\ |a| &= 0 \quad \forall a \end{aligned}$$

- Objective: All normal vectors of pivot planes have to be parallel to the displacement vectors (Spin).

$$\Delta \mathbf{x}_j^T \cdot \mathbf{n}_{\pi,j} = 1$$

- Constraint: All normal vectors have to plot inside the corners joint pyramid. (Inequality constraint). m_j is the number of corners.

$$\Delta \mathbf{x}_j^T \cdot \mathbf{n}_{i,c} \geq 0 \quad \text{with } j = 1, \dots, m_j \quad \text{and } i \text{ is the number of joints at the corner}$$

- Constraint: The normal vectors have to remain unit vectors (Equality constraint).

$$\sum_{i=1}^3 \Delta x_{j,i}^2 - 1 = 0$$

Although geometrically clearly defined, the solution of this problem is hard to find. Especially the objective functions are ill-posed and behave unsteadily.

5.3.3.2 Penalty values

Improvements of the former approach are the reduction of the number of objectives and constraints. It makes the problem geometrically simpler. In order to attain the same objectives and constraints a numerical method related to the penalty method (Courant 1943) is used. It turns the constrained optimization problem into an unconstrained one by adding the penalty function to the objective function. Penalty functions give a measure for the severeness of a constraint violation.

Let us assume an arbitrary axis serving us as a rotation axis. The corresponding displacement vectors are calculated using expression (82). This inherently preserves the spin and eliminates the problem of multiple rotation axes. In general, the calculated displacements will violate the constraints at the block corners. Now we have to guide an optimisation to a position and orientation of the rotation axis without any constraint violation. This is done by penalty functions related to each constraint. If there is no constraint violation, the penalty value is zero while a constraint violation causes a penalty.

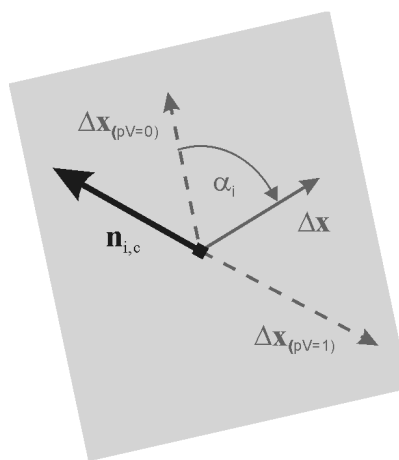


Figure 69: Constraint criterion and determination of penalty values

The penalty is assigned according to the severeness of violation. The angle between the joint plane and the displacement vector serves as a penalty measure (Figure 69). Note that penalties are only required if the displacement vector plots inside the rock mass (constraint space). If the angle is 90° , the penalty is one while if it is zero, the penalty is zero as well. Between those limits the penalties are assigned according to a continuous function with decreasing gradient considering a zero gradient at the zero position. This eases the use of gradient methods for the optimisation. The penalty functions may be polynomials of the

order two or higher. In this case a phase-shifted cosine function as shown in expression (89) has been used. Figure 70 highlights the shape of the used penalty function.

$$pV_i = 1 - \cos\left(\alpha_i - \frac{\pi}{2}\right) \quad \text{with } \alpha_i = \arccos\left(\frac{\Delta\mathbf{x}^T \cdot \mathbf{n}_{i,c}}{\|\Delta\mathbf{x}\|} \cdot D_s(i)\right) \quad (89)$$

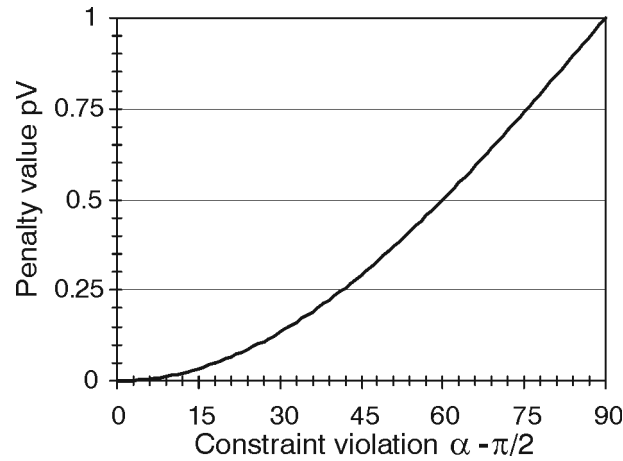


Figure 70: Penalty function depending on the magnitude of constraint violation

Penalties are calculated for each constraint and updated in every iteration. The objective function is the sum of all penalties which has to be minimised. The described approach requires also an equality constraint: The orientation vector of the rotation axis has to be a unit vector in order to preserve pure rotation (without any shearing and stretching) in the optimisation. The used optimisation algorithm is a medium scale finite difference gradient method included in Matlab's *fmincon* function.

In case of a solution space the encountered solution depends on the start values. Using gradient methods the solution is a minimum of the objective function which is also prone to find local minima not representing a solution of the physical problem. The selection of the appropriate numerical method requires a discussion and description of the objective function's properties. Stochastic methods should be used to increase the probability of finding the global minimum of the objective function. They include a variation of the start values within a defined volume and an iterative optimisation with a guided selection of start values according to the minimum penalty values obtained in the previous iteration. The author recommends an extensive mathematical discussion of the objective function and the solution strategy as well.

The penalty function approach is also able to find a slumping mode. Slumping is a remote axis rotation in which the block keeps in simultaneous contact (sliding) with the constraint space at two different planes. Identifying this case requires an extension of the validity of expression (89) for displacements towards the blockside halfspace for the sliding planes. For all other planes of the constraint space expression (89) still remains valid for the rockside halfspace only; the penalty value for the blockside halfspace is zero.

5.4 Illustrative examples

The following sections illustrate the methods outlined and developed in the previous sections. The first example describes a convex block and the second a non-convex block similar to the first one. It shows that the method is similarly applied but significantly different results are obtained. The last example discusses the kinematics of a block in a tunnel crown and highlights specific topics.

5.4.1 Convex block

The convex block has four joint planes and two free faces each forming convex edges. Figure 71 shows its geometry with annotations and Table 16 gives the data on plane orientations, positions and halfspaces. Table 17 shows the resulting coordinates of the vertices. The block's block pyramid code is 000111 and the joint pyramid code is thus 0001.

Table 16: Data on block geometry for the block shown in Figure 71:
Orientations, locations and halfspaces of planes

Planes	Orientation		Point on plane			Halfspace
	Dip direction [°]	Dip angle [°]	X [m]	Y [m]	Z [m]	
Joint plane 1	230	55	40.00	0.00	0.00	upper
Joint plane 2	115	65	-30.00	0.00	0.00	upper
Joint plane 3	170	35	0.00	0.00	-10.00	upper
Joint plane 4	345	80	0.00	10.00	0.00	lower
Free face 1	180	10	0.00	0.00	0.00	lower
Free face 2	180	60	0.00	0.00	0.00	lower

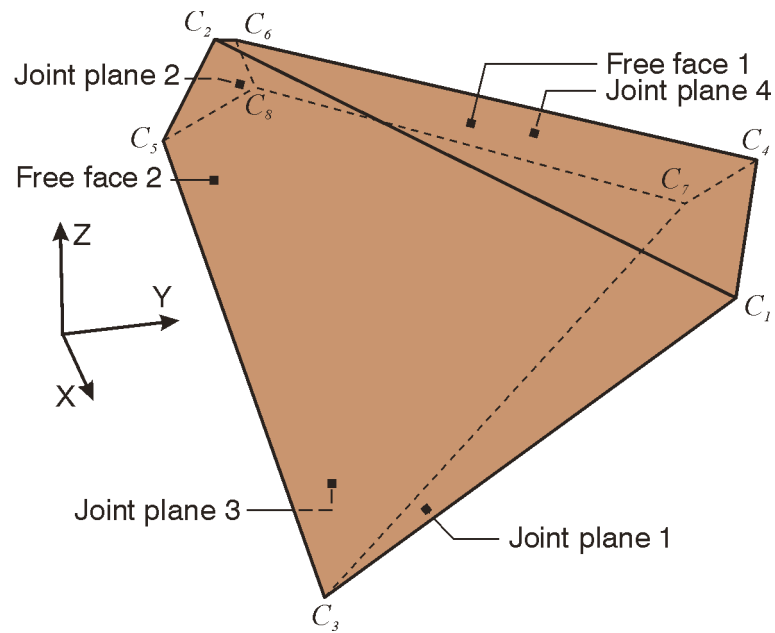


Figure 71: Perspective view of the convex block 000111 consisting of four joint planes, two free faces and eight corners

Table 17: Data on corner coordinates for the block shown in Figure 71

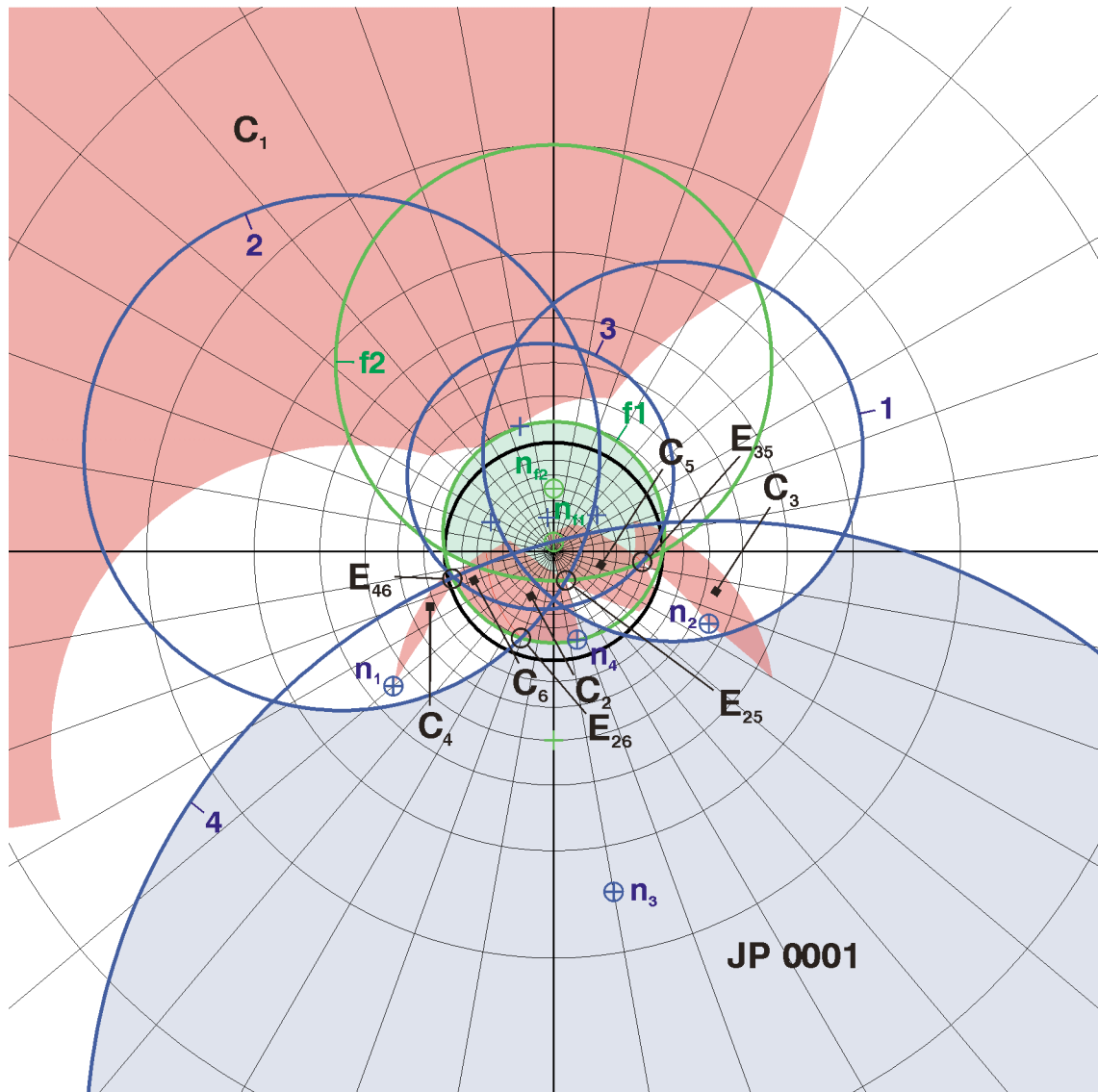
Corners	Coordinates		
	X [m]	Y [m]	Z [m]
C_1	40.00	0.00	0.00
C_2	-30.00	0.00	0.00
C_3	30.24	-13.12	-22.72
C_4	28.43	17.07	3.01
C_5	-27.28	-6.41	-11.10
C_6	-29.21	2.11	0.37
C_7	24.61	16.84	-1.38
C_8	-26.06	3.79	-4.22

Figure 72 gives an overview of the spatial situation. It plots the four joint planes as blue great circles and the two free face planes as green great circles in an upper focal point projection. Note that the upper halfspace of a plane plots outside the great circle and the lower halfspace inside. Since all edges are convex, the excavation pyramid (shaded in green) as well as the joint pyramid (shaded in blue) are the intersections of the halfspaces of free faces and joints, respectively. It can clearly be observed that the joint pyramid entirely plots outside the excavation pyramid. Thus, the block is removable. Possible modes of failure are falling or lifting, sliding on joints 1, 2, 3, and 4, and sliding along the intersections between joints 1-3, 1-4, 2-3, and 2-4.

Figure 72 provides also information on the rotatability of the block. It plots the rotation space pyramids for all corners about which feasible rotational displacements can take place. Hence, the block is corner rotatable about all vertices lying on the free faces which are C1, C2, C3, C4, C5, and C6. An appropriate annotation indicates the rotation space pyramid. The rotation space pyramid for C1 is isolated while the others are seemingly connected, i.e. it indicates a coincident orientation of a rotation axis but going through different corners. Rotation axes of different but connected rotation spaces become only physically coincident if they include an edge of the block. This special case describes the rotatability of a block about an edge. This block is edge rotatable about edges E25, E26, E35, and E46.

A static rotation corner can have either one or two joints (as it lies on the free face). If the rotation space pyramid of a certain corner includes one of the normal vectors of the corresponding joints, then the block may rotate in a sliding rotation mode about this corner keeping in contact with a joint plane. For this block a sliding rotation mode is possible for joint plane 1 about C4 and joint plane 4 about C6. If any other joint normal vector plots inside a rotation space pyramid, the block also keeps in sliding contact with the joint while rotating about the corner. In this case the static rotation point is not included in the sliding plane. Thus, this mode is more complex and not included in the basic kinematic modes described in section 5.1.3.2. These modes are possible for joint plane 4 about corners C1 and C2, and joint plane 2 about corner C3.

Stereographic projection - equal angle - upper focal point



- joint planes
- free face
- reference circle
- ⊕ block side pole
- + rock or space side pole
- C_i** rotation space for corner C_i
- JP** joint pyramid
- EP** excavation pyramid
- E_{ij}** edge from C_i to C_j

Figure 72: Stereographic projection of the rotation space and joint pyramid of the convex polyhedron shown in Figure 71

5.4.2 Non-convex block

In this example a non-convex block has six joint planes and two free faces which altogether form 12 corners. A perspective view of the block is shown in Figure 73. All edges are convex except the edge between corners C11 and C12. Data on the block faces and halfspaces are found in Table 18. The coordinates of the block corners can be found in Table 19. Due to its non-convex nature it is not possible to describe the block with only one halfspace code. It is a union of several sub-blocks each of which convex. A possible block pyramid code is $00010211 \cup 20021012$. The joint pyramid is the intersection of joint halfspaces; thus it is 000100.

Table 18: Data on block geometry for the block shown in Figure 73:
Orientations, locations and halfspaces of planes

Planes	Orientation		Point on plane			Halfspace
	Dip direction [°]	Dip angle [°]	X [m]	Y [m]	Z [m]	
Joint plane 1	230	55	40.00	0.00	0.00	upper
Joint plane 2	115	65	-30.00	0.00	0.00	upper
Joint plane 3	170	35	0.00	0.00	-10.00	upper
Joint plane 4	345	80	0.00	10.00	0.00	lower
Joint plane 5	170	20	0.00	0.00	-9.00	upper
Joint plane 6	280	80	0.00	0.00	0.00	upper
Free face 1	180	10	0.00	0.00	0.00	lower
Free face 2	180	60	0.00	0.00	0.00	lower

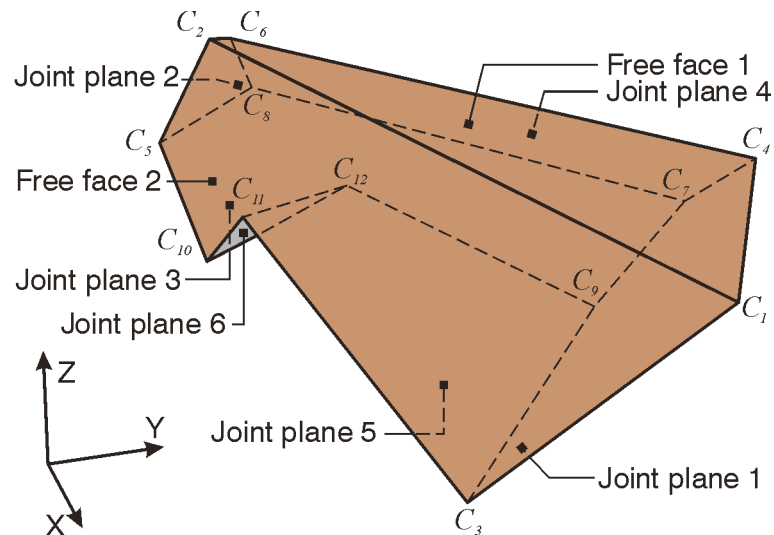


Figure 73: Perspective view of the non-convex block $00010211 \cup 20021012$ consisting of six joint planes, two free faces and twelve corners

Table 19: Data on corner coordinates for the block shown in Figure 73

Corners	Coordinates		
	X [m]	Y [m]	Z [m]
C_1	40.00	0.00	0.00
C_2	-30.00	0.00	0.00
C_3	33.96	-8.11	-14.06
C_4	28.43	17.07	3.01
C_5	-27.28	-6.41	-11.10
C_6	-29.21	2.11	0.37
C_7	24.61	16.84	-1.38
C_8	-26.06	3.79	-4.22
C_9	26.33	7.66	-7.92
C_{10}	-4.42	-9.08	-15.72
C_{11}	-3.12	-6.41	-11.10
C_{12}	-0.91	2.86	-7.92

Figure 74 gives an overview of the spatial situation. It plots the six joint planes as blue great circles and the two free face planes as green great circles in an upper focal point projection. Since the edges of the excavation pyramid are all convex, the excavation pyramid (shaded in green) is the intersections of the halfspaces of free faces. The joint pyramid as the intersection of all joint halfspaces is shaded in blue. It can clearly be observed that the joint pyramid entirely plots outside the excavation pyramid. Thus, the block is removable. Possible modes of failure are falling or lifting, sliding on joints 2, 4, 5, and 6, and sliding along the intersections between joints 2-4, 2-5, 4-6, and 5-6. Note that the intersections 2-5 and 4-6 do physically not exist.

Corner rotation is possible about C1, C4, C5, and C10. C4 has a very narrow rotation space pyramid almost horizontal parallel to the excavation pyramid's edge. Each rotation space pyramid is isolated (even C5 and C10) and in consequence edge rotation is not feasible. Sliding rotation is not possible for any of the static rotation corners. Nevertheless, the block may remain in sliding contact with joint plane 4 when rotating about C1 and joint plane 6 when rotating about C5.

Stereographic projection - equal angle - upper focal point

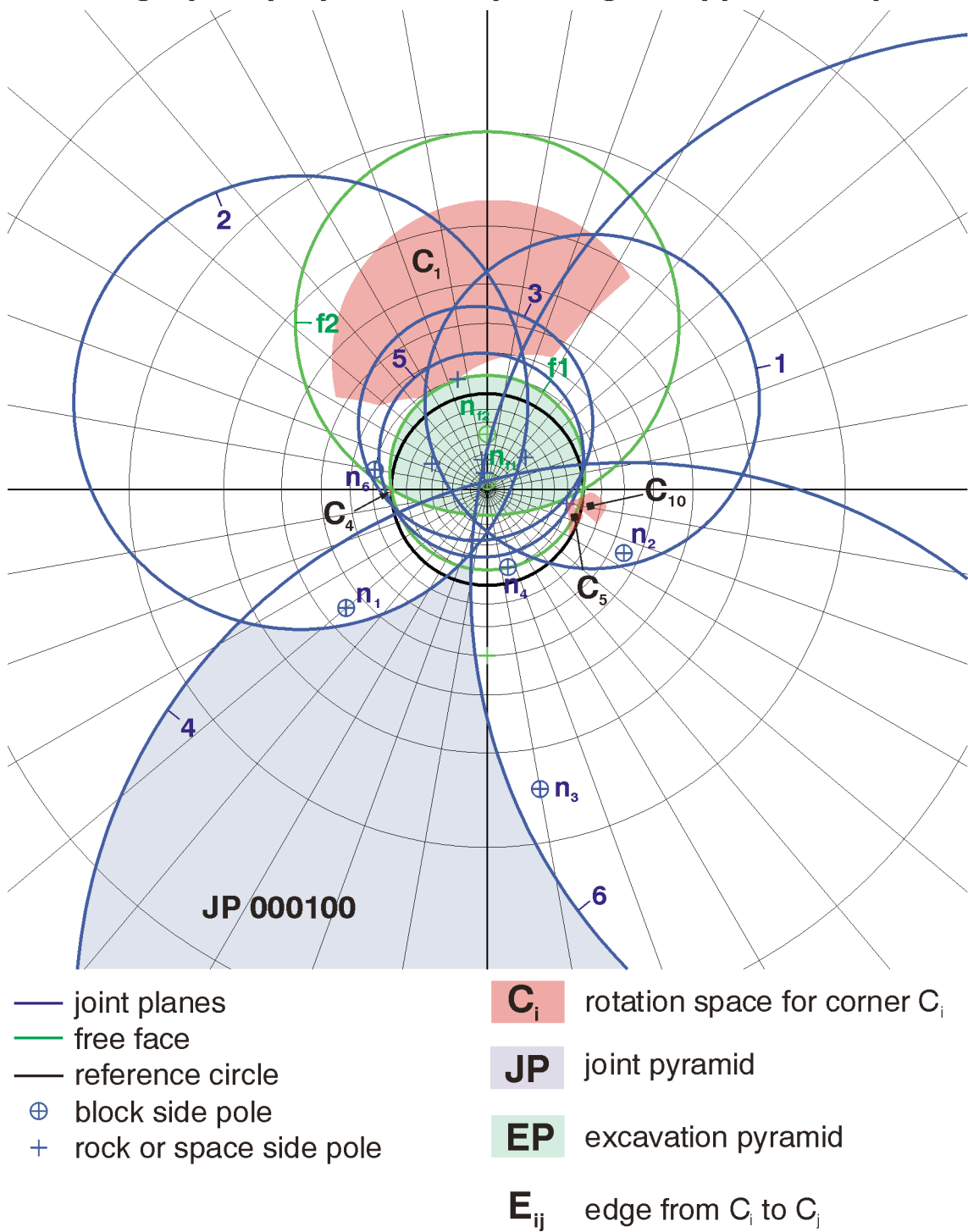


Figure 74: Stereographic projection of the rotation space and joint pyramid of the non-convex polyhedron shown in Figure 73

5.4.3 Block in a tunnel crown

This example examines a convex block in the crown of a tunnel. The block is bounded by five joint planes and one free face. Figure 75 gives a spatial overview of the situation. The free face is horizontal and forms the lower bound of the block. Four steeply dipping joints form the convex hull of the block. Additionally, the block is cut by a regularly spaced and flatly dipping joint set which changes the geometry of the individual blocks. The data on the joint orientations and halfspaces is found in Table 20.

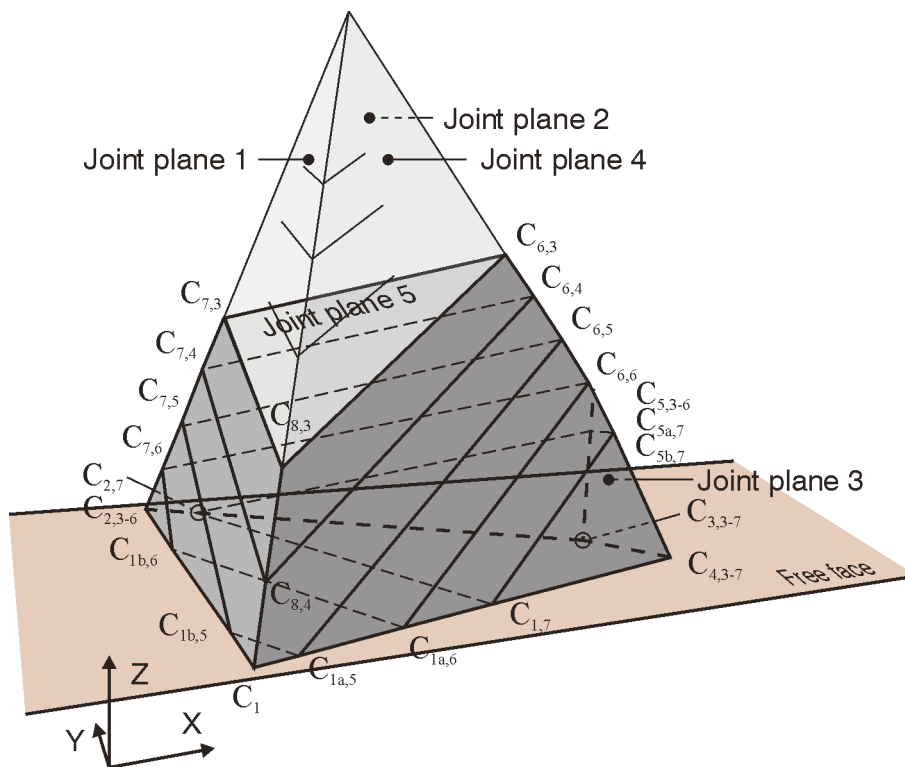


Figure 75: Block in a tunnel crown intersected by a regularly spaced joint set.

In the following it is considered that the free face remains constant and the lower bound of the block. The height of the block is decreased slice-wise according to the intersections caused by joint set 5. The corners belonging to different individual blocks are indicated by a number suffix. For block suffices smaller than 5 joints of joint set 5 do not daylight within the polygonal at the free face.

Figure 76 gives an overview of the spatial situation. It plots the five joint planes as blue great circles and one free face plane as a green great circle in a lower focal point projection. Note that in this projection the upper halfspace plots inside the great circle and the lower halfspace outside. Thus, the green shaded area represents the blocks excavation pyramid.

Stereographic projection - equal angle - lower focal point

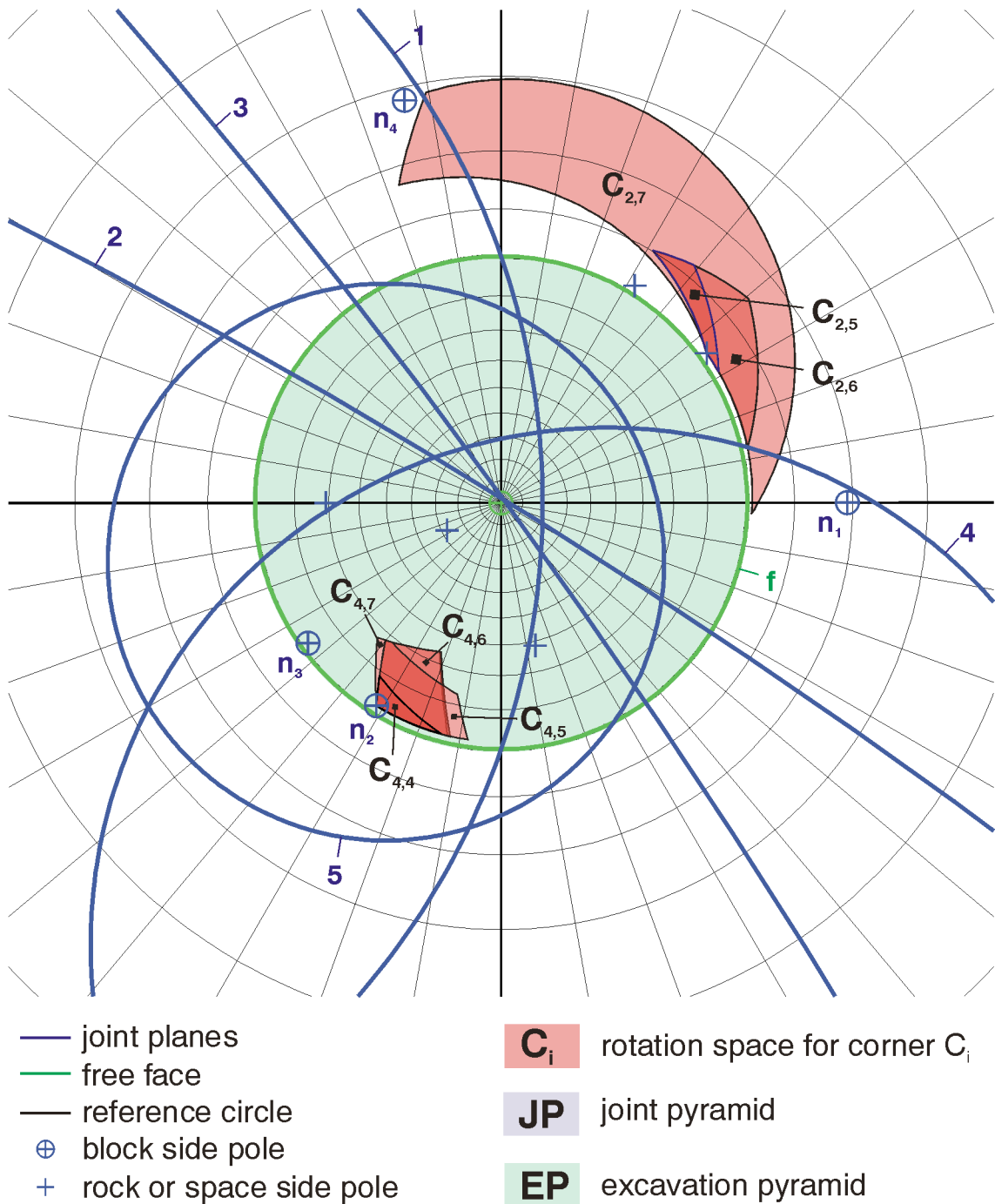


Figure 76: Stereographic projection of the rotation space and excavation pyramid of the polyhedral blocks shown in Figure 75.

The blocks are removable as the joint pyramid is not empty and plots entirely outside the excavation pyramid. Note that the joint pyramid plots outside the shown area in Figure 76.

Possible modes of failure are falling, sliding on joints 1, 2, 3, and 4, and sliding along the intersections between joints 1-4, 1-2, 2-3, and 3-4. For block level 7 the possible failure modes change to falling, sliding on joints 2, 3, 4, and 5, and sliding along the intersections between joints 2-3, 2-5, 3-4, and 4-5. Joint plane 1 becomes completely undercut by joint 5.

The block is non-rotatable for block level equal or smaller than 3. The rotation space is empty for all potential rotation corners. For block level 4 it becomes corner rotatable about $C4_4$ with increasing aperture of the rotation space pyramid to block level 7. At block level 5 it also becomes corner rotatable about $C2_5$ with increasing aperture of the rotation space pyramid to block level 7. The corner $C2_7$ does not coincide with the other corners $C2_{5-6}$ and causes a significant increase of the rotation space aperture. None of the investigated blocks has a connected rotation space; they are not edge rotatable. Sliding rotation is not possible for these configurations neither. Nevertheless, the block may remain in sliding contact with joint plane 2 when rotating about $C4_{4-7}$ and joint plane 3 when rotating about $C2_{5-7}$. This example highlights the influence of the block geometry on the kinematic movability of a polyhedral block. Although the blocks have the same joint pyramid (except for block level 7), their rotatability is significantly different ranging from non-rotatable to rotatable at several corners. Especially non-daylighting joints have an influence on the rotatability though do not affect the joint pyramid. This has also been addressed in Pötsch & Schubert (2006).

Table 20: Data on block geometry for the blocks shown in Figure 75:
Orientations, locations and halfspaces of planes

Planes	Orientation		Point on plane			Halfspace
	Dip direction [°]	Dip angle [°]	X [m]	Y [m]	Z [m]	
Joint plane 1	270.00	70.83	0.00	0.00	0.00	lower
Joint plane 2	211.64	88.02	8.00	3.63	0.00	upper
Joint plane 3	234.01	88.18	8.00	3.63	0.00	upper
Joint plane 4	166.50	61.54	0.00	0.00	0.00	lower
Joint plane 5 ⁽¹⁾	242.78	27.74	6.47	4.82	5.85	lower
Free face	0	0	0.00	0.00	0.00	upper

⁽¹⁾ Position only f or block level 3. Joint set normal spacing 0,94 cm

Another aspect usually disregarded in kinematic analyses is related to remote axis rotation. Let us consider the block formed by block level seven as shown in Figure 75. We already proved its removability and rotatability. Let us now examine the influence of a stiff lining applied to the tunnel crown. Figure 77

shows a situation with application of the lining in positive X direction. The lining meets the block at first at corner $C_{2,7}$. In this case the block is still unaffected by the lining. With any further application the analytical analyses of translations and rotations immediately would give a non-removable and non-rotatable block. In the former case the joint pyramid is empty indicating a tapered block (If we consider the contact between block and lining as a joint, the block is tapered by the lining). If we consider the constraints outlined in section 5.3.3.2 and perform a constrained optimisation using penalty values, we find a remote rotation axis allowing feasible block displacements.

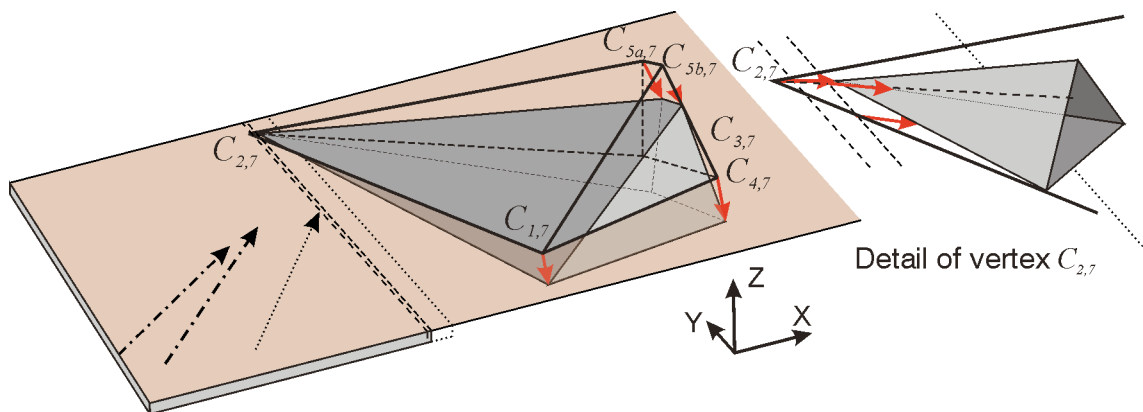


Figure 77: Remote axis rotation of the block at level 7 (see Figure 75) when a stiff lining is applied. Lining is applied in positive X direction.

The dot and dashed arrows in Figure 77 indicate valid remote rotation axes corresponding to a lining chainage (from $C_{2,7}$) of 0.06 m and 0.16 m. The dotted arrow is the solution at a chainage of 0.66 m but already causes strong constraint violations; thus it has no physical meaning. The corresponding lining chainages are drawn as dashed and dotted lines, respectively. The exaggerated incipient displacement vectors are drawn as red arrows together with the displaced block position corresponding to the lining chainage 0.16 m. The block position and displacement vectors adjacent to corner $C_{2,7}$ are shown in the detail on the right hand side. Figure 78 shows the same block with the lining application in direction of the negative X axis. The lining meets the block at first at corner $C_{4,7}$. The dot and dashed arrows indicate valid remote rotation axes corresponding to a lining chainage (from $C_{4,7}$) of 0.16 m and 0.36 m. The dotted arrow is the solution at a chainage of 0.56 m but already causes strong constraint violations; thus it has no physical meaning. The corresponding lining chainages are drawn as dashed and dotted lines, respectively. The exaggerated incipient displacement vectors are drawn as red arrows together with the displaced block position corresponding to the lining chainage 0.36 m.

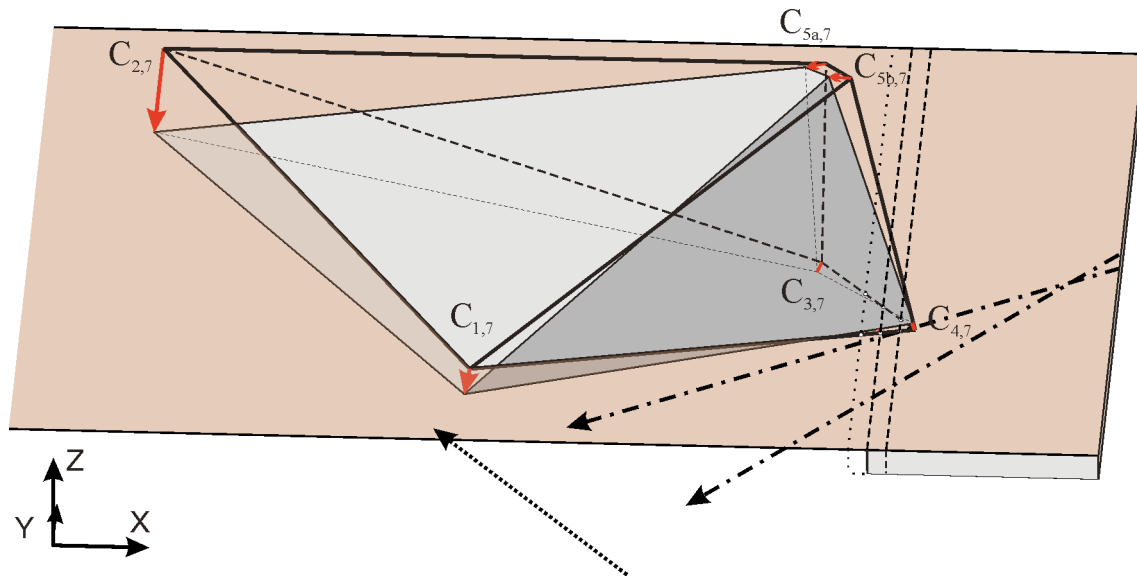


Figure 78: Remote axis rotation of the block at level 7 (see Figure 75) when a stiff lining is applied. Lining is applied in negative X direction.

The last example showed that blocks still may be kinematically movable even if the analytical methods indicate non-movability (non-removable and non-rotatable). Anyhow, only a small stretch of lining was necessary to prevent the block from movement at all. The basis for this statement is that the block perfectly matches the rock mass and the lining and that each of them is rigid. Open joints, soft infillings or weak linings increase the kinematic movability again. This flexibility can be quantified by an angle between the displacement vector and the joint plane similar to Figure 69. The penalty function expression (89) could be used to control the flexibility by meeting the zero penalty at a larger angle (describing the flexibility limit).

5.5 Summary

This chapter described extensively the kinematics of a rigid polyhedral block constrained by joint planes. It also introduced methods for the kinematic analysis for both, translational and rotational modes of motion. First of all, the kinematic relationships in terms of displacements, velocities, and accelerations were discussed with special attention on large displacements. These relationships resulted in the formulation of 16 basic kinematic modes for blocks. The determination of the current kinematic mode, however, required control over the reactive forces which would only be obtained together with the equations of motion. In consequence, a simplified approach considering infinitesimal displacements was introduced in order to provide a basis for the subsequent analysis methods of kinematic movability.

The translational analysis following Goodman & Shi's block theory was reviewed, presenting the basic ideas in kinematically feasible displacement, the theorem of removability and the graphical and vector methods for the analysis. Following the same ideas a method for the rotational analysis of arbitrary polyhedral blocks based on Mauldon's theory of rotations of tetrahedra was developed. The developed method allowed analysing the corner and edge rotatability of an arbitrary finite polyhedral block. The principles of the analysis were outlined and graphical and vector methods for performing the analysis presented. Another section examined the relationships of remote axis rotation. It became obvious that this kinematics would lead to nonlinear systems of equations which could only be solved using numerical methods. A formulation was developed which could be solved with an algorithm for constrained minimisation of the objective function.

The chapter closed with three illustrative examples including a convex and a non-convex block, as well as a block assembly in the crown of a tunnel. The examples showed the application of the kinematic analysis and the interpretation of the obtained results.

The importance of block kinematics is manifold. Any mechanically sound dynamic or equilibrium analysis of a block can only be properly performed if the kinematic relationships are correctly considered. The presented kinematic modes are used in a mechanical model for constraining the block motion and calculating the reaction forces. For the hierarchical block analysis the engineer is interested in the kinematic movability of a block prior to mechanically analysing the block stability. The presented analytical and numerical methods are powerful tools to efficiently determine the movability of a finite polyhedral block. In the following the key findings of this chapter are summarised:

- Determining the kinematic mode of a block requires, apart from the consideration of the constraints control on the reaction forces
- Simple analytical and numerical methods for the kinematic analysis consider only infinitesimal displacements
- Joint orientations only determine the kinematic movability for translations (removability)
- Joint orientations and positions influence the kinematic movability for rotations (rotatability). Especially non-daylighting joints have a noticeable impact, even turning non-rotatable blocks into rotatable blocks (although the joint pyramid is the same).

- If no information on the block geometry is available, conclusions on the rotatability still can be drawn, yet Mauldon's law on rotatability of tetrahedral blocks still holds for arbitrary polyhedral blocks:
 - A block *is* non-rotatable (for corner and edge rotation) if the corner joint pyramid of a corner adjacent to the static rotation point is non-rotatable
 - A block *may be* corner or edge rotatable if the corner joint pyramid of a corner adjacent to the static rotation point is rotatable.
- Remote axis rotation is an optimisation problem. Finding a kinematically feasible rotation axis depends on the block geometry, the constraints and, significantly, on the selection of start values. The conclusion whether a block is movable about a remote axis, can only be drawn with a certain degree of probability.

6 Dynamic Behaviour and Stability Analysis

6.1 Introduction

The previous chapters addressed properties of blocks and their determination, the kinematics of rigid blocks and the properties and mechanical behaviour of rock joints. This chapter will address the mechanical behaviour of a rigid block under different load situations. The methods outlined below will use the findings of the previous chapters. The mechanical behaviour of a rigid body is fully described by Newton's and Euler's equations of motion enhanced by kinematic constraint equations. The required input parameters involve the inertia properties such as mass and inertia matrix, the (non-linear) shear and normal behaviour of joints, the algebraic equations of kinematic constraints based on block geometry, and also the different loads such as gravity, water pressure, etc.

The equations of motion are a set of differential equations that require integration over a time interval in order to describe the response of the block system. The first section shows the derivation of the set of differential and algebraic equations of a constrained rigid body using matrix and Euler parameter formalism. Subsequently, the numerical time integration of these equations is addressed in order to obtain the solution of the system. These methods form the basis for any dynamic analysis of a rigid block.

Equilibrium is a special case of the dynamic behaviour, which needs separate treatment. Finding the equilibrium position of a rigid body is a highly non-linear problem. One section presents the application of the continuation method for finding a block's equilibrium position under the exposed loads. The basic solution is the equilibrium path showing the block positions while continuously increasing the external loads until equilibrium. The block stability analysis takes advantage of the properties of the equilibrium path. The results of the block stability analysis are the static and dynamic mode of failure, the factor of safety, as well as the stability of the equilibrium path for a non-conservative mechanical system. An example of a block in the roof of a cavern illustrates the application of the method.

6.2 Literature review

Simple attempts to assess the stability of a block use the model of a block on an inclined plane using Mohr-Coulomb shear resistance – this is already taught in undergraduate physics classes. More specific methods of block stability in rock

mechanics are related to Londe et al. (1969, 1970) and John (1968). These authors examine the stability of tetrahedral blocks against translational and rotational failure modes taking into account the tetrahedral geometry and Mohr-Coulomb shear resistance. The early work of Wittke (1965) (cited in Wittke 1984) already addressed rotation of a block about an edge. Today, block stability analysis is often performed based on block models designed for specific problems such as the sliding block, the wedge, the wedge with tensile fracture, etc. Models for slopes and underground excavations are described in Hoek & Bray (1981) and Hoek & Brown (1990). The analysis of toppling failure has been introduced by Goodman & Bray (1977).

Warburton (1981) and Goodman & Shi (1985) published a method for the stability analysis of arbitrary blocks. Especially, Goodman & Shi's method is widely applied and known as "Block Theory". These methods provide the factor of safety of a block under static loads. They integrated Talobre's friction cone concept (Talobre 1957 cited in John 1968) into block theory. Block theory is a comprehensive method providing an analytical solution but it is limited to translations, static forces acting through the block's centre of gravity, and a Mohr-Coulomb sliding law. Mauldon & Goodman (1990 and 1996), Mauldon (1992) and Tonon (1998) attempted to extend block theory to rotational failure modes. The enhancements included rotational stability analysis for corner and edge rotation (Mauldon & Goodman's theory) and general loading conditions (Tonon 1998). The methods are applicable to tetrahedral blocks and pure rotation modes only. Rotational slides are not included although Tonon (1998) addressed conditions when rotational sliding takes place. Chan & Einstein (1981) presented a limit equilibrium method for block rotations based on artificial supports.

Further attempts to extend block theory are the works of Yow & Goodman (1987) and Karzulovic (1988) using the block reaction curve. The block reaction curve relates the block displacement to the acting forces. Basically, it is a displacement controlled equilibrium path. The approach allowed considering more sophisticated (non-linear) joint constitutive models, initial rock mass stresses and arbitrary block geometries. Pötsch (2002) showed the application of the block reaction curve method to pyramidal blocks in the crown of a tunnel subjected to self weight and an initial stress field. The joint response followed the Barton-Bandis (Barton 1977, Bandis et al. 1985) joint model in a Saeb-Amadei (1992) implementation. The major drawback of the block reaction curve is that the block displacement, i.e. the failure mode, has to be predefined. Interaction between forces and displacements takes place only in one direction (from displacement to force) and not vice versa. Results from block reaction curves are only feasible if they comply with the real failure mode of the block.

A comprehensive method for analysing the mechanical behaviour of blocks has to be based on the equations of motion of a rigid body. In general, their solution requires a numerical method. Three general approaches are available (Dietmair 2007):

- Minimising the potential energy of the system:
The system approaches the equilibrium position if its potential energy is minimised. This approach is limited to systems which possess a potential of forces.
- Dynamic relaxation:
The motion towards equilibrium or failure is calculated using a damped integration of the equations of motion. The system finds the equilibrium position (if there is any) after a sufficiently large time interval.
- Continuation method:
The loads and/or displacements are continuously increased until equilibrium or failure takes place. During calculation the block complies always with force and momentum equations, and kinematics.

Various computer codes are available which provide a numerical solution of the equations of motion: the 3D discrete element code (3DEC), the 3D discontinuous deformation analysis (3D-DDA), and the block-spring-method 3D (BSM3D). They are designed for the analysis of block systems with many blocks. Tonon (2007b) identifies the following drawbacks when analysing single blocks using one of these codes:

- An approximate scalar moment of inertia is used by 3DEC. This may lead to a wrong dynamic mode of failure. 3DEC is based on the dynamic relaxation method where the inertia matrix plays a major role.
- The application of constraint forces is based on geometrical but not mechanical principles in 3DEC.
- 3D-DDA assumes a potential for all forces. The system must therefore be conservative and all forces positional.
- Path dependency of joints can only be modelled with increased effort in describing the internal block geometry in 3DEC since contact points change in each iteration.
- All three methods require the shear strength reduction method in order to determine the factor of safety of the block system. This is computationally extensive.

Tonon (2007b) presents a method for the analysis of single blocks for general failure modes under conservative and non-conservative forces. It is based on the continuation method by Felippa (1987) for non-linear finite element methods. The method includes the determination of static and dynamic failure modes, factor of safety, treatment of bifurcation and stability of the equilibrium path.

6.3 The equations of motion

6.3.1 General

The equations of motion originally formulated by Newton for translations and Euler for rotations relate accelerations of bodies to the forces and moments acting on the body. Solving the equations of motion allows determining the position, velocity and acceleration of bodies together with the interacting forces and moments.

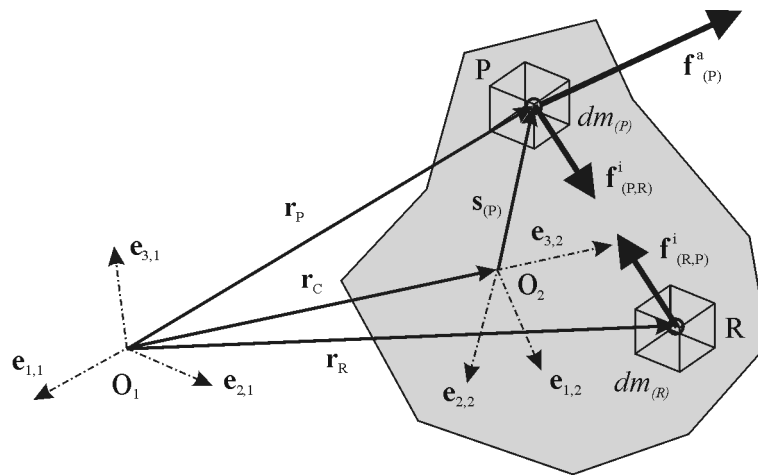


Figure 79: Internal and external force acting on a rigid body

The following discussion is based on these equations of motion for which three basic assumptions for internal forces are included (Figure 79):

1. For each internal force acting from point P to point R there is a corresponding reaction force acting from point R to point P (*actio est reactio* after Newton)

$$\mathbf{F}_{P,R} = -\mathbf{F}_{R,P} = f(m_P, m_R, |\mathbf{r}_P - \mathbf{r}_R|) \quad (90)$$

2. The considered body is rigid, i.e. the distance between two arbitrary points P and R of the body remains constant throughout the motion

$$(\mathbf{r}_P - \mathbf{r}_R) \cdot (\mathbf{r}_P - \mathbf{r}_R) = C \dots const. \Rightarrow (\delta \mathbf{r}_P - \delta \mathbf{r}_R) \cdot (\mathbf{r}_P - \mathbf{r}_R) = 0 \quad (91)$$

3. Action and reaction of internal forces act along the same line (after Euler)

$$\mathbf{F}_{P,R} = K \cdot (\mathbf{r}_P - \mathbf{r}_R) \quad K \dots const. \quad (92)$$

Based on these assumptions the equations of motion can be formulated as the vanishing sum of virtual works of the rigid body. The basic coordinate system O_1 must be an inertial system. The index (1) indicates this basic coordinate system. Equation (93) shows the equations of motion for a body-fixed coordinate system O_2 centred in the centre of mass of the body.

$$\delta \mathbf{r}_C^{(1)T} \cdot [m \cdot \ddot{\mathbf{r}}_C^{(1)} - \mathbf{F}^{a(1)}] + \delta \boldsymbol{\pi}^{(2)T} \cdot [\mathbf{J}^{(2)} \cdot \dot{\boldsymbol{\omega}}^{(2)} + \boldsymbol{\omega}^{*(2)} \cdot \mathbf{J}^{(2)} \cdot \boldsymbol{\omega}^{(2)} - \mathbf{M}^{a(2)}] = 0 \quad (93)$$

Equation (93) describes the motion for an unconstrained body. Kinematic constraints are not considered in the formulation yet. In constrained conditions the virtual translations and rotations depend on each other and must not be arbitrarily chosen. The terms in parenthesis in equation (93) thus cannot be treated separately. Equation (94) shows the dependence between the virtual displacements using the Jacobian matrices of the kinematic constraint equations. This is a boundary condition to the equations of motion.

$$\delta \mathbf{r}^{(1)T} \cdot \boldsymbol{\Theta}_r^T + \delta \boldsymbol{\pi}^{(2)T} \cdot \boldsymbol{\Theta}_\pi^{(2)T} = 0 \quad (94)$$

The Lagrange multiplier theorem allows introducing the boundary condition of equation (94) into the equations of motion which is shown in equation (95). The virtual displacements now can be chosen arbitrarily and consequently the terms in parenthesis must vanish. Equation (95) delivers six single differential equations with unknowns of six plus the number of constraints.

$$\delta \mathbf{r}_C^{(1)T} \cdot [m \cdot \ddot{\mathbf{r}}_C^{(1)} - \mathbf{F}^{a(1)} + \boldsymbol{\Theta}_r^T \cdot \boldsymbol{\lambda}] + \delta \boldsymbol{\pi}^{(2)T} \cdot \begin{bmatrix} \mathbf{J}^{(2)} \cdot \dot{\boldsymbol{\omega}}^{(2)} + \boldsymbol{\omega}^{*(2)} \cdot \mathbf{J}^{(2)} \cdot \boldsymbol{\omega}^{(2)} \\ -\mathbf{M}^{a(2)} + \boldsymbol{\Theta}_\pi^{(2)T} \cdot \boldsymbol{\lambda} \end{bmatrix} = 0 \quad (95)$$

The lacking equations for completely defining the constrained body problem can be obtained from the relationships for the kinematic acceleration analysis as outlined in the previous chapter.

$$\boldsymbol{\Theta}_r \cdot \ddot{\mathbf{r}}^{(1)} + \boldsymbol{\Theta}_\pi^{(2)} \cdot \dot{\boldsymbol{\omega}}^{(2)} = \boldsymbol{\gamma} \quad (96)$$

With equations (95) and (96) the first order differential-algebraic system of the equations is obtained. Expression (97) shows the equations of motion of a

constrained body in Newton-Euler formalism. It is a first order system since the angular accelerations $\dot{\omega}$ can only be integrated to angular velocities ω .

$$\begin{bmatrix} \mathbf{m} & \mathbf{0} & \Theta_r^T \\ \mathbf{0} & \mathbf{J}^{(2)} & \Theta_\pi^{(2)T} \\ \Theta_r & \Theta_\pi^{(2)} & \mathbf{0} \end{bmatrix} \cdot \begin{bmatrix} \ddot{\mathbf{r}}^{(1)} \\ \dot{\omega}^{(2)} \\ \lambda \end{bmatrix} = \begin{bmatrix} \mathbf{F}^{a(1)} \\ \mathbf{M}^{a(2)} - \omega^{*(2)} \cdot \mathbf{J}^{(2)} \cdot \omega^{(2)} \\ \gamma \end{bmatrix} \quad (97)$$

The first order system of equations (97) can be transformed into a second order differential-algebraic system of equations which can be integrated over accelerations and velocities. It is formulated in Euler parameter space applying the following relationships and constraints:

$$\omega^{(2)} = 2 \cdot \mathbf{G} \cdot \dot{\mathbf{p}} \text{ and } (\mathbf{G} \cdot \dot{\mathbf{p}})^* = \mathbf{G} \cdot \dot{\mathbf{G}}^T \quad (98)$$

$$\dot{\omega}^{(2)} = 2 \cdot \mathbf{G} \cdot \ddot{\mathbf{p}} \text{ considering that } \dot{\mathbf{G}} \cdot \dot{\mathbf{p}} = \mathbf{0} \quad (99)$$

Equations (98) and (99) represent the relationships between derivatives of Euler parameters and angular velocities and accelerations.

$$\Theta_r \cdot \ddot{\mathbf{r}}^{(1)} + \Theta_p \cdot \ddot{\mathbf{p}} = \gamma \quad (100)$$

$$\Theta_p^P \cdot \ddot{\mathbf{p}} = \lambda^P \quad (101)$$

Equations (100) and (101) represent the second derivatives of the kinematic constraint equations and Euler parameter normalisation condition. The result of the transformation is shown in equation (102) which is a second order differential-algebraic system of equations. It can be integrated over velocities and accelerations.

$$\begin{bmatrix} \mathbf{m} & \mathbf{0} & \Theta_r^T & \mathbf{0} \\ \mathbf{0} & 4 \cdot \mathbf{G}^T \cdot \mathbf{J}^{(2)} \cdot \mathbf{G} & \Theta_p^T & \Theta_p^{PT} \\ \Theta_r & \Theta_p & \mathbf{0} & \mathbf{0} \\ \mathbf{0} & \Theta_p^P & \mathbf{0} & \mathbf{0} \end{bmatrix} \cdot \begin{bmatrix} \ddot{\mathbf{r}}^{(1)} \\ \ddot{\mathbf{p}} \\ \lambda \\ \lambda^P \end{bmatrix} = \begin{bmatrix} \mathbf{F}^{(1)} \\ 2 \cdot \mathbf{G}^T \cdot \mathbf{M}^{(2)} + 8 \cdot \mathbf{G}^T \cdot \mathbf{G} \cdot \dot{\mathbf{G}}^T \cdot \mathbf{J}^{(2)} \cdot \dot{\mathbf{G}} \cdot \dot{\mathbf{p}} \\ \gamma \\ \gamma^P \end{bmatrix} \quad (102)$$

The solution of the equations of motion complies with the constraints at the velocity (103) and positional (104) integration level.

$$\Theta_r \cdot \dot{\mathbf{r}}^{(1)} + \Theta_p \cdot \dot{\mathbf{p}} = \mathbf{0} \quad \text{and} \quad \Theta_p^P \cdot \dot{\mathbf{p}} = \mathbf{0} \quad (103)$$

$$\Theta(\mathbf{r}^{(1)}, \mathbf{p}, t) = \mathbf{0} \quad \text{and} \quad \Theta^P = \mathbf{0} \quad (104)$$

The integration over time is an initial value problem. Initial values are required to determine the values for \mathbf{p} , γ , γ_p , \mathbf{G} , Θ_p , and Θ_r . Initial values must also comply with the kinematic constraints (105) and constrained velocities (106):

$$\Theta^{\text{ini}}(\mathbf{r}^{(1)}, \mathbf{p}, t_{\text{ini}}) = \mathbf{0} \quad (105)$$

$$\mathbf{B}_r^{\text{ini}} \cdot \dot{\mathbf{r}}^{(1)} + 2 \cdot \mathbf{B}_\pi^{\text{ini}} \cdot \mathbf{G} \cdot \dot{\mathbf{p}} = \mathbf{v}^{\text{ini}} \quad (106)$$

6.3.2 Time integration of the equations of motion

In order to obtain information about the mechanical response of a constrained block under external loads the integration of the system of equations (102) over time is necessary. There could be analytical solutions for a number of special cases but the great majority of the problems can only be solved by applying numerical methods. Methods for numerical integration of ordinary differential equations have been thoroughly investigated with respect to robustness, efficiency, convergence, and accuracy (e.g. García de Jalón & Bayo 1994, Heuser 2009, Aulbach 2004). This is not completely true for differential-algebraic equations where the theory is still incomplete (e.g. García de Jalón & Bayo 1994, Brenan et al. 1989, Kunkel & Mehrmann 2006). Solutions are difficult to establish and may not be unique. Existing algorithms are computationally extensive.

This section describes the numerical integration of the equations of motion using well-established methods for ODEs. The steps towards the solution include the elimination of the algebraic equations in order to obtain ODEs, transformation of the system of second order ODEs into a system of first order ODEs in order to use off-the-shelf algorithms, and the numerical integration of the ODEs in subsequent time steps. For some problems it is necessary to monitor the constraint forces which will be calculated by an inverse dynamic routine.

6.3.2.1 Elimination of the algebraic equations

ODE solvers, in the simplest case explicit forward Euler methods, can be used to integrate the ODE system (102). With a sufficiently small time step the algebraic

equations in equations (102) and also equations (103) and (104) are satisfied. Unfortunately, the kinematic acceleration equations used in (102) show less information compared to the original constraint equations due to differentiation. With proceeding time or increasing time steps the algebraic equations are permanently violated, consequently leading to large drifting errors in the geometry. Finally, the integration fails. This method called direct integration is unstable. Methods for considering the constraint equations during integration, such as mixed integration (Steigerwald 1990) or stabilisation of constraints (Baumgarte 1972), are also prone to stability problems.

The penalty method proposed by Bayo et al. (1988) eliminates the constraint equations from (102) and results in a system of sole ordinary differential equations. An augmented Lagrangian formulation of the penalty method ensures numerically conditioned integration. This formulation overcomes also problems related to kinematic singular configurations and redundant constraints.

$$\text{Let } \tilde{\mathbf{m}} = \begin{bmatrix} \mathbf{m} & \mathbf{0} \\ \mathbf{0} & 4 \cdot \mathbf{G}^T \cdot \mathbf{J}^{(2)} \cdot \mathbf{G} \end{bmatrix}, \quad \tilde{\mathbf{Q}} = \begin{bmatrix} \mathbf{F}^{a(1)} \\ 2 \cdot \mathbf{G}^T \cdot \mathbf{M}^{a(2)} + 8 \cdot \mathbf{G}^T \cdot \mathbf{G} \cdot \dot{\mathbf{G}}^T \cdot \mathbf{J}^{(2)} \cdot \dot{\mathbf{G}} \cdot \mathbf{p} \end{bmatrix},$$

$$\tilde{\Theta}_q^T = \begin{bmatrix} \Theta_r^T & \mathbf{0} \\ \Theta_p^T & \Theta_p^{PT} \end{bmatrix}, \quad \tilde{\boldsymbol{\lambda}} = \begin{bmatrix} \boldsymbol{\lambda} \\ \boldsymbol{\lambda}^p \end{bmatrix}, \quad \text{and } \tilde{\mathbf{q}} = \begin{bmatrix} \dot{\mathbf{r}}^{(1)} \\ \dot{\mathbf{p}} \end{bmatrix}.$$

The equations of motion can then be written without the kinematic acceleration equations as:

$$\tilde{\mathbf{m}} \cdot \ddot{\mathbf{q}} + \tilde{\Theta}_q^T \cdot \tilde{\boldsymbol{\lambda}} = \tilde{\mathbf{Q}} \quad (107)$$

The penalty method introduces fictitious terms such as the fictitious potential V^* and fictitious kinetic energy T^* , and dissipative forces G_k in order to iteratively replace the Lagrange multipliers $\boldsymbol{\lambda}$ while determining $\tilde{\mathbf{Q}}$.

$$V^* = \frac{1}{2} \cdot \Theta^T \cdot \boldsymbol{\alpha} \cdot \boldsymbol{\Omega}^2 \cdot \Theta$$

$$T^* = \frac{1}{2} \cdot \dot{\Theta}^T \cdot \boldsymbol{\alpha} \cdot \dot{\Theta} \quad (108)$$

$$G_k = -2 \cdot \boldsymbol{\alpha} \cdot \boldsymbol{\Omega} \cdot \boldsymbol{\mu} \cdot \dot{\Theta}$$

By determining the Lagrangian $L^* = T^* - V^*$, the work done by the dissipative forces, and application of the Euler-Lagrange equations and proper substitutions⁴ one obtains the convergent recursive rule:

⁴ The whole derivation is shown in García de Jalón & Bayo, J. 1994, 164ff.

$$\left(\tilde{\mathbf{m}} + \tilde{\Theta}_q^T \cdot \boldsymbol{\alpha} \cdot \tilde{\Theta}_q\right) \cdot \ddot{\mathbf{q}}_{i+1} = \tilde{\mathbf{m}} \cdot \ddot{\mathbf{q}}_i - \tilde{\Theta}_q^T \cdot \boldsymbol{\alpha} \cdot \left(-\tilde{\gamma} + 2 \cdot \boldsymbol{\Omega} \cdot \boldsymbol{\mu} \cdot \dot{\tilde{\Theta}} + \boldsymbol{\Omega}^2 \cdot \tilde{\Theta}\right) \quad (109)$$

with $\tilde{\mathbf{m}} \cdot \ddot{\mathbf{q}}_0 = \tilde{\mathbf{Q}}$

Expression (109) uses (110) to approximate the Lagrange multipliers $\boldsymbol{\lambda}$ in expression (107) and iteratively eliminates them. The penalty system determined by $\boldsymbol{\alpha}$, $\boldsymbol{\Omega}$ and $\boldsymbol{\mu}$ only introduces values in (109) if the motion violates the kinematic constraints. García de Jalón & Bayo (1994) describe the physical interpretation of the penalty system.

$$\boldsymbol{\lambda}_{i+1} - \boldsymbol{\lambda}_i = \boldsymbol{\alpha} \cdot \left(\ddot{\tilde{\Theta}} + 2 \cdot \boldsymbol{\Omega} \cdot \boldsymbol{\mu} \cdot \dot{\tilde{\Theta}} + \boldsymbol{\Omega}^2 \cdot \tilde{\Theta}\right) \quad (110)$$

The same set of penalty values for each constraint equations has been successfully applied by the author, i.e. $\boldsymbol{\alpha} = \alpha \mathbf{I}$, $\boldsymbol{\Omega} = \Omega \mathbf{I}$, and $\boldsymbol{\mu} = \mu \mathbf{I}$. Values of $\alpha=10\text{E}4$, $\Omega=10$, $\mu=1$ have been used.

6.3.2.2 Transformation into a first order system of ODE

ODE solvers typically integrate only first order ODE systems. As the current ODE system of the equations of motion is a second order system, it is necessary to transform the equations into a first order system. It is trivial by defining equation (111) and replacing it into (109).

$$\hat{\mathbf{q}} = \dot{\tilde{\mathbf{q}}} \quad \text{and} \quad \dot{\hat{\mathbf{q}}} = \ddot{\tilde{\mathbf{q}}} \quad (111)$$

Expression (112) shows the first order system of ODEs. The number of equations doubles compared to (109). For a single block 14 ordinary differential equations are necessary. The first row represents the ODE at the velocity level, while the second row are the ODEs at the acceleration level. Starting values have to be provided for each of the equations for the initial value problem.

$$\dot{\tilde{\mathbf{q}}} = \hat{\mathbf{q}}$$

$$\left(\tilde{\mathbf{m}} + \tilde{\Theta}_q^T \cdot \boldsymbol{\alpha} \cdot \tilde{\Theta}_q\right) \cdot \dot{\hat{\mathbf{q}}}_{i+1} = \tilde{\mathbf{m}} \cdot \dot{\hat{\mathbf{q}}}_i - \tilde{\Theta}_q^T \cdot \boldsymbol{\alpha} \cdot \left(-\tilde{\gamma} + 2 \cdot \boldsymbol{\Omega} \cdot \boldsymbol{\mu} \cdot \dot{\tilde{\Theta}} + \boldsymbol{\Omega}^2 \cdot \tilde{\Theta}\right) \quad (112)$$

6.3.2.3 Numerical integration

A number of methods for the numerical integration of the equations of motion as an initial value problem are available. The selection of a numerical integration method is a trade-off between different competing properties, for instance efficiency and accuracy. The following non-exhaustive list summarises the principal properties which should be considered (Dahlquist 1956, García de Jalón & Bayo 1994, Butcher 2008):

- Stability is a method's property of keeping errors of the numerical integration bounded in subsequent integration steps. Using an unstable method the errors increase exponentially after some time steps. Stability depends on the selected method and the type of problem. Stable algorithms may be
 - conditionally stable: stable for a restricted range of time spans
 - stiffly stable: stable for stiff problems except oscillatory motion
 - A-stable (unconditionally stable): stable for any range of time spans
- Consistency describes whether the algorithm basically solves the problem. Methods with an order greater than zero are consistent.
- Convergence is the property that the numerical solution approaches the exact solution with decreasing time steps. Consistency and stability are necessary and sufficient for convergence.
- Accuracy is the difference between the numerical and the exact solution. Since the latter is unknown, the difference is estimated using the local truncation error. The step size and the order of the method control the accuracy of the solution.

The stiffness of a problem is an important factor. Stiffness in this context is not universally defined but depends on the context of the problem. Stiff problems show a behaviour which can numerically only be solved by dramatically changing the step sizes even a couple of orders of magnitude. Stiff behaviour may arise from huge mass, stiffness or damping differences, the discretisation, or constraint violations. Stiff problems call for A-stable algorithms especially if oscillatory motion takes place (García de Jalón *et al.* 1994).

A few more properties describe the architecture of the numerical methods affecting efficiency, accuracy, and memory requirements:

- Explicit methods use only already determined function values to calculate future function values while implicit methods also use future function values. Implicit methods need therefore a recursive calculation.

- Single step methods use only the current function value to determine the future function value while multi-step methods use also past function values. Single step methods require more function evaluations and thus are less efficient than multistep methods but they need less memory and are self-starting.
- Methods may use fixed step sizes or adaptive step sizes. Methods using the latter increase or decrease the step sizes based on the estimated local error. They are more efficient but harder to implement. Multi step methods with adaptive step sizes shall be implemented as multi value methods (Press et al. 2007).

The Adams-Bashforth-Moulton (ABM) predictor-corrector method is suitable for integrating the equations of motion (112). It is a multistep method, i.e. previous function values are used to calculate the function value at the next time step. The method uses an explicit predictor and an implicit corrector term to numerically approximate the solution. Let the n^{th} step be at a time t_n the solution at a time t_{n+1} is predicted by expression (113). s determines the order of the method. The coefficients β_j^P are the Adams-Bashforth terms. They depend on the order of the method and can be taken from textbooks on numerical mathematics (e.g. Butt 2007). The left column of

Table 21 shows the terms for the fourth order method.

$$\begin{bmatrix} \tilde{\mathbf{q}}_{n+1} \\ \hat{\mathbf{q}}_{n+1} \end{bmatrix}^P = \begin{bmatrix} \tilde{\mathbf{q}}_n \\ \hat{\mathbf{q}}_n \end{bmatrix} + \Delta t \cdot \sum_{j=0}^s \beta_j^P \cdot \begin{bmatrix} \dot{\tilde{\mathbf{q}}}(t_{n-j}, \tilde{\mathbf{q}}_{n-j}) \\ \dot{\hat{\mathbf{q}}}(t_{n-j}, \hat{\mathbf{q}}_{n-j}) \end{bmatrix} \quad (113)$$

The predicted solution is used in the implicit correction (114) as the additional required input. β_{j+1}^C are the Adams-Moulton terms which also depend on the order of the method. The right column of

Table 21 shows the terms for the fourth order method.

$$\begin{bmatrix} \tilde{\mathbf{q}}_{n+1} \\ \hat{\mathbf{q}}_{n+1} \end{bmatrix}^C = \begin{bmatrix} \tilde{\mathbf{q}}_n \\ \hat{\mathbf{q}}_n \end{bmatrix} + \Delta t \cdot \sum_{j=-1}^{s-1} \beta_{j+1}^C \cdot \begin{bmatrix} \dot{\tilde{\mathbf{q}}}(t_{n-j}, \tilde{\mathbf{q}}_{n-j}) \\ \dot{\hat{\mathbf{q}}}(t_{n-j}, \hat{\mathbf{q}}_{n-j}) \end{bmatrix} \quad (114)$$

Table 21: ABM terms for fourth order method

	β^P	β^C
β_0	0	-9/24
β_1	-55/24	-19/24
β_2	59/24	5/24
β_3	-37/24	-1/24
β_4	9/24	0

Figure 80 outlines the numerical integration scheme using the ABM predictor-corrector method. The derivatives of past time steps are used to predict the function values from the current time step \tilde{q}_n to the future time step \tilde{q}_{n+1}^P with expression (113). The evaluation of expression (112) leads to derivatives for the future time step \tilde{q}_{n+1}^C . This is indicated by the grey slopes in Figure 80. It is used in expression (114) to improve the function values \tilde{q}_{n+1}^C . For non-stiff problems a recursive iteration between function evaluation and corrector steps is sufficient. For stiff problems a Newton-Raphson iteration is mandatory (Press et al. 2007). Iteration is repeated until subsequent function values stay within a predefined accuracy threshold.

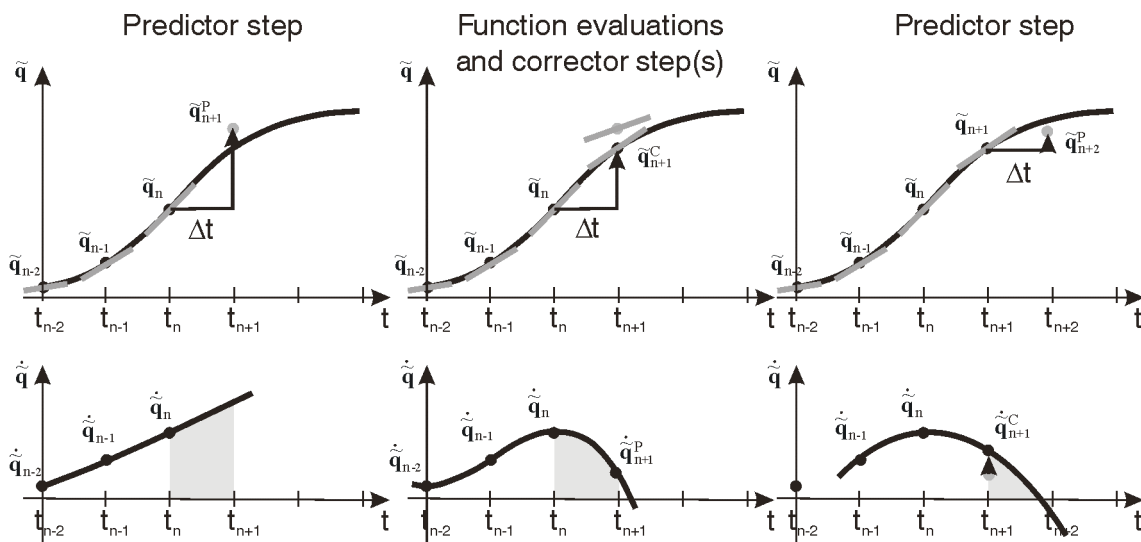


Figure 80: Numerical integration scheme of an Adams-Bashforth-Moulton predictor corrector method. Sketch modified after Hairer & Wanner (2009)

6.3.2.4 Determination of constraint forces

The forces transmitted through the kinematic constraints have not been addressed so far. They do not appear in the presented formulation since only virtual displacements and rotations of the block are considered. In any case, the sum of the virtual works must remain zero for the same mechanical system independent of the formulation. If the constraints are released, it is necessary to apply reaction forces in order to keep the mechanical system consistent. Since the motion should stay the same, the virtual work stays the same as well. Hence, the term describing the virtual work of the reaction forces has to be null as well.

$$\delta \mathbf{r}_{Pi}^{(2)T} \cdot \left(\mathbf{F}_{i,kin}^{(2)} + \mathbf{A}^{(12)T} \cdot \Theta_{r,i,kin}^T \cdot \boldsymbol{\lambda}_{kin} \right) + \delta \boldsymbol{\pi}_i^{(2)T} \cdot \left(\mathbf{M}_{i,kin}^{(2)} + \Theta_{\pi,i,kin}^T \cdot \boldsymbol{\lambda}_{kin} + \mathbf{s}_i^{*(2)T} \cdot \mathbf{A}^{(12)T} \cdot \Theta_{r,i,kin}^T \cdot \boldsymbol{\lambda}_{kin} \right) = 0 \quad (115)$$

Virtual displacements and rotations are arbitrary, thus follow expressions (116) and (117). The index i refers to the constraint i and the index kin indicates parameters related to kinematic constraints. These expressions include the Lagrange multipliers for the kinematic constraints. They comply with expression (102) and could be determined from it.

$$\mathbf{F}_{i,kin}^{(2)} = -\mathbf{A}^{(12)T} \cdot \Theta_{r,i,kin}^T \cdot \boldsymbol{\lambda}_{kin} \quad (116)$$

$$\mathbf{M}_{i,kin}^{(2)} = -\Theta_{\pi,i,kin}^T \cdot \boldsymbol{\lambda}_{kin} - \mathbf{s}_i^{*(2)T} \cdot \mathbf{A}^{(12)T} \cdot \Theta_{r,i,kin}^T \cdot \boldsymbol{\lambda}_{kin} \quad (117)$$

In the proposed numerical integration scheme they have been eliminated. It is, thus, necessary to append a so-called inverse dynamics routine. It is the equations of motion with the parameters on the motion given and solving them for the Lagrange multipliers (118). It is a linear system in $\boldsymbol{\lambda}$.

$$\begin{bmatrix} \Theta_r^T \\ \Theta_{\pi}^{T(2)} \end{bmatrix} \cdot \boldsymbol{\lambda} = \begin{bmatrix} \mathbf{F}^{a(1)} - m \cdot \ddot{\mathbf{r}}^{(1)} \\ \mathbf{M}^{a(2)} - \boldsymbol{\omega}^{*(2)} \cdot \mathbf{J}^{(2)} \cdot \boldsymbol{\omega}^{(2)} - \mathbf{J}^{(2)} \cdot \dot{\boldsymbol{\omega}}^{(2)} \end{bmatrix} \quad (118)$$

6.3.3 Equilibrium

Finding the equilibrium position is a core task in the block stability analysis. A consistent analysis does not require assumptions on force magnitudes at limit equilibrium, or force orientations but delivers these parameters. The equilibrium position is a special configuration complying with the equations of motion where velocities and accelerations vanish. Expression (119) shows the equations of equilibrium of a constrained block in Newton-Euler formalism. The left hand side represents the kinematic constraints, more specifically the constraint forces.

They must equilibrate with the external forces on the right hand side. It is a system of nonlinear equations since the entire left hand side is unknown.

$$\begin{bmatrix} \Theta_r^T \\ \Theta_\pi^{(2)T} \end{bmatrix} \cdot \lambda = \begin{bmatrix} \mathbf{F}^{a(1)} \\ \mathbf{M}^{a(2)} \end{bmatrix} \quad (119)$$

The results have to additionally comply with the kinematic equations (García de Jalón & Bayo 1994). Solution strategies include minimisation of potential energy for systems having a potential, dynamic relaxation, and continuation methods. The former is not applicable for the current purpose since non-conservative forces such as friction and follower loads such as water pressure are present in a rock environment. The latter two provide the framework for solving the equilibrium problem – both of them still pose shortcomings. Dynamic relaxation uses the entire set of dynamic equations including dampers. The body approaches the equilibrium position during a time integration procedure. The method can cope with all kinds of forces and constraints but the result requires interpretation. The equilibrium position is not uniquely defined and requires artificial termination criteria. Continuation methods solve the equilibrium problem by determining the equilibrium path. The body approaches the equilibrium position by incrementally increasing the external loads. It either finds the final position or, alternatively, a failure point. One drawback of the method is that at current rigid kinematic constraints cannot be considered in the approach. As an approximation they have to be introduced as stiff constraints.

The following section describes the concept of a continuation method as implemented in this work. The framework for dynamic relaxation has already been introduced in the previous section.

6.3.3.1 Continuation method

Continuation methods are used to find the approximate solution of non-linear systems of the form $\mathbf{F}(\mathbf{u})=\mathbf{0}$ where \mathbf{u} is a so-called state vector. If \mathbf{u} is the displacement vector of the block and \mathbf{F} are the equations of equilibrium continuation methods provide as a result the equilibrium position (or displacement) and the reactive forces.

Let $\mathbf{Q} = [\mathbf{F}^{a(1)} \ \mathbf{M}^{a(2)}]^T$ then the equilibrium equations without kinematic constraints render the well-known expression (120).

$$\mathbf{Q}(\mathbf{q}) = \mathbf{0} \quad (120)$$

\mathbf{q} is the state vector representing displacements and rotations. Algebraic equations related to kinematic constraints are not considered in this approach.

Finding the solution of the non-linear system is directly not possible different sources of loads interact with complex reactions. Like with the equations of motion a numerical solution in general is necessary. The idea of the solution scheme is a step-by-step application of loads while determining the intermediate equilibrium position. The result is the equilibrium path consisting of the discrete equilibrium points showing the path to the final equilibrium position. The properties of the equilibrium path allow also for insights into the behaviour of the block while approaching equilibrium or failure.

One widely used procedure of continuation methods, for instance in chemical engineering, dynamic analysis, physics, etc., is the predictor-corrector approach. The complex non-linear problems are formulated in a staged incremental-iterative procedure. Loads are applied to the system in subsequent stages where only one category of load is considered on one stage, for instance, self weight, dead loads, initial stresses, water forces, etc. The sequence of load shall reflect the sequence in real world and also numerical reasoning. Within one stage the load is incrementally applied from the initial value to the final value. The load increment is proportional to a stage control parameter. Within each increment the intermediate equilibrium positions are determined by using a non-linear optimisation scheme which aims at complying expression (120).

Staging is necessary since direct superposition is not applicable in non-linear analysis, especially with path-dependent problems such as friction. Staging allows also for a single scalar stage control parameter. The end result of one stage serves as the input for the subsequent stage. Incrementation is necessary to provide initial values close enough to the equilibrium point to support convergence of the non-linear optimisation, allows treatment of critical points encountered along the equilibrium path, provides a means for decreasing the path-dependence of non-linear material behaviour, and also provides insights into the behaviour of the system while approaching equilibrium or failure.

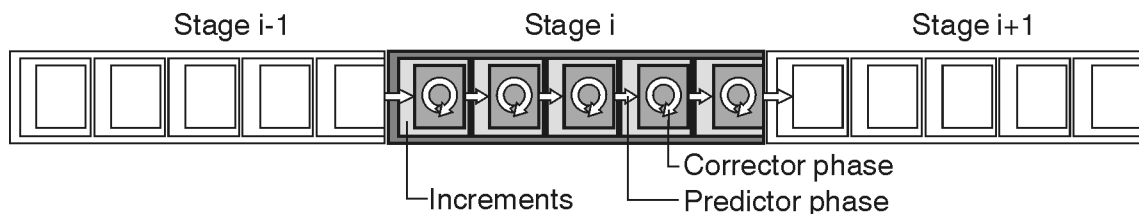


Figure 81: Concept of the applied continuation method using a predictor-corrector approach

The iteration comprises a predictive phase in which the initial values for the subsequent corrective phase are provided. The corrective phase basically is a

non-linear optimisation. Figure 81 shows the concept of the applied continuation method. Subsequent stages comprise several load increments. Each increment starts with a predictive phase which provides initial values for the corrective phase. Each increment results in a new equilibrium point of the equilibrium path.

The basis for determining the equilibrium path is the residual force equation shown in expression (121). \mathbf{res} is the residual force vector determined from the external force and moment vector \mathbf{Q} and vanishes for equilibrium. The active force vector \mathbf{Q}^a and constrained force vector \mathbf{Q}^c determine the residual force vector. Constrained forces are those which do not exhibit active force but only react on block displacement. Both, the active forces and the constrained forces, depend on the state vector \mathbf{q} which contains displacements and rotations.

$$\mathbf{res} = \mathbf{Q}(\mathbf{q}) = \mathbf{Q}^c(\mathbf{q}) + \mathbf{Q}^a(\mathbf{q}) = \mathbf{0} \quad (121)$$

The active force vector \mathbf{Q}^a is incrementally increased from the initial (usually zero) to the final value of the stage. The increments are related to the stage control parameter λ_{stage} . The stage control parameter and the constrained force vector are iteratively accommodated for the current increment in order to comply with the residual force equation (122).

$$\mathbf{res}(\mathbf{q}, \lambda_{stage}) = \mathbf{Q}^c(\mathbf{q}) + \lambda_{stage} \cdot \mathbf{Q}^a(\mathbf{q}) = \mathbf{0} \quad (122)$$

The recursive computation starts from the last known equilibrium point of the previous increment. Expression (123) shows the incremental form of the residual force equation.

$$\frac{\partial \mathbf{res}}{\partial \mathbf{q}} \dot{\mathbf{q}} + \frac{\partial \mathbf{res}}{\partial \lambda_{stage}} \dot{\lambda}_{stage} = \mathbf{0} \quad (123)$$

Let us introduce the tangential stiffness matrix of the equilibrium path \mathbf{K} . The active force vector \mathbf{Q}^a can also be interpreted as a tangential load vector.

$$\mathbf{K} = -\frac{\partial \mathbf{res}}{\partial \mathbf{q}} \quad \text{and} \quad \mathbf{Q}^a = \frac{\partial \mathbf{res}}{\partial \lambda_{stage}} \quad (124)$$

Inserting (124) into (123) and rearranging renders the relationship between load vector variation and displacement vector variation (125).

$$\mathbf{K} \cdot \dot{\mathbf{q}} = \mathbf{Q}^a \cdot \dot{\lambda}_{stage} \quad \text{or linearised} \quad \mathbf{K} \cdot \Delta \mathbf{q} = \mathbf{Q}^a \cdot \Delta \lambda_{stage} \quad (125)$$

Expression (122) and (125) comprise n equations but $n+1$ unknowns due to the introduction of the stage control parameter. In order to uniquely solve these systems of equation an additional equation is necessary. It is provided by the increment control strategy. The increment control strategy constrains the stage

control parameter to an external condition. The constraint is, geometrically, a hypersurface⁵ which aims to intersect the equilibrium path. The intersection between the hypersurface and the equilibrium path is the new equilibrium point.

The simplest increment control is load control where $\Delta\lambda_{\text{stage}}$ is a constant value L_{step} . The corresponding constraint surface is a horizontal hyperplane. The predictor finds an intersection of the tangential hyperplane with the horizontal hyperplane. During the corrective phase iterations take place along the surface of the constraint surface requiring only a variation of displacements. The condition is:

$$\Delta\lambda_{\text{stage}} - L_{\text{step}} = 0 \quad (126)$$

Load control is easy to implement but has significant drawbacks when analysing failure or stability problems. Load controlled increments do not take the shape of the equilibrium path into account (Figure 82 left). When approaching failure the equilibrium path becomes more and more parallel to the constraint surface. A further increment may exceed the bearing capacity of the system inhibiting the intersection between equilibrium path and constraint surface. The approximate determination of failure can only be achieved with small increments resulting in excessive computational effort.

A more comprehensive increment control strategy is the arclength control. There are several arclength controls available referring to the shape of the constraint surface. They can be summarised as hyperplanar (Riks 1972, Wempner 1971), hyperspherical (Crisfield 1981), and hyperellipsoidal (e.g. Ritto-Corrêa & Camotim 2008) methods. The size of the increment (now considering load increase and displacement) is related to the arclength of the equilibrium path⁶. In this basic method the hypersphere is centred at the last known equilibrium point (Figure 82 right). The predictor finds an intersection of the tangential hyperplane with the constraint surface. During the corrective phase iterations take place along the surface of the constraint surface requiring a variation of displacements and load. The condition for the used hyperspherical arclength control is shown in expression (127).

$$\Delta\lambda_{\text{stage}}^2 + \Delta\mathbf{q}^T \cdot \mathbf{S}^2 \cdot \Delta\mathbf{q} - L_{\text{step}}^2 = 0 \quad (127)$$

⁵ It is a hypersurface because it is formulated in $n+1$ dimensional space.

⁶ Actually, it is the pseudo-arclength since the measure is not taken at the curved equilibrium path but at the tangential hyperplane.

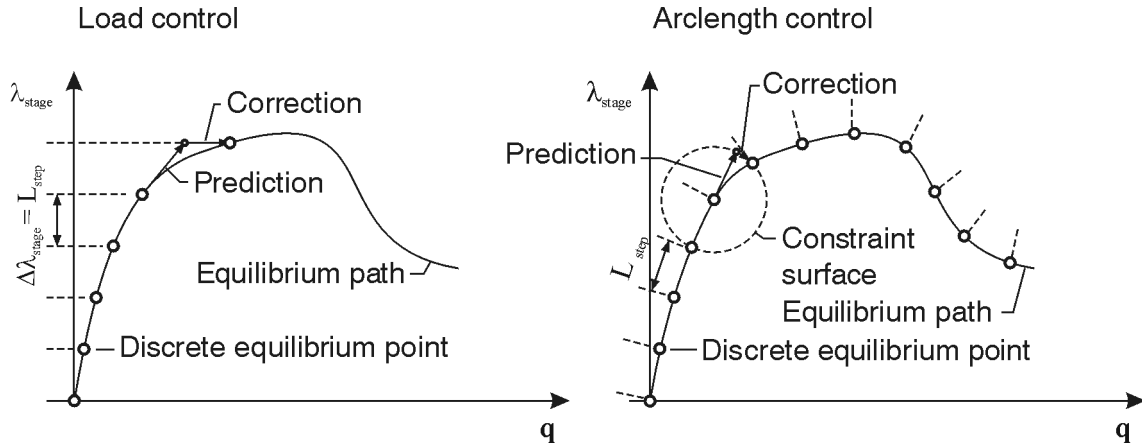


Figure 82: Load control vs arclength control

Expression (127) is dimensionally not consistent. $\Delta\lambda_{\text{stage}}$ is dimensionless while $\Delta\mathbf{q}$ carries displacements, Euler parameters for rotations, and possibly Lagrange multipliers (see section 6.3.3.4). The scaling matrix \mathbf{S} is introduced to render expression (127) dimensionally consistent (128).

$$\mathbf{S} = \begin{bmatrix} \omega_r \cdot \mathbf{I}_{3 \times 3} & \mathbf{0} & \mathbf{0} \\ \mathbf{0} & \omega_p \cdot \mathbf{I}_{4 \times 4} & \mathbf{0} \\ \mathbf{0} & \mathbf{0} & \omega_\lambda \cdot \mathbf{I}_{m \times m} \end{bmatrix} \quad (128)$$

ω_r , ω_p , and ω_λ are scaling factors for each category of the state vector. They can be kept constant throughout the procedure at values representing the system scale unless abrupt scale changes occur. In order to overcome problems with scale changes scaling factors can be adjusted at each increment. Cardona & Huespe (1998) suggest to use values to render for displacements as shown in expression (129). The index 0 indicates values taken at the first increment or, in case of adjusting algorithm, at the increment preceding the current one.

$$\omega_r = 1 \quad \omega_p = \frac{\|\mathbf{r}_0\|}{\|\mathbf{p}_0\|} \quad \omega_\lambda = \frac{\|\mathbf{r}_0\|}{\|\boldsymbol{\lambda}_0\|} \quad (129)$$

Felippa (1987) proposes to use the stiffness matrix \mathbf{K} for scaling the state vector. This has been applied, for instance, by Tonon (2007b).

6.3.3.2 Incrementation – the predictor phase

Incrementation starts at the last known equilibrium point. The predictor points along the tangential hyperplane (130) and its length constrained by (127).

$$\Delta \mathbf{q} = \mathbf{K}^{-1} \cdot \mathbf{Q}^a \cdot \Delta \lambda_{stage} \quad (130)$$

Feeding (130) into (127) one can calculate the arclength controlled load increment as shown in expression (131). It has obviously two roots referring to the two intersections of the equilibrium path with the (closed) constraint surface.

$$\Delta \lambda_{stage}^P = \pm \frac{L_{step}}{\sqrt{\mathbf{q}^{QT} \cdot \mathbf{S}^2 \cdot \mathbf{q}^Q + 1}} \quad \text{where } \mathbf{q}^Q = \mathbf{K}^{-1} \cdot \mathbf{Q}^a \quad (131)$$

The sign in expression (131) shall always be positive at the first load step. In subsequent increments the sign is based on the previous increment such that current predictor points outward the previous constraint surface (Figure 83). One should keep in mind that the orientation of \mathbf{q}^Q always points towards the upward direction of the tangential hyperplane.

$$sign(\Delta \lambda_{stage,i}^P) = sign(\Delta \mathbf{q}_{i-1}^{CT} \cdot \mathbf{S}^2 \cdot \mathbf{q}_i^Q + \Delta \lambda_{stage,i-1}^C) \quad (132)$$

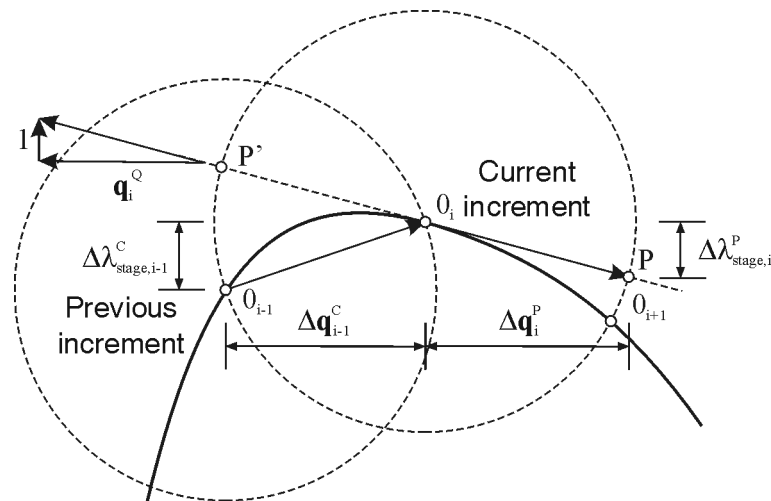


Figure 83: Selection of the sign of the predictor increment based on the previous increment

With a sufficiently small increment size the predictive phase only can be used to determine the equilibrium path. The predicted values approach the true equilibrium path with decreasing increment size. One should be aware of the inherent drift error involved with this kind of incrementation (forward Euler) (Figure 84). Minimising the drift error while maintaining a reasonable increment size can only be achieved with a subsequent iterative corrective phase.

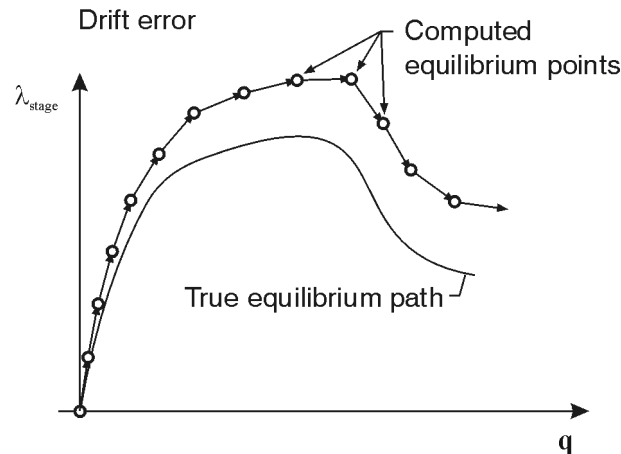


Figure 84: Drift error related to pure incrementation with forward Euler method

6.3.3.3 Iteration – the corrective phase

The iterative corrective phase eliminates (or at least reduces) the drift error while satisfying both, the equilibrium and the increment control. During iteration the corrected solutions march along the constraint surface towards the equilibrium point (Felippa 1987). As mentioned above, load control comes with a horizontal hyperplane as constraint surface. As a consequence intersection points with the equilibrium path, in particular when approaching failure, is not ensured. A closed constraint surface such as a hypersphere ensures intersection with the equilibrium path if it is centred at the last known equilibrium point.

Figure 85 shows the relationships between the predictive and the corrective phase approaching a new equilibrium point using a hyperspherical constraint surface. The last known equilibrium point is θ and the predicted point is A . Prediction has been outlined in the previous section. The equilibrium point is A' for the same block displacement $\Delta \mathbf{q}^P$. The residual forces between A and A' are defined by expression (122) – the residual force equation. The correction is a full Newton-Raphson method and thus requires the calculation of the tangent stiffness matrix at $\Delta \mathbf{q}^P$. The vectors \mathbf{q}^R and \mathbf{q}^Q are determined (133).

$$\mathbf{q}^R = \mathbf{K}_{A'}^{-1} \cdot \mathbf{res}_A \quad \text{and} \quad \mathbf{q}^Q = \mathbf{K}_{A'}^{-1} \cdot \mathbf{Q}^a \quad (133)$$

The vector equation for the new corrected point B is thus:

$$\begin{bmatrix} \Delta \mathbf{q}^C \\ \Delta \lambda_{stage}^C \end{bmatrix} = \begin{bmatrix} \Delta \mathbf{q}^P \\ \Delta \lambda_{stage}^P \end{bmatrix} + \begin{bmatrix} \mathbf{q}^R \\ 0 \end{bmatrix} + \delta \lambda_{stage}^C \cdot \begin{bmatrix} \mathbf{q}^Q \\ 1 \end{bmatrix} \quad (134)$$

Note that the prefix Δ refers to incremental change while the prefix δ refers to iterative change.

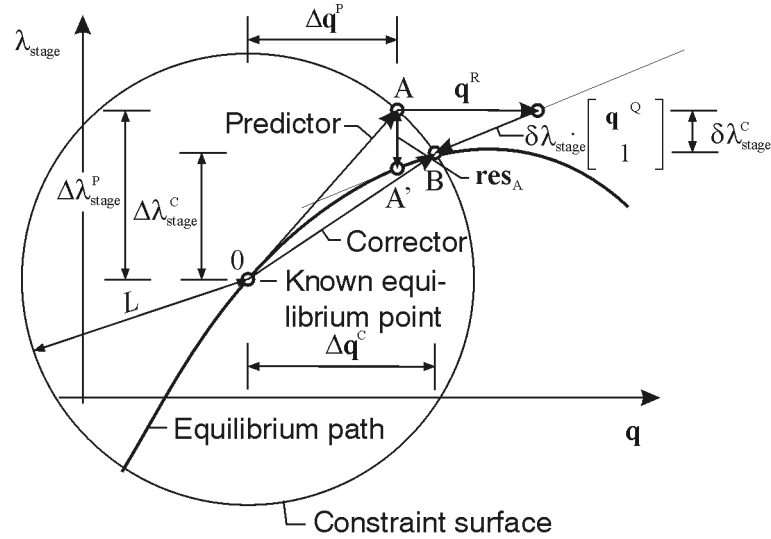


Figure 85: Predictive and corrective phase using a hyperspherical constraint surface centred in the last known equilibrium point

Since B has to lie on the constraint surface, it also has to comply with expression (127). This leads to the quadratic equation in $\delta \lambda_{stage}$ (135)

$$\begin{aligned} & \delta \lambda_{stage}^{C2} \cdot [\mathbf{q}^{QT} \cdot \mathbf{S}^2 \cdot \mathbf{q}^Q + 1] + \delta \lambda_{stage}^C \cdot 2 \cdot [\mathbf{q}^{QT} \cdot \mathbf{S}^2 \cdot (\mathbf{q}^R + \Delta \mathbf{q}^P) + \Delta \lambda_{stage}^P] + \dots \\ & \dots + [(\Delta \mathbf{q}^P + \mathbf{q}^R)^T \cdot \mathbf{S}^2 \cdot (\Delta \mathbf{q}^P + \mathbf{q}^R) + \Delta \lambda_{stage}^{P2} - L_{step}^2] = 0 \end{aligned} \quad (135)$$

Expression (136) represents the solution of (135). Once again, it has two roots corresponding to the intersection of the linearised equilibrium line with the constraint surface.

$$\delta\lambda_{stage}^C = \frac{-b \pm \sqrt{b^2 - 4 \cdot a \cdot c}}{2 \cdot a} \quad (136)$$

$$\text{where } a = \mathbf{q}^{QT} \cdot \mathbf{S}^2 \cdot \mathbf{q}^Q + 1$$

$$b = 2 \cdot \left[\mathbf{q}^{QT} \cdot \mathbf{S}^2 \cdot (\mathbf{q}^R + \Delta\mathbf{q}^P) + \Delta\lambda_{stage}^P \right]$$

$$c = (\Delta\mathbf{q}^P + \mathbf{q}^R)^T \cdot \mathbf{S}^2 \cdot (\Delta\mathbf{q}^P + \mathbf{q}^R) + \Delta\lambda_{stage}^{P2} - L_{step}^2$$

Several different criteria for selecting the proper corrector root have been reported. If double-backing (strong directional changes) of the equilibrium path is not expected and shall be prevented, the root closest to the prediction or previous correction shall be selected. This is accomplished by maximising the product between the predictor (or previous corrector) and the current corrector. It is only necessary to consider terms which depend on $\Delta\lambda_{stage}$.

$$\delta\lambda_{stage}^C = \begin{cases} \delta\lambda_{stage,1}^C & \text{if } t \cdot \delta\lambda_{stage,1}^C > t \cdot \delta\lambda_{stage,2}^C \\ \delta\lambda_{stage,2}^C & \text{otherwise} \end{cases} \quad (137)$$

$$\text{where } t = \Delta\mathbf{q}^P \cdot \mathbf{S}^2 \cdot \mathbf{q}^Q + \Delta\lambda_{stage}^P$$

The iteration is repeated until it complies with defined convergence criteria, i.e. the residual force vector approximately vanishes. Relative criteria are preferred over absolute ones (138). \mathbf{res}_A is the residual force vector after the predictor step.

$$\frac{\|\mathbf{res}\|}{\|\mathbf{res}_A\|} < 10^{-4} \quad \text{and} \quad \frac{\|\Delta\mathbf{q}_i^C - \Delta\mathbf{q}_{i-1}^C\|}{\|\Delta\mathbf{q}^P\|} < 10^{-2} \quad (138)$$

Although this approach is not susceptible to divergence, divergence criteria (139) shall be monitored and, at compliance, cause interruption or countermeasures. The number of iterations is limited to 20 to avoid periodic bouncing about a solution.

$$\frac{\|\mathbf{res}\|}{\|\mathbf{res}_A\|} > 10^3 \quad \text{or} \quad \frac{\|\Delta\mathbf{q}_i^C - \Delta\mathbf{q}_{i-1}^C\|}{\|\Delta\mathbf{q}^P\|} > 10^3 \quad (139)$$

The proposed procedure only converges if the square root in expression (136) has real roots. Complex roots happen when the linearised equilibrium line does not intersect the constraint surface. In this case the iteration shall be interrupted and a new prediction with a decreased increment size (e.g. 50%) executed (Ritto-

Corrêa & Camotim 2008). Decrease of the increment size has to take place until the square root in expression (136) becomes real. Another way to overcome complex roots is a line search algorithm. Another convergence issue may occur in case of sudden snap-back of the equilibrium path together with the proposed corrector root selection.

6.3.3.4 Consideration of kinematic constraints

Kinematic constraints have not yet been considered in the formulation. Again, the Lagrange multiplier method helps to set up a concept for solving the equilibrium problem of a kinematically constraint block. The equilibrium problem in other words is to find the minimum of expression (122), the residual force equation. In this expression displacements can be arbitrary. With the presence of kinematic constraints, displacements have to be feasible with the constraint equations. The constraint equations according to section 0 are introduced in expression (122) using Lagrange multipliers (Houlsby et al. 2000). In case of the incremental formulation the Jacobian matrices of the constraint equations have to be used. This approach ensures kinematically feasible displacements while marching along the equilibrium path using an incremental/iterative procedure. The conceptual formulation is shown in expression (140). Since artificial displacements are not imposed at the kinematic constraints, the right hand side for the corresponding constraint equations remains zero. If displacements are imposed, one can use the formulation of Dutta & White (1997).

$$\begin{bmatrix} \mathbf{K} & \begin{bmatrix} \Theta_r^T \\ \Theta_\pi^{(2)T} \end{bmatrix} \\ \begin{bmatrix} \Theta_r & \Theta_\pi^{(2)} \end{bmatrix} & \mathbf{0} \end{bmatrix} \cdot \begin{bmatrix} \dot{\mathbf{q}} \\ \lambda \end{bmatrix} = \dot{\lambda}_{stage} \cdot \begin{bmatrix} \mathbf{Q}^a \\ \mathbf{0} \end{bmatrix} \quad (140)$$

At this stage it shall be noted that kinematic constraints can cause indeterminacy if the constraints have a higher degree than the degrees of freedom of the block (Tonon 2007b). Redundant constraints have to be treated specifically, for instance, by introducing additional criteria. One criterion is for instance that the norm of the Lagrange multiplier vector shall be minimal (García de Jalón & Bayo 1994).

6.4 Stability analysis

The section about block stability analysis shows the application of the methods developed in the previous sections for determining stability or the failure mode of a block. The approach is based on the continuation method. At first, a conceptual block model is introduced describing the principal elements of the mechanical block system. The subsequent section describes the application of loads (forces and moments) irrespective of whether they are active or responsive. The section includes also the determination of the stiffness matrix contributions. Finally, the status of the block while marching along the equilibrium path is monitored. Critical conditions can be encountered and allow conclusion about the stability condition of the block.

6.4.1 Block model

The block model is a three-dimensional mechanical system including a rigid body, loads (forces, moments) acting on the rigid body, springs with linear or nonlinear characteristic constraining the rigid body, and rigid kinematic constraints (Figure 86).

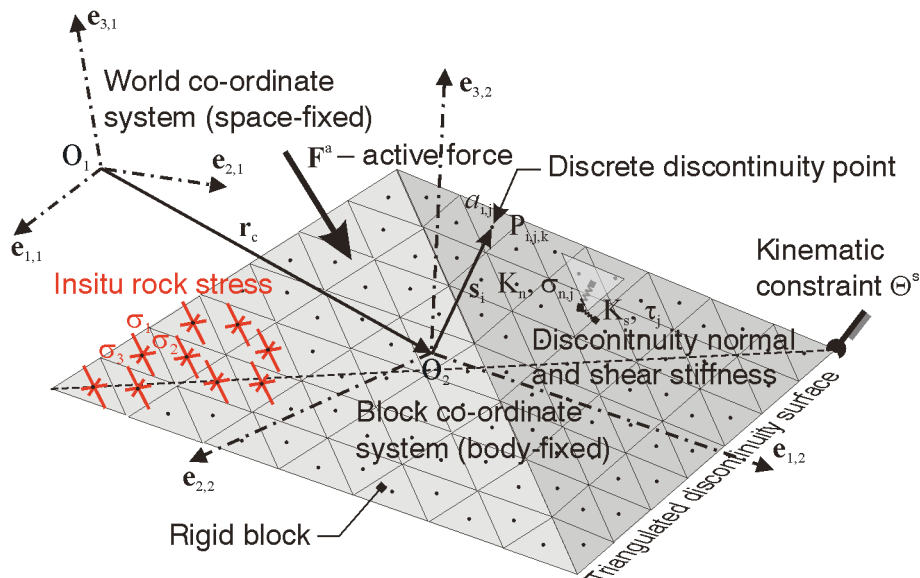


Figure 86: Conceptual mechanical model of a block comprising the rigid body, a triangulated discontinuity surface, kinematic constraints, active and constraint forces.

Unlike free faces discontinuities possess a triangulation. The centre of gravity of each triangle locates a point at which contact between block and rock mass is checked, and at which forces resulting from stresses are applied. Points in contact pose a constraint normal and shear force corresponding to the characteristic of the applied spring. The characteristic can be linear or non-linear. Kinematic constraints are applied following the descriptions of chapter 5. If present, insitu rock mass stresses can be considered at the discrete discontinuity points in contact.

Since discontinuities can only sustain compressive stresses, the block may detach from the adjacent rock mass. In order to correctly apply constraint forces it is necessary to check the contact status. Tonon (2007b) describes a contact logic for determining whether discrete points lie inside or outside the constraint space. The constraint space is a closed volume adjacent to the investigated block. If a block's discontinuity is inside the constraint space, it is in contact. Otherwise, if the block lies outside the constraint space, the point has detached. The constraint space is a subset of the rock mass. A point may lie inside or outside the constraint space. It changes its status if the iterative displacement of the point has an odd number of intersections with the surface of the constraint space. When entering the constraint space, one can also determine the displacement performed inside the constraint space within one iteration.

6.4.2 Forces and moments

6.4.2.1 Forces and moments fixed in space

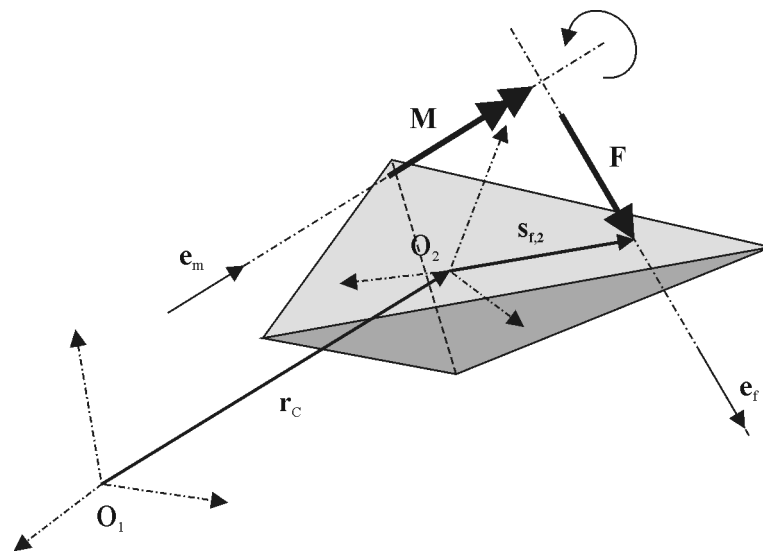


Figure 87: Force and moment acting on a block

Forces and moments which are fixed in space keep their orientation throughout block motion. If their magnitude depends on the block displacement, they contribute to the stiffness matrix (see section 6.3.3.1). Expression (141) shows the formulation in the space fixed coordinate system. Forces usually induce moments on the block. This is represented by the first term of the right hand side of the moment's equation in expression (141).

$$\begin{aligned}\mathbf{F}^{(1)} &= F \cdot \mathbf{e}_f^{(1)} \\ \mathbf{M}^{(1)} &= F \cdot \left(\mathbf{A}_0^{(12)} \cdot \mathbf{s}_{f,2}^{(2)} \right)^* \cdot \mathbf{e}_f^{(1)} + M \cdot \mathbf{e}_m^{(1)}\end{aligned}\quad (141)$$

Inertia forces are proportional to the body's mass and act in its centre of mass. In consequence, all moments are zero as shown in expression (142). Typical inertia forces are gravity or loads resulting from seismic acceleration.

$$\begin{aligned}\mathbf{F}^{(1)} &= m \cdot |\mathbf{a}| \cdot \mathbf{e}_f^{(1)} \\ \mathbf{M}^{(1)} &= \mathbf{0}\end{aligned}\quad (142)$$

6.4.2.2 Forces and moments fixed to the block

Forces and moments that are fixed to the block change their orientation according to the motion of the block. These kinds of loads are called follower forces and contribute to the stiffness matrix in any case. Expression (143) shows the general formulation of follower forces in the space-fixed coordinate system.

$$\begin{aligned}\mathbf{F}^{(1)} &= F \cdot \mathbf{A}^{(12)} \cdot \mathbf{e}_f^{(2)} \\ \mathbf{M}^{(1)} &= F \cdot \mathbf{A}^{(12)} \cdot \mathbf{s}_{f,2}^{*(2)} \cdot \mathbf{e}_f^{(2)} + M \cdot \mathbf{A}^{(12)} \cdot \mathbf{e}_m^{(2)}\end{aligned}\quad (143)$$

6.4.2.3 Hydrostatic water forces

Water forces act perpendicularly onto a surface i in direction of the blockside normal vector \mathbf{n}_i . Their magnitude depends on the local pressure head. Block surfaces subjected to water forces are discretised into a number m of local planar triangles. The vertices's position vectors $\mathbf{r}_{p,i,j,k}$ outline the triangles. For each vertex there is a corresponding pressure head given by the vectors $\mathbf{r}_{w,i,j,k}$. The situation is shown in Figure 88.

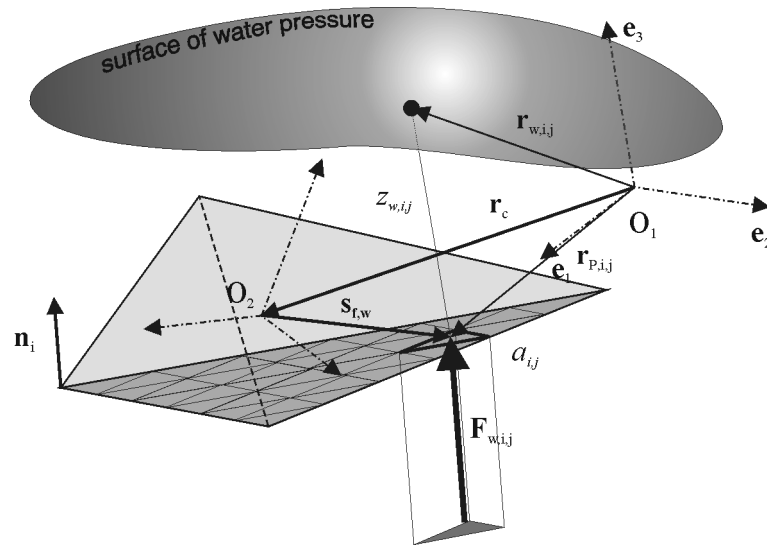


Figure 88: Water pressure acting on block surface

Expression (144) gives the force and moment vectors for each surface i based on a triangulated discretisation. The pressure head may vary with time.

$$z_{w,i,j} = \|\mathbf{r}_{w,i,j} - \mathbf{r}_{p0,i,j}\| \quad \text{and}$$

$$\mathbf{e}_{1,1}^T \cdot (\mathbf{r}_{w,i,j} - \mathbf{r}_{p,i,j}) = 0 \quad \text{and} \quad \mathbf{e}_{1,2}^T \cdot (\mathbf{r}_{w,i,j} - \mathbf{r}_{p,i,j}) = 0$$

$$\mathbf{F}_{w,i}^{(1)} = \gamma_w \cdot \sum_{j=1}^m a_{i,j} \cdot (z_{w,i,j} - \mathbf{e}_{1,3}^{(1)T} \cdot \mathbf{v}_P) \cdot \mathbf{n}_i^{(1)} \quad (144)$$

$$\mathbf{M}_{w,i}^{(1)} = \gamma_w \cdot \sum_{j=1}^m a_{i,j} \cdot (\mathbf{A}^{(12)} \cdot \mathbf{s}_{f,w}^{(2)})^* \cdot (z_{w,i,j} - \mathbf{e}_{1,3}^{(1)T} \cdot \mathbf{v}_P) \cdot \mathbf{n}_i^{(1)}$$

$$z_{w,i,j} = f(\mathbf{v}_P, \mathbf{e}_{1,1}, \mathbf{e}_{1,2})$$

6.4.2.4 Discontinuity normal response

Discontinuity normal forces act perpendicularly to the contact area. They are always directed towards the rock mass, since per definition joints do not sustain tensile stress.

$$\begin{aligned}\mathbf{F}_{\text{jn},i}^{(1)} &= a_{i,j} \cdot \sigma_n \cdot \mathbf{n}_i^{(1)} \\ \mathbf{M}_{\text{jn},i}^{(1)} &= a_{i,j} \cdot \sigma_n \cdot \left(\mathbf{A}^{(12)} \cdot \mathbf{s}_i^{(2)} \right)^* \cdot \mathbf{n}_i^{(1)}\end{aligned}\quad (145)$$

Displacement components comprise those originating from block motion, joint dilation, the normal displacement caused by shear displacement of a rough joint, and the deformability of the block and rock mass.

A required constitutive model is necessary to define the magnitude of the normal stress σ_n at a discrete displaced position of the block. The exemplary establishment of a discontinuity constitutive model has been shown in chapter 3. Likewise, the determination of the discontinuity normal stiffness is also shown in chapter 3. Expression (146) shows a simple linear constitutive model for the discontinuity normal stress.

$$\sigma_n = -k_n \cdot \mathbf{v}_p^{\text{T}(1)} \cdot \mathbf{n}_i^{(1)} \quad (146)$$

Expression (146) applies only if the observed point is in contact with the rock mass. In case of missing contact, it vanishes. In case the point gets into contact within an iteration, only the displacement travelled after contact detection shall be considered.

6.4.2.5 Discontinuity shear response

Discontinuity shear forces act in the contact area and are directed against the shear displacement increment. The shear displacement can easily be calculated from the difference between total and normal displacement of a point.

$$\Delta \mathbf{v}_s = \Delta \mathbf{v}_p - \Delta \mathbf{v}_n = \Delta \mathbf{v}_p - \mathbf{n}_i \cdot \mathbf{n}_i^{\text{T}} \cdot \Delta \mathbf{v}_p = \left(\mathbf{I} - \mathbf{n}_i \cdot \mathbf{n}_i^{\text{T}} \right) \cdot \Delta \mathbf{v}_p \quad (147)$$

Two cases must be distinguished. In the first one the shear stress depends on the shear displacement, for instance when mobilising the shear resistance.

$$\tau_{(l)} = \tau_{(l-1)} + k_s \cdot \|\Delta \mathbf{v}_s\| \quad (l) \text{ refers to the current increment} \quad (148)$$

The corresponding forces and moment applied to the block result in expression (149). Note that the force direction is related to the total shear displacement.

$$\begin{aligned} \mathbf{F}_{js,i}^{(1)} &= -\frac{a_{i,j} \cdot \tau}{\|\mathbf{v}_s^{(1)}\|} \cdot \mathbf{v}_s^{(1)} = -\frac{a_{i,j} \cdot \tau}{\|\mathbf{v}_s^{(1)}\|} \cdot (\mathbf{I} - \mathbf{n}_i \cdot \mathbf{n}_i^T) \cdot \mathbf{v}_p \\ \mathbf{M}_{js,i}^{(1)} &= -\frac{a_{i,j} \cdot \tau}{\|\mathbf{v}_s^{(1)}\|} \cdot (\mathbf{A}^{(12)} \cdot \mathbf{s}_i^{(2)})^* \cdot \mathbf{v}_s^{(1)} \end{aligned} \quad (149)$$

In the second case, the shear resistance has been reached – the shear stress is independent of the shear displacement. Expression (150) shows a simple Mohr-Coulomb shear strength criterion. One should note that φ in this formulation comprises all frictional components such as basic friction, roughness, dilation, etc. Other constitutive relationships can be derived similarly such as those shown in chapter 3 or in Tonon (2007b).

$$\tau = \sigma_n \cdot \tan(\varphi) \quad (150)$$

The corresponding forces and moment applied to the block result in expression (151). Note that the force direction is related to the shear displacement increment.

$$\begin{aligned} \mathbf{F}_{js,i}^{(1)} &= -\frac{a_{i,j} \cdot \tau}{\|\Delta \mathbf{v}_s^{(1)}\|} \cdot \Delta \mathbf{v}_s^{(1)} \\ \mathbf{M}_{js,i}^{(1)} &= -\frac{a_{i,j} \cdot \tau}{\|\Delta \mathbf{v}_s^{(1)}\|} \cdot (\mathbf{A}^{(12)} \cdot \mathbf{s}_i^{(2)})^* \cdot \Delta \mathbf{v}_s^{(1)} \end{aligned} \quad (151)$$

Shear forces only apply if the observed point is in contact with the rock mass. In case of missing contact, it vanishes. In case the point gets into contact within an iteration, only the displacement travelled after contact detection shall be considered.

6.4.2.6 Insitu rock mass stresses

Insitu rock mass stresses act initially on discontinuities in contact with the rock mass. Stresses are given with the stress tensor (152) at a discrete discontinuity point.

$$\boldsymbol{\sigma} = \begin{bmatrix} \sigma_{11} & \tau_{12} & \tau_{13} \\ \tau_{12} & \sigma_{22} & \tau_{23} \\ \tau_{13} & \tau_{23} & \sigma_{33} \end{bmatrix} \quad (152)$$

The corresponding shear and normal stress at the discrete discontinuity point are:

$$\begin{aligned} \text{a) } \sigma_{n,i,ini} &= \mathbf{n}_i^T \cdot \boldsymbol{\sigma} \cdot \mathbf{n}_i \\ \text{b) } \tau_{i,ini} &= \left\| \left(\boldsymbol{\sigma} - \sigma_{n,i} \cdot \mathbf{I} \right) \cdot \mathbf{n}_i \right\| \end{aligned} \quad (153)$$

The discontinuity displacements have to be adjusted in order to comply with the initial normal and shear stress. If dilation is not considered, the normal and shear stress is not coupled. Hence, the normal and shear displacement can be individually determined.

$$\begin{aligned} \text{a) } \mathbf{v}_n &= -\frac{\sigma_{n,i,ini}}{k_n(v_n)} \cdot \mathbf{n}_i \\ \text{b) } \mathbf{v}_s &= \frac{\tau_{i,ini}}{k_s(v_s)} \cdot \mathbf{t}_i \quad \text{where } \mathbf{t}_i = \frac{1}{\tau_{i,ini}} \cdot \left(\boldsymbol{\sigma} - \sigma_{n,i} \cdot \mathbf{I} \right) \cdot \mathbf{n}_i \end{aligned} \quad (154)$$

If the joint shows a dilational behaviour, the normal and shear stress is coupled. A displacement solution complying simultaneously for normal and shear stress must be found. The joint tangent stiffness matrix after Saeb & Amadei (1992) constitutes the relationship between joint normal and shear stress and displacement, respectively. They also show the derivation of the components of the joint tangent stiffness matrix for a simple dilation model. Pötsch (2002) shows the derivation for the Barton-Bandis joint model.

$$\begin{bmatrix} v_{n,i} \\ v_{s,i} \end{bmatrix} = \begin{bmatrix} k_{nn,i} & k_{ns,i} \\ k_{sn,i} & k_{ss,i} \end{bmatrix}^{-1} \begin{bmatrix} \sigma_{n,i,ini} \\ \tau_{i,ini} \end{bmatrix} \quad (155)$$

In both cases the shear stress $\tau_{i,ini}$ must remain smaller than the maximum shear stress allowable by the constitutive model. In the latter case dilation may cause a significant increase of the allowable shear stress. If the shear stress $\tau_{i,ini}$ exceeds the maximum shear stress, $\tau_{i,ini}$ has to be set equal to the maximum shear stress. The corresponding initial shear displacement is unknown.

The joint displacements caused by initial stresses must be accounted in the contact detection routines. The constraint planes shall be displaced by the initial joint displacements.

6.4.3 Stiffness matrix

6.4.3.1 General

According to expression (124) the tangent stiffness matrix \mathbf{K} is the partial derivative of displacement dependent loads. In general, elements causing reactive forces such as constraint forces contribute to the tangent stiffness matrix. Another group of forces which cause a contribution to the tangent stiffness matrix are follower forces. Follower forces are active forces which depend on the current configuration of the mechanical system. For instance, water pressure always acts perpendicular to the block face. Since the block face may change its orientation throughout displacement, the active water force also changes. This is especially prominent when considering large displacements. The contribution to the tangent stiffness matrix originating from follower forces is called load stiffness.

The load vectors comprise usually six entries; the upper three correspond to forces while the lower three correspond to moments. The stiffness matrix \mathbf{K} is a 7×7 matrix since the formulation takes place in Euler parameter space. The first three rows of the stiffness matrix are determined by expression (156) through derivating the force terms and considering expression (72).

$$\mathbf{K}_{3 \times 7} = \frac{\partial \mathbf{F}(\mathbf{v}_p)}{\partial \mathbf{q}} = \frac{\partial \mathbf{F}(\mathbf{v}_p)}{\partial \mathbf{v}_p} \cdot \frac{\partial \mathbf{v}_p}{\partial \mathbf{q}} = \frac{\partial \mathbf{F}(\mathbf{v}_p)}{\partial \mathbf{v}_p} \cdot \mathbf{D}_p(\mathbf{p}) \quad (156)$$

Likewise, the lower four rows of the stiffness matrix are determined by derivating the moment terms and transforming them into Euler parameter space while considering expressions (72) and (74) as shown in expression (157).

$$\begin{aligned}
\mathbf{K}_{4 \times 7} &= 2 \cdot \mathbf{E}^T \cdot \frac{\partial \mathbf{M}(\mathbf{v}_P)}{\partial \mathbf{q}} = 2 \cdot \mathbf{E}^T \cdot \frac{\partial \left[\left(\mathbf{A}^{(12)} \cdot \mathbf{s}^{(2)} \right)^* \cdot \mathbf{F}(\mathbf{v}_P) \right]}{\partial \mathbf{q}} \\
\mathbf{K}_{4 \times 7} &= -2 \cdot \mathbf{E}^T \cdot \mathbf{F}(\mathbf{v}_P)^* \cdot \frac{\partial \left(\mathbf{A}^{(12)} \cdot \mathbf{s}^{(2)} \right)}{\partial \mathbf{q}} + 2 \cdot \mathbf{E}^T \cdot \left(\mathbf{A}^{(12)} \cdot \mathbf{s}^{(2)} \right)^* \cdot \frac{\partial \mathbf{F}(\mathbf{v}_P)}{\partial \mathbf{q}} \quad (157) \\
\mathbf{K}_{4 \times 7} &= -2 \cdot \mathbf{E}^T \cdot \mathbf{F}(\mathbf{v}_P)^* \cdot \mathbf{H}_P \left(\mathbf{A}^{(12)} \cdot \mathbf{s}^{(2)}, \mathbf{p} \right) + \\
&\quad \dots + 2 \cdot \mathbf{E}^T \cdot \left(\mathbf{A}^{(12)} \cdot \mathbf{s}^{(2)} \right)^* \cdot \frac{\partial \mathbf{F}(\mathbf{v}_P)}{\partial \mathbf{v}_P} \cdot \mathbf{D}_P(\mathbf{p})
\end{aligned}$$

Subsequently, the two parts, the upper and the lower part, have to be assembled to the complete stiffness matrix (158).

$$\mathbf{K} = \begin{bmatrix} \mathbf{K}_{3 \times 7} \\ \mathbf{K}_{4 \times 7} \end{bmatrix} \quad (158)$$

Both, expressions (156) and (157) require the force components \mathbf{F} and partial derivatives $\partial \mathbf{F} / \partial \mathbf{v}_P$ of the force components.

6.4.3.2 Normal stiffness matrix

Expression (159) shows the normal force components and corresponding partial derivative. These matrices have to be used in expression (156) and (157) for the contribution of the discontinuity normal stiffness to the global block stiffness matrix.

$$\mathbf{F}_n = a_{i,j} \cdot \sigma_n \cdot \mathbf{n}_i^{(1)} \quad \frac{\partial \mathbf{F}_n}{\partial \mathbf{v}_P} = -a_{i,j} \cdot K_{tot,j} \cdot \mathbf{n}_i^{(1)} \cdot \mathbf{n}_i^{(1)T} \quad (159)$$

6.4.3.3 Shear stiffness matrix

Expression (160) shows the shear force components and corresponding partial derivative. These matrices have to be used in expression (156) and (157) for the contribution of the discontinuity shear stiffness to the global block stiffness matrix.

$$\mathbf{F}_s = -\frac{a_{i,j} \cdot \tau}{\|\mathbf{v}_s^{(1)}\|} \cdot (\mathbf{I} - \mathbf{n}_i \cdot \mathbf{n}_i^T) \cdot \mathbf{v}_p$$

$$\frac{\partial \mathbf{F}_s}{\partial \mathbf{v}_p} = a_{i,j} \cdot k_s \cdot (\mathbf{I} - \mathbf{n}_i^{(1)} \cdot \mathbf{n}_i^{(1)T})^T \cdot (\mathbf{I} - \mathbf{n}_i^{(1)} \cdot \mathbf{n}_i^{(1)T}) \cdot \frac{\Delta \mathbf{v}_s^T}{|\Delta \mathbf{v}_s|} \cdot \frac{\mathbf{v}_p}{|\mathbf{v}_p|}$$
(160)

6.4.3.4 Load stiffness matrix from hydrostatic water forces

Expression (161) shows the normal forces components and corresponding partial derivative directly after $\partial \mathbf{q}$. This partial derivative replaces expression (156) and can be directly input into the second row of expression (157).

$$\mathbf{F}_{w,i}^{(1)} = \gamma_w \cdot \sum_{j=1}^m a_{i,j} \cdot (z_{w,i,j} - \mathbf{e}_{1,3}^{(1)T} \cdot \mathbf{v}_p) \cdot \mathbf{n}_i^{(1)}$$

$$\frac{\partial \mathbf{F}_{w,i}}{\partial \mathbf{q}} = \gamma_w \cdot \sum_{j=1}^m a_{i,j} \cdot \left(\begin{array}{c} \frac{\partial z_{w,i,j}}{\partial \mathbf{q}} \cdot \mathbf{n}_i^{(1)} + z_{w,i,j} \cdot \frac{\partial \mathbf{n}_i^{(1)}}{\partial \mathbf{q}} - \dots \\ \dots - \mathbf{n}_i^{(1)} \cdot \mathbf{e}_{1,3}^{(1)T} \cdot \frac{\partial \mathbf{v}_p}{\partial \mathbf{q}} - \mathbf{e}_{1,3}^{(1)T} \cdot \mathbf{v}_p \cdot \frac{\partial \mathbf{n}_i^{(1)}}{\partial \mathbf{q}} \end{array} \right)$$
(161)

$$\frac{\partial \mathbf{F}_{w,i}}{\partial \mathbf{q}} = \gamma_w \cdot \sum_{j=1}^m a_{i,j} \cdot \left(\frac{\partial z_{w,i,j}}{\partial \mathbf{q}} \cdot \mathbf{n}_i^{(1)} + (z_{w,i,j} - \mathbf{e}_{1,3}^{(1)T} \cdot \mathbf{v}_p) \cdot \mathbf{H}_p - \mathbf{n}_i^{(1)} \cdot \mathbf{e}_{1,3}^{(1)T} \cdot \mathbf{D}_p \right)$$

6.4.3.5 Consideration of dilation

Dilation is the normal displacement of a rough joint induced by a shear displacement. As a point on a block's joint face displaces, an additional displacement component takes place perpendicularly to the discontinuity face. The term for $\partial \mathbf{v}_p / \partial \mathbf{q}$ in expressions (152) and (153) has to be modified to according to the following relationships (Tonon 2007b):

$$\mathbf{v}_{p,tot} = \mathbf{v}_p + \mathbf{v}_{dil}$$

$$\frac{\partial \mathbf{v}_{p,tot}}{\partial \mathbf{q}} = \frac{\partial \mathbf{v}_p}{\partial \mathbf{q}} + \frac{\partial \mathbf{v}_{dil}}{\partial \mathbf{q}} = \mathbf{D}_p(\mathbf{p}) + \frac{\partial \mathbf{v}_{dil}}{\partial \mathbf{v}_p} \cdot \frac{\partial \mathbf{v}_p}{\partial \mathbf{q}} = \left(\mathbf{I} + \frac{\partial \mathbf{v}_{dil}}{\partial \mathbf{v}_p} \right) \cdot \mathbf{D}_p(\mathbf{p})$$
(162)

For a simple dilation model with a constant dilation angle over a limited shear displacement \mathbf{v}_{dil} can be calculated as:

$$\mathbf{v}_{\text{dil}} = \tan i \cdot (\mathbf{I} - \mathbf{n}_i \cdot \mathbf{n}_i^T) \cdot \mathbf{v}_p \quad (163)$$

The derivative $\partial \mathbf{v}_{\text{dil}} / \partial \mathbf{v}_p$ of (163) after \mathbf{v}_p is consequently the well-know expression (164).

$$\frac{\partial \mathbf{v}_{\text{dil}}}{\partial \mathbf{v}_p} = \tan i \cdot (\mathbf{I} - \mathbf{n}_i \cdot \mathbf{n}_i^T) \quad (164)$$

Expression (164) remains valid for a shear displacement smaller than $\mathbf{v}_{s,\text{max}}$. After exceeding $\mathbf{v}_{s,\text{max}}$ the dilation component vanishes again. For a more sophisticated dilation model as presented in chapter 3.3 (including mobilisation of dilation, joint roughness and its degradation, normal stress dependence, etc.) the derivative $\partial \mathbf{v}_{\text{dil}} / \partial \mathbf{v}_p$ becomes significantly more complex. Feasible consideration of a dilation model also requires the consideration of dilation and contraction in case of shear sense reversal. This has been discussed by Tonon (2007b).

6.4.3.6 Assembly of the total tangent stiffness matrix

Recalling the residual force equation (165) one realises that some of the force components depend on \mathbf{q} (especially normal and shear forces of discontinuities), some depend on \mathbf{q} and λ_{stage} (for instance, hydrostatic water forces), and finally some do not depend on displacements but on the stage control parameter (for instance, inertia forces).

$$\text{res}(\mathbf{q}, \lambda_{\text{stage}}) = \mathbf{Q}_n(\mathbf{q}) + \mathbf{Q}_s(\mathbf{q}) + \lambda_{\text{stage}} \cdot (\mathbf{Q}_{w,i}(\mathbf{q}) + \mathbf{Q}_{\text{ex}}) = \mathbf{0} \quad (165)$$

The block's tangent stiffness matrix has to be assembled in an analogue way. Derivatives of forces which do not depend on \mathbf{q} , do not contribute to the stiffness matrix \mathbf{K} . Derivatives of forces which do only depend on \mathbf{q} , contribute with their full magnitude to the stiffness matrix \mathbf{K} . Derivatives of forces which depend on both, \mathbf{q} and λ_{stage} , contribute with a stiffness magnitude proportional to the stage control parameter λ_{stage} . This is shown in expression (166).

$$\mathbf{K} = \mathbf{K}_n + \mathbf{K}_s + \lambda_{\text{stage}} \cdot \mathbf{K}_{w,i} \quad (166)$$

6.4.4 Equilibrium path

6.4.4.1 Properties of the equilibrium path

The equilibrium path undergoes typical stages while increasing the stage control parameter. At the very beginning the response of the block is linear. With increasing load, material and/or geometric non-linearities become more prominent. The path starts deviating from the linear stretch. Typically, the stiffness of the block system decreases.

A critical point is encountered when the tangent stiffness vanishes and the tangent becomes horizontal. This point is called a limit point at which no further load increase is possible. Limit points are related to the peak strength of the block system. Load controlled procedures fail in determining limit points and cannot calculate beyond it. Arclength controlled procedures can traverse limit points and enter the post failure region. Limit points are relevant for determining the stability and factor of safety of a block system.

A second type of critical points is the bifurcation point. At bifurcation points the equilibrium path branches out in two or more branches. At a bifurcation point the tangent stiffness is not uniquely defined and an abrupt transition from one deformation mode to another takes place. Bifurcation points cannot be traversed either with load controlled or arclength controlled procedures and thus require special attention and treatment. Figure 89 shows the equilibrium path of a mechanical system with the initial linear response, and a limit and a bifurcation point.

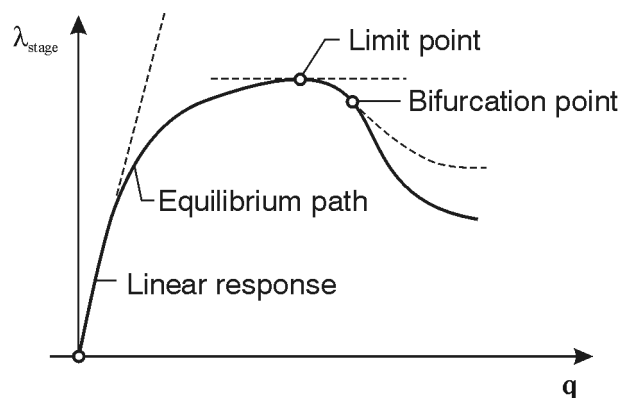


Figure 89: Equilibrium path and critical points

Critical points involve a differential movability of the block (beyond the compliance of the constraints). Kinematically feasible motions are a set of vectors defined by the null space \mathbf{z} of the stiffness matrix \mathbf{K} (Strang 1976), i.e. all possible differential displacements and rotations belong to the null space. \mathbf{z} is determined by singular value decomposition (SVD) of \mathbf{K} . Any $m \times n$ matrix can be decomposed into a product of three matrices \mathbf{USV}^T such that \mathbf{U} is an $m \times m$ square matrix whose rows are orthonormal, \mathbf{S} is a matrix containing the singular values in its diagonal and zeros in other cells, and \mathbf{V} is the $n \times n$ adjunct matrix to \mathbf{U} . The null space \mathbf{z} are the rows of \mathbf{V} corresponding to zero singular values.

A critical point is encountered once the nullspace of the stiffness matrix is non-empty, i.e. when the stiffness matrix has a rank deficiency. Critical points must be differentiated into limit and bifurcation points. For conservative systems, i.e. the stiffness matrix is symmetric, Spence & Jepson (1985) proposed the following relationships (167) for distinguishing critical points. Dutta & White (1997) and formerly Bažant (1989) showed that the criteria for non-conservative systems (asymmetric stiffness matrix) reduce to the criteria for conservative systems.

$$\begin{aligned} a. \quad & \mathbf{K} \cdot \mathbf{z} = \mathbf{0} \Leftrightarrow \mathbf{z}^T \cdot \mathbf{K} = \mathbf{0} \\ b. \quad & \mathbf{z}^T \cdot \mathbf{K} \cdot d\mathbf{u} = \mathbf{z}^T \cdot \mathbf{Q}_{failure}^a \cdot d\lambda = \mathbf{0} \end{aligned} \quad (167)$$

$\mathbf{Q}_{failure}^a$ refers to the active external load at the instant of encountering a critical point. Two different cases can be distinguished:

$$\begin{aligned} a. \quad & \mathbf{z}^T \cdot \mathbf{Q}_{failure}^a \neq 0 \\ b. \quad & \mathbf{z}^T \cdot \mathbf{Q}_{failure}^a = 0 \end{aligned} \quad (168)$$

In case (168a) the load increment must be zero, i.e. the active load cannot be increased further. This is a limit point. Case (168b) detects a bifurcation point characterised by abrupt transmission of one deformation mode to another. Practically, the critical points will not be encountered exactly. Limit and bifurcation points are distinguished by the incremental work. In case of a limit point, the incremental work always changes its sign while it does not for bifurcation points (Dutta & White 1997).

6.4.4.2 Static failure modes and factor of safety

Static failure modes are associated with differential movability of the block under its constraints. They relate to a slow change of boundary conditions such that dynamic effects do not play a role. The differential movability is determined by the null space of the stiffness matrix at a limit point. The rank of the null space

defines the number of static failure modes. The motion will be forced in direction of the active resultant. Expression (169) shows the determination of the static failure modes related to each of the rows of the null space.

$$\mathbf{q}_{f,static} = \mathbf{z} \cdot \text{sign}(\mathbf{z}^T \cdot \mathbf{Q}^a) \quad (169)$$

Tonon (2007b) found that the factor of safety of the block is equal to the stage control parameter λ_{stage} at the last converged increment. Traditionally, the factor of safety is the ratio between resisting forces (constrained forces) and driving forces (active forces) in direction of motion at limit equilibrium (170).

$$FoS = \frac{|\mathbf{q}_{f,static}^T \cdot \mathbf{Q}^c|}{|\mathbf{q}_{f,static}^T \cdot \mathbf{Q}^a|} \quad (170)$$

From expression (122) we can defer for an equilibrium point that $\mathbf{Q}^c = -\lambda_{stage} \mathbf{Q}^a$. Thus, expression (170) can be rearranged to (171). The factor of safety is implicitly given by the stage control parameter corresponding to the first limit point encountered along the equilibrium path. It always corresponds to the failure mode defined by expression (169). No shear strength reduction method has to be applied for determining the block's factor of safety. Shear strength reduction method will result in a different failure mode than the one which is actual critical, e.g. sliding instead of rotation, as intensively discussed by Tonon (2007b).

$$FoS = \frac{|\mathbf{q}_{f,static}^T \cdot \lambda_{stage} \cdot \mathbf{Q}^a|}{|\mathbf{q}_{f,static}^T \cdot \mathbf{Q}^a|} = \lambda_{stage} \quad (171)$$

6.4.4.3 Dynamic failure modes

Dynamic failure modes are associated with the incipient motion of the block under its constraints considering a sudden removal of constraints or change of boundary conditions (Tonon 2007b). They account for dynamic effects involved with inertia assuming the constraints to be rigid regardless of the constitutive model applied when determining the equilibrium path. The determination of the dynamic failure mode includes the following steps:

- Determination of the contact points
- Determination of kinematic constraints
- Determination of the incipient motion

6.4.4.3.1 Determination of points in contact

Forces are only transferred to the block if it is in contact with the rock mass. This is checked at the contact points. The dynamic motion at failure is governed by the active contact points at the last converged increment. The unconstrained motion of the block is used to determine those contact points from the active ones at which a kinematic constraint has to be applied. Expression (172) determines the acceleration of the block from rest (incipient unconstrained motion), i.e. velocities are also zero. The vector of accelerations must therefore be the same as vector of the incipient displacements.

$$\begin{bmatrix} \ddot{\mathbf{r}}^{(1)} \\ \dot{\boldsymbol{\omega}}^{(2)} \end{bmatrix} = \begin{bmatrix} \mathbf{m} & \mathbf{0} \\ \mathbf{0} & \mathbf{J}^{(2)} \end{bmatrix}^{-1} \cdot \begin{bmatrix} \mathbf{F}_{\text{failure}}^{a(1)} \\ \mathbf{M}_{\text{failure}}^{a(2)} \end{bmatrix} \quad (172)$$

Active contact points have to be kinematically constrained if the unconstrained motion at the contact point is directed into the constraint space (173).

$$\mathbf{n}_i^T \cdot [\ddot{\mathbf{r}}^{(1)} + \mathbf{A}^{(12)} \cdot \dot{\boldsymbol{\omega}}^{(2)*} \cdot \mathbf{s}^{(2)}] < 0 \quad (173)$$

6.4.4.3.2 Determination of kinematic constraints

Points in contact with the constraint space can have two different statuses defined by joint properties and stress condition. They can be on the yield surface of the joint constitutive model. The contact point is considered to be sheared. A sheared contact point is able to move only parallel to the joint surface. The kinematic constrained can be introduced by the algebraic equations developed in the previous chapter. Since it has to maintain contact throughout the incipient motion, it constrains motion only in one direction. One algebraic equation (174) is sufficient.

$$\Theta^{d2}(\mathbf{n}_i, \mathbf{d}_i) = 0 \quad (174)$$

\mathbf{n}_i is the normal vector of joint plane containing the i^{th} contact point. \mathbf{d}_i is the displacement vector of the i^{th} contact point defined by expression (175). The index $_l$ refers to the position at failure before the start of dynamic motion; the index $_{disp}$ refers to a position an infinitesimal small time increment later.

$$\mathbf{d}_i = \mathbf{r}_{disp}^{(1)} + \mathbf{A}^{(1,disp)} \cdot \mathbf{s}_i^{(disp)} - \mathbf{r}_l^{(1)} - \mathbf{s}_l^{(1)} \quad (175)$$

Note that this criterion maintains contact of a contact point. Rotation about the contact point is admitted.

If the contact point lies within the yield surface of the joint constitutive law, it is fixed in space with rotation allowed. It requires three algebraic equations

$$\Theta^s(\mathbf{r}_{\text{disp}}, \mathbf{r}_1, \mathbf{s}_i) = \mathbf{0} \quad (176)$$

6.4.4.3.3 Determination of incipient motion

The equations of motion of a constrained body in Newton-Euler formalism (177) are used to determine the incipient motion of the block. Newton-Euler formalism is possible since time integration is not necessary. The dynamic failure mode is related to the block accelerations $\ddot{\mathbf{r}}$ and $\dot{\boldsymbol{\omega}}$. Reaction forces in the contact points are obtained from the Lagrange multipliers $\boldsymbol{\lambda}$ following expressions (116) and (117). The system (177) is linear in the generalised coordinates $\ddot{\mathbf{r}}$, $\dot{\boldsymbol{\omega}}$, and $\boldsymbol{\lambda}$.

$$\begin{bmatrix} \mathbf{m} & \mathbf{0} & \Theta_r^T \\ \mathbf{0} & \mathbf{J}^{(2)} & \Theta_\pi^{(2)T} \\ \Theta_r & \Theta_\pi^{(2)} & \mathbf{0} \end{bmatrix} \cdot \begin{bmatrix} \ddot{\mathbf{r}}^{(1)} \\ \dot{\boldsymbol{\omega}}^{(2)} \\ \boldsymbol{\lambda} \end{bmatrix} = \begin{bmatrix} \mathbf{F}_{\text{failure}}^{a(1)} \\ \mathbf{M}_{\text{failure}}^{a(2)} \\ \boldsymbol{\gamma} \end{bmatrix} \quad (177)$$

6.4.4.4 Bifurcation

At bifurcation points two or more equilibrium paths cross. The rank of the null space defines the number of equilibrium path branches. These branches are related to motion orthogonal to the original path towards the infinitesimal movability of the null space. Bifurcation points cannot be traversed with the methods described above but require further measures. A simple method for avoiding motion towards the bifurcation paths is the application of perturbation springs oriented in the null space. The stiffness of these springs shall be added to the original stiffness matrix. This stabilises the block in these directions and allows following the original equilibrium path (Felippa 1987). Bifurcation of mechanical systems is a complex topic and still a field of active research (e.g. Mühlhaus et al. 2001, Ikeda & Murota 2010, Sulem 2010). No further details are discussed in this work.

In structural analysis bifurcation points are related to buckling of structural elements. Tonon (2007b) observes bifurcation points when analysing the equilibrium path of blocks subjected to corner rotation and slumping.

6.4.4.5 Stability of the equilibrium path

The equilibrium path consists of a set of discrete equilibrium points. Critical points along the equilibrium path have already been discussed. Nothing has been said about the stability of equilibrium determined while marching along the equilibrium path. Equilibrium can be stable, indifferent, or unstable. In conservative systems the equilibrium path is always stable (principle of the minimum potential energy).

Stability can be characterised by analysing the dynamic behaviour of a block subjected to a small perturbation of its equilibrium position. The equations of motion of an unforced block are used to describe the problem. Damping is neglected. The analysis refers to the local surrounding of the equilibrium point but does not consider global stability. Expression (178) shows the equations of motion of the undamped and unforced block.

$$\mathbf{M} \cdot \ddot{\mathbf{q}} + \mathbf{K} \cdot \mathbf{q} = \mathbf{0} \quad \text{with } \mathbf{M} = \begin{bmatrix} \mathbf{m} & \mathbf{0} \\ \mathbf{0} & \mathbf{J}^{(2)} \end{bmatrix} \quad (178)$$

Using the eigenmode expansion of the state vector $\mathbf{q} = \sum_i \mathbf{z}_i \cdot e^{p_i \cdot t}$ one can defer the generalised asymmetric eigenproblem:

$$(\mathbf{K} + p_i^2 \cdot \mathbf{M}) \cdot \mathbf{z}_i = \mathbf{0} \quad (179)$$

i refers to the dimension of the state vector (degrees of freedom). p_i are the characteristic exponents and also the square roots of the negative eigenvalues. \mathbf{z}_i are the corresponding eigenvectors or characteristic modes.

The eigenvalues p_i^2 can take two different cases due to the properties of the involved stiffness and mass matrices – \mathbf{K} is asymmetric and \mathbf{M} is symmetric and positive definite. They can be either real or complex (Felippa 1987).

Case 1: p_i^2 real negative

If all eigenvalues are real negative and distinct, the corresponding characteristic values are imaginary numbers and allow transforming the solution to a harmonic oscillation (180). The motion is bounded and oscillates about the equilibrium point (Figure 90 left). In case of damping and especially with conservative systems, the motion converges to the static equilibrium point. The equilibrium can be considered as dynamically stable.

$$\mathbf{q} = \sum_i \mathbf{z}_i \cdot [C_{1,i} \cdot \cos(\omega_i \cdot t) + C_{2,i} \cdot \sin(\omega_i \cdot t)] \quad (180)$$

with $\omega_i = |\text{imag}(p_i)|$

Case 2: p_i^2 real positive

If one eigenvalue is real positive, the corresponding characteristic values are real numbers. The negative characteristic value gives rise to an exponentially vanishing motion while the positive one is related to an aperiodic exponentially growing motion. The latter one overwhelms the former one for a sufficiently large time t . The equilibrium is dynamically unstable and the block has to be considered as failed by divergence (Figure 90 middle).

$$\mathbf{q} = \sum_i \mathbf{z}_i \cdot e^{p_i \cdot t} \quad (181)$$

Case 3: p_i^2 complex

The stiffness and mass matrix are both real matrices. Complex eigenvalues thus appear only in conjugate pairs. The square root of a complex number in general is also a complex number. Expression (182) shows the square of a complex number.

$$(a + b \cdot i)^2 = (a^2 - b^2) + 2 \cdot a \cdot b \cdot i \quad (182)$$

The characteristic values thus take positive and negative values for both the real part and the imaginary part of the complex number. The imaginary part is related to harmonic oscillation no matter of its sign. The real part is related to exponential growth which at final dominates the other motion components. The motion in this case is a periodic exponentially growing motion. The equilibrium is dynamically unstable and the block has to be considered as failed by flutter (Figure 90 right).

$$\mathbf{q} = \sum_i \mathbf{z}_i \cdot [e^{a_i \cdot t} + C_{1,i} \cdot \cos(b_i \cdot t) + C_{2,i} \cdot \sin(b_i \cdot t)] \quad (183)$$

Since the characteristic values appear in conjugate pairs and these pairs define the motion, the block moves from one corresponding mode to the other. In consequence, it is necessary to have a coalescence of at least two natural frequencies for flutter instability.

Tonon (2007b) reports flutter instability of a block subjected to hydrostatic and hydrodynamic water pressures considered as follower forces. This can typically appear in case of a scour event.

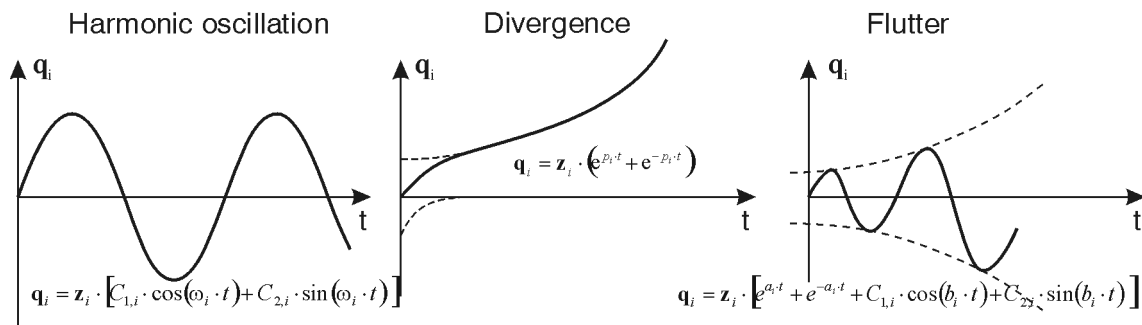


Figure 90: Schematic behaviour of the local dynamic behaviour of an equilibrium point (after Felippa 1987). *Left*: Harmonic oscillation (stable). *Middle*: Divergence (unstable). *Right*: Flutter (unstable).

6.5 Illustrative example

This example investigates the behaviour of a rock block in the crown of a cavern. Previous investigations with this example included block theory analyses and numerical analyses with the three-dimensional distinct element code. These analyses have been carried out by Hein-Stumpp (2009) and presented by Preh *et al.* (2009). The following analysis is based on the block theory analysis and highlights the application of the presented continuation method to identify the correct mode of failure and factor of safety.

6.5.1 Description of the situation

The cavern has length of 100 m and a width of 30 m. Only blocks in the crown are considered, thus the cavern's height is not relevant. Possible blocks in the sidewalls and intersections are not taken into account in this example. Figure 91 shows a plan view of the cavern.

The cavern is located in a jointed rock mass with four joint sets with different orientations. The joints are regularly spaced at 5 m and 6 m, respectively. The joints obey a Mohr-Coulomb sliding criterion. Table 22 outlines the discontinuity parameters.

The rock density is 2700 kg/m³. The normal and shear stiffness for joints in contact is constant at 1000 MPa/m each. Joint dilation and initial rock mass stresses are not considered.

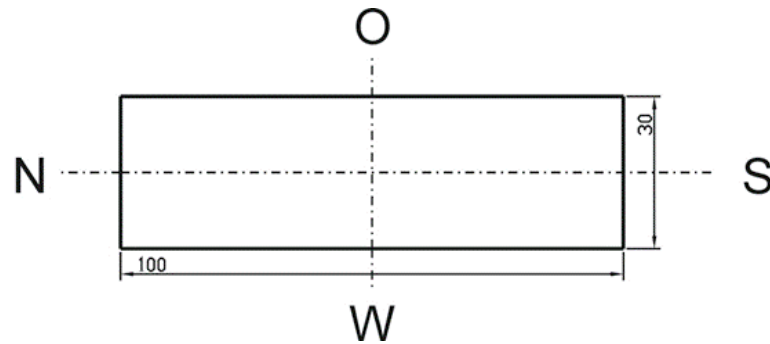


Figure 91: Plan view of the cavern (from Preh et al. 2009)

Table 22: Overview of the discontinuity parameters

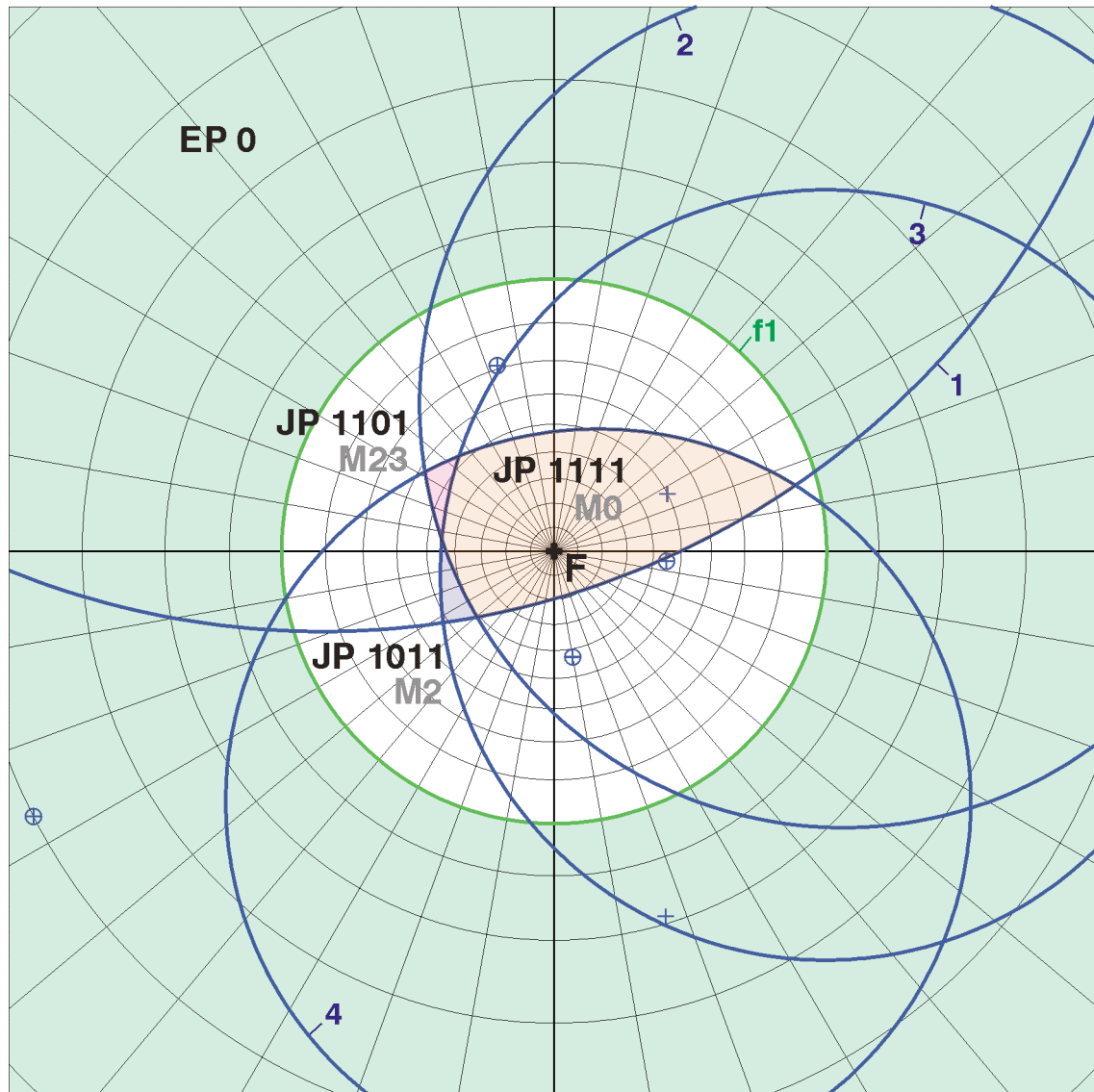
Plane sets	Orientation		Shear parameters		Spacing [m]
	Dip direction [°]	Dip angle [°]	Friction angle [°]	Cohesion [MPa]	
Joint 1	163	71	15.0	0.04	5.0
Joint 2	243	50	30.0	0.40	6.0
Joint 3	275	45	30.0	0.40	5.0
Joint 4	350	43	25.0	0.10	6.0
Free face	0	0			

6.5.2 Removable blocks, kinematics and stability according to block theory

Figure 92 shows the great circles of joints 1 to 4 and the free face fl. It shows the entire sphere in an equal angle stereographic projection with upper focal point. The great circle of fl coincides with the equator of the sphere; the excavation pyramid is the upper hemisphere. The space pyramid is the lower hemisphere.

Three four-joint joint pyramids which plot entirely in the space pyramid have been encountered. The joint pyramids correspond to the codes JP 1111, JP 1101, and JP 1011. The blocks corresponding to these joint pyramids are kinematically removable. Two more removable blocks which are not drawn, are present. They correspond to the three-joint blocks JP 1121 and JP 1211.

Stereographic projection - equal angle - upper focal point



- joint planes
- free face
- reference circle
- ⊕ block side pole
- + rock or space side pole
- JP** joint pyramid
- EP** excavation pyramid

Figure 92: Stereographic projection of joints and the free face. Three removable blocks corresponding to JP 1111, JP 1101, and JP 1011 have been encountered. Their modes of failure under self weight **F** comprise falling (M0), sliding on intersection 23 (M23), and sliding on joints 2 (M2), respectively.

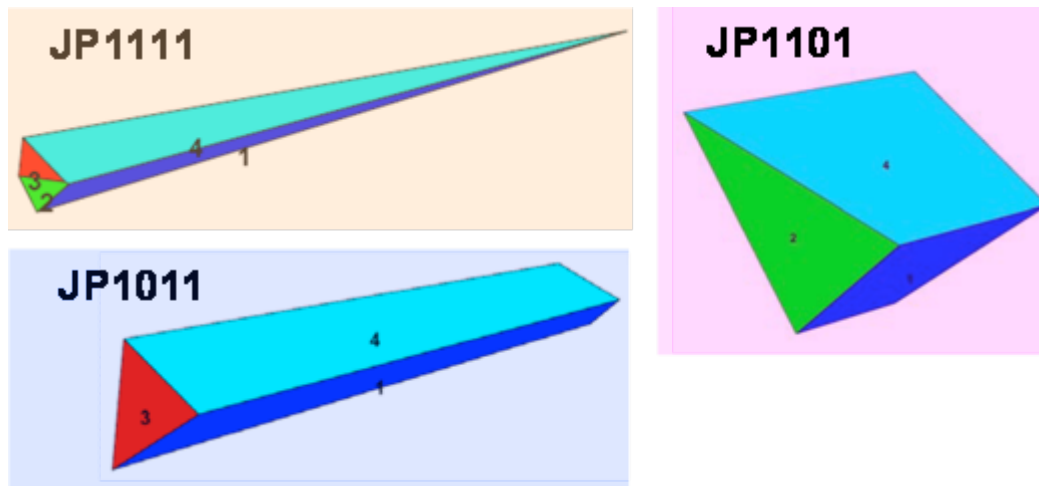


Figure 93: Plan view of the removable four-joint blocks (from Preh et al. 2009)

The only active force is self weight F . It plots in the centre of the stereographic projection. Under this load JP 1111 exhibits a falling mode (M0), JP 1101 slides along the intersection between joint 2 and 3 (M23), and JP 1011 slides on plane 2 (M2). Both three-joint blocks exhibit also a falling mode.

Figure 93 shows the three encountered four-joint blocks in a plan view. The blocks are maximised in accordance to the joint set spacings and the geometry of the cavern. Table 23 shows the factors of safety for the three four-joint blocks for each mode of failure. According to its falling mode JP 1111 has a factor of safety of zero. This is only true when joint dilation and initial rock mass stresses are neglected. JP 1011 exhibits a sliding mode on joint 2. Sliding equilibrium can almost be achieved – the factor of safety is 0.97. JP 1101 exhibits a sliding mode on intersection 23. It is stable with a factor of safety of 5.38.

Table 23: Failure modes and factor of safety for the four-joint blocks (Preh et al. 2009)

Block	Failure mode	Factor of Safety
JP 1111	Falling	0
JP 1011	Sliding on plane 2	0.97
JP 1101	Sliding on intersection 2 and 3	5.38

6.5.3 Single block analysis

According to block theory JP 1011 exhibits a sliding mode on plane 2. It inherently assumes that only translations take place. When examining the block geometry this assumption is questionable for this block. Figure 94 shows that only a minor part of the joints, joint plane 2, stays in contact. Due to its distance from the block's centre rotational displacements are suspected.

6.5.3.1 Block description

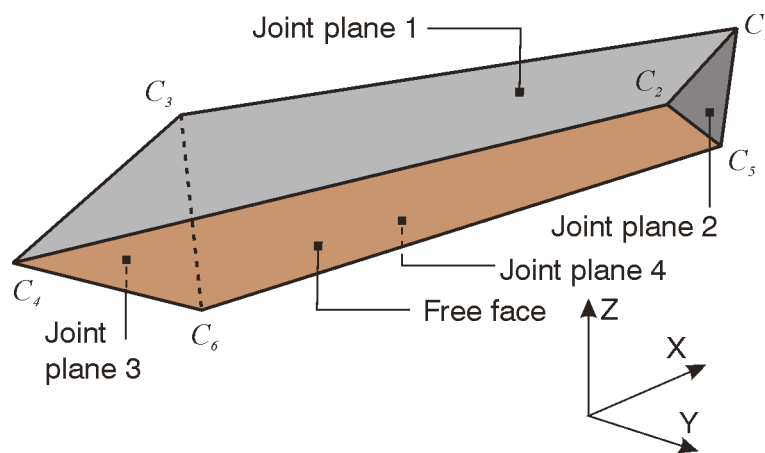


Figure 94: Perspective view of block JP 1011.

Figure 94 shows block 1011 in a perspective view with annotations of planes and corners. It is bounded by five planes and has six vertices, four of them at the free face. Table 24 summarises the data of the planes while Table 25 shows the vertex coordinates of the block. Table 26 summarises the geometric and inertia properties of the block.

Table 24: Plane orientations and locations of block 1011

Planes	Orientation		Point on plane			Halfspace
	Dip direction [°]	Dip angle [°]	X [m]	Y [m]	Z [m]	
Joint plane 1	163	71	30.49	10.42	3.04	lower
Joint plane 2	243	50	30.49	10.42	3.04	upper
Joint plane 3	275	45	5.60	3.61	5.26	lower
Joint plane 4	350	43	30.49	10.42	3.04	lower
Free face 1	0	10	0.00	0.00	0.00	upper

Table 25: Vertex coordinates of block 1011

Corners	Coordinates		
	X [m]	Y [m]	Z [m]
C_1	30.49	10.42	3.04
C_2	28.50	8.71	0.00
C_3	5.60	3.61	5.26
C_4	0.00	0.00	0.00
C_5	26.31	12.99	0.00
C_6	0.74	8.48	0.00

Table 26: Geometric and inertia properties of block 1011

		JP 1011	
Volume	[m ³]	V	377.18
Mass	[t]	m	1018.39
Centroid	[m]	x_c	12.991
		y_c	6.756
		z_c	1.449
Moments of Inertia	[kgm ²]	J_{xx}	6.649E+06
		J_{yy}	5.687E+07
		J_{zz}	6.126E+07
Products of Inertia	[kgm ²]	J_{xy}	1.364E+07
		J_{xz}	-4.497E+05
		J_{yz}	-5.084E+05

6.5.3.2 Kinematic analysis

The kinematic analysis includes the translational and rotational analysis. The translational analysis has already been done in the previous section 6.5.2. The block is removable. This section completes the kinematic analysis with the rotational aspect.

Figure 95 shows the stereographic projection of the great circles of limit planes for rotation about vertex C_2 . A thorough inspection of the figure, or more easily, the vector computation of section 5.3.2.2 reveals that the intersection of limit plane halfspaces is empty. Thus, the rotation space for corner C_2 is empty. It can be proved that the rotation space is empty for all block corners at the free face such as C_2 , C_4 , C_5 , and C_6 . As a consequence, the block is not corner rotatable and not edge rotatable.

In contrast to pure rotation the analysis for remote axis rotation reveals kinematic movability. This is obvious since the block is removable. Four remote axes leading to kinematically feasible displacements have been encountered with the method introduced in section 5.3.3.2. Table 27 shows the data of the obtained axes. Figure 96 highlights the axes in context with the block in a perspective view. The block is also shown in the according displaced position.

Table 27: Position and orientation for four encountered remote axes leading to kinematically feasible block displacements (1011).

Remote axis	Axis point			Axis orientation		
	X [m]	Y [m]	Z [m]	X [m]	Y [m]	Z [m]
1	32.59	67.77	-61.62	0.35	-0.92	0.18
2	2.76	31.08	12.47	0.76	0.08	-0.65
3	-3.20	31.29	17.39	0.79	-0.03	-0.62
4	30.58	-0.23	-0.33	-0.14	-0.93	0.34

Block 1011 is removable and can displace about remote axes. The sliding mode obtained by block theory may not be the critical mode of failure, since block theory cannot treat this kind of rotational mode.

Stereographic projection - equal angle - upper focal point

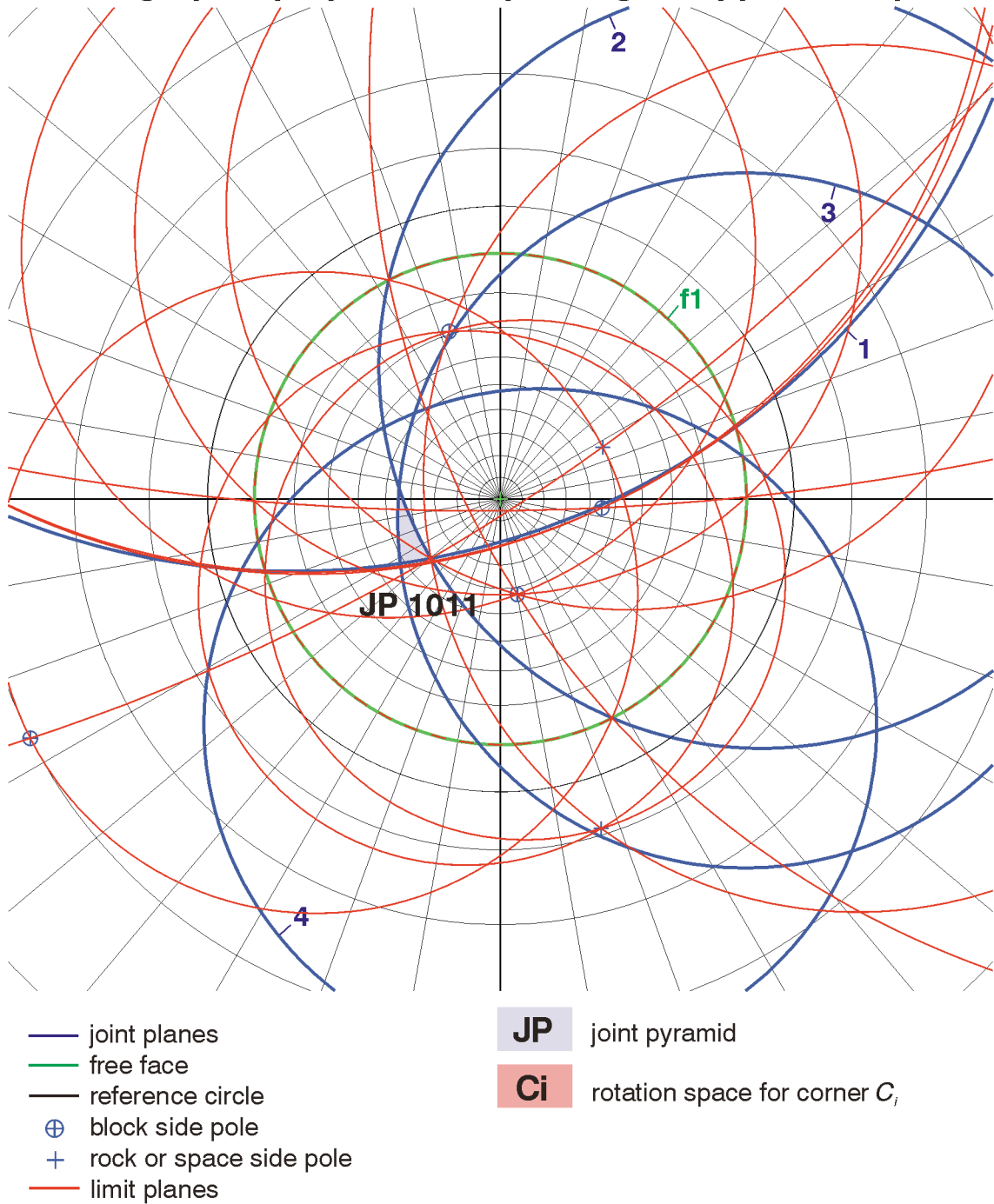


Figure 95: Stereographic projection of the joint pyramid, limit planes and rotations space of block 1011 for rotation about vertex C₂.

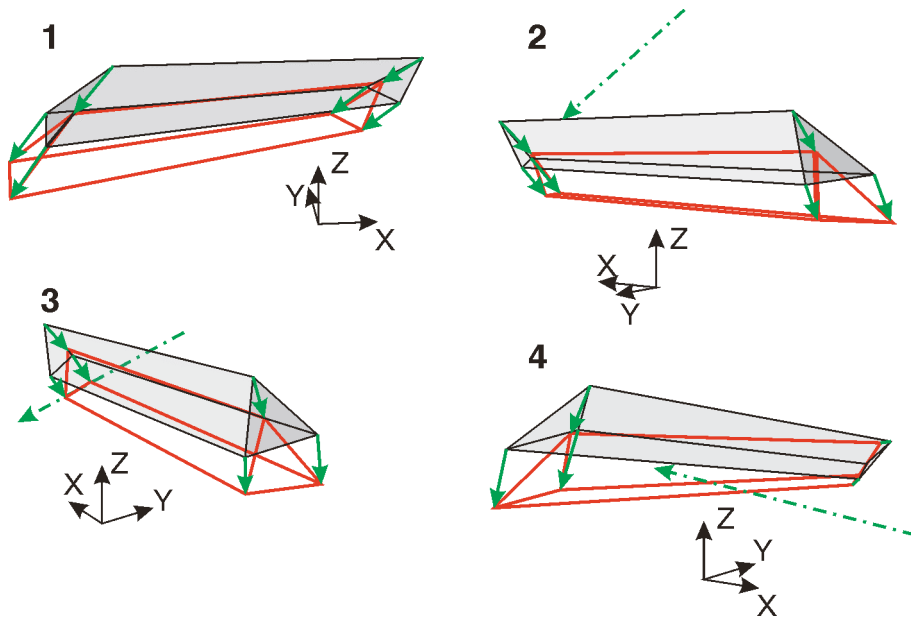


Figure 96: Perspective views of the original and displaced block position due to remote axis rotation about the four encountered axes. Data from Table 27. Displacements are exceeded.

6.5.3.3 Stability analysis

A stability analysis has been performed using the continuation method. The surface of the block has been discretised with 374 discrete discontinuity points at which contact and joint laws are calculated. The analysis has been structured into two stages.

- First stage: Calculation for initial condition.
The parameters have been selected as described above. The free face has also been constrained in order to prevent from large motion into the free space. Self weight has been successively applied proportionally to the stage control parameter λ_{stage} .
- Second stage: Calculation for failure.
The constraints at the free face have been removed. Equivalent reaction forces have been decreased proportionally to the stage control parameter λ_{stage} . Due to block detachment the control parameter increments have been small (0.001).

In the following paragraphs only the second stage is considered.

Figure 97 shows the equilibrium paths for block 1011 subjected to self weight in stage 2. On the upper left the equilibrium path is plotted against the block stiffness in percent, i.e. how much stiffness the block loses during the

displacement. The right diagram shows the equilibrium path against the vertical displacement of the centre of gravity, the lower left diagram against the rotation about the x-axis. The displacement and rotation values are small, though one can derive the behaviour. The equilibrium path follows a nearly linear response up to a stage control parameter of 0.6 (stiffness) or almost 0.7 (displacements). Rotations already start at a value of about 0.3. After the linear behaviour the equilibrium paths show a sudden change of behaviour. This indicates a rapid increase of motion and a sudden failure. At a stage control parameter of 0.7 the stiffness matrix becomes singular indicating failure of the system.

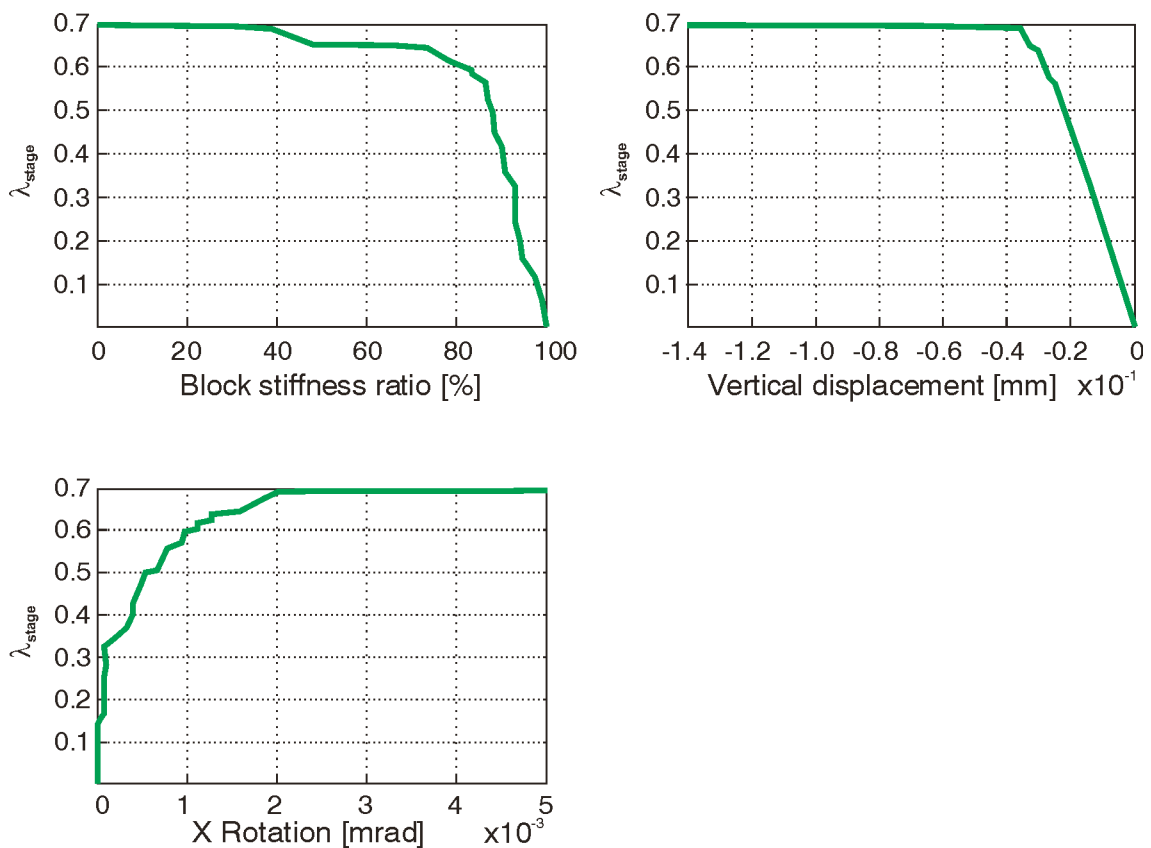


Figure 97: Equilibrium paths of block 1011 in stage 2. Stage control parameter vs block stiffness (upper left), vertical displacement (right), and rotation about the x-axis (lower left)

Figure 98 show perspective sketches of the block 1011 at discrete values of the stage control parameter when approaching failure. Green areas indicate contact with an elastic shear response while red areas indicate the contact at the yield surface (Mohr-Coulomb joint law). White areas indicate block detachment.

At the left top there is the configuration at the beginning of the stage 2 with the entire joints in contact. It follows an almost linear response up to λ_{stage} of about 0.6. From this point detaching and shearing of the contacts take place rapidly. The block rotates towards corners C_3 and C_4 and at the same time it supports at joint 4. It moves away from C_2 and the adjacent joint 4. Close to failure the support at joint 1 moves back from C_3 to C_2 and also keeps contact at joint 2. Failure takes place at λ_{stage} of 0.7 at which the stiffness matrix becomes singular. Only few sheared contacts are left which provides infinitesimal movability.

The factor of safety of the block is equal to λ_{stage} at failure of 0.7. The identified static failure mode is sliding along intersection of joints 1 and 2 $[-0.4967, -0.4244, -0.7571, 0, 0, 0]^T$. This factor of safety and failure mode is different from the one identified with block theory (sliding on plane 2, FoS 0.97). The static failure mode refers to a behaviour when constraints are removed very slowly. The static failure mode of the block is indicated at the right bottom sketch in Figure 98.

For a sudden removal of the constraints the dynamic failure mode is relevant. It considers dynamic effects in the instant of failure when removing the horizontal constraint plane after stage 1. The dynamic failure mode is a simultaneous translation and rotation. The vertical downward displacement dominates. $[-0.3014, -0.1536, -2.6689, 0.0478, -0.0184, -0.0022]^T$ (m/s, rad/s).

Figure 99 shows two different perspectives of the motion of the block after failure. It includes a time interval of two seconds and shows the block positions every 0.2 seconds. After failure sliding on edge 2-5 takes place with simultaneous rotation about this edge. A simultaneous x-rotation is also connected to the motion.

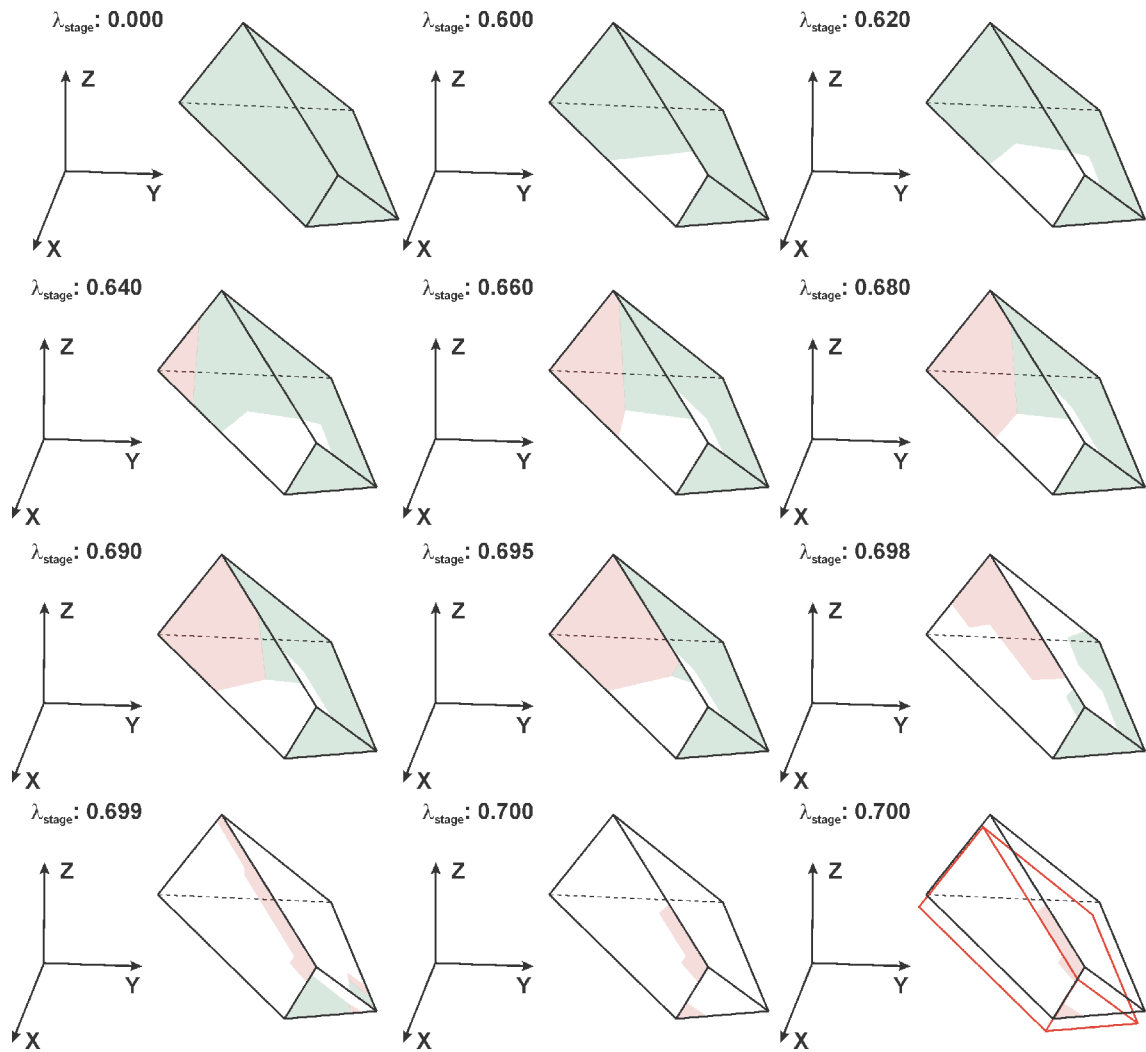


Figure 98: Perspective view of the block and contact status when approaching failure. The sketches are related to a discrete stage control parameter. Green areas indicate contact with elastic shear response, red areas indicate contact at the yield surface, and white areas indicate no contact.

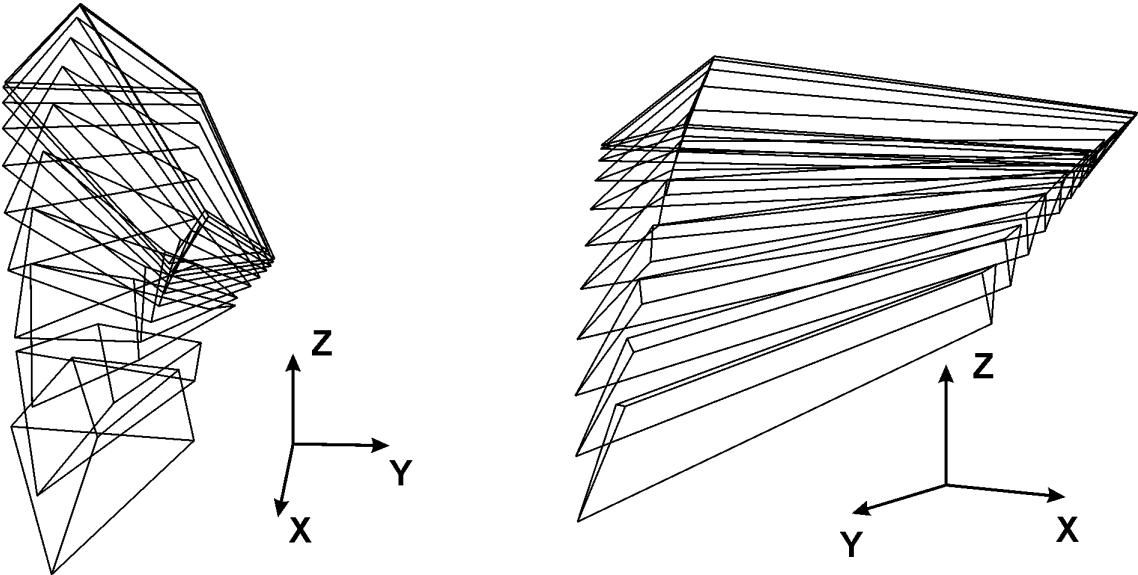


Figure 99: Two perspective views of the sequence of block positions two seconds after failure in 0.2 sec increments.

7 Conclusion

This dissertation deals with the analysis of rock blocks and their associated failure mechanisms. It follows a hierarchical procedure including the acquisition of required field data, the determination of the mechanical behaviour of joints, the determination of block geometries and related properties, the analysis of block kinematics, and the analysis of the dynamic behaviour and the stability of rock blocks.

Image based remote sensing technologies recently emerged in the field of engineering geology and rock mechanics. The three-dimensional image based measurement system ShapeMetriX3D was applied for gathering geometric information on rock joints in the field (either at slopes or underground excavations). Based on practically feasible field procedures this technology was integrated in the procedure for rock block analysis. The obtained data among others included the geometry of the rock structure and the geometry of the joint system including the position, orientation, and the size of joints at the surface. The synthesis of the data led to a network of joint traces on the excavation surface.

The trace network was the basis for an algorithmic search for defined volumes of rock, so called finite blocks. Finite blocks were found by analysing the trace network for closed polygons and testing the joint system bounding the polygon for finiteness relative to the polygon surface. Existing algorithms from computational geometry and rock mechanics were applied and, where necessary, extended to enable the intended application. Once finite blocks had been identified, their geometric and inertia properties were calculated.

The identified finite blocks were subsequently analysed with respect to their movability from the rock mass towards the free space. The theory of kinematics of a rigid body was discussed and applied for rock blocks. Methods for the kinematic analysis of a finite block were reviewed. The concept of the kinematic analysis after block theory for translations was outlined while a new method based on the same concept was introduced for pure block rotations. A numerical method for analysing the movability of a block about a remote axis was also introduced. Several examples outlined the application of the newly introduced methods.

The contact between the rock block and the adjacent rock mass is the rock joint. One chapter is dedicated to the mechanical behaviour of rock joints in order to quantify the interaction between block and rock mass. Approaches to quantify the behaviour of rock joints were reviewed. Focussing on rough unfilled rock joints the typical stages and related behaviours during joint displacement were discussed. The drawn conclusions formed the basis for establishing a constitutive

model for rock joints under shear and normal loading with confined boundary conditions and degrading rock joint roughness. Typical responses of the constitutive model to varying input parameters were addressed in a parametric study.

Judging the stability of a rock block is the prime interest of a rock mechanics analysis. Traditional approaches had predominantly focussed on limit equilibrium methods. Within this work a framework for the mechanical analysis of a rock block based on the equations of motion of a constrained rigid body was developed. Suitable numerical methods for solving the dynamic and static equations were discussed and peculiarities of their application outlined. The proposed stability analysis followed the concept of the single block analysis, a recently introduced numerical method for analysing critical states of rock blocks. The concept of the single block analysis was adjusted to fit into the framework of the previously established dynamic environment. Several typical load cases were also described. The steps of the method were highlighted in an illustrative example of a rock block in the crown of a cavern.

The work required the synthesis of methods from different disciplines including engineering geology, digital photogrammetry, computer vision, digital image processing (all three were basically used in the imaging system ShapeMetriX3D), computational geometry, numerical analysis, laboratory testing, general mechanics, and finally rock mechanics. The aim was to inform solutions with analytic approaches. It became obvious that for many of the mechanical problems only numerical methods would provide consistent solutions.

The proposed method for rock block analysis integrates 3D imaging as a new technology into a method for rock mechanics taking advantage of advances in other non-geoscience related disciplines, and increased computational power and imaging capabilities. The primary result, the 3D image, represents a new quality standard in data acquisition, documentation, and presentation allowing for an enhanced number of measurements. This improvement in data acquisition called also for new methods in the subsequent processing and analysis of the data. The enhanced general solutions for traditional but limited approaches, for instance for treatment of arbitrary block geometries, arbitrary block motion, etc, eased the algorithmic analysis of arbitrary joint systems.

The methods for the kinematic analysis provide information on the movability of rock blocks only with geometric data. They are computationally efficient, thus results are obtained quickly. Movable blocks are distinguished from constrained or tapered blocks for all possible displacements. The presented static and dynamic methods are capable of describing any feasible motion and related failure mode. There are no feasible limits with respect to block geometry and load cases. With modern computer equipment results are also available within a short time. The consistent approach provides insights into the behaviour of a block on its way to equilibrium or failure. Post-failure analysis is also possible.

Since the identified failure mode is not limited to strict assumptions or simplifications, the methods help to avoid unconservative or wrong design of excavation and support.

The author recommends further research in identifying unstable united blocks (blocks composed of several single blocks) from trace networks, implementing robustly a sophisticated joint constitutive model together with modelling dilation and initial rock stresses, implementing support elements such as pre-tensioned cable anchors, grouted rock bolts, and shotcrete, and implementing additionally time-dependent loads (seismicity, blasts, vibrations) in the dynamic analysis. For calculating initial stress fields the integration of the boundary element method seems to be reasonable.

References

- 3G Software & Measurement GmbH. 2006. *Report on determination of relative camera orientations*. unpublished.
- 3G Software & Measurement GmbH. 2010. *ShapeMetriX3D User Manual Version 3.5*. self-published.
- Archambault, G., Fortin, M., Gill, D. E., Aubertin, M. & Ladanyi B. 1990. Experimental investigations for an algorithm simulating the effect of variable normal stiffness on discontinuities shear strength. In *Proc. Int. Symp. on Rock Joints*. Barton & Stephansson (eds.). Leon, Norway, 4-6 June 1990: 141-148.
- Aulbach, B. 2004. *Gewöhnliche Differentialgleichungen*. 2. Auflage, Elsevier, Spektrum Akad. Verl., München.
- Baecher, G. B., Lanney, N. A. & Einstein, H. H. 1977. Statistical Description Of Rock Properties And Sampling. In *18th U.S. Symposium on Rock Mechanics (USRMS)*, 22 – 24 June 1977 , Golden, CO, 5C1.1–5C1.8.
- Bandis, S. C., Lumsden, A. C. & Barton, N. 1983. Fundamentals of Rock Joint Deformation. *Int. J. Rock Mech. Min. Sci. & Geomech. Abstr.* 20: 249-268.
- Bandis, S. C., Barton, N. & Christianson, M. 1985. Application of a new numerical model of joint behaviour to rock mechanics problems. In *Proc. Int. Symp. on Fundamentals of Rock Joints*. Björkliden, 15-20 September 1985: 345-355.
- Bandis, S. C. 1990. Mechanical properties of rock joint. In *Proc. Int. Symp. on Rock Joints*. Barton & Stephansson (eds.). Leon, Norway, 4-6 June 1990: 125-140.
- Barton, N. 1971. *A model study of the behaviour of steep excavated rock slopes*. Thesis, Univ. Lond., 376pp.
- Barton, N. 1973. Review of a new shear strength criterion for rock joints. *Engineering Geology* 7: 287-332.
- Barton, N. & Choubey, V. 1977. The Shear Strength of Rock Joints in Theory and Practice. *Rock Mechanics* 10: 1-54.
- Baumgarte, J. 1972. Stabilization of Constraints and Integrals of Motion in Dynamical Systems. *Computer Methods in Applied Mechanics and Engineering*, Vol. 1, 1-16
- Bayo, E., García de Jalón, J., & Serna, M. A. 1988. A Modified Lagrangian Formulation for the Dynamic Analysis of Constrained Mechanical Systems”, *Computer Methods in Applied Mechanics and Engineering*, Vol. 71, 183-195.
- Bažant, Z. P. 1989. Bifurcations and Thermodynamic Criteria of Stable Paths of Structures exhibiting Plasticity and Damage Propagation. In *Computational Plasticity (COMPLAS 2)* Proc. 2nd Int. Conf. held in Barcelona, Spain, Owen, Hinton & Oñate (eds.), Pineridge Press, Swansea, 1-25.
- Bellian, J. 2003. Laser intensity mapping of outcrop geology. *Oil IT Journal*, www.oilit.com online January 2009.

- Beer, A. J., Stead, D. & Coggan, J. S. 2002. Estimation of the Joint Roughness Coefficient (JRC) by Visual Comparison. *Rock Mech. Rock Eng.* 35(1): 65-74.
- de Berg, M., van Kreveld, M., Overmars, M. & Schwarzkopf, O. 2000. *Computational Geometry – Algorithms and Applications*. 2nd Edition, Springer, Berlin, Heidelberg, New York.
- Boehm, W. & Müller, A. 1999. On de Casteljau's algorithm. *Computer Aided Geometric Design* 16: 587-605.
- Boulon, M., Armand, G., Hoteit, N. & Divoux, P. 2002. Experimental investigations and modelling of shearing of calcite healed discontinuities of granodiorite under typical stresses. *Engineering Geology* 64: 117-133.
- Brady, B. H. G. & Brown, E. T. 2004. *Rock Mechanics for Underground Mining*. Kluwer Academic Publishers: Dordrecht, The Netherlands
- Brayton, R. K., Director, S. W., Hachtel G. D. & Vidigal, L. 1979. A New Algorithm for Statistical Circuit Design Based on Quasi-Newton Methods and Function Splitting, *IEEE Transactions on Circuits and Systems*, Vol. CAS-26 (9), 784-794.
- Brenan, K. E, Campbell, S. L. & Petzold, L. R. 1989. *The Numerical Solution of Initial Value Problems in Differential-Algebraic Equations*. SIAM, New York.
- Brosch, F. J., Pischinger, G., Steidl A., Vanek R. & Decker, K. 2001. Improved site investigation results by kinematic discontinuity analysis on drill cores. In *Int. Proc. of the EUROCK 2001 symposium, Rock mechanics – a challenge for society*. Särkkä, P. & Eloranta, P. (eds.), Espoo, Finland, 4-7 June 2001, 41-45.
- Brown, D. C. 1971. Close-Range Camera Calibration. *Photogrammetric Engineering* Vol. 37 No. 8, 855-866.
- Bulut, F. & Tüdes, S. 1996. Determination of discontinuity traces on inaccessible rock slopes using electronic tacheometer: an example from the Ikizdere (Rize) Region, Turkey. *Engineering Geology* Vol. 44, 229-233.
- Butcher, J. C. 2008. *Numerical methods for ordinary differential equations*. John Wiley & Sons Ltd, West Sussex, England
- Butt, R. 2007. *Introduction to Numerical Analysis Using Matlab*. Jones & Bartlett Publ.
- Button, E. A. 2004. *A Contribution to the Characterization of Phyllitic and Schistose Rock Masses for Tunnelling*. Doctoral Thesis, Institute for Rock Mechanics and Tunnelling, Graz University of Technology.
- Cardona, A. & Huespe, A. 1998. Continuation methods for tracing the equilibrium path in flexible mechanism analysis. *Engineering Computations*, Vol. 15 No. 2, 190-220.
- Chan, H. C. & Einstein, H. H. 1981. Approach to complete limit equilibrium analysis for rock wedges. The method of 'artificial supports'. *Rock Mechanics and Rock Engineering* 14: 59-86.
- Chan, L.-Y. 1987. *Application of block theory and simulation techniques to optimum design of rock excavations*. Ph.D. dissertation, University of California, Berkeley, USA.

- Coggan, J. S., Wetherelt, A., Gwynn, X. P. & Flynn, Z. N. 2007. Comparison of hand-mapping with remote data capture systems for effective rock mass characterisation. In *Proc. 11th Congress ISRM - the second half century of rock mechanics*, Sousa, E. L., Olalla, C. & Grossman, N. F. (eds.), Volume 1, Lisbon, Portugal, 9-13 July 2007, 201-205.
- Coulson, J. H. 1970. *The effects of surface roughness on the shear strength of joints in rock*. Thesis. Univ. Illinois. U.S. Dept. Army Corps Eng., Miss. River Div., Omaha, Nebr., Tech. Rep. MRD-2-20: 283pp.
- Courant, R. 1943. Variational methods for the solution of problems of equilibrium and vibrations. *Bull. Amer. Math. Soc.* 49, 1-23.
- Crisfield, M. A. 1981. A fast incremental/iterative solution procedure that handles 'snap-through', *Comput. Struct.* 13, 55-62
- Crosta, G. 1997. Evaluating Rock Mass Geometry From Photogrammetric Images. *Rock Mechanics and Rock Engineering* 30(1): 35-38.
- Daehnke, A., Watson, B. P., Roberts, D., Acheampong, E. & van Zyl, M. 2000. *The impact of soft loading conditions on the performance of elongate support elements*. Final project report GAP613, Safety in Mines Research Advisory Committee, CSIR Division of Mining Technology.
- Dahlquist, G. 1956. Convergence and stability in the numerical integration of ordinary differential equations. *Math. Scand.* 4, 33-53
- Deere, D. U., Hendron, A. J., Patton, F. D. & Cording, E. J. 1966. Design of surface and near-surface construction in rock. In *Proc. 8th U.S. Rock Mech. Symp.*
- Dietmair, P. 2007. *Dynamik von Mehrkörpersystemen*. Lecture notes, unpublished, Graz University of Technology
- Dong, J.-J. & Pan, Y.-W. 1992. A Hierarchical Model of Rough Rock Joints Based on Micromechanics. *Int. J. Rock Mech. Min. Sci. & Geomech. Abstr.* 33(2): 111-123.
- Drozd, K. 1967. Variations in the shear strength of a rock mass depending on the displacements of the test blocks. In *Proc. 13th Symp. Rock Mech.*, Urbana, Ill., 1971. Am. Soc. Civ. Eng., New York, N.Y.: 77-105.
- Dutta, A. & White, D. W. 1997. Automated solution procedures for negotiating abrupt non-linearities and branch points. *Engineering Computations* 14 (1): 31-56.
- Eberhardt, E. 2003. *Rock Slope Stability Analysis - Utilization of Advanced Numerical Techniques*. Vancouver, Canada: Earth and Ocean Sciences, University of British Columbia.
- Edelsbrunner, H. 1995. Algebraic decomposition of non-convex polyhedra. *Proc. 36th Ann. Symp. Found. Comp. Sci.*, 23-25 October 1995, Milwaukee, WI, 248-257.
- Falcao, A. X., Udupa, J. K. & Miyazawa, F. K. 2000. An ultra-fast user-steered image segmentation paradigm: Live-wire-on-the-fly. *IEEE Trans. on Medical Imaging* 19(1): 55-62.
- Fardin, N., Stephansson, O. & Jing, L. 2001. The scale dependence of rock joint surface roughness. *Int. J. Rock Mech. Min. Sci.* 38: 659-669.

- Fardin, N., Feng, Q. & Stephansson, O. 2004. Application of a new in situ 3D laser scanner to study the scale effect on the rock joint surface roughness. *Int. J. Rock Mech. Min. Sci.* 41: 329-335.
- Fasching, A., Gaich, A. & Schubert, W. 2001. Data acquisition in Engineering Geology. An improvement of Acquisition Methods for Geotechnical Rock Mass Parameters. *Felsbau* 19 (5), 93-101.
- Faugeras, O. 1993. *Three-Dimensional Computer Vision*. MIT Press, Boston, MA.
- Fecker, E. & Rengers, N. 1971. Measurement of large scale roughness of rock planes by means of profilograph and geological compass. *Proc. Symp. Soc. Int. Mécanique des Roches*, Nancy, France, 1-18.
- Felippa, C. 1987. *Nonlinear Finite Element Methods*. Department of Aerospace Engineering, University of Colorado at Boulder, downloaded on July 28, 2009 from www.colorado.edu/engineering/CAS/courses.d/NFEM.d/
- Feng, Q., Sjogren, P., Stephansson, O. & Jing, L. 2001. Measuring fracture orientation at exposed rock faces by using a non-reflector total station. *Engineering Geology* 59: 133-146.
- Ferrero, A. M., Forlani, G., Roncella R. & Voyat, H. I. 2008. Advanced Geostructural Survey Methods Applied to Rock Mass Characterization. *Rock Mech. Rock Eng.* DOI 10.1007/s00603-008-0010-4, online June 21, 2008.
- Fischler, M. & Bolles, R. 1981. Random sample consensus: a paradigm for model fitting with application to image analysis and automated cartography. In *Commun. Assoc. Comp. Mach.* 24(3): 81-95.
- Franklin, J. A., Maerz, N. H. & Bennet, C. P. 1988. Rock mass characterisation using photoanalysis. *Int. Journal of Mining and Geological Engineering* 6: 97-112.
- Gaich, A., Fasching, A. & Schubert, W. 2003. Improved site investigation. Acquisition of geotechnical rock mass parameters based on 3D computer vision. In Beer, G. (ed.) *Numerical Simulation in Tunnelling*: 13-46, Springer, Wien.
- Gaich, A., Pötsch, M., Fasching, A. & Schubert, W. 2004. Measurement of rock mass parameters using 3D imaging. In G. Barla & M. Barla (eds.), *Caratterizzazione degli amassi rocciosi nella progettazione geotecnica: X Ciclo di Conferenze di Meccanica ed Ingegneria delle Rocce*, Torino, 24-25 November 2004: 21-45. Pàtron editore: Bologna.
- García de Jalón, J. & Bayo, E. 1994. *Kinematic and Dynamic Simulation of Multibody Systems: The Real Time Challenge*. Springer-Verlag, New York
- Garey, M. R., Johnson, D. S., Preparata, F. P. & Tarjan, R. E. 1978. Triangulating a simple polygon. *Inform. Process. Lett.* 7: 175-179.
- Gembicki, F. W. 1974. *Vector Optimization for Control with Performance and Parameter Sensitivity Indices*, Ph.D. Dissertation, Case Western Reserve Univ., Cleveland, OH, .
- Gentier, S., Riss, J., Archambault, G., Flamand, R. & Hopkins, D. 2000. Influence of fracture geometry on shear behavior. *Int. J. Rock Mech. Min. Sci.* 37: 161-171.

- Ghirotti, M. & Genevois, R. 2007. A complex rock slope failure investigated by means of numerical modelling based on laser scanner technique. In *Proc. 1st Canada-U.S. Rock Mechanics Symposium – Rock Mechanics, Meeting Society's Challenges and Demands*, Stead & Eberhardt (eds.), Vancouver, Canada, 27-31 May 2007, 917 – 924.
- Gianni, G. P. 1992. *Rock Slope Stability Analysis*. Balkema, Rotterdam Brookfield.
- Goldstein, H., Poole, C. P. & Safko, J. L. 2006. *Klassische Mechanik – 3. Auflage*. Weinheim: Wiley-VCH-Verlag.
- Gonzalez-Ochoa, C., McCammon, S. & Peters, J. 1998. Computing Moments of Objects Enclosed by Piecewise Polynomial Surfaces. *ACM Transaction on Graphics* 17(3): 143-157.
- Goodman, R. E. 1976. *Methods of Geological Engineering in Discontinuous Rocks*. West Publishing Co., 472 pp.
- Goodman, R. E. & Bray, J. W. 1977. Toppling of rock slopes. *Proc. Spec. Conf. on Rock Engng. for Found. And Slopes*, Vol. 2, 201-234.
- Goodman, R. E. & Shi, G.-H. 1985. *Block Theory and Its Application to Rock Engineering*. Prentice-Hall, New Jersey.
- Goodman, R. E. 1995. Block theory and its application. The Rankine Lecture. *Géotechnique* 45 (3), 383-423.
- Grasselli, G. 2001. *Shear strength of rock joints based on quantified surface description*. PhD dissertation, EPFL, Switzerland.
- Grasselli, G., Wirth, J. & Egger, P. 2002. Quantitative three-dimensional description of a rough surface and parameter evolution with shearing. *Int. J. Rock Mech. Min. Sci.* 39: 789–800.
- Grasselli, G. & Egger, P. 2003. Constitutive law for the shear strength of rock joints based on three-dimensional surface parameters. *Int. J. Rock Mech. Min. Sci.* 40: 25–40.
- Hagan, T. O. 1980. A Case for Terrestrial Photogrammetry in Deep-Mine Rock Structure Studies. *Int. J. Rock Mech. Min. Sci.* 17: 191-198.
- Hairer, E. & Wanner, G. 2009. Article *Linear multistep method* at http://www.scholarpedia.org/article/Linear_multistep_method
- Han, S. P. 1977. A Globally Convergent Method For Nonlinear Programming. *J. Optimization Theory and Applications*, Vol. 22, p. 297.
- Handanyan, J. M., Danek, E. R., D'Andrea, R. A. & Sage, J. D. 1990. The role of tension in failure of jointed rock. In *Proc. Int. Symp. on Rock Joints*. Barton & Stephansson (eds.), Leon, Norway, 4-6 June 1990: 195-202.
- Haneberg, W. C. 2008. Using close range terrestrial digital photogrammetry for 3-D rock slope modeling and discontinuity mapping in the United States. *Bulletin of Engineering Geology and the Environment*, Vol. 67 (4), 457-469.
- Harer, G. 2009. Koralm tunnel – Benefits of a structured investigation process for a large tunnel project – the clients view. In *Proc. World Tunnel Congress 2009*, 23–28 May 2009, Budapest, Hungary,
- Harries, N., Noon, D. & Rowley, K. 2006. Case Studies of Slope Stability Radar used in Open Cut Mines. *Proc. Int. Symp. Stability of Rock Slopes*. The

- South African Institute for Mining and Metallurgy, April 3-6, 2006, 335-342
- Hart, R., Cundall, P. & Lemos, J. 1988. Formulation of a Three-Dimensional Distinct Element Model - Part II: Mechanical Calculations for Motion and Interaction of a System Composed of Many Polyhedral Blocks. *Int. J. Rock Mech., Min. Sci. & Geomech. Abstr.* 25, 117-126.
- Hein-Stumpff, M. 2009. *Vergleichende Standsicherheitsuntersuchungen von Kavernen in geklüftetem Fels mittels Blocktheorie und 3DEC*. Diploma Thesis, Institute for Geotechnics, Vienna University of Technology, Austria (in German)
- Heuser, H. 2009. *Gewöhnliche Differentialgleichungen. Einführung in Lehre und Gebrauch*. 6. Auflage, Vieweg + Teubner, Wiesbaden
- Hoek, E. & Bray, J. W. 1981. *Rock Slope Engineering*. 3rd edition. Taylor & Francis, New York.
- Hoek, E. & Brown, E. T. 1990. *Underground Excavations in Rock*. Taylor & Francis, Oxon
- Homand, F., Belem, T. & Souley, M. 2001. Friction and degradation of rock joint surfaces under shear loads. *Int. J. Num. Anal. Meth. in Geomech.* 25: 973-999.
- Houlsby, G. T., Liu, G. & Augarde, C. E. 2000. A tying scheme for imposing displacement constraints in finite element analysis. *Commun. Numer. Meth. Engng.* 16: 721-732.
- Huang, X., Haimson, B. C., Plesha, M. E. & Qiu, X. 1993. An Investigation of the Mechanics of Rock Joints - Part I. *Int. J. Rock Mech. Min. Sci. & Geomech. Abstr.* 30(3): 257-269.
- Hutson, R. W. & Dowding, C. H. 1990. Joint asperity degradation during cyclic shear. *Int. J. Rock Mech. Min. Sci. & Geomech. Abstr.* 27(2): 109 -119.
- Ikeda, K. & Murota, K. 2010. *Imperfect Bifurcation in Structures and Materials*. 2nd edition, Springer, New York
- Indraratna, B. & Haque, A. 2000. *Shear Behaviour of Rock Joints*. Balkema: Rotterdam, Brookfield.
- Indraratna, B., Welideniya, H. S. & Brown, E. T. 2005. A shear strength model for idealised infilled joints under constant normal stiffness. *Géotechnique* 55(3): 215-226.
- Indraratna, B., Jayanathan, M. & Brown, E. T. 2008. Shear strength model for overconsolidated clay-infilled idealised rock joints. *Géotechnique* 58(1): 55-65.
- ISRM Committee on field test, 1977. International Society for Rock Mechanics, Commission on Standardization of Laboratory and Field Tests. Suggested Methods for the Quantitative Description of Discontinuities in Rock Masses. *Int. J. Rock Mech. Min. Sci. & Geomech. Abstr.* 15: 319-368.
- Jing, L. 2000. Block system construction for three-dimensional discrete element models of fractured rocks. *Int. J. Rock Mech. Min. Sci.* 37: 645-659.
- Joeckel, R., Stober, M. & Huep, W. 2008. *Elektronische Entfernungsmessung und Richtungs-messung und ihre Integration in aktuelle Positionierungsverfahren*. 5. Auflage, Wichmann, Heidelberg.

- John, K. W. 1968. Graphical stability analysis of slopes in jointed rock. *J. Soil Mech. Found. Div. ASCE* 94 (2): 497-526.
- John, K. W. & Deutsch, R. 1974. Die Anwendung der Lagenkugel in der Geotechnik. In *Festschrift Leopold Müller – Salzburg, Zum 65. Geburtstag*. Fecker, E., Götz, H.-P., Sauer, G. & Spaun, G. (eds.), Karlsruhe, 137-159.
- Karzulovic, A. L. 1988. *The Use of Keyblock Theory in the Design of Linings and Supports for Tunnels*. Ph.D. Dissertation. University of California, Berkeley.
- Kemeny, J., Mofya, E. & Handy, J. 2003. The use of digital imaging and laser scanning technologies for field rock fracture characterization. Proc. Soil Rock America 2003 (*12th PanAmerican Conf. Soil Mech. Geotech. Eng. and the 39th US Rock Mechanics Symposium*), Eds. J. Culligan, H. Einstein, A. White, Massachusetts Institute of Technology, Cambridge, MA, 117-122.
- Kemeny, J. & Post, R. 2003. Estimating three-dimensional rock discontinuity orientation from digital images of fracture traces. *Computers & Geosciences* 29: 65–77.
- Kemeny, J., Turner, K. & Norton, B. 2006. LIDAR for Rock Mass Characterization: Hardware, Software, Accuracy and Best-Practices. In *Laser and Photogrammetric Methods for Rock Face Characterization*. Tonon, F. & Kottenstette, J. (eds.), Report on a workshop, June 17-18, 2006, Golden, Colorado, 49-61.
- Kieffer, D. S. 1998. *Rock Slumping: A Compound Failure Mode of Jointed Hard Rock Slopes*. Ph.D. dissertation. University of California at Berkeley, USA.
- Klee, V. 1959. Some characterizations of convex polyhedra. *Acta Math.* 102, 79-107.
- Kovári, K. & Fritz, P. 1978. Slope Stability with Plane, Wedge and Polygonal Sliding Surfaces. In *Proc. Int. Symp. Rock Mechanics Related To Dam Foundations – Special Print*, 27-29 September 1978, Rio de Janeiro, Brazil, 103–124.
- Kuipers, J. B. 1998. *Quaternions and Rotations Sequences*. Princeton University Press.
- Kulatilake, P. H. S. W., Shou, G., Huang, T. H. & Morgan, R. M. 1995. New Peak Shear Strength Criteria for Anisotropic Rock Joints. *Int. J. Rock Mech. Min. Sci.* 32(7): 673-697.
- Kulatilake, P. H. S. W., Balasingam, P., Park, J. & Morgan, R. 2006. Natural rock joint roughness quantification through fractal techniques. *Geotech. Geolog. Eng.* 24: 1181-1202.
- Kulhawy, F. H. 1975. Stress deformation properties of rock and rock discontinuities. *Engineering Geology* 9, 327-350
- Kunkel, P. & Mehrmann, V. 2006. *Differential-algebraic equations: analysis and numerical solution*. EMS Textbooks in Mathematics, EMS Publishing House, Zürich.

- Ladanyi, B. & Archambault, G. 1970. Simulation of shear behavior of a jointed rock mass. In *Proc. 11th Symp. on Rock Mechanics: Theory and Practice*, AIME, New York, 105-125.
- Lee, D. T. & Preparata, F. P. 1977. Location of a point in a planar subdivision and its applications. *SIAM J. Comput.* 6: 594-606.
- Lee, H. S., Park, Y. J., Cho, T. F. & You, K. H. 2001. Influence of asperity degradation on the mechanical behaviour of rough rock joints under cyclic shear loading. *Int. J. Rock Mech. & Min. Sci.* 38(7): 967 - 980.
- Lee, Y., Ryu, D.-W. & Lee, H.-K. 2000. An Application of Stereophotogrammetry in Investigating Rock Discontinuity Orientation. *Geosystem Eng.* 3(2): 71-80.
- Lemy, F. & Hadjigeorgiou, J. 2003. Discontinuity trace map construction using photographs of rock exposures. *Int. J. Rock Mech. Min. Sci.* 40: 903-917.
- Lien, S.-L. & Kajiyama, J. T. 1984. A Symbolic Method for Calculating the Integral Properties of Arbitrary Non-convex Polyhedra. *Computer Graphics and Applications, IEEE*: 35-41.
- Linkwitz, K. 1963. Terrestrisch-photogrammetrische Kluftmessung. *Rock Mech. Eng. Geol.* I:152-159.
- Londe, P., Vigier, G. & Vormeringer, R. 1969. Stability of rock slopes, a three-dimensional study. *J. Soil Mech. Found. Div.*, ASCE 95 (1), 235-262.
- Londe, P., Vigier, G. & Vormeringer, R. 1970. Stability of rock slopes – graphical methods. *J. Soil Mech. Found. Div.*, Proc. ASCE 96 (4), 1411-1434.
- Lopez, P., Riss, J. & Archambault, G. 2003. An experimental method to link morphological properties of rock fracture surfaces to their mechanical properties. *Int. J. Rock Mech. Min. Sci.* 40: 947-954.
- Lu, J. 2002. Systematic identification of polyhedral rock blocks with arbitrary joints and faults. *Computers and Geotechnics* 29: 49-72.
- Magnus, K. & Müller, H. H. 1990. *Grundlagen der Technischen Mechanik*. Stuttgart: Teubner.
- Maksimovic, M. 1996. The Shear Strength Components of a Rough Rock Joint. *Int. J. Rock Mech. Min. Sci. Geomech. Abstr.* 33(8): 769-783.
- Markland, J. T. 1972. A useful technique for estimating the stability of rock slopes when the rigid wedge slide type of failure is expected. *Imperial College Rock Mechanics Research Report* 19, 10 pp.
- Mauldon, M. & Goodman, R. E. 1990. Rotational kinematics and equilibrium of blocks in a rock mass. *Int. J. Rock Mech. Min. Sci. & Geomech. Abstr.* 27 (4), 291-301.
- Mauldon, M. & Goodman, R. E. 1991. Supplement to Mauldon & Goodman 1990. *Int. J. Rock Mech. Min. Sci. & Geomech. Abstr.* 28 (5), 457.
- Mauldon, M. 1992. *Rotational failure modes in jointed rock: A generalization of block theory*. Ph.D. dissertation. University of California at Berkeley, USA.
- Mauldon, M. & Goodman, R. E. 1996. Vector Analysis of Keyblock Rotations. *J. Geotech. Engng.* 122 (12), 976-987.
- Mirtich, B. 1996. Fast and accurate computation of polyhedral mass properties. *J. Graphics Tools* 1(2): 31-50.

- Mühlhaus, H.-B., Dyskin, A. & Pasternak, E. (eds.) 2001. *Bifurcation and Localisation Theory in Geomechanics*. Proc. 5th workshop. Perth, Australia.
- Nguyen, T. S. & Selvadurai, P. S. 1998. A Model for Coupled Mechanical and Hydraulic Behaviour of a Rock Joint. *Int. J. for Numerical and Analytical Methods in Geomechanics* 22(1): 29-48.
- Ninomiya, Y., Fu, B. & Cudahy, T. J. 2005. Detecting lithology with Advanced Spaceborne Thermal Emission and Reflection Radiometer (ASTER) multispectral thermal infrared “radiance-at-sensor” data. *Remote Sensing of Environment* 99, 127-139.
- Ohanian, O. J. 2005. Mass Properties in VTOL UAV Conceptual Design Software, Part I: Overview and General Algorithms. *Proc. 64th Ann. Conf. Soc. All. Weight Eng.*, Annapolis, Maryland, 16-18 May, 2005, SAWE Paper No. 3327, Cat. No. 12, 26 pp.
- Ohnishi, Y. & Dharmaratne, P. G. R. 1990. Shear behaviour of physical models of rock joints under constant normal stiffness conditions. In *Proc. Int. Symp. on Rock Joints*. Barton & Stephansson (eds.). Leon, Norway, 4-6 June 1990: 267-273.
- Olsson, R. & Barton, N. 2001. An improved model for hydromechanical coupling during shearing of rock joints. *Int. J. Rock Mech. Min. Sci.* 38: 317-329.
- Patton, F. D. 1966. Multiple modes of shear failure in rock. In *Proc. 1st Congr. Int. Soc. Rock Mech.*, Vol. 1: 509-513: Lisboa.
- Persson, B. N. J. 2000. *Sliding Friction – Physical Principles and Applications, Second Edition*. Springer: Berlin, Heidelberg.
- Pischinger, G. 2006. Modern rock face characterization techniques – a quarry application. In *Proc. Workshop on Modern rock face characterization techniques*, part 6, December 1, 2006, Graz, Austria.
- Plesha, M. 1987. Constitutive models for rock discontinuities with dilatancy and surface degradation. *Int. J. for Numerical and Analytical Methods in Geomechanics* 11(4): 345-362.
- Pötsch, M. 2002. *The influence of the three-dimensional stress condition at the tunnel face on the stability of removable blocks*. Diploma thesis, Institute for Rock Mechanics and Tunnelling, Graz University of Technology, Austria.
- Pötsch, M. & Schubert, W. 2006. Rotational kinematics of rock block with arbitrary geometries. *Felsbau* 24 (3), 30-36.
- Pötsch, M., Blümel, M., Schieg, T. & Seywald, C. 2007. The dilation potential of rough rock joints under CNL and CNS conditions. In *Proc. 11th Congr. Int. Soc. Rock Mech. – The second half century of rock mechanics*, Ribeiro e Sousa, Olalla & Grossmann (eds.), July 9-13, 2007, Lisbon, Portugal, 455-460.
- Powell, M. J. D. 1978. A Fast Algorithm for Nonlinear Constrained Optimization Calculations. Numerical Analysis, Watson G. A. (ed.), *Lecture Notes in Mathematics*, Vol. 630, Springer Verlag
- Preh, A., Poisel, R. & Hein-Stumpp, M. 2009. Vergleichende Untersuchungen zur Standsicherheit von Klufkörpern mittels Blocktheorie und

- 3DEC. in: *Online Datenerfassung, berührungslose Messverfahren, 3D-Modellierung und geotechnische Analyse in Geologie und Geotechnik*, Proc. COG conference, Marschallinger, R., Wanker, W. & Zobl, F. (eds.), 8th July, 2009, Salzburg, 113-123.
- Press, W. H., Teukolsky, S. A., Vetterling, W. T. & Flannery, B. P. 2007. *Numerical Recipes. The Art of Scientific Computing*. 3rd edition. Cambridge University Press.
- Priest, S. D. 1993. *Discontinuity analysis for rock engineering*. Chapman & Hall: London.
- Prost, G. 1980. Alteration mapping with airborne multispectral scanners. *Economic Geology*, Vol. 75 (6), 894-906.
- Przybilla, H.-J. 2006. Fusion of terrestrial laserscanning and digital photogrammetry. *Int. Archives of Photogrammetry, Remote Sensing and Spatial Information Sciences* Vol. 36 (5), Dresden, Germany.
- Qiu, X., Plesha, M. E., Huang, X. & Haimson, B. C. 1993. An Investigation of the Mechanics of Rock Joints - Part II. *Int. J. Rock Mech. Min. Sci. & Geomech. Abstr.* 30(3): 271-287.
- Reid, T. R. & Harrison, J. P. 2000. A semi automated methodology for discontinuity trace detection in digital images of rock mass exposures. *Int. J. Rock Mech. Min. Sci.* 37: 1073-1089.
- Rengers, N. 1967 Terrestrial Photogrammetry: A Valuable Tool for Engineering Geological Purposes. *Rock Mech. Eng. Geol.* V: 150-154.
- Riedmüller, G., Steidl, A., Pölsler, P. & Seren, S. 2002. Site Investigation for the Final Design of the Birecik Dam. *Felsbau* 20 (4), 40-46.
- Riks, E. 1972. The application of Newton's method to the problem of elastic stability. *J. Appl. Mech. (ASME)*, Vol. 39, 1060-1065
- Ritto-Corrêa, M. & Camotim, D. 2008. On the arc-length and other quadratic control methods: Established, less known and new implementation procedures. *Computers and Structures* 86, 1353-1368
- Roberts, G. & Poropat, G. 2000. Highwall mapping in 3-D at the Moura Mine using SIROJOINT. In *Beeston, J. W. (ed.) Bowen Basin Symposium 2000 Proceedings*, 371-377.
- Roberson, R. E. & Schwertassek, R. 1988. *Dynamics of Multibody Systems. An Introduction*. Springer Verlag
- Rorke, A. J. & Brummer, R. K. 1985. A Stereographic Mapping Technique. In: *SANGORM Symposium on Rockmass Characterisation*. November 1985, Randburg: MINTEK, 117-119.
- Ross-Brown, D. M., Wickens, D. H., & Markland, J. T. 1973. Terrestrial photogrammetry in open pits. Part 2. An aid to geological mapping. *Trans. Inst. Mining & Metallurgy, Sect. A*, Vol. 83(803), 115-130.
- Ruppert, J. & Seidel, R. 1992. On the difficulty of triangulating three-dimensional non-convex polyhedra. *Discrete and Computational Geometry* 7(1): 227-253.
- Saeb, S. & Amadei, B. 1992. Modelling Rock Joints under Shear and Normal Loading, *Int. J. Rock Mech. Min. Sci. & Geomech. Abstr.* 29(3): 267-278.

- Schieg, T. 2006. *Investigations on the shear behaviour of artificial rock joints*. Diploma Thesis, Institute for Rock Mechanics and Tunnelling, Graz University of Technology, Austria.
- Seidel, J. P. & Haberfield, C. M. 1995a. Towards an Understanding of Joint Roughness. *Rock Mech. Rock Eng.* 28(2): 69-92.
- Seidel, J. P. & Haberfield, C. M. 1995b. The Application of Energy Principles to the Determination of the Sliding Resistance of Rock Joints. *Rock Mechanics and Rock Engineering* 28(4): 211-226.
- Seidel, J. P. & Haberfield, C. M. 2002. A theoretical model for rock joints subjected to constant normal stiffness direct shear. *Int. J. Rock Mech. Min. Sci.* 39: 539-553.
- Seywald, C. 2006. *Investigations on the relationship between surface roughness and dilation of rock joints in direct shear*. Diploma Thesis, Institute for Rock Mechanics and Tunnelling, Graz University of Technology, Austria.
- Slama, Ch. C. (ed.) 1980. *Manual of Photogrammetry*. 4th edition. American Society of Photogrammetry, Falls Church, VA.
- Slob, S., Hack, H. R. G. K. & Turner, K. 2002. An approach to automate discontinuity measurements of rock faces using laser scanning techniques. In *Proc. ISRM EUROCK 2002*, Funchal, Portugal, Dinid da Gama, C. & Riberia e Sousa, L. (eds.), Lisboa, Sociedade Portuguesa de Geotecnia, 25-28 November 2002, 87-94.
- Slob, S., Hack, R., van Knapen, B., Turner, K. & Kemeny, J. 2005. A method for automated discontinuity analysis of rock slopes with 3D laser scanning. *Transport Research Board 84th Annual Meeting*, January, 2005, 187-194.
- Sonka, M. Hlavac, V. & Boyle, R. 1999. *Image Processing: Analysis, and Machine Vision*. 2nd edition, Pacific Grove et al.: PWS Publishing.
- Spence, A. & Jepson, A. D. (1985). Folds in the solution of two parameter systems and their calculation. Part I, *SIAM J. Numer. Anal.*, 22, 347-368.
- Steigerwald, M. F. 1990. BDF Methods for DAEs in Multibody Dynamics: Shortcomings and Improvements. In: *Real-Time Integration Methods for Mechanical System Simulation*, NATO ASI Series, Vol. 69, 345-352.
- Strang, G. 1976. *Linear Algebra and its Applications*. Academic Press, New York.
- Strouth, A. & Eberhardt, E. 2006. The use of LiDAR to overcome rock slope hazard data collection challenges at Afternoon Creek, Washington. In *Laser and Photogrammetric Methods for Rock Face Characterization*. Tonon, F. & Kottenstette, J. (eds.), Report on a workshop, June 17-18, 2006, Golden, Colorado, 109-120.
- Sturzenegger, M., Yan, M., Stead, D. & Elmo, D. 2007. Application and limitations of ground-based laser scanning in rock slope characterisation. *Proc. 1st Canada-U.S. Rock Mechanics Symposium*. Vancouver B.C., 27-31 May 2007, 29-36.
- Sturzenegger, M. & Stead, D. 2009. Quantifying discontinuity orientation and persistence on high mountain rock slopes and large landslides using terrestrial remote sensing techniques. *Nat. Hazards Earth Syst. Sci.* 9, 267-287

- Sulem, J. 2010. Bifurcation theory and localization phenomena. *European Journal of Environmental and Civil Engineering* 14(8-9), 989-1009
- Szymakowski, J. B. & Haberfield, C. M. 2001. Direct shear testing of large, jointed, soft rock masses – preliminary results. In *Proc. Int. Symp. Rock Mechanics – a Challenge for Society*. Särkkä & Eloranta (eds.): 307 – 312.
- Talobre, J. 1957. *La Mécanique des Roches (Rock Mechanics)*. Dunod, Paris, 39-44.
- Tonon, F. 1998. Generalization of Mauldon's and Goodman's Vector Analysis of Keyblock Rotations. *J. Geotech. Geoenviron. Engineering* 124 (10), 913-922.
- Tonon, F. 2004. Explicit Exact Formulas for the 3-D Tetrahedron Inertia Tensor in Terms of its Vertex Coordinates. *J. Math. Stat.* 1(1): 8-11.
- Tonon, F. 2007a. Analytical formulas for the geometric and inertia quantities of the largest removable blocks around tunnels. *Int. J. Num. and Analyt. Meth. in Geomech.* 31: 1301-1327.
- Tonon, F. 2007b. Analysis of single rock blocks for general failure modes under conservative and non-conservative forces. *Int. J. Numer. Anal. Meth. Geomech.* 31: 1567-1608.
- Tseng, Y.-H. & Wang, M. 2005. Automatic Plane Extraction from LIDAR Data Based on Octree Splitting and Merging Segmentation. *Proc. IEEE Int. Symp. Geoscience and Remote Sensing*, Vol. 5, July 25-29, 2005, 3281-3284.
- Ueng, T.-S., Peng, I.-H. & Jou, Y.-J. 2003. Size effect on shear strength of computer-aided-manufactured joints. *Proc. 10th congress of the ISRM 2003–Technology roadmap for rock mechanics*, South African Institute of Mining and Metallurgy: 1251-1256.
- U.S. Department of Transportation, Federal Highway Administration. 2008. GROUND-BASED LiDAR - Rock Slope Mapping and Assessment. Publication No. FHWA-CFL/TD-08-006, 103pp.
- Vieten, W. 1970. Die Ermittlung tektonischer Gefügedaten aus stereophotogrammetrischen Bruchwandaufnahmen. *Clausthaler Tektonische Hefte*. Heft 10, 319-336-
- Voyat, I., Roncella, R., Forlani, G. & Ferrero, A. M. 2006. Advanced techniques for geo structural surveys in modelling fractured rock masses: application to two Alpine sites. In *Laser and Photogrammetric Methods for Rock Face Characterization*. Tonon, F. & Kottenstette, J. (eds.), Report on a workshop, June 17-18, 2006, Golden, Colorado, 97-108.
- Warburton, P. M. 1981. Vector stability analysis of an arbitrary polyhedral rock block with any number of free faces. *Int. J. Rock Mech. Min. Sci. & Geomech. Abstr.* 25, 415-427.
- Wempner, G. A. 1971. Discrete approximations related to nonlinear theories of solids. *Int. J. Solids and Structures*, Vol. 7, 1581–1599
- Wittke, W. 1965. Methods to analyze the stability of rock slopes with and without additional loading. *Rock Mech. Engng. Geol. Suppl.* 11, 52-79.
- Wittke, W. 1984. *Felsmechanik*. Berlin: Springer Verlag.
- Wolf, P.R. & Dewitt, B.A. 2000. *Elements of Photogrammetry*. 3rd edition. McGraw-Hill, Boston.

- Yang, Z. Y., Di, C. C. & Yen, K. C. 2001. The effect of asperity order on the roughness of rock joints. *Int. J. Rock Mech. Min. Sci.* 38: 745-752.
- Yow, J. L. & Goodman, R. E. (1987). A Ground Reaction Curve Based Upon Block Theory. *Rock Mechanics and Rock Engineering* 20, 167-190.
- Zhang, Z. & Kulatilake, P. H. S. W. 2003. A new stereo-analytical method for determination of removal (sic!) blocks in discontinuous rock masses. *Int. J. Num. and Analyt. Meth. in Geomech.* 27(10): 791-811.